Draft version 2

# ATLAS NOTE

December 4, 2013

# Measurement of event-plane correlations in Pb-Pb collisions at $\sqrt{s_{NN}}$=2.76 TeV

Jiangyong Jia[a,c] and Soumya Mohapatra[a]

[a]*Department of Chemistry,Stony Brook University, Stony Brook, NY 11794, USA*
[c]*Brookhaven National Laboratory, Physics Department, Bldg. 510A, Upton, NY 11973, United States of America*

## Abstract

A measurement of correlations between reaction plane angles $\Phi_n$ is presented as a function of centrality for Pb-Pb collisions at $\sqrt{s_{\mathrm{NN}}} = 2.76$ TeV. These correlations are estimated from correlations of event plane angles $\Psi_n$ reconstructed using the calorimeters over a large pseudorapidity range $|\eta| < 4.8$, followed by a resolution correlation that accounts for the dispersion of $\Psi_n$ relative to $\Phi_n$. Significant positive correlation signals are observed for $4(\Phi_2 - \Phi_4)$, $6(\Phi_2 - \Phi_6)$, $6(\Phi_3 - \Phi_6)$, $2\Phi_2 + 3\Phi_3 - 5\Phi_5$ and $2\Phi_2 + 4\Phi_4 - 6\Phi_6$ and $-10\Phi_2 + 4\Phi_4 + 6\Phi_6$, while the correlation signals are negative for $2\Phi_2 - 6\Phi_3 + 4\Phi_4$. These results may shed light on the nature of the fluctuation of the created matter at the initial state as well as the subsequent hydrodynamic evolution.

# Contents


**1 Introduction** 2

**2 Event and track selections** 4

**3 Methodology** 7
- 3.1 Observables . . . 7
- 3.2 Calibration of $\Psi_n$ . . . 10
- 3.3 Procedure for obtaining correlation function and applying the resolution correction . . . 11
- 3.4 Determining the resolution . . . 13
- 3.5 Source of systematic errors . . . 14
- 3.6 Choice of Detectors . . . 15

**4 Two-plane correlation analysis** 15
- 4.1 Correlation function and extraction of raw signal . . . 15
- 4.2 Resolution determination . . . 23
  - 4.2.1 2SE results . . . 23
  - 4.2.2 3SE results . . . 25
  - 4.2.3 Resolution results . . . 26
- 4.3 Corrected results . . . 26
- 4.4 Cross checks . . . 33
  - 4.4.1 Dependence on the $\eta$ gap . . . 33
  - 4.4.2 Comparison of results obtained for different detectors . . . 37

**5 Three-plane correlation analysis** 40
- 5.1 Analysis with default detector . . . 40
- 5.2 Cross check with other detectors . . . 48

**6 Other systematics** 50
- 6.1 Trigger and event selections . . . 50
- 6.2 Run-by-run dependence . . . 50

**7 Summary of results** 54

**8 Weighted correlations** 58

**9 Two-Plane Correlations Weighted** 59
- 9.1 Raw Correlations . . . 59
- 9.2 Resolution . . . 62
- 9.3 Single-plane resolutions . . . 62
- 9.4 Systematic Errors for resolution . . . 63
  - 9.4.1 Sine terms in two-subevent resolution . . . 65
  - 9.4.2 Three-subevent resolution cross-checks . . . 67
- 9.5 Uncorrelated resolution errors . . . 72
- 9.6 Final Plots . . . 76
  - 9.6.1 Raw Correlations . . . 76
  - 9.6.2 Combined resolutions . . . 77
  - 9.6.3 Corrected Correlations . . . 79
  - 9.6.4 Cross-checks with tracking detectors . . . 81

**10 Three-plane correlations: Weighted** **84**
- 10.1 Raw Correlations . . . . . 84
- 10.2 Resolutions . . . . . 89
- 10.3 Uncorrelated errors . . . . . 94
- 10.4 Corrected correlations . . . . . 100
- 10.5 Final Plots . . . . . 102

**11 Appendix-I : Two-plane corrselations from tracking detectors** **105**
- 11.1 Raw Correlations . . . . . 105
- 11.2 Resolutions . . . . . 105
  - 11.2.1 Final Plots . . . . . 113

**12 Appendix-II : Three-plane correlations from tracking detectors** **114**

**13 Appendix III: $|Q_n|$ for symmetric detectors (Weighted correlations)** **124**

**14 Appendix IV: $|Q_n|$ weighted correlations** **129**

**15 Appendix V: Cross-check to evaluate effects of statistical fluctuations on weighted correlations** **131**

**16 Appendix VI: Some proofs** **132**

# 1 Introduction

The central focus of the heavy ion program at RHIC and LHC is to understand the properties of the strongly interacting Quark Gluon Plasma (sQGP) created in heavy ion collisions. A common tool used to study the properties of the sQGP is the azimuthal anisotropy of particles emitted in the transverse plane. A non-zero anisotropy can be traced to the elliptic shape of the initial fireball and the strong final state interaction, which transfers such spatial asymmetry into the transverse momentum ($p_{\mathrm{T}}$) space. Such final state interactions lead to an effective anisotropic pressure gradient in the overlap region, with a larger pressure gradient along the shorter axis of the fireball. This anisotropic pressure gradient drives an anisotropic collective expansion (or flow) of the fireball, which can be modeled via relativistic viscous hydrodynamic models. The magnitude of the azimuthal anisotropy is sensitive to properties of the sQGP, such as the ratio of the shear viscosity to the entropy density and to the equation of state [1, 2].

If we treat the nucleus as a smooth function described by Woods-Saxon geometry, then the overlap region has an almost elliptic shape (see Fig. 1). This spatial asymmetry can be quantified by the eccentricity of the overlap region and its direction:

$$\epsilon_2 = \frac{\langle y^2\rangle - \langle x^2\rangle}{\langle y^2\rangle + \langle x^2\rangle} = \frac{\sqrt{\langle r^2\cos 2\phi\rangle^2 + \langle r^2 \sin 2\phi\rangle^2}}{\langle r^2\rangle} \tag{1}$$

$$\tan 2\Phi_2^* = \frac{\langle r^2 \sin 2\phi\rangle}{\langle r^2\cos 2\phi\rangle} \tag{2}$$

where $(x, y)$ and $\phi$ are the position and azimuthal angle of a participating nucleon defined in a frame shifted to the center-of-gravity (i.e. $\langle x\rangle = \langle y\rangle = 0$), $y$ is along the major axis direction, and $r^2 = x^2 + y^2$. The spatial asymmetry leads to momentum anisotropy of final state particle $dN/d\phi \propto 1+2v_2 \cos 2(\phi-\Phi_2)$, where $\Phi_2$ is direction of maximum emission (called reaction plane or RP) which is strongly aligned with minor axis of the fireball: $\Phi_2^* + \pi/2$. The coefficient $v_2 = \langle\cos 2(\phi - \Phi_2)\rangle$ characterizes the magnitude of the anisotropy. Measurements from RHIC and LHC suggest that $v_2 \propto \epsilon_2$, with the proportional constant being sensitive to shear viscosity to entropy density ratio and EOS [3].

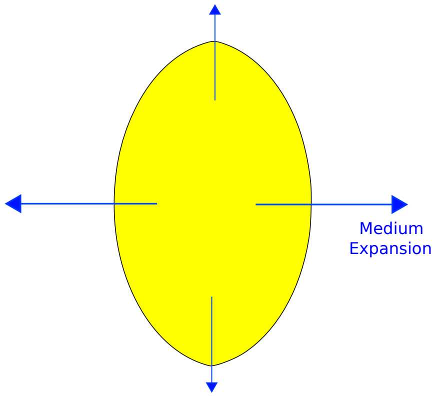


Figure 1: The elliptic fireball formed in a heavy-ion collision. The pressure gradient is larger along the minor axis (called reaction plane) than along the major axis. This results in a greater yield of particles along the minor axis direction. The reaction plane (RP) is defined by the directions of beam and minor axis.

So far we just considered the elliptic component of the overlap region. In general, the fireball may have other higher-order shape deformations. This is because each nucleus is consists of finite number of nucleons whose positions could fluctuate from event to event. Such fluctuations can lead to significant additional shape components, each at a different angular scale (illustrated in the top-left panel of Fig 2). The amplitude and the directions of these shape components can be estimated from the participating nucleons via a simple Glauber model as:

$$\epsilon_n = \frac{\sqrt{\langle r^n \cos n\phi\rangle^2 + \langle r^n \sin n\phi\rangle^2}}{\langle r^n\rangle}, \tag{3}$$

$$\tan n\Phi_n^* = \frac{\langle r^n \sin n\phi\rangle}{\langle r^n \cos n\phi\rangle} \tag{4}$$

These shape deformations, similar to $\epsilon_2$, can be transferred into higher-order azimuthal anisotropy in the $p_{\mathrm{T}}$ space via hydrodynamic evolution, leading to additional Fourier moments in the azimuthal distribution of particles:

$$dN/d\phi \propto 1 + 2\sum_{n=1}^{\infty} v_n \cos n(\phi - \Phi_n) \tag{5}$$

where $v_n$ and $\Phi_n$ represent the magnitude and phase of the $n^{th}$-order anisotropy (or flow) at corresponding angular scale $(2\pi/n)$, and $v_n = \langle \cos n(\phi - \Phi_n)\rangle$.

Experimentally, RP angles $\Phi_n$ are estimated using the azimuthal distribution of particles in the event. The precision of such estimation depends on the kinematic selection of the particles such as $p_{\mathrm{T}}$ or $\eta$. The estimated direction $\Psi_n$ is known as event-plane (EP) to distinguish from the reaction plane. With the above definition, $\Phi_n$,$\Psi_n$ and $\Phi_n^*$ all have a periodicity of $2\pi/n$, and are uniformly distributed over $[-\pi/n, \pi/n]$ in heavy ion collisions.

When fluctuations are small, one expect $v_n \propto \epsilon_n$, and the $\Phi_n$ to be correlated with minor-axis direction $\Phi_n^* + \pi/n$. However, model calculations show that the values of $\epsilon_n$ are large, and the alignment between $\Phi_n$ and $\Phi_n^* + \pi/n$ are strongly violated for $n > 2$ due to non-linear effects in hydrodynamic evolution [4].

Detailed measurements of $v_n$ have been performed at the LHC, and significant signals are observed for $n \leq 6$ [5, 6, 7]. In contrast, not much attention has been given to the study of $\Phi_n$, in particular the correlation between them. If the fluctuations are small and totally random, the orientations of the RP of different order are expected to be uncorrelated. Calculations based on a simple Glauber model show that the initial geometry have strong correlation between $\Phi_2^*$ and $\Phi_4^*$ in mid-central or peripheral collisions, while the correlation is generally weak in central collisions [9]. Furthermore, correlations

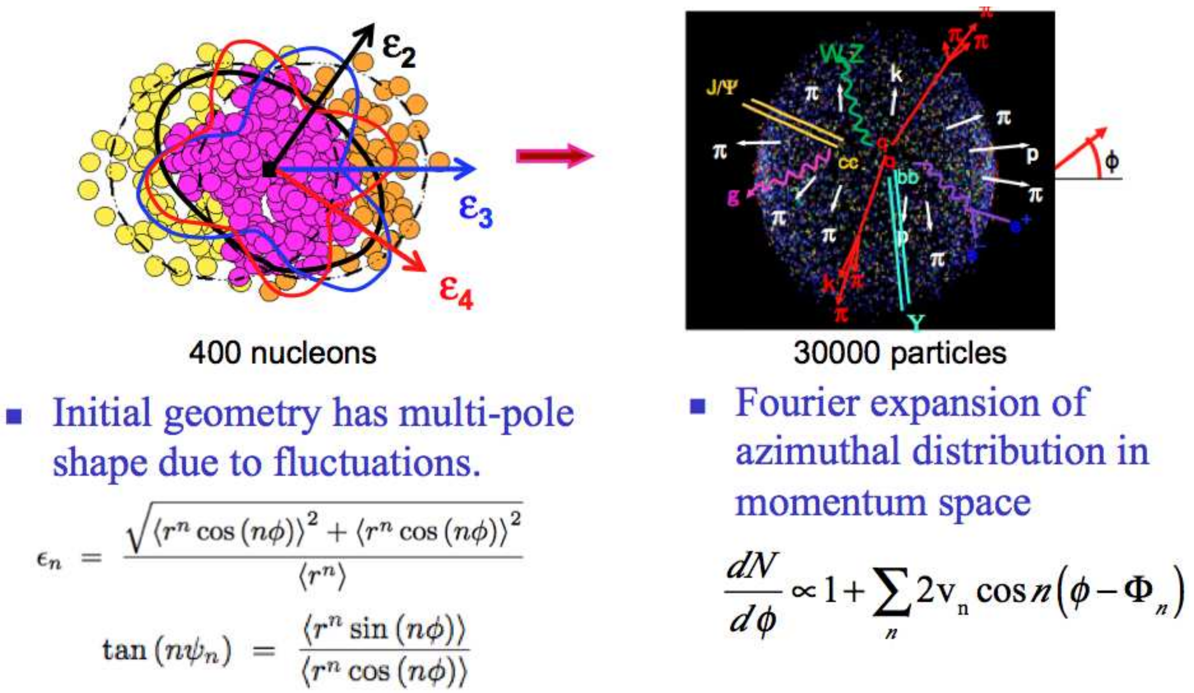


Figure 2: The schematic view of the different shape components arising from fluctuations of nucleons in the initial state (left panel), and Fourier expansion of particle azimuthal anisotropy in the transverse momentum space (right panel).

involving odd planes for $n > 2$ are found to be generally weak, e.g. between $\Phi_2^*$ and $\Phi_3^*$ or between $\Phi_2^*$ and $\Phi_5^*$, except in very peripheral collisions [8]. Previous measurements at RHIC and the LHC support a strong correlation between $\Phi_2$ and $\Phi_4$ [10], and a weak correlation between $\Phi_2$ and $\Phi_3$ [11, 12]. The correlations among three event-planes of different order have also been investigated recently in a model framework [9, 13, 15], but no experimental measurements exist to date. Hence a detailed measurement of the correlation between two and three event-planes can shed light on the nature of the fluctuation of the initial state geometry and dynamic mixing between different $\Phi_n$ during hydrodynamic evolution in the final state.

This measurement focuses on event-planes with $n \leq 6$, using the transverse energies in the electromagnetic calorimeters ECal and Forward calorimeters FCal within rapidity range $|\eta| < 4.9$. ECal and FCal are divided into a set of subevents, each covering a different rapidity range. The correlation signals are obtained from the relative angle distributions between the EPs of these subevents. This note is organized as follows. We first lay out the basic framework for measuring the correlations; we then present analysis details for two-plane correlators, including the EP measurement, resolution determination, and estimation of systematic uncertainties; we then discuss the measurement of three-plane correlators, followed by a summary of the main physics plots. The details of additional cross-checks of the measurement are included in the Appendix I and II.

## 2 Event and track selections

This analysis is based on the Pb-Pb data collected in 2010. The list of runs and cut conditions are summarized at https://twiki.cern.ch/twiki/bin/viewauth/Atlas/HeavyIonRunList. The minimum bias events are selected with the following set of standard selection criteria as in previous analysis:

| Run | Good LBs | Total Luminosity ($mb^{-1}$) | Run | Good LBs | Total Luminosity ($mb^{-1}$) |
|---|---|---|---|---|---|
| 169045 | 333 | 75.6 | 169136 | 545 | 171.7 |
| 169175 | 458 | 376.1 | 169206 | 374 | 186.9 |
| 169207 | 56 | 76.7 | 169223 | 405 | 378.4 |
| 169224 | 96 | 45.6 | 169226 | 366 | 257.2 |
| 169270 | 311 | 298.1 | 169564 | 140 | 123.7 |
| 169566 | 192 | 126.2 | 169567 | 114 | 69.7 |
| 169627 | 385 | 364.6 | 169648 | 63 | 66.5 |
| 169693 | 568 | 396.3 | 169750 | 368 | 199.3 |
| 169751 | 163 | 96.1 | 169765 | 307 | 161.8 |
| 169783 | 63 | 31.5 | 169839 | 222 | 197.2 |
| 169864 | 240 | 231.7 | 169927 | 575 | 526.5 |
| 169961 | 326 | 314.0 | 169964 | 93 | 94.6 |
| 169966 | 121 | 83.1 | 170002 | 462 | 522.8 |
| 170004 | 409 | 421.6 | 170015 | 161 | 236.1 |
| 170016 | 206 | 227.3 | 170080 | 27 | 28.2 |
| 170082 | 116 | 147.9 | 170398 | 380 | 392.6 |
| 170459 | 295 | 253.2 | 170482 | 212 | 314.3 |
| | | | Sum | 9269 | 7493.1 |

Table 1: List of runs used in this analysis.

- The event must be from a good lumi-block
- The event must pass at least one of the following triggers after prescale:
  - MBTS_1_1
  - MBTS_2_2
  - MBTS_3_3
  - MBTS_4_4
  - L1_ZDC_AND
  - L1_ZDC_A_C
- The event must pass L1_ZDC_AND or L1_ZDC_A_C triggers before prescale.
- It must have good MBTS timing defined as follows:
  - $|\mathrm{time}_A|$ or $|\mathrm{time}_C|$ must not equal 75 or 0 ns
  - $|\mathrm{time}_A - \mathrm{time}_C| < 3$ ns
- It must have a reconstructed vertex

In addition, the events passing the trigger selection are required to have a reconstructed z-vertex within 150 mm of the nominal center. A total of 48 million events are obtained from 34 runs. The list of runs and associated luminosity information is summarized in Table 1.

The Pb-Pb event centrality is characterized with the total transverse energy ($\sum E_T$) deposited in the FCal over the pseudorapidity range $3.2 < |\eta| < 4.9$ at the electromagnetic energy scale. An analysis of this distribution after all trigger and event selections gives an estimate of the fraction of the sampled non-Coulomb inelastic cross-section to be 98 ± 2% [14]. This estimate is obtained from a shape analysis of the measured FCal $\sum E_{\mathrm{T}}$ distributions compared with a convolution of proton-proton data with a Monte Carlo Glauber calculation. The FCal $\sum E_{\mathrm{T}}$ distribution is then divided into a set of 5% or 10% percentile bins, together with bins defined for the 5% most central events in 1% bins. The uncertainty associated with the centrality definition is evaluated by varying the effect of trigger and event selection inefficiencies as well as background rejection requirements in the most peripheral FCal $\sum E_{\mathrm{T}}$ interval. An example FCal energy distribution passing the above trigger selection criteria and the corresponding centrality percentile distributions are shown in Fig. 3. Note that the central collisions correspond to smaller centrality number, e.g. centrality (0-5)% corresponds to the 5% events with the highest FCal $E_{\mathrm{T}}$.

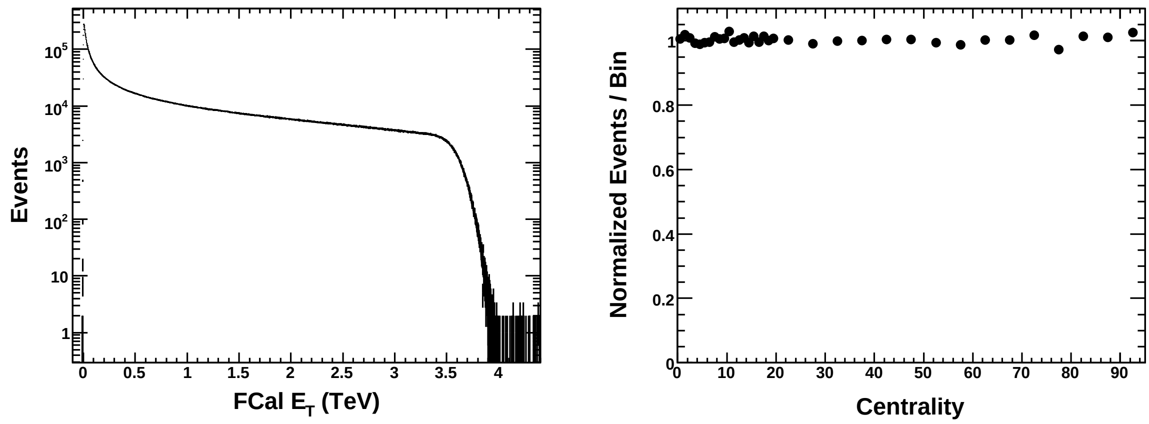


Figure 3: $E_T$ distribution in the FCal and the corresponding centrality percentile distribution (normalized to unity).

While the majority of the analysis uses only Calorimeter information, the charged tracks from the inner detector (ID)care used for cross-checks. The default selection criteria from previous $v_2$ and $v_n$ papers are used [6, 16]. They are listed here for completeness (more detailed definition can be found in [17]):

- Number of B-Layer hits > 0 if expected number of B-layer hits=1
- Number of Pixel hits > 0
- Number of Pixel holes = 0
- Number of SCT Hits > 7
- Number of SCT Holes <2
- $0.5 < p_T < 20GeV$
- $2.5 < \eta < 2.5$
- $\chi^2/ndf < 6.0$
- $|d_0| < 1mm$
- $|z_0 \times \sin(\theta)| < 1mm$

Note that the cuts on $|d_0|$ and $|z_0 \times \sin(\theta)|$ used here are 1.5 mm rather than the 1 mm cuts used in [6, 16]. Loosening this cut increases the number of tracks and thus increases the resolution for determining the EP correlations.

# 3 Methodology

This section sets out the basic mathematical framework for measuring the plane correlations. The observables used to quantify the event-plane correlations are defined, and the analysis steps for determining the correlation strength are presented.

## 3.1 Observables

As illustracted in Fig. 4, the $n^{\text{th}}$-order harmonic plane $\Phi_n$ has $n$-fold symmetry in azimuth. A general definition of the relative angle between two reaction planes $a_n\Phi_n + a_m\Phi_m$ has to be invariant under a phase shift:

$$\Phi_n \to \Phi_n + \frac{2\pi}{n} \text{ or } \Phi_m \to \Phi_m + \frac{2\pi}{m}\ , \tag{6}$$

and a global rotation by any angle $\theta$:

$$\Phi_n \to \Phi_n + \theta \text{ and } \Phi_m \to \Phi_m + \theta \tag{7}$$

The first condition requires $a_n$ ($a_m$) has to be multiple of n (m), while the second condition requires that the sum of the coefficients has to be zero $a_n + a_m = 0$. The relative angle $\Phi_{n,m} = k(\Phi_n - \Phi_m)$, with k being the least common multiple (LCM) of n and m, satisfies these constraints, as does any integral multiple of $\Phi_{n,m}$. The correlation between the reaction planes $\Phi_n$ and $\Phi_m$ is completely described by the differential distribution $dN_{\text{evts}}/(d\,(k(\Phi_n - \Phi_m))$. This distribution is an even function due to symmetry, hence it can be expanded into the following Fourier series:

$$\frac{dN_{\text{evts}}}{d\,(k(\Phi_n - \Phi_m))} \propto 1 + 2\sum_{j=1}^{\infty} V^j_{n,m} \cos jk(\Phi_n - \Phi_m) \tag{8}$$

$$V^j_{n,m} = \langle \cos jk(\Phi_n - \Phi_m)\rangle \tag{9}$$

The measurement of the two-plane correlation boils down to measuring the event average of a set of cosine functions $\langle \cos jk(\Phi_n - \Phi_m)\rangle$.

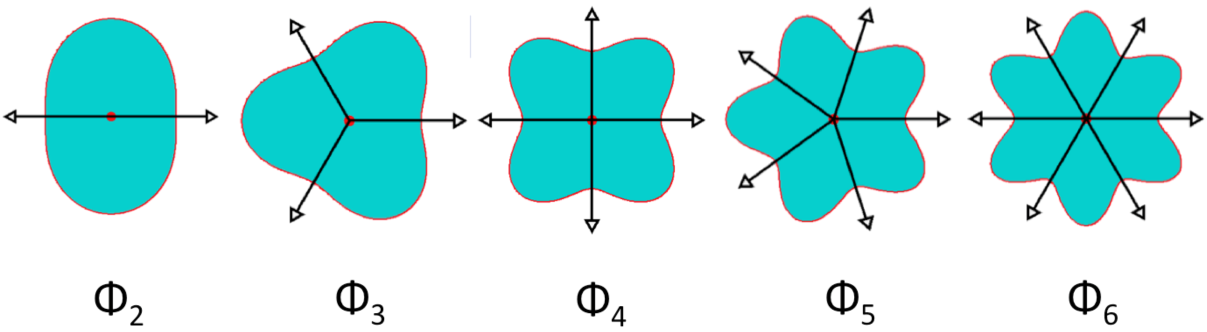


Figure 4: Illustration of the azimuthal shape of the harmonic component n=2-6. The angle of $n^{th}$-order harmonic shape $\Phi_n$ has n-fold ambiguity, i.e. $dN_{\text{evts}}/d\Phi_n$ has to be invariant under transformation: $\Phi_n \to \Phi_n + \frac{2\pi}{n}$.

This discussion can be generalized for correlation involving three reaction planes or more. The multi-plane correlator can be written as $\langle \cos(c_1\Phi_1 + 2c_2\Phi_2 ... + lc_l\Phi_l)\rangle$, with the constraint [13]:

$$c_1 + 2c_2 ... + lc_l = 0. \tag{10}$$

where $n^{\text{th}}$-order RP angle $\Phi_n$ always appears as multiple of $n\Phi_n$ in the correlator due to its $n$-fold symmetry. Furthermore, since experiment has no control on the overall orientation of the collision geometry, the relative angle has to be invariant under arbitrary global rotation. This leads to Eq. 10. The two-plane correlator defined in Eq.9, satisfies this constraint. For convenience, we shall refer to correlation involving two event-planes $\Phi_n$, $\Phi_m$ as "n-m" correlation, and three event-planes, $\Phi_n$, $\Phi_m$ and $\Phi_h$ as "n-m-h" correlation.

The multi-plane correlators are interesting because they carry additional information not accessible through two-plane correlators. The relative angle containing three or more $\Phi_n$ can be generally expressed as a linear combination of several two-plane relative angles. For example:

$$\begin{aligned}
2\Phi_2 + 4\Phi_4 - 6\Phi_6 &= 4(\Phi_4 - \Phi_2) - 6(\Phi_6 - \Phi_2) \\
-10\Phi_2 + 4\Phi_4 + 6\Phi_6 &= 4(\Phi_4 - \Phi_2) + 6(\Phi_6 - \Phi_2) \\
2\langle \sin 4(\Phi_4 - \Phi_2) \sin 6(\Phi_6 - \Phi_2)\rangle &= \langle \cos(2\Phi_2 + 4\Phi_4 - 6\Phi_6)\rangle - \langle \cos(-10\Phi_2 + 4\Phi_4 + 6\Phi_6)\rangle \quad (11)
\end{aligned}$$

and

$$\begin{aligned}
2\Phi_2 + 3\Phi_3 - 5\Phi_5 &= 3(\Phi_3 - \Phi_2) - 5(\Phi_5 - \Phi_2) \\
-8\Phi_2 + 3\Phi_3 + 5\Phi_5 &= 3(\Phi_3 - \Phi_2) + 5(\Phi_5 - \Phi_2) \\
2\langle \sin 3(\Phi_3 - \Phi_2) \sin 5(\Phi_5 - \Phi_2)\rangle &= \langle \cos(2\Phi_2 + 3\Phi_3 - 5\Phi_5)\rangle - \langle \cos(-8\Phi_2 + 3\Phi_3 + 5\Phi_5)\rangle \quad (12)
\end{aligned}$$

Therefore the combination of two three-plane correlators reflects the correlation of two angles relative to the third: if $\Phi_4$ and $\Phi_6$ preferably appear on the same side of $\Phi_2$, then the sine product in Eq. 11 would be positive, otherwise it would be negative. Recent study via a simple Glauber simulation suggests that some three-plane correlators may also be large and can be measured experimentally. One example is the famous $\langle \cos(\Phi_1 + 2\Phi_2 - 3\Phi_3)\rangle$ [9], but unfortunately this requires the determination of $\Phi_1$, which is complicated by effects from global momentum conservation. Momentum conservation does not affect higher-order planes. More detailed Glauber model simulations also suggest other three-plane correlators may be important [15], including $\langle \cos(2\Phi_2 + 4\Phi_4 - 6\Phi_6)\rangle$ and $\langle \cos(2\Phi_2 + 3\Phi_3 - 5\Phi_5)\rangle$. To date, no experimental measurements of three-plane correlations exist. As we will demonstrate in this analysis, these three-plane correlators are large and can be measured experimentally.

The discussion so far focuses on the correlation of true reaction planes. In a real experiment, the underlying reaction plane directions $\Phi_n$ are unattainable due to limited detector acceptance and finite multiplicity. They are approximated by the measured event-plane angle, $\Psi_n$, calculated from the azimuthal distribution of particles or energy in the detector acceptance. The coefficients $\langle \cos(c_1\Phi_1 + 2c_2\Phi_2 ... + lc_l\Phi_l)\rangle$ can be obtained by measuring the raw coefficients, followed by a simple correction for finite event-plane resolution (see appendix for a simple derivation for this formula):

$$\begin{aligned}
\langle \cos(c_1\Phi_1 + ... + lc_l\Phi_l)\rangle &= \frac{\langle \cos(c_1\Psi_1 + ... + lc_l\Psi_l)\rangle}{\mathrm{Res}\{c_1\Psi_1\}...\mathrm{Res}\{c_l l\Psi_l\}} \quad (13) \\
\mathrm{Res}\{c_n n\Psi_n\} &= \langle \cos c_n n(\Psi_n - \Phi_n)\rangle \quad (14) \\
& \quad (15)
\end{aligned}$$

The resolution factor $\mathrm{Res}\{c_n n\Psi_n\}$ can be determined using the standard two-subevent or three-subevent methods [20]. For convenience, we shall introduce a short-hand notation for the products of the resolution factors:

$$\mathrm{Res}\{c_1\Psi_1 + ... + lc_l\Psi_l\} \equiv \mathrm{Res}\{c_1\Psi_1\}...\mathrm{Res}\{c_l l\Psi_l\}. \quad (16)$$

To avoid auto-correlations, the various $\Psi_n$ should be measured using subevents covering different $\eta$ ranges, preferably with a gap in between.

A very large number of correlators could be studied. However, the measurability of these correlators is dictated by the experimental resolution factors: correlators may not be measurable if the associated resolutions for the event-planes are poor. To get a qualitative feeling, recall that the EP resolution depends on the resolution parameter $\chi_n$ as [20]:

$$\mathrm{Res}\{j n\Psi_n\} = \langle \cos jn(\Psi_n - \Phi_n)\rangle = \frac{\chi_n\sqrt{\pi}}{2} e^{-\frac{\chi_n^2}{2}} \left[ I_{(j-1)/2}(\frac{\chi_n^2}{2}) + I_{(j+1)/2}(\frac{\chi_n^2}{2}) \right] \tag{17}$$

$$\approx \begin{cases} 1 - \frac{j^2}{8z} + \frac{j^2(j^2-4)}{128z^2} - \frac{j^2(j^2-4)(j^2-16)}{3072z^3}, z = \chi_n^2/2 & \text{for large } \chi_n \\ \frac{\sqrt{\pi}}{2^j\Gamma(\frac{j+1}{2})}\chi_n^j & \text{for small } \chi_n \end{cases} ,$$

where the modified Bessel functions, $I_\alpha$, have been Taylor-expanded in the limit of large $\chi_n$ and small $\chi_n$. Such dependence of resolutions on $n$ (through $\chi_n$) and $j$ limits the types of two- and three-plane correlations one can study in practice.

Our previous publication [6] has demonstrated that the ATLAS calorimeters provide good resolution, $\mathrm{Res}\{n\Psi_n\}$, for $n = 2-6$ using FCal (see Fig. 5). The value of the $\chi_n$ is controlled by the magnitude of the physical flow signal; they typically decrease very quickly with increasing $n$ as shown by Fig. 5 for the FCal detector. Therefore, $\mathrm{Res}\{jn\Psi_n\}$ are expected to decrease very quickly for increasing $n$ (the right panel of Fig. 5 shows the case for j=1). However, they should decrease more slowly with $j$ for fixed $n$, especially for n=2 and 3 cases when $\chi_n$ is bigger than 1. Note that the previous analysis [6] chooses FCal for the EP measurement, primarily to maintain a clear separation in rapidity from the ID, which provided the differential $v_n$ measurement for charged tracks. Since this analysis concerns only the determination of the event planes, we can use the full calorimeter. The only limitation is that different event-planes involved in Eq. 13 should be measured using subevents covering different $\eta$ ranges to avoid auto-correlations. For two-plane correlation, $\Phi_n$ and $\Phi_m$ can be determined using the positive $\eta$ and negative $\eta$ side of a symmetric detector. For three-plane correlation, one can divide the full detector into three non-overlapping subevents with comparable resolution.

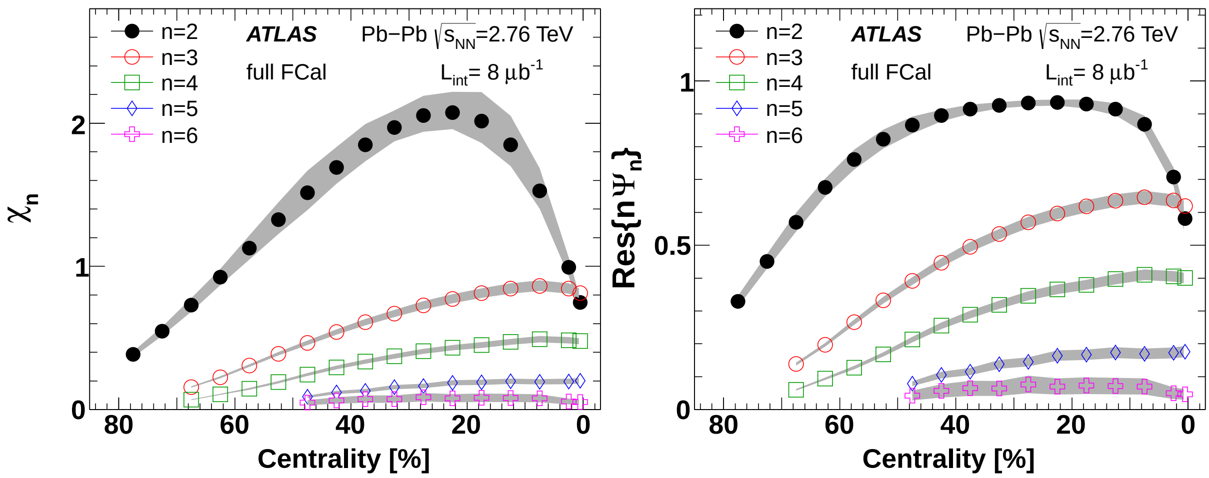


Figure 5: The FCal resolution parameter $\chi_n$ (left) and and EP resolution factor $\mathrm{Res}\{n\Psi_n\}$ (right) vs. centrality for n = 2–6. Figure taken from the $v_n$ paper [6].

Table 2 gives a summary of the set of two-plane correlations and required resolution terms in this analysis, and the corresponding information for the three-plane correlations is shown in Table 3. These lists are identified by requiring $n = 2-6$ and the combined resolution to be at least a few % (they can be identified from Fig. 28). The two-plane and three-plane correlations are listed separately, because different detectors are used (discussed in Section 3.6), which requires the separate evaluation of the resolution corrections. The key to this analysis is to determine correctly the resolution correction as a function of centrality.

| | |
|---|---|
| $\langle\cos 4(\Phi_2 - \Phi_4)\rangle$ | Res$\{4\Psi_2\}$, Res$\{4\Psi_4\}$ |
| $\langle\cos 8(\Phi_2 - \Phi_4)\rangle$ | Res$\{8\Psi_2\}$, Res$\{8\Psi_4\}$ |
| $\langle\cos 12(\Phi_2 - \Phi_4)\rangle$ | Res$\{12\Psi_2\}$, Res$\{12\Psi_4\}$ |
| $\langle\cos 6(\Phi_2 - \Phi_3)\rangle$ | Res$\{6\Psi_2\}$, Res$\{6\Psi_3\}$ |
| $\langle\cos 6(\Phi_2 - \Phi_6)\rangle$ | Res$\{6\Psi_2\}$, Res$\{6\Psi_6\}$ |
| $\langle\cos 6(\Phi_3 - \Phi_6)\rangle$ | Res$\{6\Psi_3\}$, Res$\{6\Psi_6\}$ |
| $\langle\cos 12(\Phi_3 - \Phi_4)\rangle$ | Res$\{12\Psi_3\}$, Res$\{12\Psi_4\}$ |
| $\langle\cos 10(\Phi_2 - \Phi_5)\rangle$ | Res$\{10\Psi_2\}$, Res$\{10\Psi_5\}$ |
| $\Phi_2$ plane | Res$\{4\Psi_2\}$, Res$\{6\Psi_2\}$, Res$\{8\Psi_2\}$, Res$\{10\Psi_2\}$, Res$\{12\Psi_2\}$ |
| $\Phi_3$ plane | Res$\{6\Psi_3\}$, Res$\{12\Psi_3\}$ |
| $\Phi_4$ plane | Res$\{4\Psi_4\}$, Res$\{8\Psi_4\}$, Res$\{12\Psi_4\}$ |
| $\Phi_5$ plane | Res$\{10\Psi_5\}$ |
| $\Phi_6$ plane | Res$\{6\Psi_6\}$ |

Table 2: The list of two plane correlators and associated event-plane resolution factors that need to be measured.

| | |
|---|---|
| $\langle\cos(2\Phi_2 + 3\Phi_3 - 5\Phi_5)\rangle$ | Res$\{2\Psi_2\}$, Res$\{3\Psi_3\}$, Res$\{5\Psi_5\}$ |
| $\langle\cos(2\Phi_2 + 4\Phi_4 - 6\Phi_6)\rangle$ | Res$\{2\Psi_2\}$, Res$\{4\Psi_4\}$, Res$\{6\Psi_6\}$ |
| $\langle\cos(-8\Phi_2 + 3\Phi_3 + 5\Phi_5)\rangle$ | Res$\{8\Psi_2\}$, Res$\{3\Psi_3\}$, Res$\{5\Psi_5\}$ |
| $\langle\cos(-10\Phi_2 + 4\Phi_4 + 6\Phi_6)\rangle$ | Res$\{10\Psi_2\}$, Res$\{4\Psi_4\}$, Res$\{6\Psi_6\}$ |
| $\langle\cos(2\Phi_2 - 6\Phi_3 + 4\Phi_4)\rangle$ | Res$\{2\Psi_2\}$, Res$\{6\Psi_3\}$, Res$\{4\Psi_4\}$ |
| $\langle\cos(-10\Phi_2 + 6\Phi_3 + 4\Phi_4)\rangle$ | Res$\{10\Psi_2\}$, Res$\{6\Psi_3\}$, Res$\{4\Psi_4\}$ |
| $\Phi_2$ plane | Res$\{2\Psi_2\}$, Res$\{8\Psi_2\}$, Res$\{10\Psi_2\}$ |
| $\Phi_3$ plane | Res$\{3\Psi_3\}$, Res$\{6\Psi_3\}$ |
| $\Phi_4$ plane | Res$\{4\Psi_4\}$ |
| $\Phi_5$ plane | Res$\{5\Psi_5\}$ |
| $\Phi_6$ plane | Res$\{6\Psi_6\}$ |

Table 3: The list of three plane correlators and associated event-plane resolution factors that need to be measured.

Figure 6 shows the predicted correlations from a simple Glauber model for various two- and three-plane correlators studied in this analysis [15]. They are presented as a function of number of participating nucleons($N_{\text{part}}$) in the model. Note they are calculated using the participant nucleons in configuration space,and not from the final state particles in momentum space. So detailed agreement with the results obtained in this analysis is not to be expected. Nevertheless, it is interesting that the Glauber model predicts strong correlations between $\Phi_2^*$ and $\Phi_4^*$, $\Phi_3^*$ and $\Phi_6^*$, $\Phi_2^*$ and $\Phi_6^*$ for two-plane correlations. For three-plane correlations, strong signals are predicted for $\langle\cos(2\Phi_2^* + 3\Phi_3^* - 5\Phi_5^*)\rangle$ and $\langle\cos(2\Phi_2^* + 4\Phi_4^* - 6\Phi_6^*)\rangle$.

## 3.2 Calibration of $\Psi_n$

The first step in the analysis is to measure the event-plane angles $\Psi_n$ for n=2-6. They are defined as the directions of the "flow vector" $\overrightarrow{Q}_n$, calculated from the transverse energy flow ($E_{\text{T}}$) of a given calorimeter

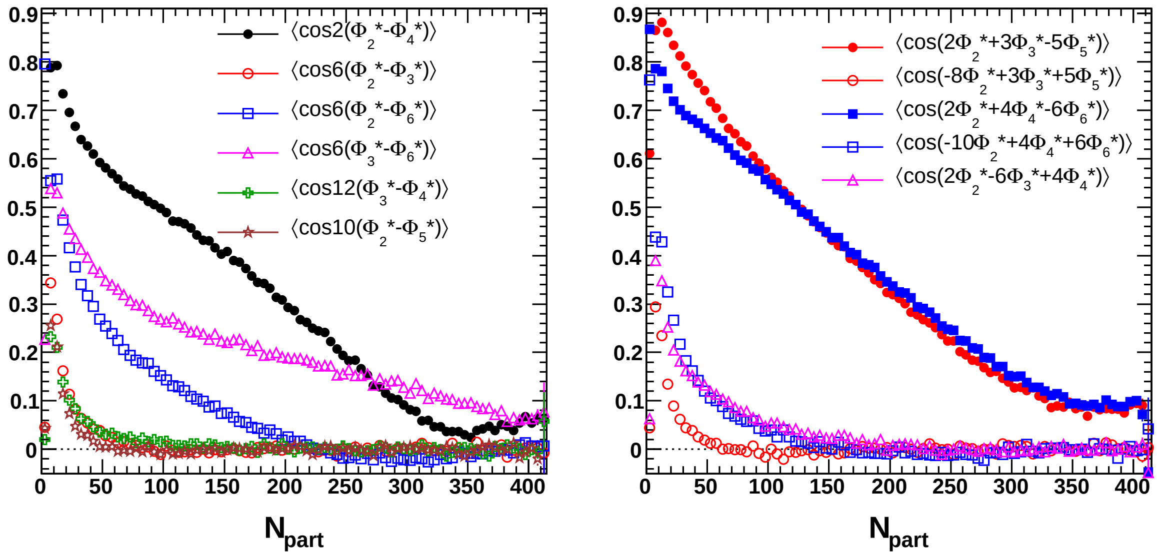


Figure 6: The correlation between the planes angles calculated in configuration space [15], as defined by Eq. 4.

detector as:

$$\begin{aligned}
\overrightarrow{Q}_n &= (Q_{x,n}, Q_{y,n}) = \left(\sum E_{\mathrm{T}}\cos n\phi - \langle\sum E_{\mathrm{T}}\cos n\phi\rangle, \sum E_{\mathrm{T}}\sin n\phi - \langle\sum E_{\mathrm{T}}\sin n\phi\rangle\right) \ , \\
\tan n\Psi_n &= \frac{Q_{y,n}}{Q_{x,n}} \ , \qquad (18) \\
\overrightarrow{Q}_n^{raw} &= (\langle Q_{x,n}^{raw}\rangle, \langle Q_{y,n}^{raw}\rangle) = (\langle\sum E_{\mathrm{T}}\cos n\phi\rangle, \langle\sum E_{\mathrm{T}}\sin n\phi\rangle) \qquad (19)
\end{aligned}$$

where the sum ranges over towers in the ECal and the first two layers of the FCal (see Section 3.6). Subtraction of the event-averaged centroid removes biases due to detector effects [21]. This re-centering is simply a Fourier expansion of the raw $E_T$ flow in the lab frame:

$$\left\langle \frac{dE_T}{d\phi} \right\rangle = Q_0 + 2\sum_{n=1}^{\infty} \left|\overrightarrow{Q}_n^{raw}\right| \cos n(\phi - \Psi_n^{raw}) \tag{20}$$

A non-zero $\left|\overrightarrow{Q}_n^{raw}\right|$ would bias the measured event-plane towards some fixed direction $\Psi_n^{raw}$, which is taken out by the re-centering. The re-centering step removes almost all non-flatness of the $\Psi_n$ distribution. A standard flattening technique is then used to remove the small residual non-uniformities in the event-plane angular distribution [22]. The calibration procedure for the ID detector is almost identical, except that the $E_{\mathrm{T}}$ is replaced with $p_{\mathrm{T}}$ of tracks everywhere. These calibration procedures are similar to those used by the RHIC experiments [21, 23]. They are performed for each detector separately. The details of the calibration for $\Psi_n$ documented in the previous analysis [16, 18].

### 3.3 Procedure for obtaining correlation function and applying the resolution correction

Each subevent provides its own measurement of event-plane $\Psi_n$ for n=2-6. However to minimize the auto-correlations, the planes involved in the correlation should not all be measured by the same detector. For example, the $\Psi_2$ and $\Psi_4$ in relative angle $4(\Psi_2 - \Psi_4)$ should be measured from non-overlapping detectors A and B, and the correlation is obtained as

$$\langle \cos 4(\Phi_2 - \Phi_4)\rangle = \frac{\langle \cos 4(\Psi_2^A - \Psi_4^B)\rangle}{\mathrm{Res}\{4\Psi_2^A\}\mathrm{Res}\{4\Psi_4^B\}}. \tag{21}$$

Ideally, the acceptance of these detectors should be chosen to maximize the product of the resolution, which requires $\mathrm{Res}\{4\Psi_2^A\} \approx \mathrm{Res}\{4\Psi_4^B\}$. Since the resolution for $4\Psi_2$ is typically larger than that of the $4\Psi_4$, detector B should be chosen to have larger acceptance than detector A, and this optimization should be done for each centrality class. The same argument also applies for correlations involving three or more planes. In practice, this optimization procedure can become rather sophisticated, and we leave it for future studies. Noting that the products of resolution factors we use are satisfactorily large.

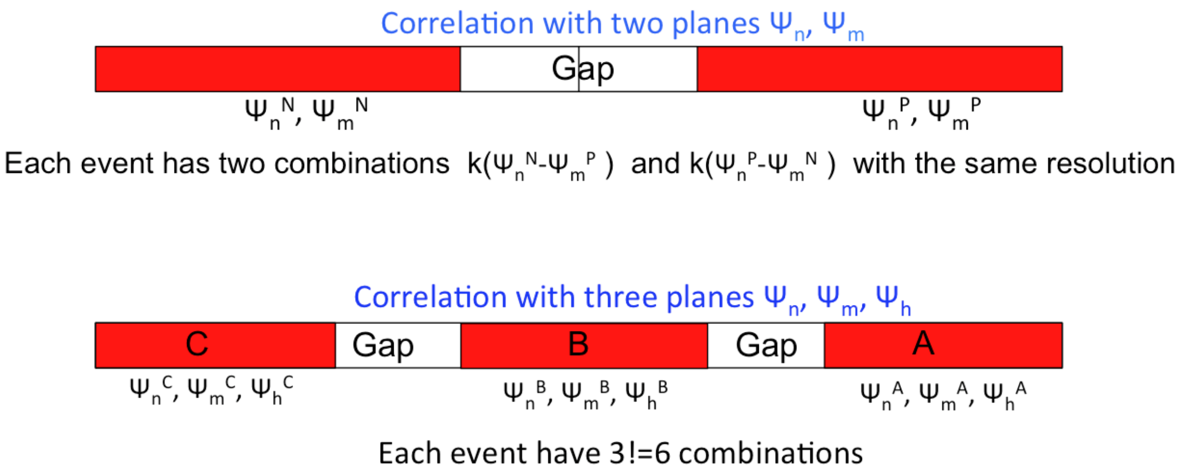


Figure 7: Schematic illustration of strategy to obtain the raw signal for two-plane correlation (top) and three-plane correlation (bottom)

In this analysis, the detectors for event-planes of different order are simply chosen to have approximately equal acceptance. Figure 7 illustrates the idea behind the two-plane and three-plane correlations. In the two-plane correlation, the two subevents are chosen to be symmetric around the center of the ATLAS detector, so they nominally have the same resolution. Each subevent provides its own measurement of the two event-planes: $\Psi_n^P$ and $\Psi_m^P$ for positive $\eta$ and $\Psi_n^N$ and $\Psi_m^N$ for negative $\eta$, resulting in two independent measurements of the correlations:

$$\langle \cos k(\Phi_n - \Phi_m)\rangle = \frac{\left\langle \cos k(\Psi_n^P - \Psi_m^N)\right\rangle}{\mathrm{Res}\{k\Psi_n^{\mathrm{P}}\}\mathrm{Res}\{k\Psi_m^{\mathrm{N}}\}} = \frac{\left\langle \cos k(\Psi_n^N - \Psi_m^P)\right\rangle}{\mathrm{Res}\{k\Psi_n^{\mathrm{N}}\}\mathrm{Res}\{k\Psi_m^{\mathrm{P}}\}} \tag{22}$$

where the resolution factors are calculated from two- or three- subevent methods discussed below. Since $\mathrm{Res}\{k\Psi_n^{\mathrm{P}}\}\mathrm{Res}\{k\Psi_m^{\mathrm{N}}\} = \mathrm{Res}\{k\Psi_n^{\mathrm{N}}\}\mathrm{Res}\{k\Psi_m^{\mathrm{P}}\}$ for symmetric detectors, we simply take the average of the two measurements for the correlation.

$$\langle \cos k(\Phi_n - \Phi_m)\rangle = \frac{\left\langle \cos k(\Psi_n^P - \Psi_m^N)\right\rangle + \left\langle \cos k(\Psi_n^N - \Psi_m^P)\right\rangle}{\mathrm{Res}\{k\Psi_n^{\mathrm{P}}\}\mathrm{Res}\{k\Psi_m^{\mathrm{N}}\} + \mathrm{Res}\{k\Psi_n^{\mathrm{N}}\}\mathrm{Res}\{k\Psi_m^{\mathrm{P}}\}} \tag{23}$$

To measure a three-plane correlation, three non-overlapping subevents, labeled as A, B and C, are chosen to have approximately the same $\eta$ ranges. Here, subevent A and C are chosen to be symmetric and have identical $\eta$ acceptance (hence same resolution), while the resolution of B in general could be different. There are 6 independent ways of obtaining the three-plane correlator. But since A and C have same resolution, only three of them are independent. For example, the three estimations for the correlation $2\Phi_2 + 3\Phi_3 - 5\Phi_5$, denoted by subscript Type1-Type3, are

$$\langle\cos(2\Phi_2 + 3\Phi_3 - 5\Phi_5)\rangle_{Type1} = \frac{\left\langle\cos(2\Psi_2^B + 3\Psi_3^A - 5\Psi_5^C)\right\rangle + \left\langle\cos(2\Psi_2^B + 3\Psi_3^C - 5\Psi_5^A)\right\rangle}{\mathrm{Res}\{2\Psi_2^B\}\mathrm{Res}\{3\Psi_3^A\}\mathrm{Res}\{5\Psi_5^C\} + \mathrm{Res}\{2\Psi_2^B\}\mathrm{Res}\{3\Psi_3^C\}\mathrm{Res}\{5\Psi_5^A\}} \tag{24}$$

$$\langle\cos(2\Phi_2 + 3\Phi_3 - 5\Phi_5)\rangle_{Type2} = \frac{\left\langle\cos(2\Psi_2^A + 3\Psi_3^B - 5\Psi_5^C)\right\rangle + \left\langle\cos(2\Psi_2^C + 3\Psi_3^B - 5\Psi_5^A)\right\rangle}{\mathrm{Res}\{2\Psi_2^A\}\mathrm{Res}\{3\Psi_3^B\}\mathrm{Res}\{5\Psi_5^C\} + \mathrm{Res}\{2\Psi_2^C\}\mathrm{Res}\{3\Psi_3^B\}\mathrm{Res}\{5\Psi_5^A\}} \tag{25}$$

$$\langle\cos(2\Phi_2 + 3\Phi_3 - 5\Phi_5)\rangle_{Type3} = \frac{\left\langle\cos(2\Psi_2^A + 3\Psi_3^C - 5\Psi_5^B)\right\rangle + \left\langle\cos(2\Psi_2^C + 3\Psi_3^A - 5\Psi_5^B)\right\rangle}{\mathrm{Res}\{2\Psi_2^A\}\mathrm{Res}\{3\Psi_3^C\}\mathrm{Res}\{5\Psi_5^B\} + \mathrm{Res}\{2\Psi_2^C\}\mathrm{Res}\{3\Psi_3^A\}\mathrm{Res}\{5\Psi_5^B\}} \tag{26}$$

Again the resolutions are determined from two- or three- subevent methods. These three measurements are statistically combined, and the spreads between them are used as estimation for the systematic uncertainty.

### 3.4 Determining the resolution

In the two-subevent (2SE) method, the event-plane angles are determined separately for either side of the symmetric detector, as illustrated in Fig. 8. The correlation of the event-planes at the "same order" between the positive $\eta$ and negative $\eta$ are related directly to the resolution for each of the subevent:

$$\begin{aligned}
\left\langle\cos k\left(\Psi_n^N - \Psi_n^P\right)\right\rangle &= \left\langle\cos k\left(\Psi_n^N - \Phi_n - (\Psi_n^P - \Phi_n)\right)\right\rangle \qquad (27)\\
&= \left\langle\cos k\left(\Psi_n^N - \Phi_n\right)\cos k\left(\Psi_n^P - \Phi_n\right)\right\rangle + \cancel{\left\langle\sin k\left(\Psi_n^N - \Phi_n\right)\sin k\left(\Psi_n^P - \Phi_n\right)\right\rangle}\\
&= \left\langle\cos k\left(\Psi_n^N - \Phi_n\right)\right\rangle\left\langle\cos k\left(\Psi_n^P - \Phi_n\right)\right\rangle\\
&= \left\langle\cos k\left(\Psi_n^{P(N)} - \Phi_n\right)\right\rangle^2 = \mathrm{Res}\{k\Psi_n\}^2\ ,\\
\mathrm{Res}\{k\Psi_n\} &= \sqrt{\left\langle\cos k\left(\Psi_n^N - \Psi_n^P\right)\right\rangle} = \mathrm{Res}\{k\Psi_n^P\} = \mathrm{Res}\{k\Psi_n^N\} = \mathrm{Res}\{k\Psi_n^{P(N)}\} \qquad (28)
\end{aligned}$$

where it is assumed that the dispersion of $\Psi_n$ relative to $\Phi_n$ is random, and the dispersion is not correlated between two subevents. In this case, all the sine terms vanish: $\langle\sin k\left(\Psi_n^{P(N)} - \Phi_n\right)\rangle = 0$. On the other hand, the detector effects (dead area, inefficiency, mis-calibration etc) may lead to non-physical correlations between the measured event-planes, and hence the values of $\langle\sin k\left(\Psi_n^P - \Psi_n^N\right)\rangle$ can be used as a measure of such detector effects [1].

In three-subevent (3SE) method, the resolution of detector A for $n^{th}$-order event-plane is calculated from its correlation with the event-planes of the reference detectors B and C at the "same-order":

$$\mathrm{Res}\{k\Psi_n^{\mathrm{A}}\} = \sqrt{\frac{\left\langle\cos k\left(\Psi_n^{\mathrm{A}} - \Psi_n^{\mathrm{B}}\right)\right\rangle\left\langle\cos k\left(\Psi_n^{\mathrm{A}} - \Psi_n^{\mathrm{C}}\right)\right\rangle}{\left\langle\cos k\left(\Psi_n^{\mathrm{B}} - \Psi_n^{\mathrm{C}}\right)\right\rangle}} \tag{29}$$

to prove this, one just needs to plug in the following relations

$$\begin{aligned}
\left\langle\cos k\left(\Psi_n^A - \Psi_n^B\right)\right\rangle &= \left\langle\cos k\left(\Psi_n^A - \Phi_n\right)\right\rangle\left\langle\cos k\left(\Psi_n^B - \Phi_n\right)\right\rangle\\
\left\langle\cos k\left(\Psi_n^A - \Psi_n^C\right)\right\rangle &= \left\langle\cos k\left(\Psi_n^A - \Phi_n\right)\right\rangle\left\langle\cos k\left(\Psi_n^C - \Phi_n\right)\right\rangle\\
\left\langle\cos k\left(\Psi_n^B - \Psi_n^C\right)\right\rangle &= \left\langle\cos k\left(\Psi_n^B - \Phi_n\right)\right\rangle\left\langle\cos k\left(\Psi_n^C - \Phi_n\right)\right\rangle \qquad (30)
\end{aligned}$$

[1] The notation used in this analysis is slightly different from what was used in previous paper [6]. We nominally use $\mathrm{Res}\{k\Psi_n\}$ to refer to the resolution for the subevents (instead of the combined event); but sometime we spell the sides out explicitly as either $\mathrm{Res}\{k\Psi_n^P\}$, $\mathrm{Res}\{k\Psi_n^N\}$ or $\mathrm{Res}\{k\Psi_n^{P(N)}\}$.

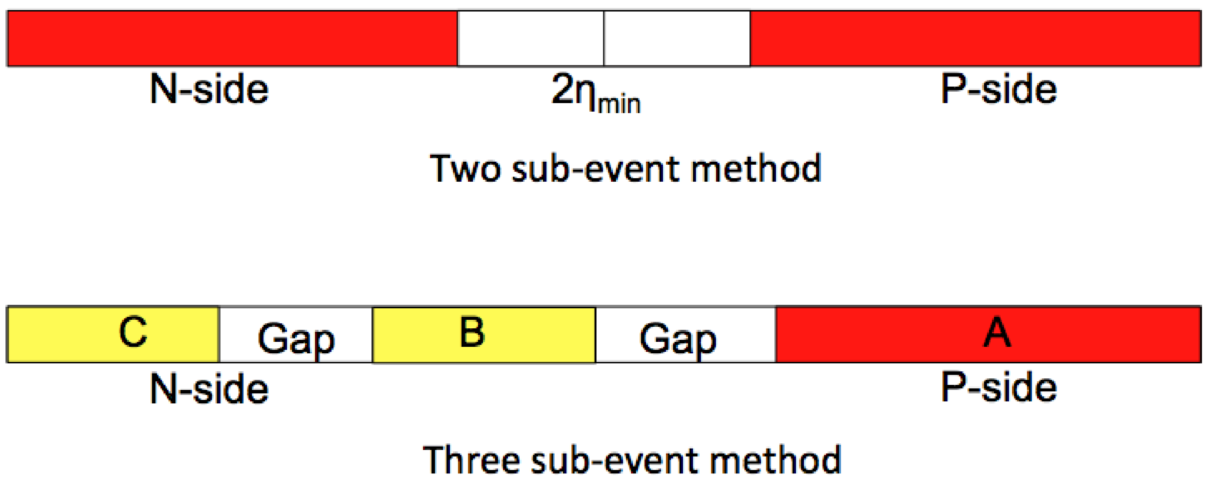


Figure 8: Schematic illustration of the two-subevent method (top) and three subevent method (bottom)

Note that A, B and C should all cover different $\eta$ regions to avoid autocorrelations. This method has the advantage of no need to assume equal resolutions as in the 2SE method, and it is quite flexible in choosing references. On the other hand, the 3SE method can suffer from systematics from the reference detectors B and C. In order words, difference from the two-subevent could be caused by the poor choice of reference detector instead of reflecting the real systematics of detector A. So one should keep this caveat in mind.

### 3.5 Source of systematic errors

It is useful to focus on the Eq. 23 and Eq. 24–26 to understand how various systematic effects enter the two- and three-plane correlations. There are two primary sources of systematic uncertainties. 1) Detector effects can bias the determination of the event-plane angle $\Psi_n$, and hence can influence both the correlation signal as well as the resolution correction. Most of these detector effects should be removed by the event-plane calibration, Section 3.2. 2) Correlations other than flow (non-flow) such as resonance decays and jet fragmentations. These correlations typically have limited range in rapidity, and can be suppressed by requiring an $\eta$ gap between the subevents used in measuring the correlation or resolution determination.

The residual systematics include the following:

- The remaining detector effects can manifest themselves as non-vanishing sine terms in the correlation function $\langle \sin jk(\Psi_n - \Psi_m)\rangle$, $\langle \sin(c_n n\Psi_n + c_m m\Psi_m + c_h h\Psi_h)\rangle$ or the 2SE and 3SE correlations $\left\langle \sin jn\left(\Psi_n^A - \Psi_n^B\right)\right\rangle$.
- The remaining non-flow effects can influence the resolution determination. For a given subevent, it is important to compare resolutions from 2SE and 3SE methods with varying $\eta$ gaps.
- Thanks to the large $\eta$ coverage of the ATLAS detector, a given two-plane or three-plane correlation can be measured independently using detectors at different $\eta$. It is useful to compare the results obtained using different detectors. However, one caveat is that the differences could also be due to $\eta$ dependence of detector bias and/or the flow physics itself.

### 3.6 Choice of Detectors

The calorimeters (EM barrel, EM end-cap and FCal) are used to determine the event planes and study their correlations. The EM-Barrel (EMBR) and EM-endcap (EMEC) are further divided into six segments each covering roughly 0.5-0.7 unit in $\eta$ as shown in Fig. 9 and listed in Table 4. These segmentations of the EMEC and EMBR and their combinations (listed in Table 4) give a large choice of subevents for both the 2SE and 3SE studies. This flexibility allows for a detailed estimation of systematic uncertainties in the measured correlations. Note that the edge towers of FCal(approximately $\eta \in 3.2-3.3$ and $4.8-4.9$) are excluded as they show large non-uniformity in azimuth (as done in previous analysis as well).

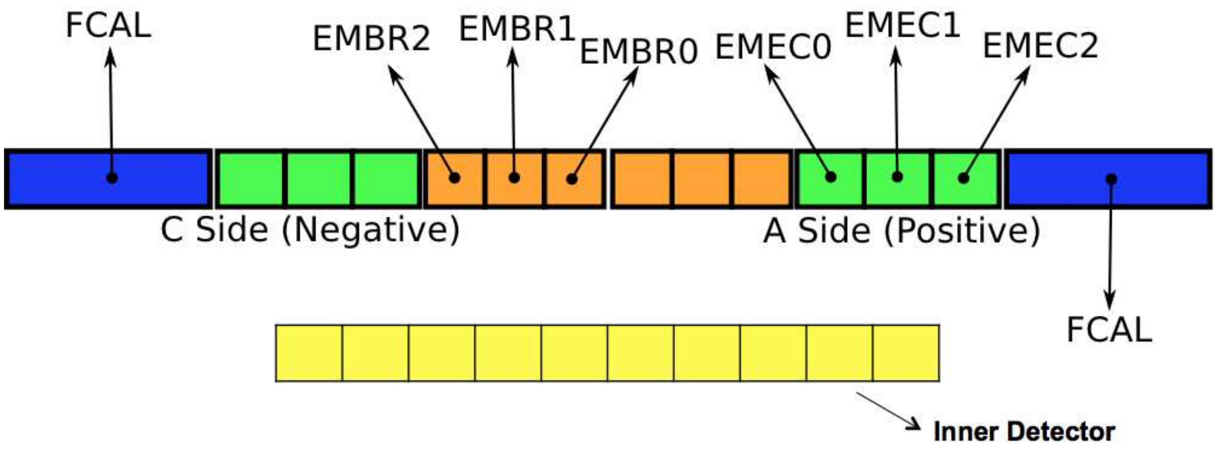


Figure 9: Schematic representation of the different detectors used for the analysis. Both the positive and negative sides of each detector are used.

The guiding principle for choosing the subevents is that they should have as large $\eta$ acceptance as possible, but still have a sufficient $\eta$ gap from each other. For two-plane correlations, the default subevents are FCal+EMCEC+EMBR12 at positive $\eta$ $(-4.8, -0.5)$ and negative $\eta$ $(0.5, 4.8)$, with a 1 unit gap in between. For three-plane correlation, the default subevents are $(\text{EMBR12+EMEC01})_P$ $(0.5 < \eta < 2.7)$, FCal $(3.3 < |\eta| < 3.8)$, and $(\text{EMBR12+EMEC01})_N$ $(-2.7 < \eta < -0.5)$. The resolution of each of these subevents is determined via various 2SE and 3SE methods.

Figure 9 also shows the $\eta$ coverage of the inner detector (ID): $|\eta| < 2.5$. The ID only detects charged particles above 0.5 GeV with about 60-80% efficiency, depending on the centrality [17]. The inefficiency leads to significant non-uniformity in the azimuthal direction. On the other hand, a calorimeters usually has better resolution for the same $\eta$ range due to its ability to detect neutral particles; The azimuthal acceptance of calorimeter is also more uniform, resulting in a smaller re-centering correction in the event plane calibration.

# 4 Two-plane correlation analysis

In this section, we discuss results obtained for default detector ECalFCal (denoted as “Det” in this section); Detailed results from tracking detectors are included in Appendix I.

### 4.1 Correlation function and extraction of raw signal

Figures 10-15 show the raw two-plane relative angle distributions for selected centrality intervals. The red and blue histograms are foreground and background distributions, respectively. The background

| Detector | Name | Description | $\lvert\eta\rvert$ coverage | Comments |
|---|---|---|---|---|
| 1 | EMBR0 | EMcal Barrel | 0.0-0.5 | |
| 2 | EMBR1 | EMcal Barrel | 0.5-1.0 | |
| 3 | EMBR2 | EMcal Barrel | 1.0-1.5 | |
| 4 | EMBR12 | EMcal Barrel | 0.5-1.5 | sum of Detectors 2 and 3 |
| 5 | EMBR | Full EMcal barrel | 0.0-1.5 | sum of Detectors 1-3 |
| 6 | EMEC0 | EMcal End Cap | 1.5-2.1 | |
| 7 | EMEC1 | EMcal End Cap | 2.1-2.7 | |
| 8 | EMEC2 | EMcal End Cap | 2.7-3.2 | |
| 9 | EMEC01 | EMcal End Cap | 1.5-2.7 | sum of Detectors 6 and 7 |
| 10 | EMEC | Full EMcal End Cap | 1.5-3.2 | sum of Detectors 6-8 |
| 11 | EMBR12+EMEC0 | EM Barrel + End Cap | 0.5-2.1 | sum of Detectors 4 and 6 |
| 12 | EMBR12+EMEC01 a.k.a. ECal | EM Barrel + End Cap | 0.5-2.7 | sum of Detectors 4 and 9 |
| 13 | FCal | Forward Calorimeter | 3.3-4.8 | layer1 and 2 excluding edge towers |
| 14 | FCal+EMEC | FCal+EMEC | 1.5-4.8 | sum of Detectors 10 and 13 |
| 15 | FCal+EMEC+EMBR2 | FCal+EMEC+EMBR | 1.0-4.8 | sum of Detectors 3,10 and 13 |
| 16 | FCal+EMEC+EMBR12 a.k.a ECalFCal | FCal+EMEC+EMBR12 | 0.5-4.8 | sum of Detectors 4, 10 and 13 |
| 17 | FCal+EMEC2 | FCal+EMEC2 | 2.7-4.8 | sum of Detectors 8 and 13 |
| 18 | Trk1234 | Tracking Dets | 0.5-2.5 | $p_T$ weighted tracks |
| 19 | Trk34 | Tracking Dets | 1.5-2.5 | $p_T$ weighted tracks |
| 20 | Trk01 | Tracking Dets | 0.0-1.0 | $p_T$ weighted tracks |

Table 4: List of detectors used for two-plane and three-plane correlations, as well as for various 2SE and 3SE methods in determining the resolution for these detectors. If only one side of the detector is used, a superscript "N" or "P" is used to indicate negative or positive $\eta$. The detectors in red are the main detectors used for the 2-Plane correlation analysis and the ones in blue are used for the 3-Plane corrrelations. The other detectors are used for 3SE checks.

distributions are calculated from mixed events, i.e. by combining the $\Psi_n$ from one event with $\Psi_m$ from another event with similar centrality (matched within 5%) and z vertex (matched within 3cm). Both the foreground and mixed-event distributions are normalized to unity. The mixed-event distribution provides an estimate of detector effects, while the foreground distribution contains both detector effects and physics. The background distributions are almost flat, but do indicate some small variations on the order of about 1/1000. To cancel these non-physical structures, the correlation functions are obtained by dividing the foreground (S) by the mixed-event distributions(B):

$$C(k(\Psi_n - \Psi_m)) = \frac{S(k(\Psi_n - \Psi_m))}{B(k(\Psi_n - \Psi_m))} \tag{31}$$

The correlation functions show significant positive signal for $4(\Psi_2 - \Psi_4)$, $6(\Psi_2 - \Psi_6)$, $6(\Psi_3 - \Psi_6)$, but the signals for $6(\Psi_2 - \Psi_3)$, $12(\Psi_3 - \Psi_4)$ and $10(\Psi_2 - \Psi_5)$ are very weak.

These correlation functions allow us to calculate the various cosine terms $\langle\cos jk(\Psi_n - \Psi_m)\rangle$ listed in Table 2 and the associated sine terms $\langle\sin jk(\Psi_n - \Psi_m)\rangle$ to estimate the systematic uncertainty in the correlation signal.

Figure 16 summarizes the centrality dependence of the raw signal together with the estimated systematic uncertainties. They are also given in 10% centrality steps in Fig. 17. The systematic errors are

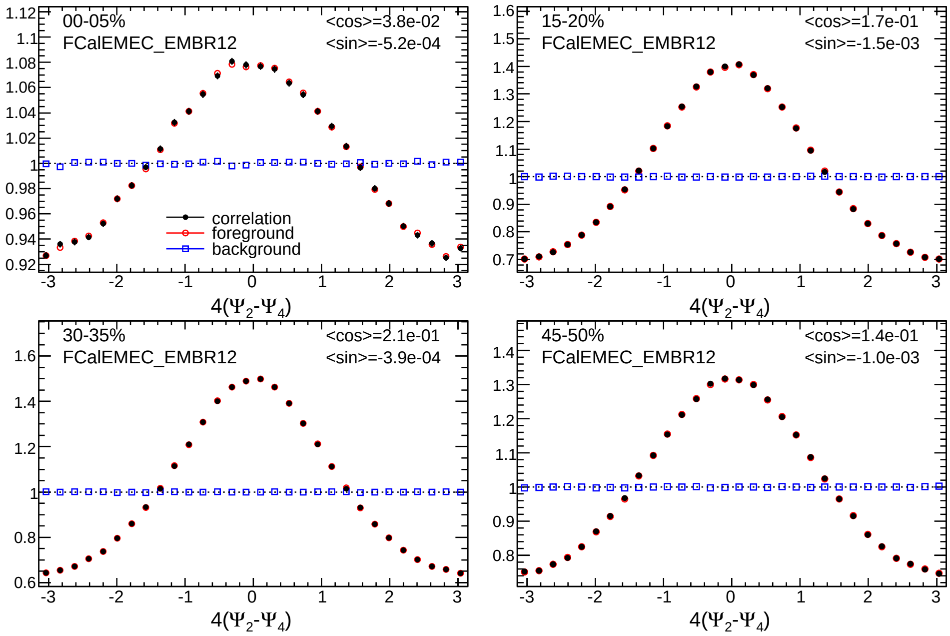


Figure 10: $4(\Psi_2 - \Psi_4)$ distributions measured in FCal+EMEC+EMBR12 for four different centralities.

caluclated from the quadrature sum of the $\langle \sin \rangle$ in the raw correlation and the $\langle \cos \rangle$ term for mixed-background events. The $\langle \sin \rangle$ and $\langle \cos \rangle_{\mathrm{mixed}}$ terms are estimated by averaging over the 0-75% centrality range. These are shown in Figs 18 and Fig. 19 respectively.

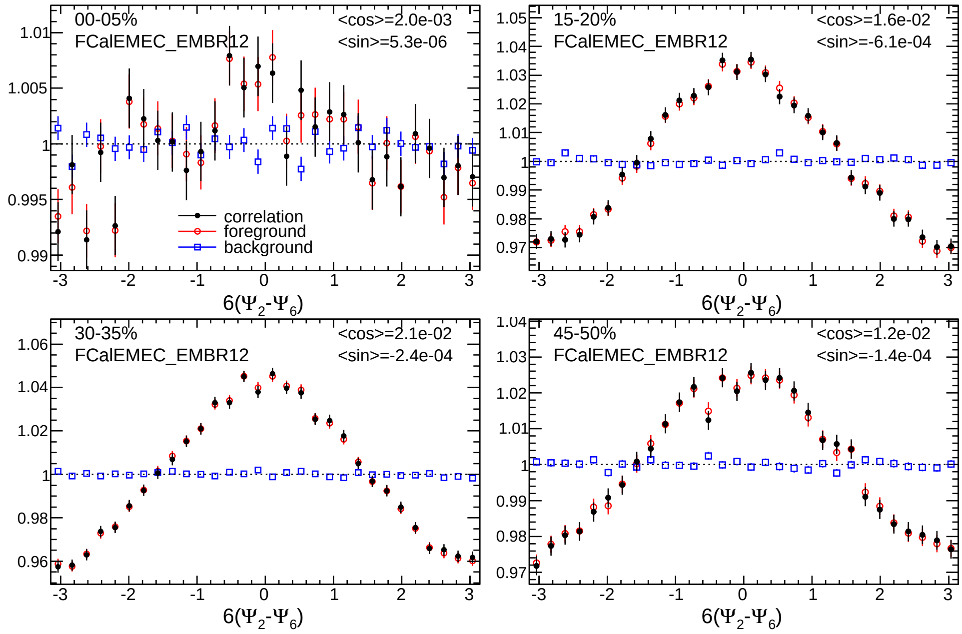


Figure 11: $6(\Psi_2 - \Psi_6)$ distributions measured in FCal+EMEC+EMBR12 for four different centralities.

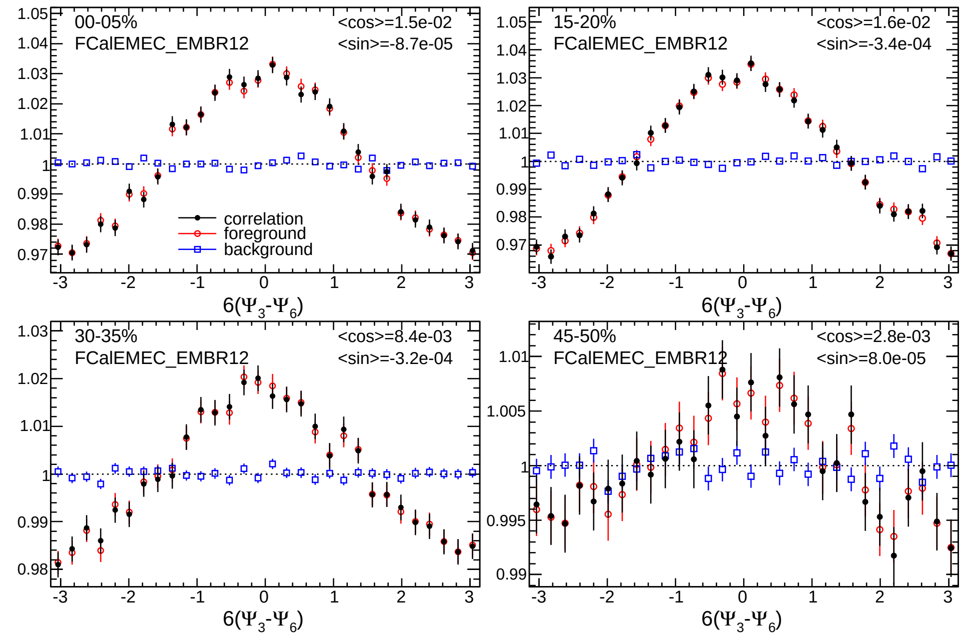


Figure 12: $6(\Psi_3 - \Psi_6)$ distributions measured in FCal+EMEC+EMBR12 for four different centralities.

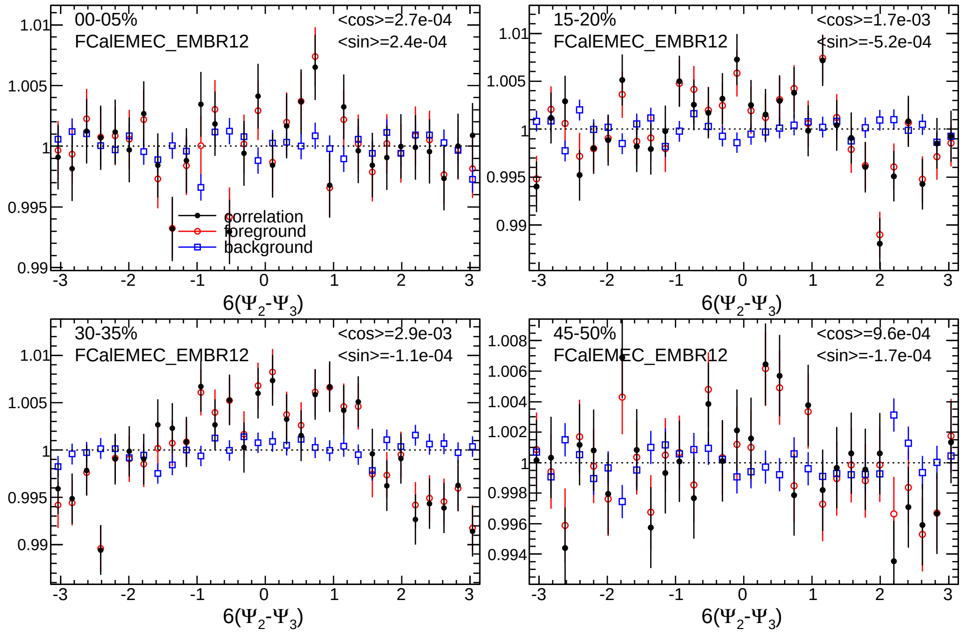


Figure 13: $6(\Psi_2 - \Psi_3)$ distributions measured in FCal+EMEC+EMBR12 for four different centralities.

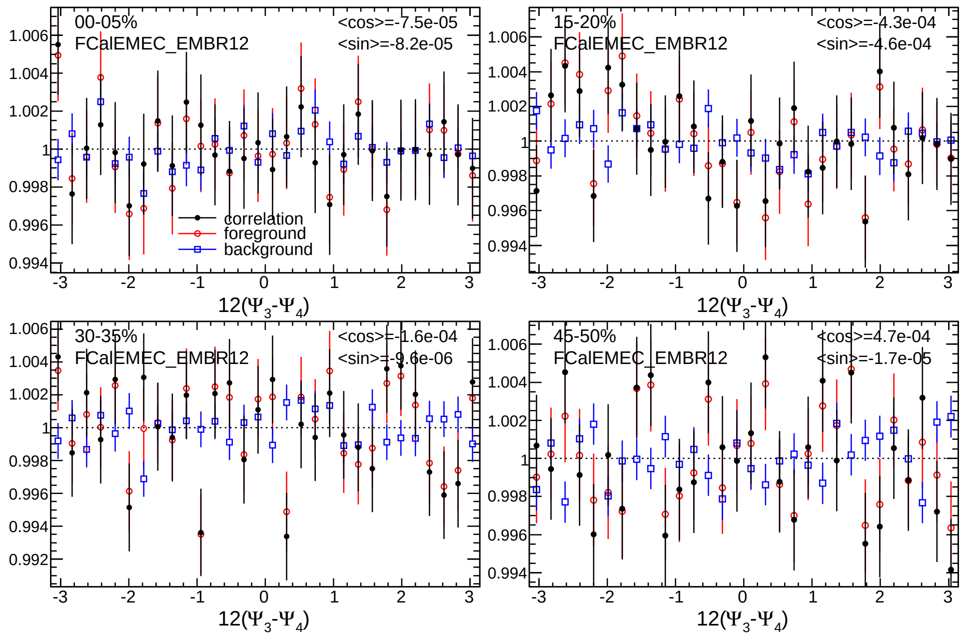


Figure 14: $12(\Psi_3 - \Psi_4)$ distributions measured in FCal+EMEC+EMBR12 for four different centralities.

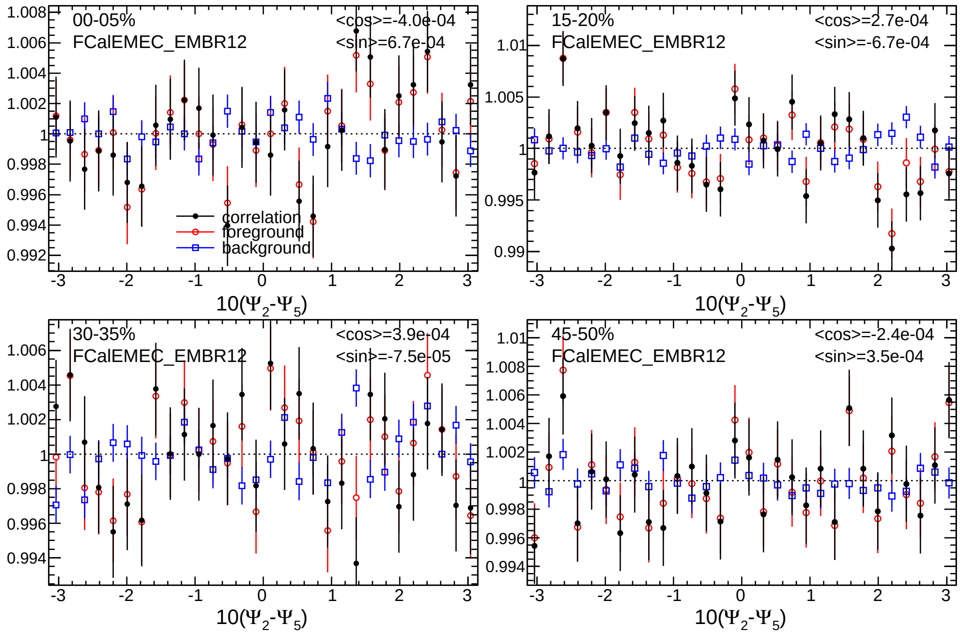


Figure 15: $10(\Psi_2 - \Psi_5)$ distributions measured in FCal+EMEC+EMBR12 for four different centralities.

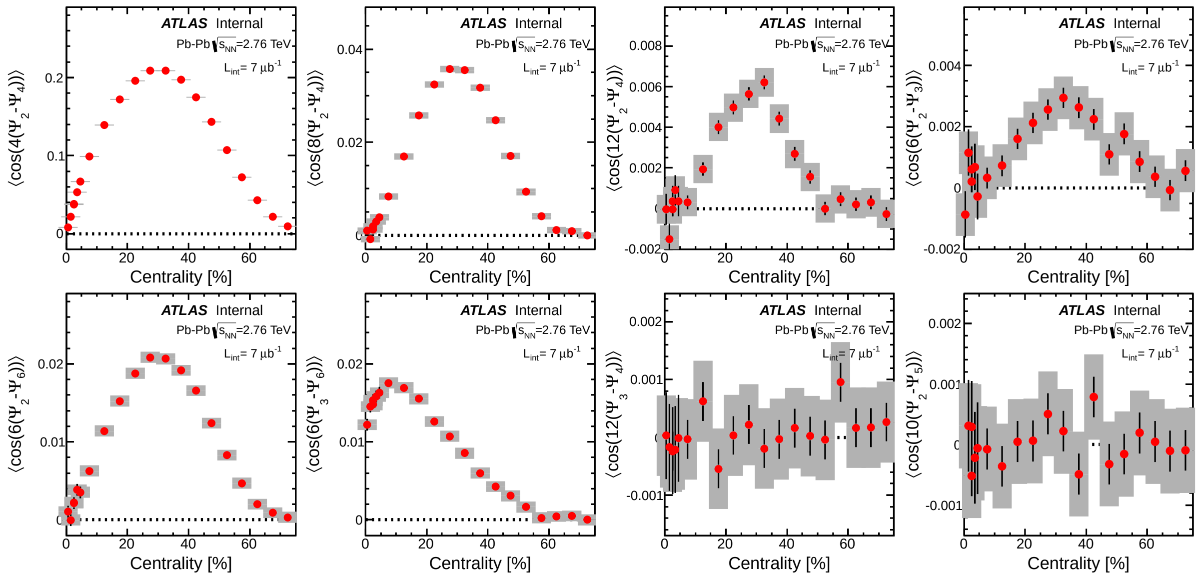


Figure 16: The centrality dependence of raw correlation signals for the eight two-plane correlators studied in this note. They are presented for 5% centrality intervals, together with a 0-1% centrality bins for the (0-5)% interval.

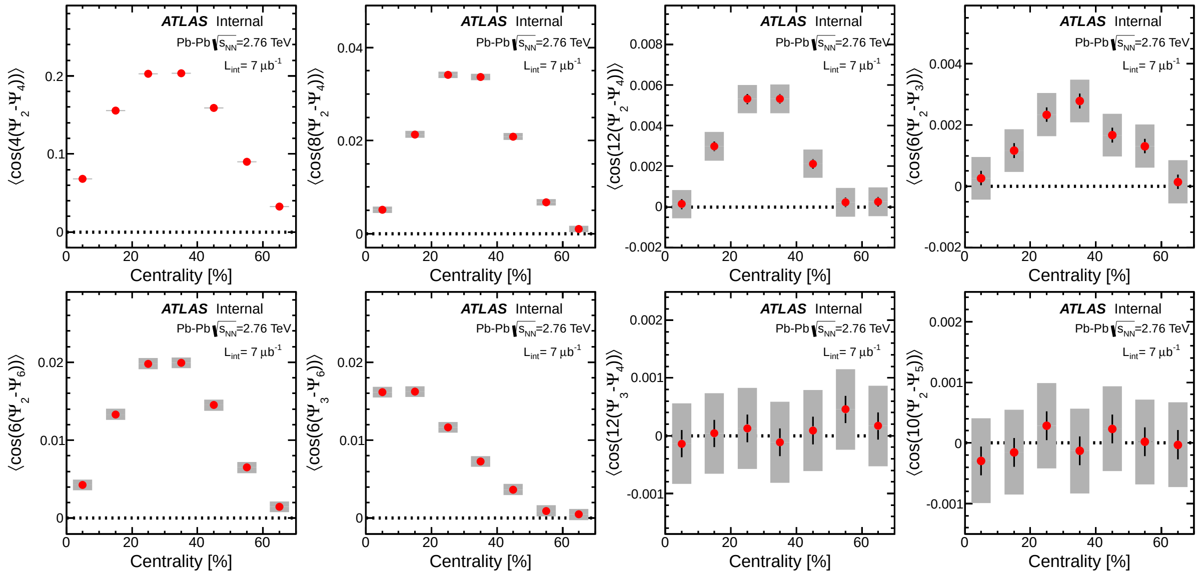


Figure 17: The centrality dependence of raw correlation signals for the eight two-plane correlators studied in this note. They are presented for 10% centrality intervals.

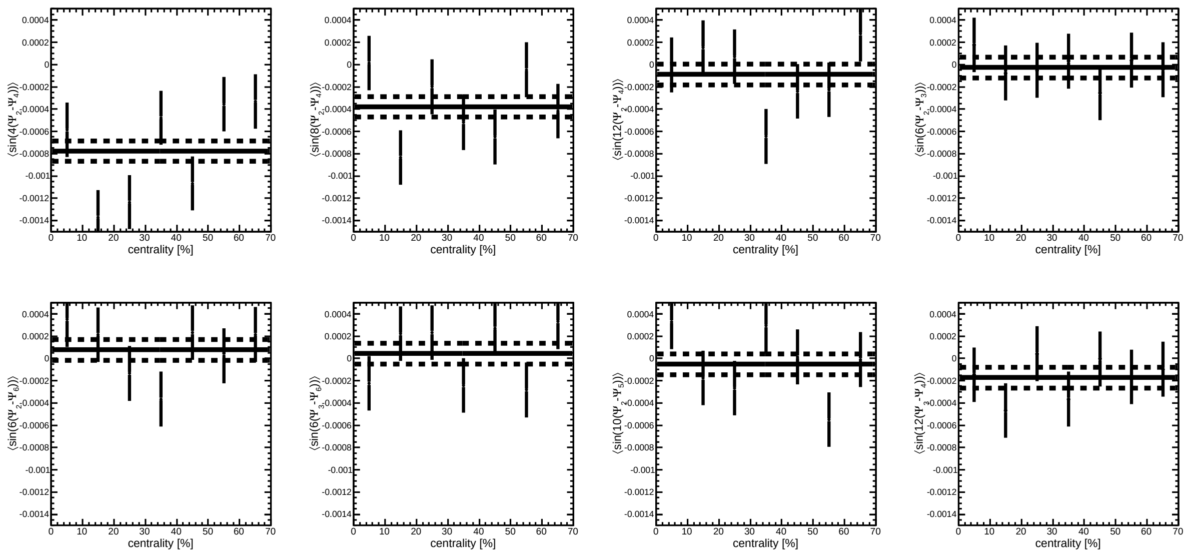


Figure 18: The centrality dependence of the sine term in the correlation signals for the eight two-plane correlators studied in this note. The solid black line shows the mean value of the sine term while the dashed lines show the 1-sigma error band of the mean.

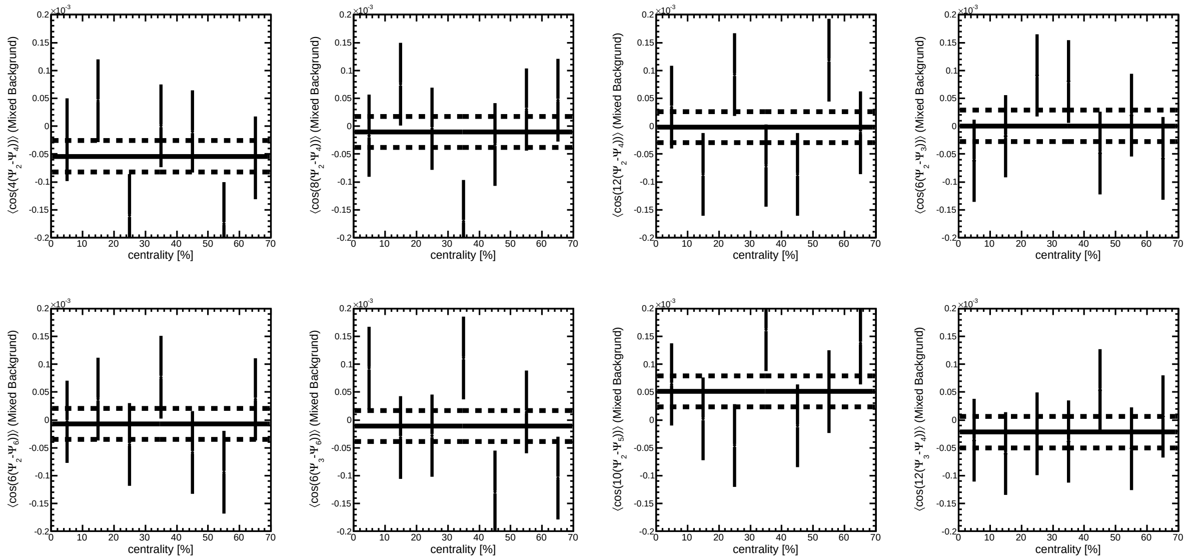


Figure 19: The centrality dependence of the mixed-background cos term for correlation signals for the eight two-plane correlators studied in this note. The solid black line shows the mean value of this term while the dashed lines show the 1-sigma error band of the mean.

## 4.2 Resolution determination

This section provides a detailed discussion of the systematic uncertainties for the resolution corrections. The nominal resolution factors are obtained via two-subevent method, and the systematic uncertainties are estimated by comparing with results obtained from various three-subevent studies.



### 4.2.1 2SE results

Figure 20 shows relative angle distribution between two subevents:$dN/d\left(n\left(\Psi_n^{\mathrm{N}} - \Psi_n^{\mathrm{P}}\right)\right)$. These are the distributions from which the resolution factors are calculated, i.e. $\mathrm{Res}\{jn\Psi_n\} = \sqrt{\left\langle \cos jn\left(\Psi_n^N - \Psi_n^P\right)\right\rangle}$. The red and blue histograms are foreground and background distributions, respectively. The background distributions are calculated from mixed-events, i.e. by combining the $\Psi_n^N$ from one event (at the N-side) with $\Psi_n^P$ from another event (at the P-side) with similar centrality (matched within 5%) and z vertex (matched within 3cm). Both the foreground and mixed-event distributions are normalized to unity. The mixed-event distributions serve as estimations of the detector effects, while the foreground distribution contains both detector effects and physics. To cancel these non-physical structures, the correlation functions are obtained by dividing the foreground by the mixed-event distributions:

$$C(n(\Psi_n^N - \Psi_n^P)) = \frac{S\,(n(\Psi_n^N - \Psi_n^P))}{B(n(\Psi_n^N - \Psi_n^P))} \tag{32}$$

The resolution factors are then calculated from these correlations functions. This procedure is almost identical to that was used to obtain the correlation signal in the Section 4.1, except here the correlations are between the event-planes of the "same order".

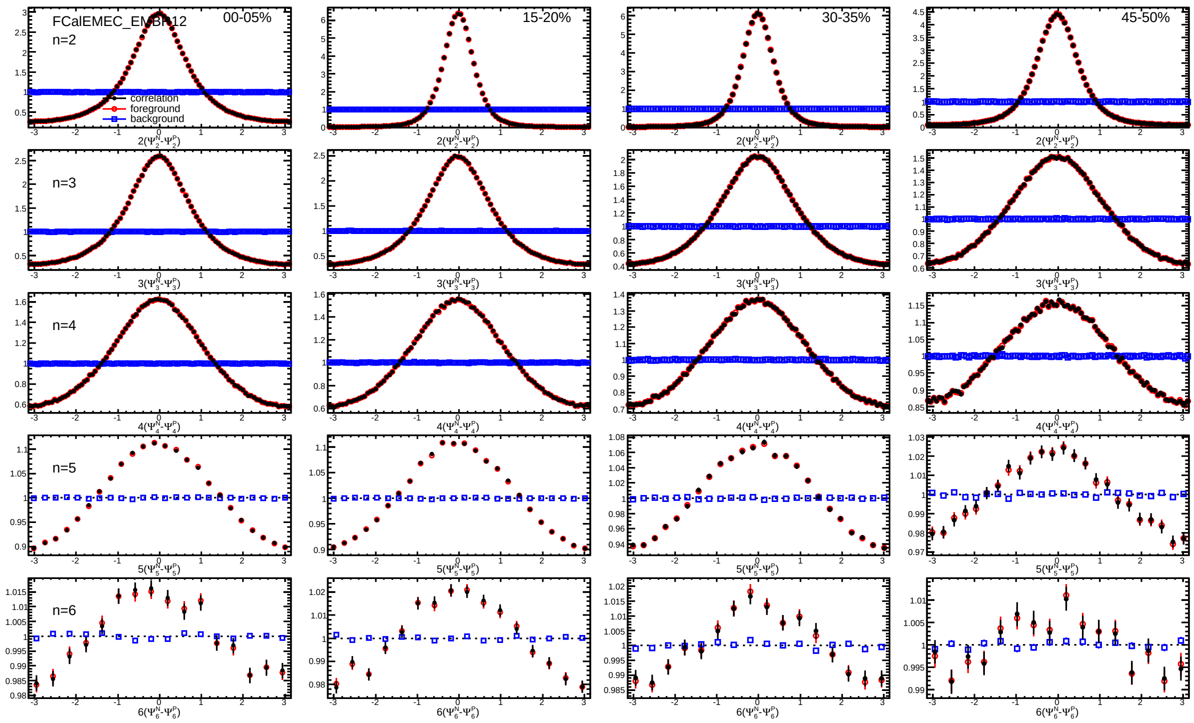


Figure 20: The 2SE correlation functions $C(n(\Psi_n^N - \Psi_n^P))$ for event-plane at same order. Top to bottom rows corresponds to n=2-6, and columns correspond to different centrality intervals.

Figure 21 shows the centrality dependence of the cosine average, $\left\langle \cos 2\left(\Psi_2^N - \Psi_2^P\right)\right\rangle$, calculated from the 2SE correlation function for n=2. According to Eq. 28, the square root of the cosine average gives the subevent resolution. The same figure also shows the values of $\left\langle \sin 2\left(\Psi_2^N - \Psi_2^P\right)\right\rangle$ as an estimate of the systematic effects. The magnitude of the sine terms correlates with the cosines and has a negative sign. The origin of these non-zero sine terms can be understood as the result of a simple rotation of $\Psi$ angle in the P-side relative to the $\Psi$ angle in the N-side. Such a rotation can arise from relative misalignment of the two sides of the ATLAS calorimeter, energy mis-calibration or dead area or low efficiency area. These effects can lead to detector level correlations between the two-sides. Denoting the systematic shift between the two-sides as $\delta$, the measured cosine and sine terms are modified due to this shift:

$$\left\langle \cos k\left(\Psi_n^{\mathrm{N}} - \Psi_n^{\mathrm{P}} + \delta\right)\right\rangle \approx \left\langle \cos k\left(\Psi_n^{\mathrm{N}} - \Psi_n^{\mathrm{P}}\right)\right\rangle \cos k\delta \tag{33}$$

$$\left\langle \sin k\left(\Psi_n^{\mathrm{N}} - \Psi_n^{\mathrm{P}} + \delta\right)\right\rangle \approx \left\langle \cos k\left(\Psi_n^{\mathrm{N}} - \Psi_n^{\mathrm{P}}\right)\right\rangle \sin k\delta \tag{34}$$

$$\frac{\left\langle \cos k\left(\Psi_n^{\mathrm{N}} - \Psi_n^{\mathrm{P}} + \delta\right)\right\rangle}{\left\langle \cos k\left(\Psi_n^{\mathrm{N}} - \Psi_n^{\mathrm{P}} + \delta\right)\right\rangle} \approx \tan k\delta \approx k\delta \tag{35}$$

$$\tag{36}$$

where the ratio is used to quantify the value of sine (systematics) relative to the cosine (signal). If the sine term is purely related to a global rotation of energy flow of one-side relative to the other side, then the ratio should be independent of centrality and proportional to $k$. Figure 21 show that the shift is indeed independent of centrality. The amount of rotation is about $\delta \approx 0.01$ radian or half a degree. Note that a pure rotation is not removed by dividing by the mixed-event distribution. This is because a rotation of a uniform distribution still yields a uniform distribution, and hence the rotation only manifests itself if the amplitude of the correlation is non-zero. Therefore the event-mixing technique accounts only for non-physical correlations that lead to non-uniform distributions in $n\left(\Psi_n^{\mathrm{N}} - \Psi_n^{\mathrm{P}}\right)$

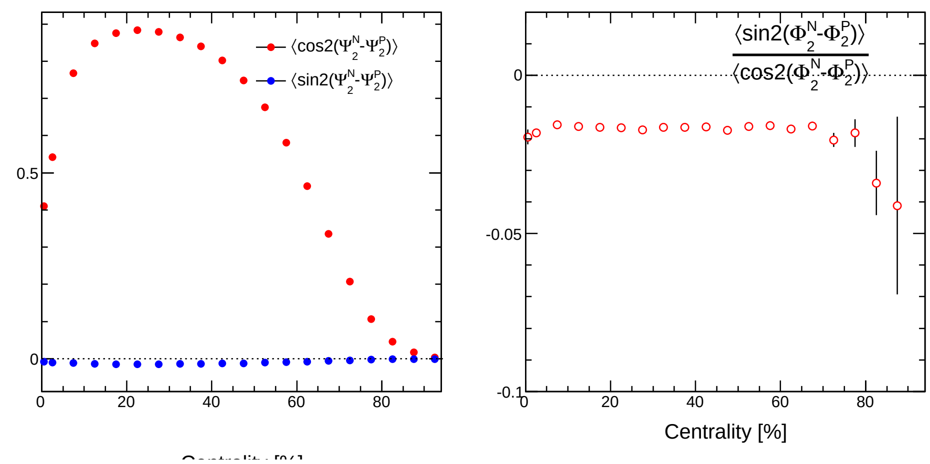


Figure 21: Centrality dependence of $\left\langle \cos 2\left(\Psi_2^N - \Psi_2^P\right)\right\rangle$ and $\left\langle \sin 2\left(\Psi_2^N - \Psi_2^P\right)\right\rangle$ (left) and the ratio between the two (right).

The same study is repeated for different $k = jn$ values: $\left\langle \cos jn\left(\Psi_n^N - \Psi_n^P\right)\right\rangle = \mathrm{Res}\{jn\Psi_n\}^2$, and the results are summarized in Fig. 22. The corresponding sine/cosine ratios are also shown and they are found to be independent of centrality and to increase linearly with $n$ and $j$. They are all consistent with the same rotation value of $\delta \sim 0.0085$, which supports the hypothesis of a small rotation. The fractional change in the cosine term due to a rotation $\delta$ is $1 - \cos k\delta \approx (k\delta)^2/2 \approx \tan^2 k\delta/2$. This is assigned as the systematic error on the resolution. Note that the contribution to the systematic error from this source is quite small: even for $k = 12$, the fractional change is only about $(0.12 * 0.085)^2/2 = 0.7\%$ in the resolution value.

#### 4.2.2 3SE results

The systematic uncertainties of the resolution correction are evaluated using the three-subevent method Eq. 29, with reference detectors taken from different $\eta$ ranges. It should be emphasized that all the cosines in Eq. 29 are calculated from the correlation function defined in Eq. 32.

The checks can be roughly divided into two types. In Type-I analysis, the resolutions are calculated separately for $\mathrm{Det}_P$ and $\mathrm{Det}_N$ in two separate 3SE studies with the reference detectors $B$ and $C$ chosen to have an $\eta$ separation greater than 1.0 from the Det and from each other.

In the Type-II analysis, we chose $A$ and $B$ as $\mathrm{Det}_N$ and $\mathrm{Det}_P$, and chose $C$ from the list of reference detectors situated between A and B. This allows us to calculate the resolution for $Det_P$ from Eq. 29. We then swap the $A$ and $B$ while keep the same $C$ and calculate the resolution for $Det_N$. Both can be compared with results from 2SE method. The Type-II checks are similar to the 2SE method, as one can see from the following equation,

$$\mathrm{Res}\{\Psi_n^{Det_P}\} = \sqrt{\frac{\left\langle\cos\left(n\left(\Psi_n^{Det_P}-\Psi_n^{B}\right)\right)\right\rangle\left\langle\cos\left(n\left(\Psi_n^{Det_P}-\Psi_n^{Det_N}\right)\right)\right\rangle}{\left\langle\cos\left(n\left(\Psi_n^{Det_N}-\Psi_n^{B}\right)\right)\right\rangle}} \tag{37}$$

$$\mathrm{Res}\{\Psi_n^{Det_N}\} = \sqrt{\frac{\left\langle\cos\left(n\left(\Psi_n^{Det_N}-\Psi_n^{B}\right)\right)\right\rangle\left\langle\cos\left(n\left(\Psi_n^{Det_P}-\Psi_n^{Det_N}\right)\right)\right\rangle}{\left\langle\cos\left(n\left(\Psi_n^{Det_P}-\Psi_n^{B}\right)\right)\right\rangle}} \tag{38}$$

In fact $\cos\left(n\left(\Psi_n^{Det_N}-\Psi_n^{B}\right)\right)$ and $\cos\left(n\left(\Psi_n^{Det_P}-\Psi_n^{B}\right)\right)$ would cancel each other if their resolution are the same, and the end results would be identical to the two-subevent formula Eq. 28. However the main advantage here is that we do not need to assume the DetN and DetP to have same resolution explicitly. The list of checks are summarized in Table 5.

| Type-I checks | Type-II checks |
|---|---|
| $\mathrm{Det_P} - \mathrm{EMBR_N} - \mathrm{FCAL_N}$ | $\mathrm{Det_P} - \mathrm{EMBR0} - \mathrm{Det_N}$ |
| $\mathrm{Det_N} - \mathrm{EMBR_P} - \mathrm{FCAL_P}$ | $\mathrm{Det_N} - \mathrm{EMBR0} - \mathrm{Det_P}$ |

Table 5: A list of 3SE checks. See Table 4 for description of the detectors.

We can now compare the resolution found by Type-I or Type-II to the resolution found by the 2SE method. Figure 23 shows, as a function of centrality, the ratio of these resolutions (i.e Type-I/2SE and Type-II/2SE) for the 2nd-order event plane (i.e n=2) and for various values of j in $\mathrm{Res}\{2j\Psi_2\}$. Type-I results show an almost centrality independent deviation from unity, which increases almost linearly with increasing $j$ values, while the Type-II results are consistent with no deviation from the 2SE results, except for very peripheral collisions. Note that the "mirror-image" behaviour of the two sets of points in the right-hand plots (Type-II/2SE) follows from the defining formulae Eq. 37 and Eq. 38 and the choice of detectors used.

These comparisons are repeated for $n = 3-6$ in Figs. 24-27, respectively. Similar systematic deviations are observed, however the deviations seem show slight centrality dependence, and the trends also seem to differ for different $n$ values. In this analysis, the systematic uncertainties are quoted as centrality independent deviations from both types of checks and then added in quadrature. They are summarized in the top part of Table 6.

### 4.2.3 Resolution results

Figure 28 summarizes the event-plane resolutions for $n = 2-6$ used in this analysis together with their systematic uncertainties. They include both contributions of the non-vanishing sine terms from the 2SE correlation, as well as the deviations of the 3SE results (error summarized in Table 6).

Figure 29 and 30 shows the combined resolution terms for the eight two-plane correlators in Table 2, using the notation of Eq. 16:

$$\mathrm{Res}\{k(\Psi_n - \Psi_m)\} \equiv \mathrm{Res}\{k\Psi_n\}\mathrm{Res}\{k\Psi_m\}\ . \tag{39}$$

These combined resolution values lie in the range of a few percent up to about 40%. They also show quite different centrality dependence trends. The systematic uncertainties for combined resolutions are propagated from individual resolution terms, and they are summarized in Table 6.

## 4.3 Corrected results

The final event-plane correlations are obtained by dividing the raw signals (Fig. 16) by the combined resolution factors (Fig. 29). They are shown in Fig. 31 and 32. The various sources of the systematic uncertainties for this measurements are summarized in Table 6.

The top part of the table lists the uncertainties for the individual event-plane resolution. They are estimated from Fig. 22 for the sine term in the 2SE correlation, as well as the deviations between the 3SE from 2SE results, estimated conservatively to cover the deviation in 0-70% centrality range (Fig. 23-Fig. 27). The bottom part of the table shows the uncertainty for the raw cosine signal of the correlation function and the combined event-plane resolution. The former is evaluated as the absolute values of the sine terms and the sine and cosine terms of the mixed-events distribution and is quoted as the absolute error on the raw signal, so is correlated with the statistical error. This error is important when either the raw signal is small or the resolution is poor. The latter is calculated via Eq. 39 using standard error propagation.

| Error for $\mathrm{Res}\{jn\Psi_n\}$ | | | | | |
|---|---|---|---|---|---|
| n | 2 | 3 | 4 | 5 | 6 |
| 3SE comparison | $0.85j\%(j\leq 2)$<br>$3\%(j{=}3)$<br>$4.5\%,6\%,8\%$ ($j$=4,5,6) | $3.0j\%$ | $2.5j\%$ | $3.5j\%$ | $9j\%$ |
| sin component | $0.5\times(0.085jn)^2\%$ | | | | |

| Error for $\langle\cos jk(\Phi_n - \Phi_m)\rangle$ correlators | | | | | | | | |
|---|---|---|---|---|---|---|---|---|
| (j,n,m) | (1,2,4) | (2,2,4) | (3,2,4) | (1,2,3) | (1,2,6) | (1,3,6) | (1,3,4) | (1,2,5) |
| $\mathrm{Res}\{jk(\Psi_n - \Psi_m)\}$ | 3.06% | 6.73% | 11.0% | 6.71% | 9.49% | 10.8% | 15.9% | 9.24% |
| Raw distribution from sine and mixed-events (absolute error on raw $\times 10^{-4}$) | 5-15 | | | | | | | |

Table 6: (top table) summary of sources of systematic uncertainties for individual $\mathrm{Res}\{jn\Psi_n\}$ terms coming from 2SE/3SE comparision (Figs. 24-27), and sine component of the 2SE correlations (Fig. 22 and the discussion at the end of Section 4.2). Note that the uncertainties of $\mathrm{Res}\{jn\Psi_n\}$ are found to be proportional to values of $j$. (bottom table) summary of sources of systematic uncertainties for the final correlators $\langle\cos jk(\Phi_n - \Phi_m)\rangle$, including those for the combined resolution caculated from $\mathrm{Res}\{jn\Psi_n\}$ terms, and the raw correlations.

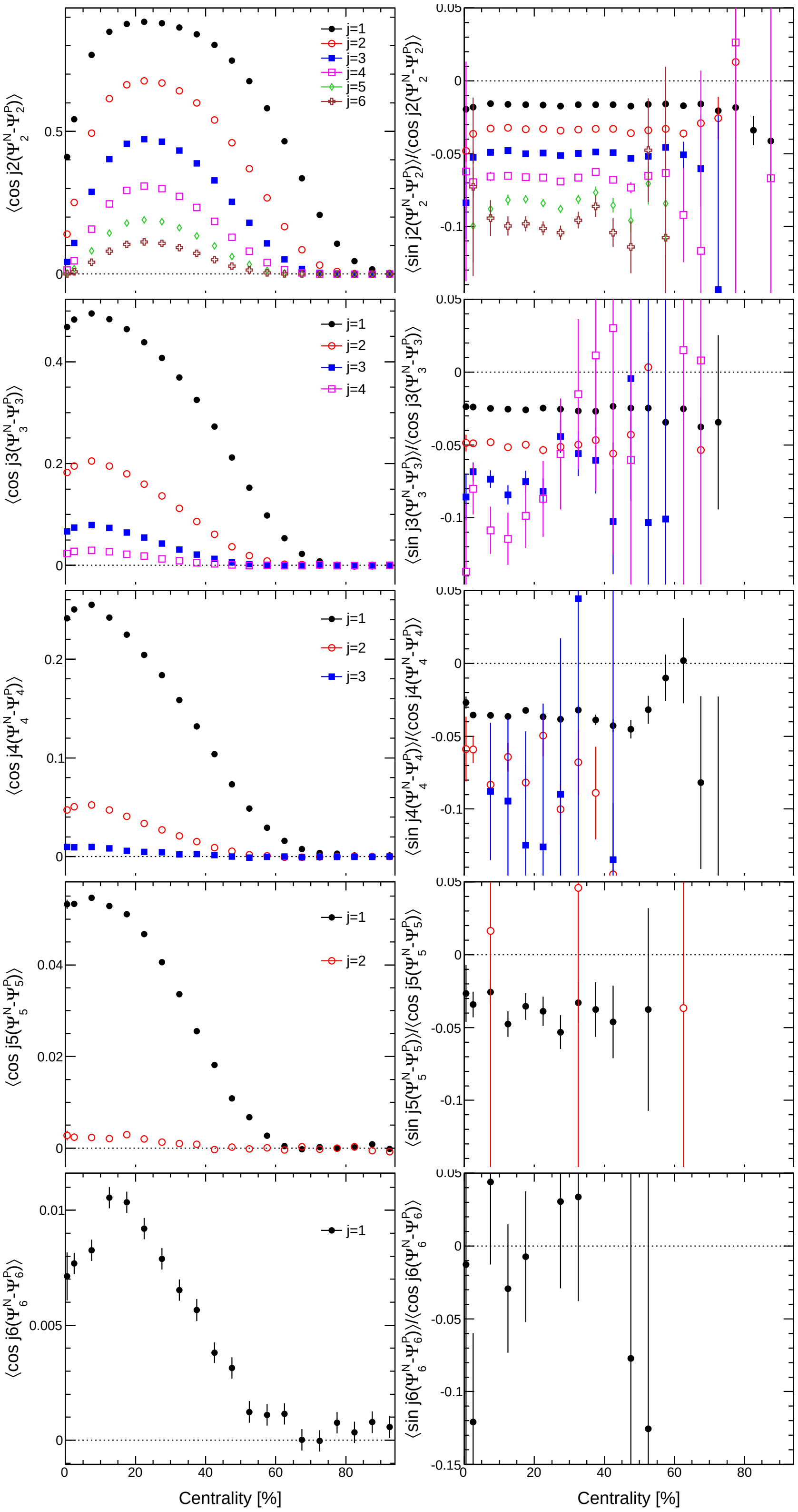

Figure 22: Centrality dependence of $\left\langle \cos jn\left(\Psi_n^N - \Psi_n^P\right)\right\rangle$ values (left panels) and $\left\langle \sin jn\left(\Psi_n^N - \Psi_n^P\right)\right\rangle / \left\langle \cos jn\left(\Psi_n^N - \Psi_n^P\right)\right\rangle$ values (right panels). Each row corresponds to the order of the event-plane ($n$ = 2–6 from top to bottom). The different symbol in each panel corresponds to different values of $j$.

Not reviewed, for internal circulation only

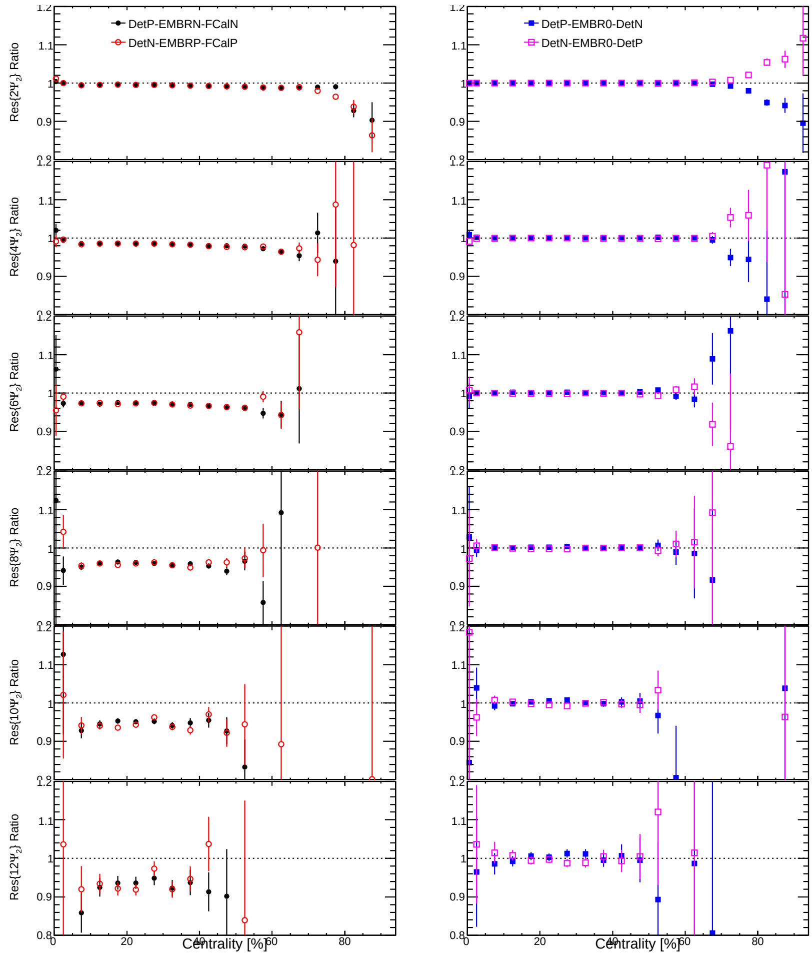


Figure 23: The centrality dependence of the ratios of 3SE results to 2SE results for Type-I (left panels) and Type-II (right panels) checks for $2^{nd}$-order event-plane. Each row is for different $j$ as in Res$\{2j\Psi_2\}$.

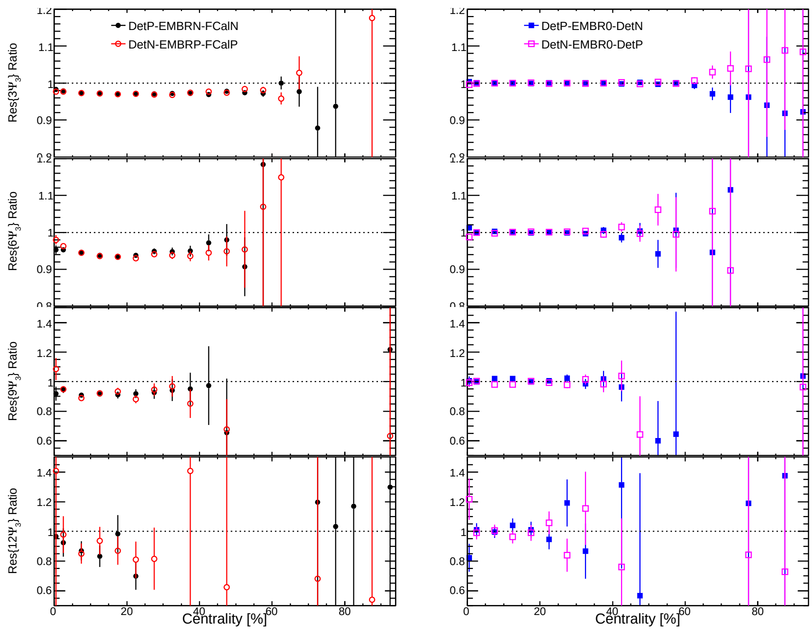


Figure 24: The centrality dependence of the ratios of 3SE results to 2SE results for Type-I (left panels) and Type-II (right panels) checks for $3^{rd}$-order event-plane. Each row is for different $j$ as in Res$\{3j\Psi_3\}$.

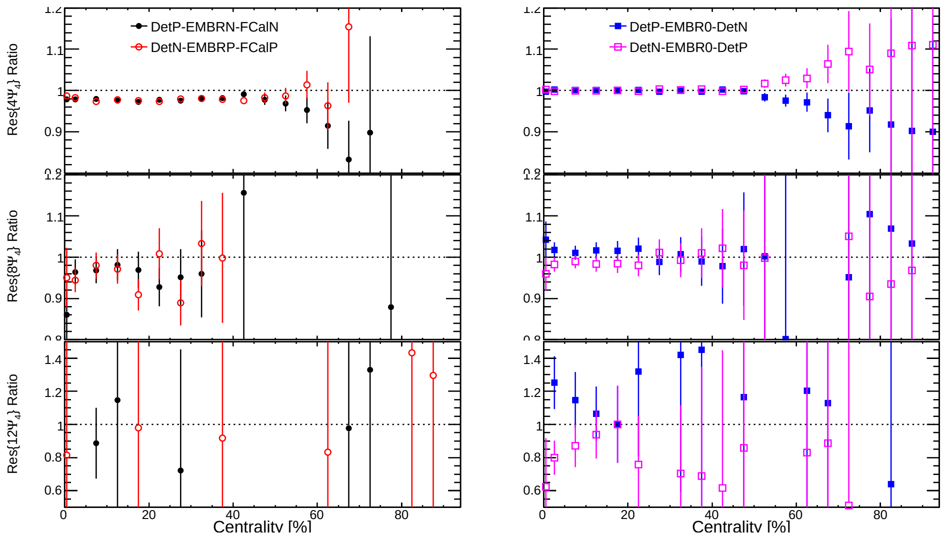


Figure 25: The centrality dependence of the ratios of 3SE results to 2SE results for Type-I (left panels) and Type-II (right panels) checks for $4^{th}$-order event-plane. Each row corresponds to different values of $j$ as in Res$\{4j\Psi_4\}$.

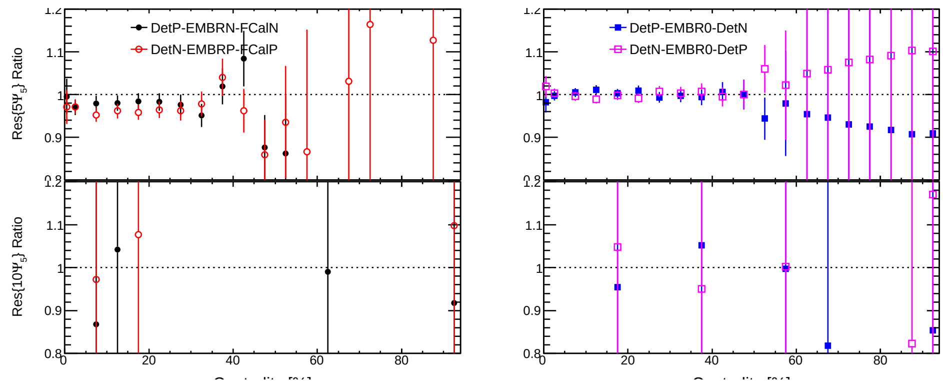


Figure 26: The centrality dependence of the ratios of 3SE results to 2SE results for Type-I (left panels) and Type-II (right panels) checks for $5^{th}$-order event-plane. Each row corresponds to different values of $j$ as in Res$\{5j\Psi_5\}$.

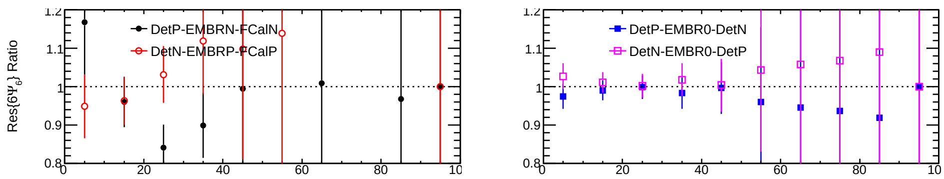


Figure 27: The centrality dependence of the ratios of 3SE results to 2SE results for Type-I (left panels) and Type-II (right panels) checks for $6^{th}$-order event-plane Res$\{6\Psi_6\}$.

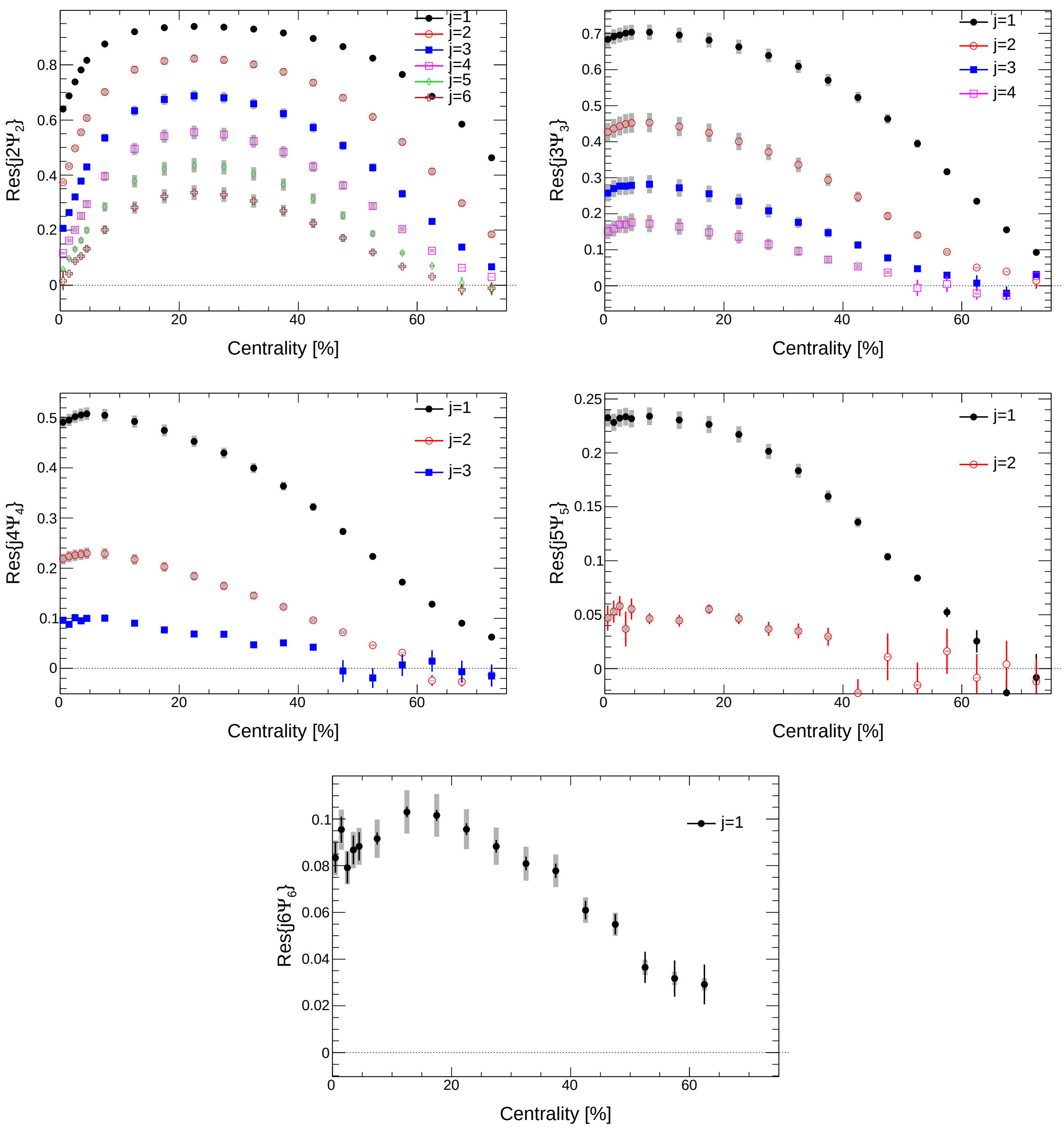


Figure 28: Summary of the event-plane resolution Res$\{jn\Psi_n\}$ and associated systematic uncertainties for n=2-6 and different values of $j$.

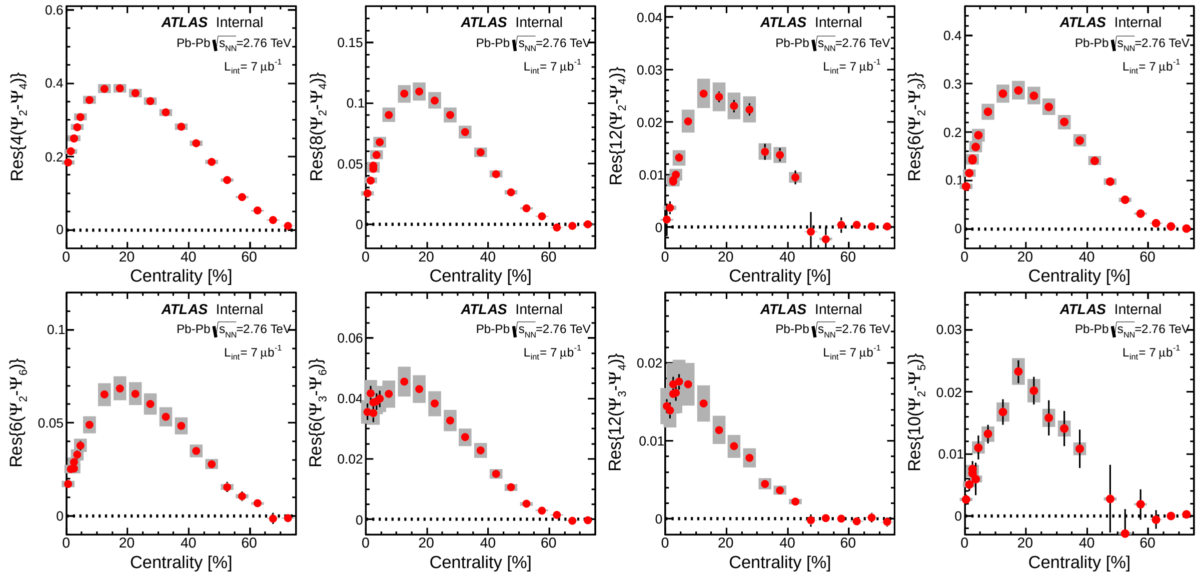


Figure 29: Combined resolution for eight cases of two-plane correlations Res$\{k(\Psi_n - \Psi_m)\}$ (Eq. 39) in fine centrality intervals, together with the systematic uncertainties.

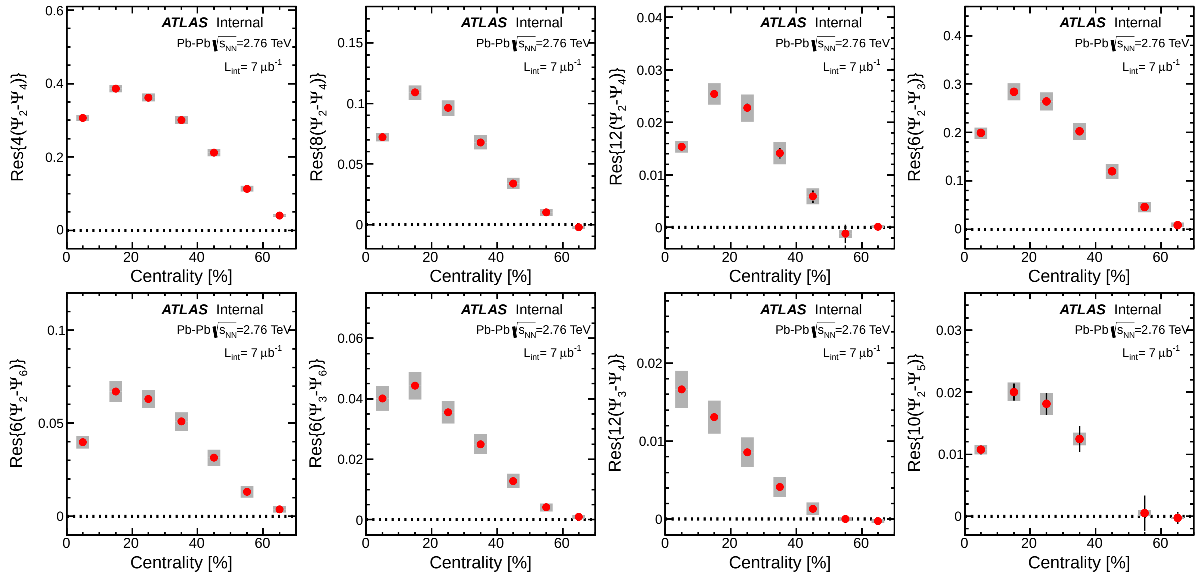


Figure 30: Combined resolution for eight cases of two-plane correlations Res$\{k(\Psi_n - \Psi_m)\}$ (Eq. 39) in coarse centrality intervals, together with the systematic uncertainties.

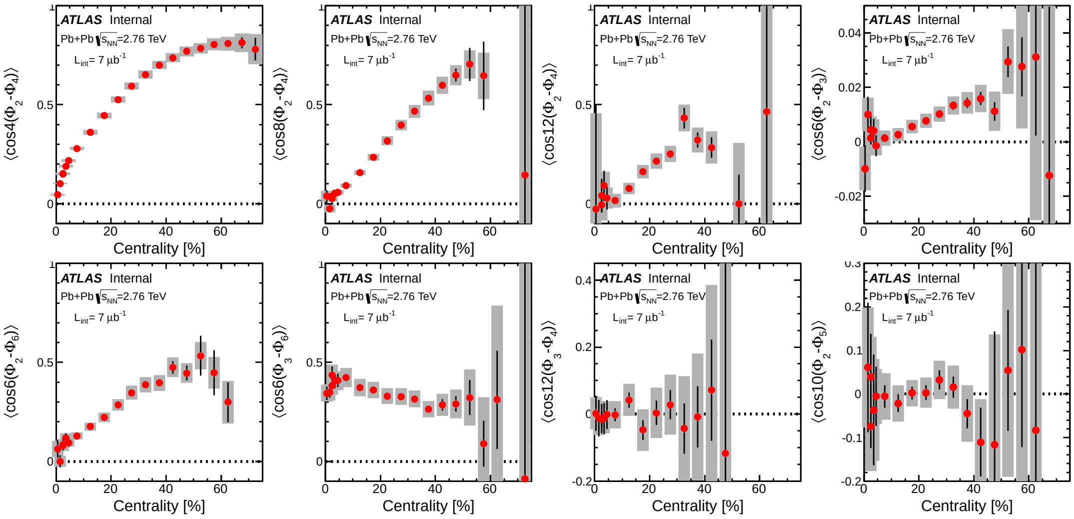


Figure 31: The centrality dependence of the two-plane correlation results in fine centrality intervals for eight cases of $\langle\cos k\,(\Phi_n-\Phi_m)\rangle$ list in Table 6.

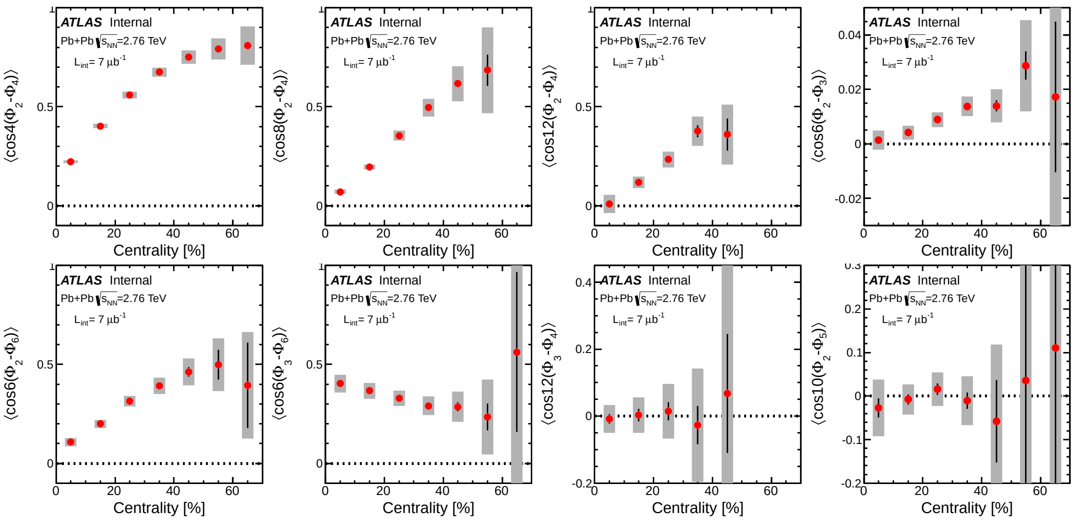


Figure 32: The centrality dependence of the two-plane correlation results in coarse centrality intervals for eight cases of $\langle\cos k\,(\Phi_n-\Phi_m)\rangle$ list in Table 6.

## 4.4 Cross checks

One potential source of the systematic uncertainty arises from non-flow effects. These effects can lead to auto-correlations between the subevents, and hence influence the correlation function and the determination of the event-plane resolutions. Therefore, it is important to check the sensitivity of the final correlation on the rapidity gap between the subevents, and/or compare the correlations obtained independently from different subevents. This is the main goal of this section.

### 4.4.1 Dependence on the $\eta$ gap

A $\Delta\eta$ gap between the $P$-side and the $N$-side subevents is necessary to reduce short-range auto-correlations (such as jets, Bose-Einstein correlation. resonance decays). By increasing the $\eta$ gap between the $P$- and $N$-side subdetectors, the influence of auto-correlations is expected to decrease, as does the resolution and raw correlation signal. Therefore a compromise must be made between maximizing the signal and suppressing the auto-correlations.

For this purpose, two-plane correlations between the P- and N-side are studied as a function of their rapidity separation. A total of 17 cases listed in Table 7 are studied. The full analysis chain is repeated independently for each case.

| Detector No | Minimum $\|\eta\|$ | Maximum $\|\eta\|$ | $\|\eta\|$ Coverage | Minimum $\Delta\eta$ gap | Average $\Delta\eta$ gap |
|---|---|---|---|---|---|
| 1 | 0.0 | 4.8 | 4.8 | 0.0 | 4.8 |
| 2 | 0.1 | 4.8 | 4.7 | 0.2 | 4.8 |
| 3 | 0.2 | 4.8 | 4.6 | 0.4 | 5.0 |
| 4 | 0.3 | 4.8 | 4.5 | 0.6 | 5.1 |
| 5 | 0.4 | 4.8 | 4.4 | 0.8 | 5.2 |
| 6 | 0.5 | 4.8 | 4.3 | 1.0 | 5.3 |
| 7 | 0.6 | 4.8 | 4.2 | 1.2 | 5.4 |
| 8 | 0.7 | 4.8 | 4.1 | 1.4 | 5.5 |
| 9 | 0.8 | 4.8 | 4.0 | 1.6 | 5.6 |
| 10 | 0.9 | 4.8 | 3.9 | 1.8 | 5.7 |
| 11 | 1.0 | 4.8 | 3.8 | 2.0 | 5.8 |
| 12 | 1.2 | 4.8 | 3.6 | 2.4 | 6.0 |
| 13 | 1.5 | 4.8 | 3.3 | 3.0 | 6.3 |
| 14 | 2.1 | 4.8 | 2.7 | 4.2 | 6.9 |
| 15 | 2.7 | 4.8 | 2.1 | 5.4 | 7.5 |
| 16 | 3.3 | 4.8 | 1.5 | 6.6 | 8.1 |
| 17 | 4.1 | 4.8 | 0.7 | 8.2 | 8.9 |

Table 7: The detectors used in studying the dependence of two-plane correlations on the minimum separation in $\eta$.

Figures 33-38 show the raw signal, combined resolution, as well as the corrected correlations as a function of the minimum $\eta$ gap between the $P$-side and $N$-side subevents. The correlation function and the resolution decrease considerably with increasing $\eta_{min}$, very often by more than a factor of 4, but the corrected correlations are remarkably stable. This gives us confidence that we are indeed measuring the global event-plane correlations.

In most cases, the raw correlation signal changes smoothly with $\eta_{min}$, even for small $\eta_{min}$ values. This is because the short-range correlations, such as resonance decays, Bose-Einstein correlation or jet fragmentation can influence individual harmonics, but the influences usually have weak correlations

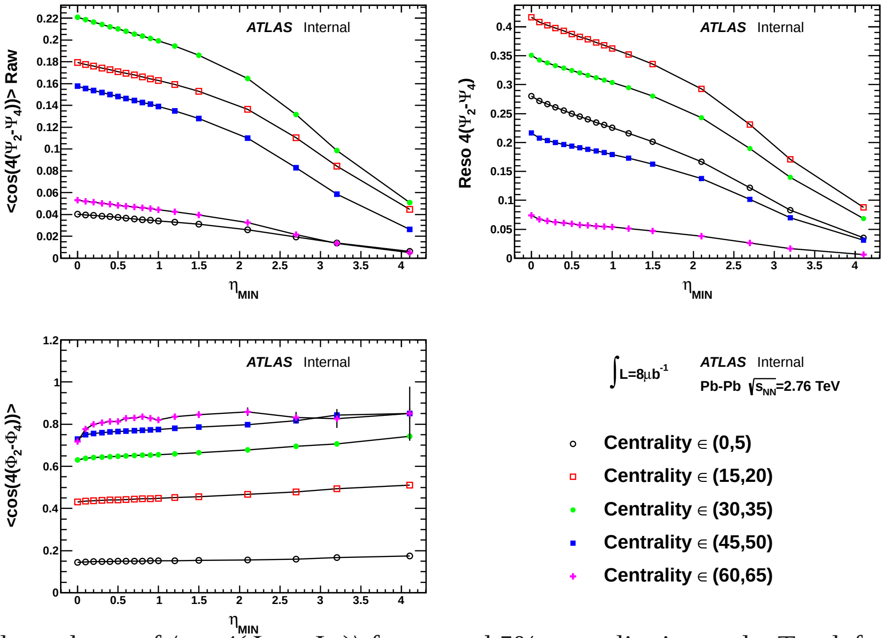


Figure 33: $\Delta\eta$ dependence of $\langle\cos 4(\Phi_2 - \Phi_4)\rangle$ for several 5% centrality intervals. Top-left panel: Correlation before resolution corrections. Second panel: The resolution factor. Third Panel: Correlation after resolution correction.

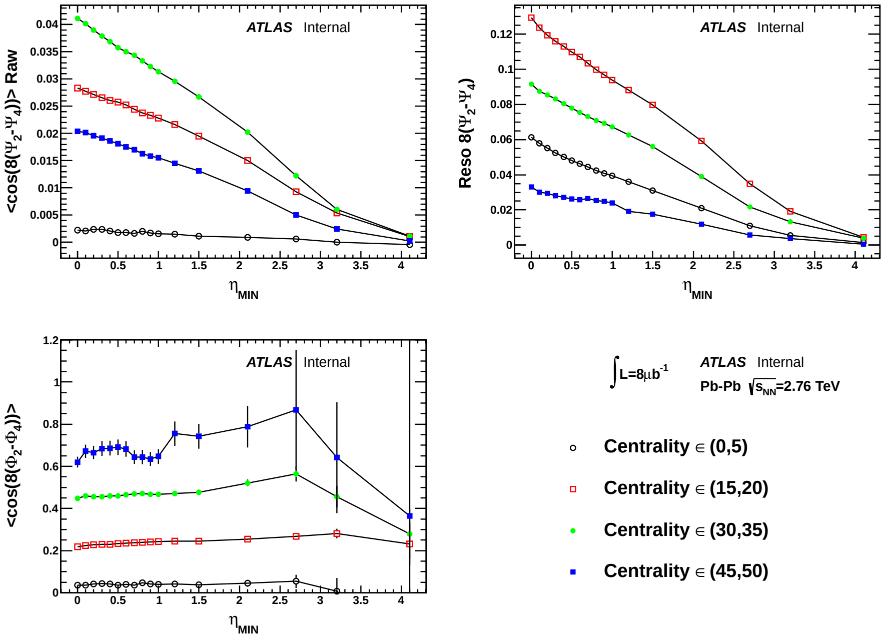


Figure 34: $\Delta\eta$ dependence of $\langle\cos 8(\Phi_2 - \Phi_4)\rangle$ for several 5% centrality intervals. Top-left panel: Correlation before resolution corrections. Top-right panel: The resolution factor. Bottom-left panel: Correlation after resolution correction.

between EPs of different order. In contrast, the estimated event-plane resolution factors have a sharp increase towards small $\eta_{min}$ for many cases. Such enhancement of the resolution leads to a suppression of the corrected correlation signal at small $\eta_{min}$. This behavior is also understandable: since the event-plane resolution is estimated from the subevent correlation of the same order, they are more affected by

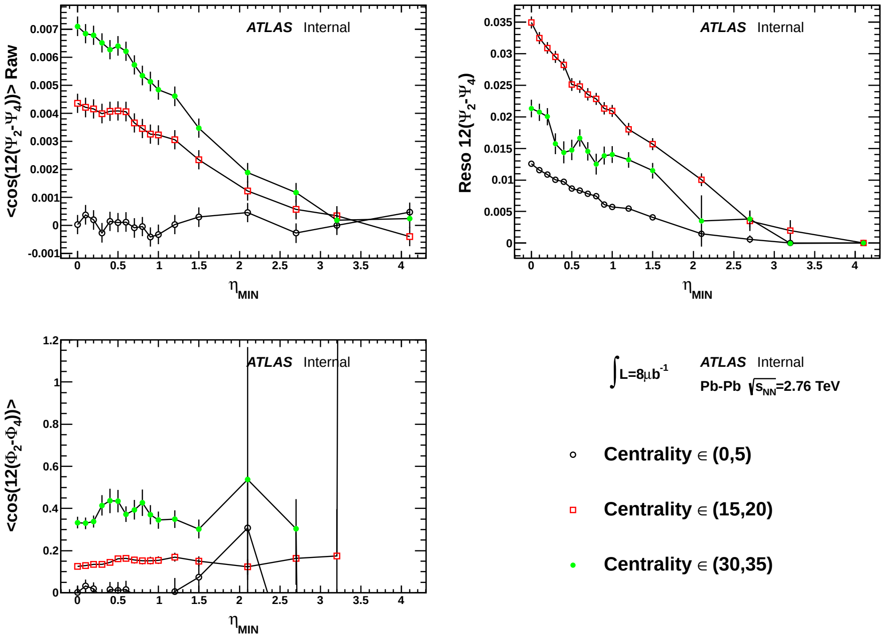


Figure 35: $\Delta\eta$ dependence of $\langle\cos 12(\Phi_2 - \Phi_4)\rangle$ for several 5% centrality intervals. Top-left panel: Correlation before resolution corrections. Top-right panel: The resolution factor. Bottom-left panel: Correlation after resolution correction.

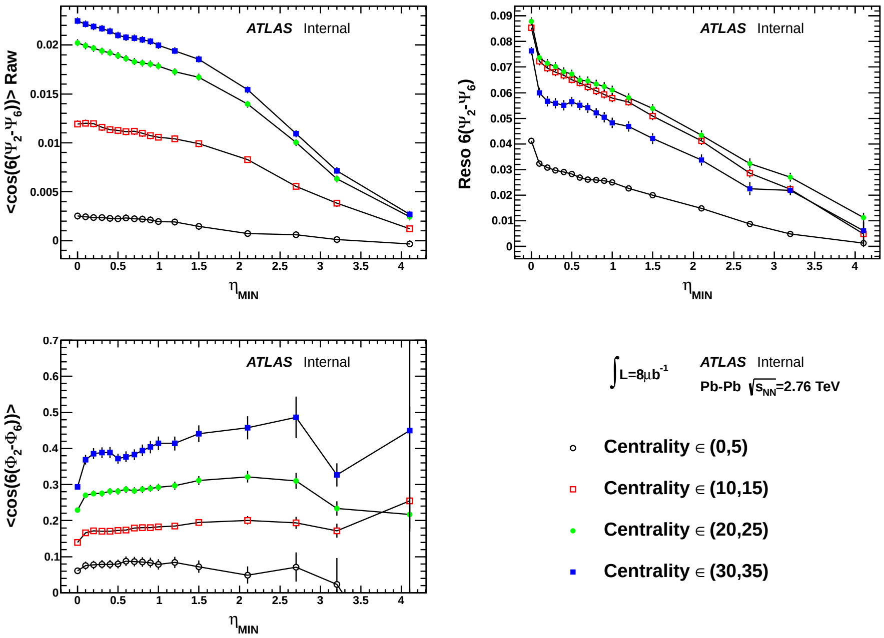


Figure 36: $\Delta\eta$ dependence of $\langle\cos 6(\Phi_2-\Phi_6)\rangle$ for several 5% centrality intervals. Top-left panel: Correlation before resolution corrections. Top-right panel: The resolution factor. Bottom-left panel: Correlation after resolution correction.

the short-range correlations. In all cases, however, these short-range correlations seem to only affect the resolution at small $\eta$ gap, and they become negligible for $\eta_{min} > 0.2$ (or equivalently a gap of $> 0.4$).

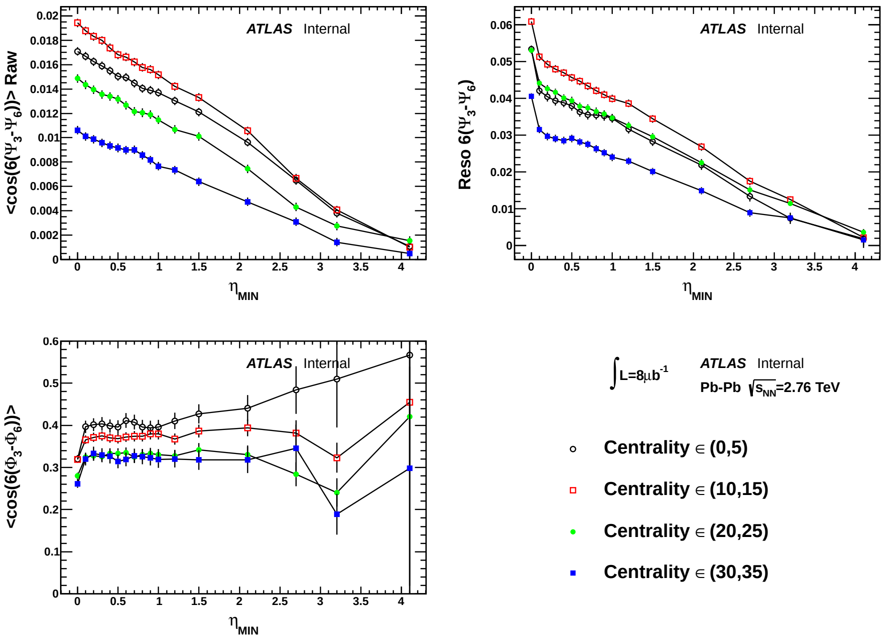


Figure 37: $\Delta\eta$ dependence of $\langle\cos 6(\Phi_3 - \Phi_6)\rangle$ for several 5% centrality intervals. Top-left panel: Correlation before resolution corrections. Top-right panel: The resolution factor. Bottom-left panel: Correlation after resolution correction.

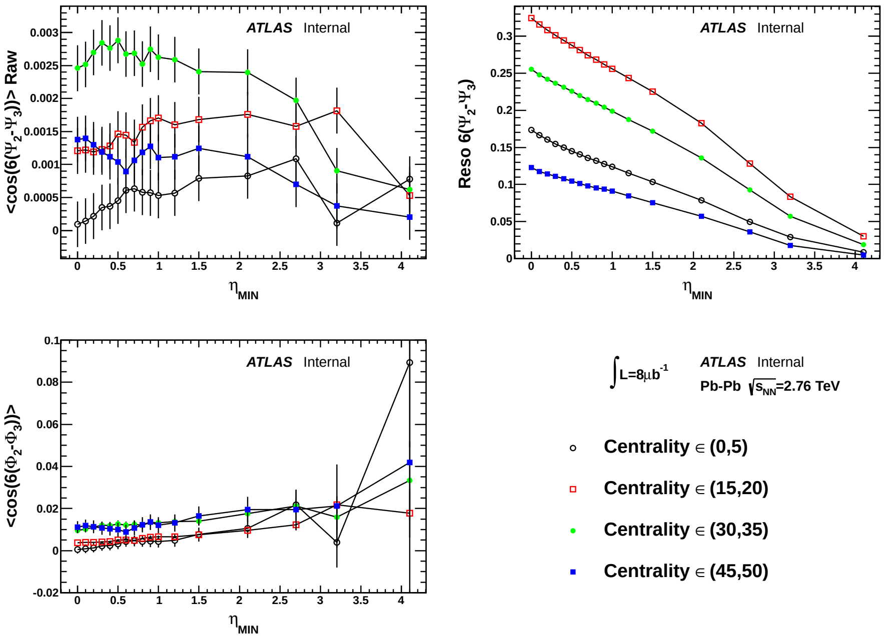


Figure 38: $\Delta\eta$ dependence of $\langle\cos 6(\Phi_2 - \Phi_3)\rangle$ for several 5% centrality intervals. Top-left panel: Correlation before resolution corrections. Top-right panel: The resolution factor. Bottom-left panel: Correlation after resolution correction.

Our default detector has a gap of 1 unit in $|\eta|$, which should be sufficient to suppress these short-range correlations.

One may also notice a lack of influence of short-range correlations on the resolution for $4(\Phi_2 - \Phi_4)$ and $6(\Phi_2 - \Phi_3)$: the sharp increase associated with short range correlation is only observed in very peripheral collisions. We believe this is because the flow signal is strong for $v_2$, $v_3$ and $v_4$, and combined resolution factor is very good (more than 0.3 as shown in Fig. 29), and so these cases are less sensitive to the non-flow effects.

### 4.4.2 Comparison of results obtained for different detectors

Results from previous study suggest that a $\eta$ gap of 1 unit is more than sufficient to suppress the short-range correlations. Table 4 gives a full list of possible symmetric detectors that satisfy such $|\eta|$ gap requirement. Each detector provides its own measurement of the two-plane correlations as well as estimation of its own systematic uncertainties. However, many of these detectors have overlapping acceptance, so the results are not fully independent from each other. Out of all these checks, the subevent FCal, EMEC, EMBR12 have non-overlapping acceptances, while the ID has different sets of systematics. Their $\eta$ coverage are summarized in Table 8. These four detectors provide a maximally independent cross-check of the measurement. The detailed results for the tracking detectors are presented in Appendix I. Here we just present the final results for comparison.

| Detector | Name | Description | $\|\eta\|$ coverage | Calorimeter-Layers |
|---|---|---|---|---|
| 1 | FCal | Forward Calorimeter | 3.3-4.8 | layer1 and 2 |
| 2 | EMEC | EM EndCap | 1.5-3.2 | EM compartments |
| 3 | EMBR12 | EM Barrel | 0.5-1.5 | EM compartments |
| 4 | ID1234 | part of Inner detector | 0.5-2.5 | tracks above 0.5 GeV |
| default | ECalFCal | ECalfCal | 0.5-4.8 | sum of Detectors 1,2,3 |

Table 8: Detectors that provide independent cross-checks for the results obtained for default detector.

Figure 39 and 40 compare the extracted raw correlation signals and the combined resolution corrections from these detectors. These detectors usually have smaller raw signal and poorer resolution, but the corrected results as shown by Fig. 41 and Fig. 42 are consistent with those obtained from the default detector. Small deviations are observed for FCal detector, especially for $\langle\cos 4(\Phi_2 - \Phi_4)\rangle$ and $\langle\cos 6(\Phi_2 - \Phi_3)\rangle$, but they are well within their own systematic uncertainties. It is possible that these differences reflect the real rapidity dependence of the underlying event-plane correlation themselves, instead of detector effects. However, we are not in a position to draw a definite conclusion on these small differences. On the other hand, the ID is an entirely different detector. It samples only charged particles above 0.5 GeV with a very different efficiency and weighting (by $p_{\mathrm{T}}$) from the Calorimeters. Hence the comparison with Calorimeter results serves a powerful check of the detector systematics. The fact that the ID results agree with the default Calorimeter measurement (well within their respective systematics), suggest that there is no need to quote additional uncertainties.

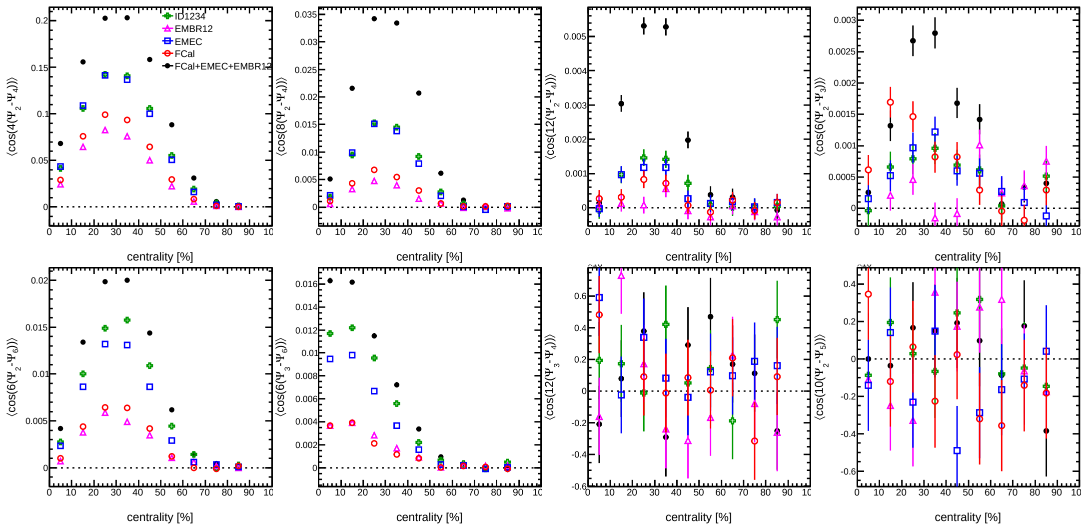


Figure 39: The centrality dependence of the two-plane raw correlation signal in 10% centrality intervals compared between different detectors for eight cases of $\langle \cos k\,(\Phi_n - \Phi_m)\rangle$.

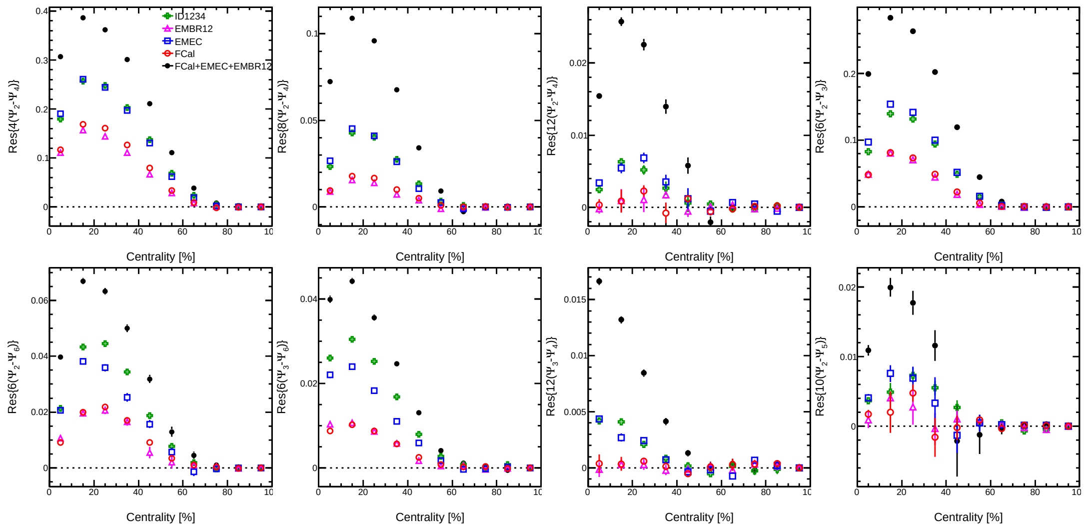


Figure 40: The centrality dependence of the combined event-plane resolution in 10% centrality intervals compared between different detectors for eight cases of $\langle \cos k\,(\Phi_n - \Phi_m)\rangle$.

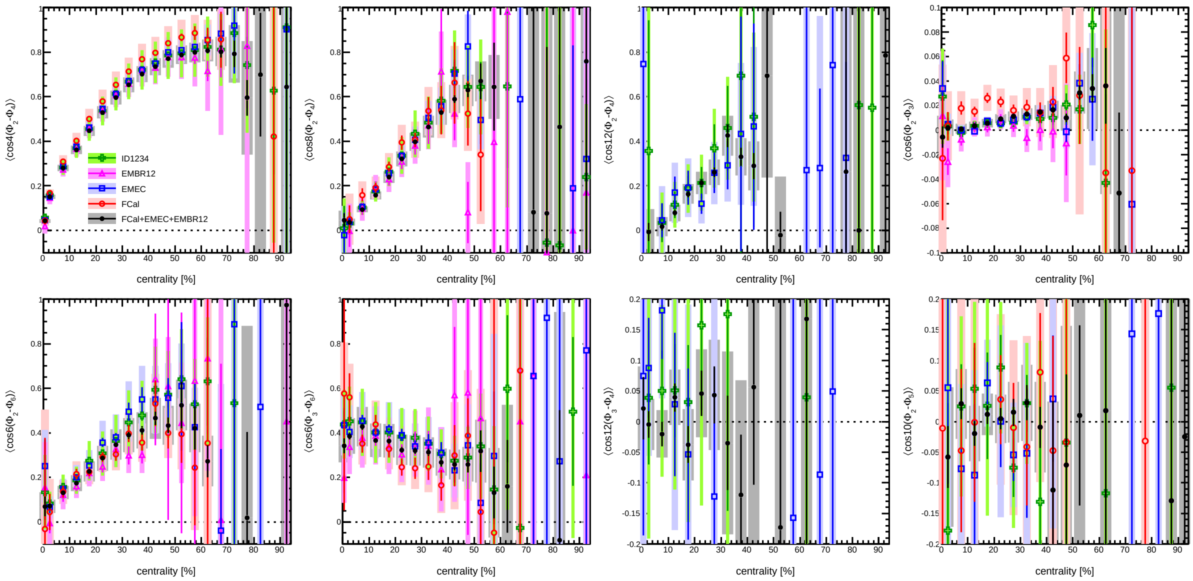


Figure 41: The centrality dependence of the combined event-plane resolution in fine centrality intervals compared between different detectors for eight cases of $\langle\cos k\,(\Phi_n - \Phi_m)\rangle$.

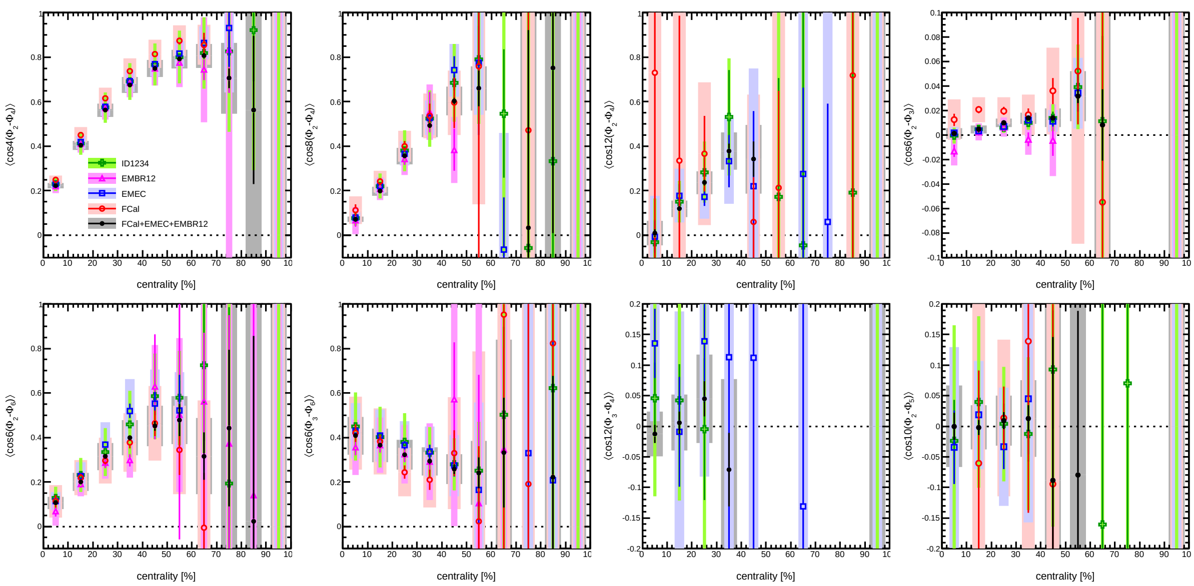


Figure 42: The centrality dependence of the combined event-plane resolution in 10% centrality intervals compared between different detectors for eight cases of $\langle\cos k\,(\Phi_n - \Phi_m)\rangle$.

# 5 Three-plane correlation analysis

## 5.1 Analysis with default detector

For three-plane correlation, the default subevents are ECal$_P$ ($0.5 < \eta < 2.7$, labeled as "A"), FCal ($3.3 < |\eta| < 3.8$, labeled as "B"), and ECal$_N$ ($-2.7 < \eta < -0.5$, labeled as "C") (see Table 4). They are schematically shown in Fig. 43. Given the symmetry between the ECal$_P$ and ECal$_N$, there are three independent measurements (see Eq. 24), which we shall label as Type 1, 2 and 3. Due to the requirement of three non-overlapping planes in the three-plane correlation, the available independent detector combinations for cross checks are limited. One such check is provided by dividing the ID into three subevents with a $\eta$ gap in between (discussed in Section 5.2). Note that the uncertainty of the resolution correction for each detector can be done via standard 2SE and 3SE methods, and this in fact has been done already in the discussion of the two-plane correlation results. Thus for this study we can apply the same systematic uncertainties discussed in the previous section.

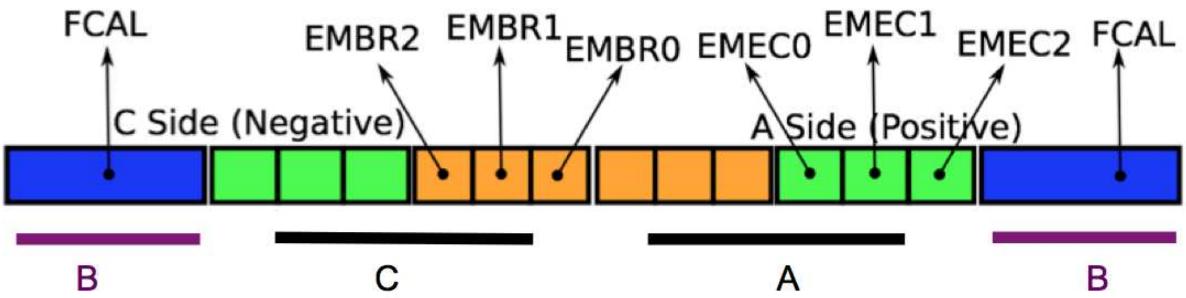


Figure 43: Schematic representation of the three detectors used for three-plane correlation analysis.

Figure 44- 49 show the correlation functions for the six three-plane correlators studied in this analysis, and for each correlator, separately for each independent measurement (Type 1,2,3). The red and blue histograms are foreground and background distributions, respectively. The background distributions are calculated from mixed events, i.e. the three individual plane angles are obtained for the corresponding subevents from three different events with similar centrality and z-vertex. Both the foreground and mixed-event distributions are normalized to unity. In the first three figures, strong correlations are already observed at the raw level, a weak signal is also seen for Fig. 48 (second to the last). In contrast, the distributions obtained by combining the angles from different events are consistent with zero signal. This mixed-event procedure gives us great confidences that the signal that we measure is real.

Figure 50 shows the extracted raw correlation signal. The magnitude is about 5-9% for $2\Psi_2 + 3\Psi_3 - 5\Psi_5$, 2-4% for $2\Psi_2+4\Psi_4-6\Psi_6$, 1-2% (but negative) for $2\Psi_2-6\Psi_3+4\Psi_4$, about 1% for $-10\Psi_2+4\Psi_4+6\Psi_6$ and consistent with 0 for $-8\Psi_2 + 3\Psi_3 + 5\Psi_5$ and $-10\Psi_2 + 6\Psi_3 + 4\Psi_4$.

Figure 51 shows the resolution terms for individual event-planes for different values of $n$ and $j$, as in Res$\{jn\Psi_n\}$, for subevents "A", "B" and "C". The systematic uncertainties were obtained via 2SE and 3SE estimates, which are discussed in great detail in section 4.2 and the appendix. Note that the resolution and systematic uncertainties associated with "A" and "C" are almost the same. This is expected as they have the same acceptance.

Once we obtain the individual resolution, they can be combined to give the total resolution for the three-plane correlators. We then obtain the corrected results by dividing the raw signal in Fig 50 with these combined resolutions. The results are summarized in Fig. 52. The systematic uncertainty comes from both the raw signal and resolution correction. The individual sources of the systematic uncertainties are summarized in Table 9. The top part of the table lists the uncertainties for the individual event-plane resolution. They are estimated from the sine term in the 2SE correlation, as well as the deviations between

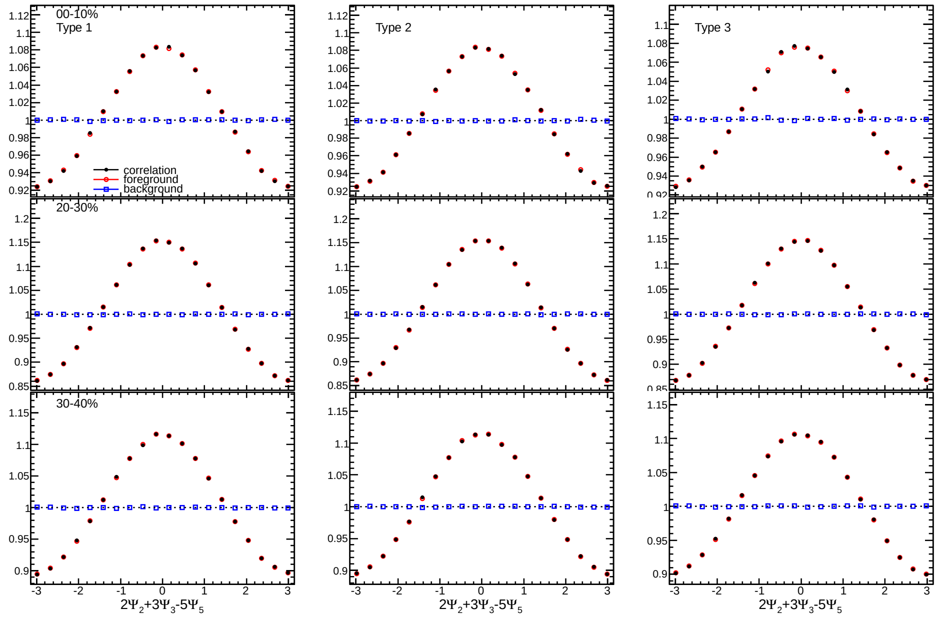


Figure 44: Distribution of $2\Psi_2 + 3\Psi_3 - 5\Psi_5$ in several centrality intervals. Each column corresponds to one type of correlation for the same correlator.

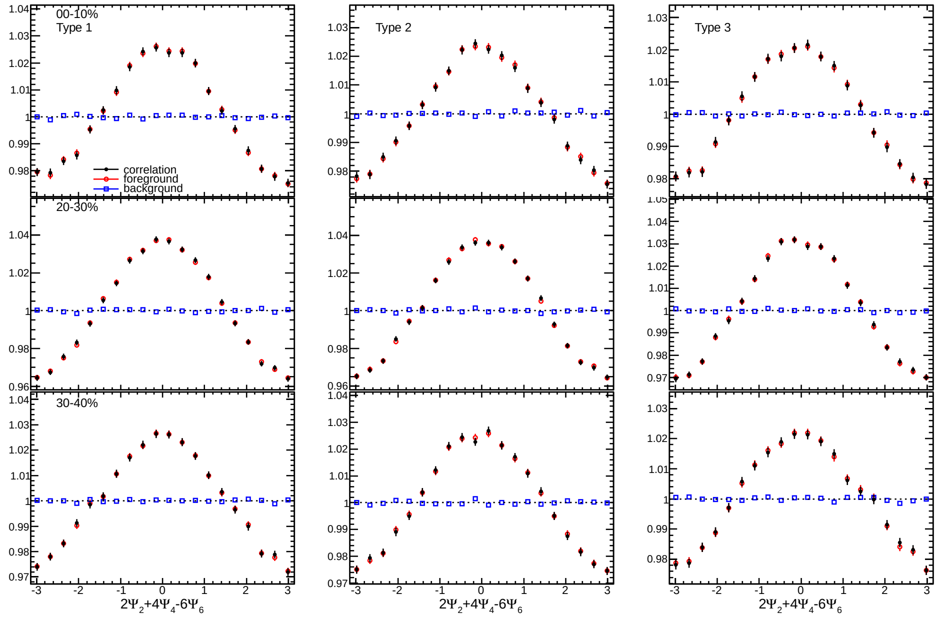


Figure 45: Distribution of $2\Psi_2 + 4\Psi_4 - 6\Psi_6$ in several centrality intervals. Each column corresponds to one type of correlation for the same correlator.

the 3SE from 2SE results. The bottom part of the table shows the uncertainties for the raw cosine signal of the correlation function and the combined event-plane resolution. The former is evaluated as the absolute values of the sine terms and the sine and cosine terms of the mixed-events distribution and is quoted as the absolute error on the raw signal, so is correlated with the statistical error.

As one can see from Table 9, most of the uncertainty arises from the resolution correction. For each

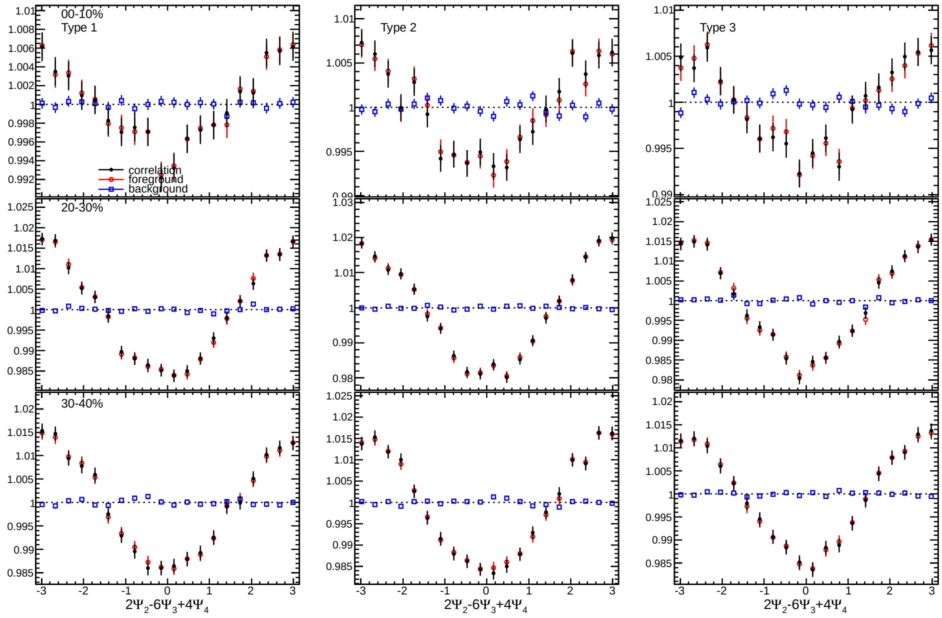


Figure 46: Distribution of $2\Psi_2 - 6\Psi_3 + 4\Psi_4$ in several centrality intervals. Each column corresponds to one type of correlation for the same correlator.

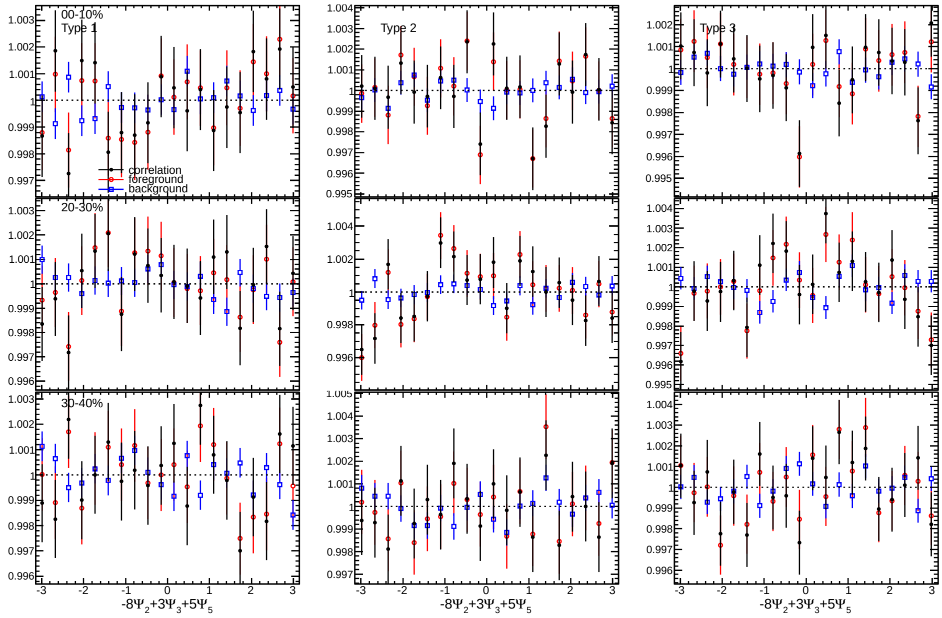


Figure 47: Distribution of $-8\Psi_2 + 3\Psi_3 + 5\Psi_5$ in several centrality intervals. Each column corresponds to one type of correlation for the same correlator.

three-plane correlator, the three independent estimates agree with each other within their uncertainties. One can then take a simple weighted average between the three measurements to obtained the final corrected correlations. The results are shown in Fig. 53. The systematic uncertainties are calculated as the quadrature sum of two sources: 1) the weighted-average of the systematic uncertainties for the three individual measurements; 2) the point-to-point differences between the three measurements.

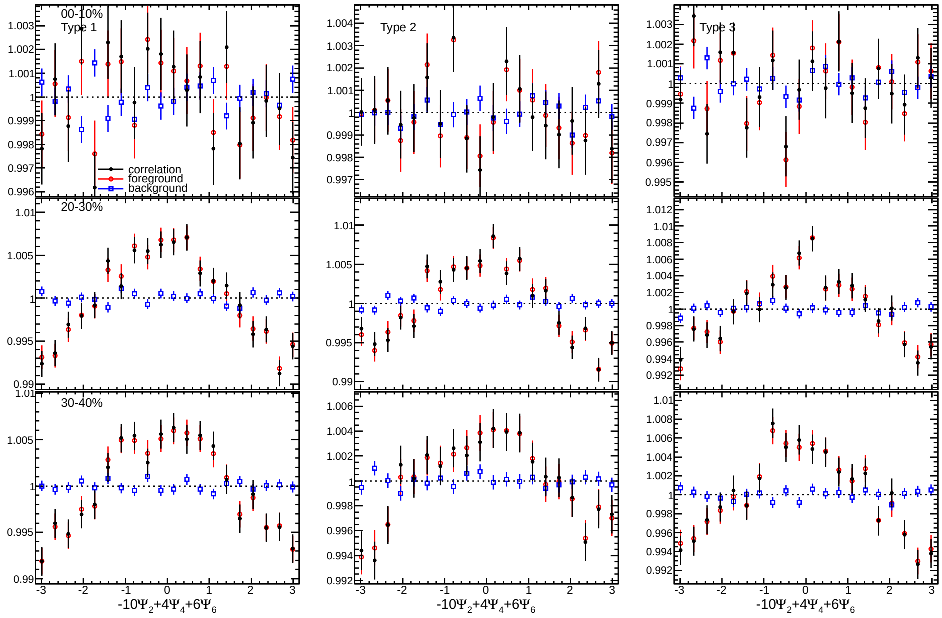


Figure 48: Distribution of $-10\Psi_2 + 4\Psi_4 + 6\Psi_6$ in several centrality intervals. Each column corresponds to one type of correlation for the same correlator.

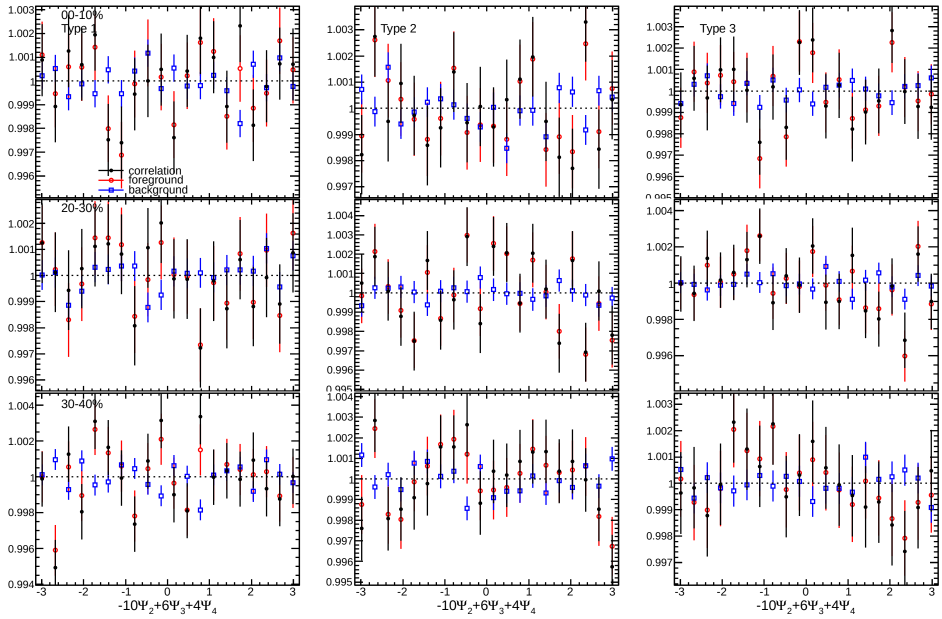


Figure 49: Distribution of $-10\Psi_2 + 6\Psi_3 + 4\Psi_4$ in several centrality intervals. Each column corresponds to one type of correlation for the same correlator.

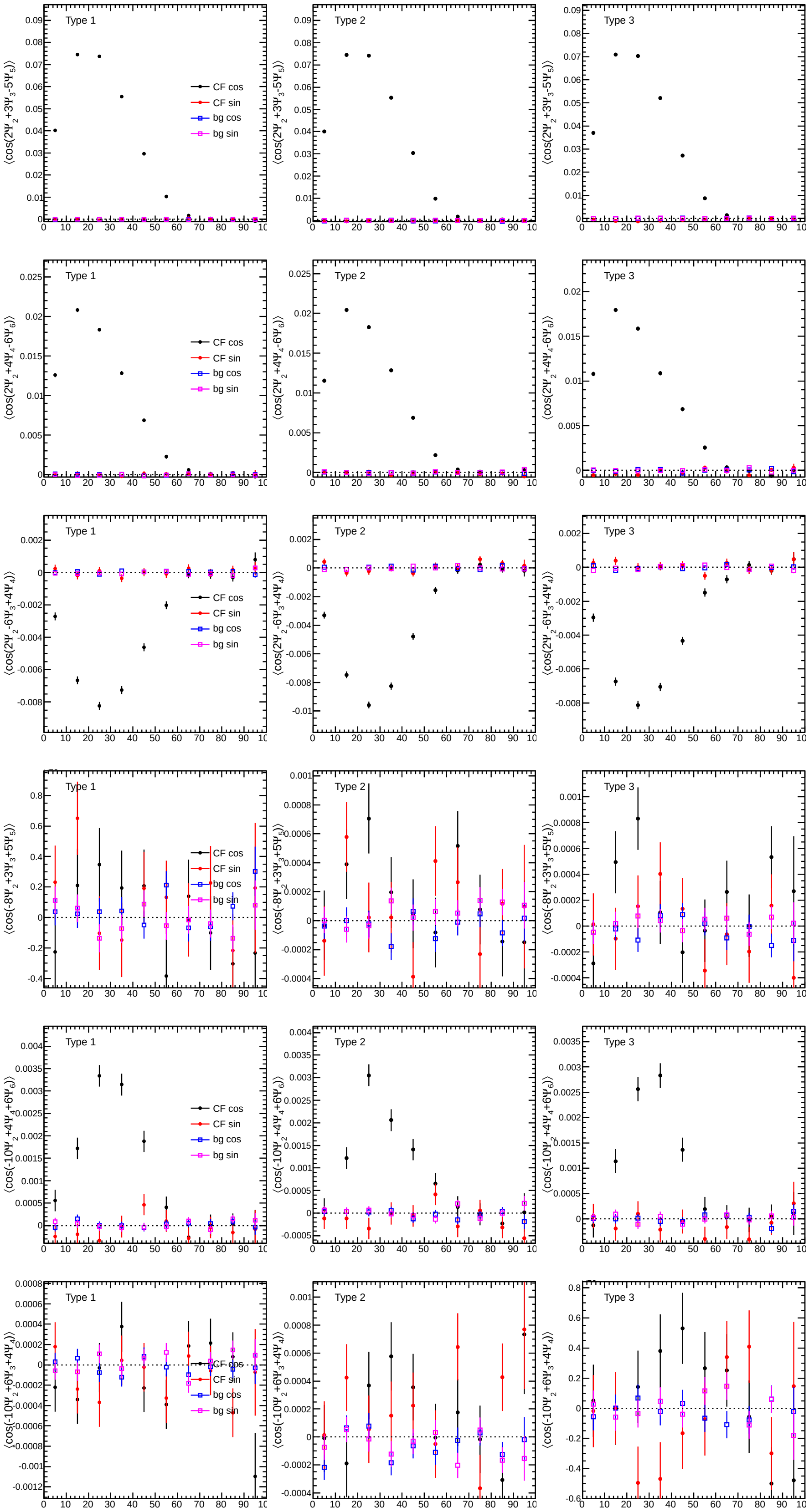


Figure 50: Centrality dependence of the raw cosine signal for six three-plane correlators. They are compared with the sine values as well as the sine and cosine obtained from mixed-events.

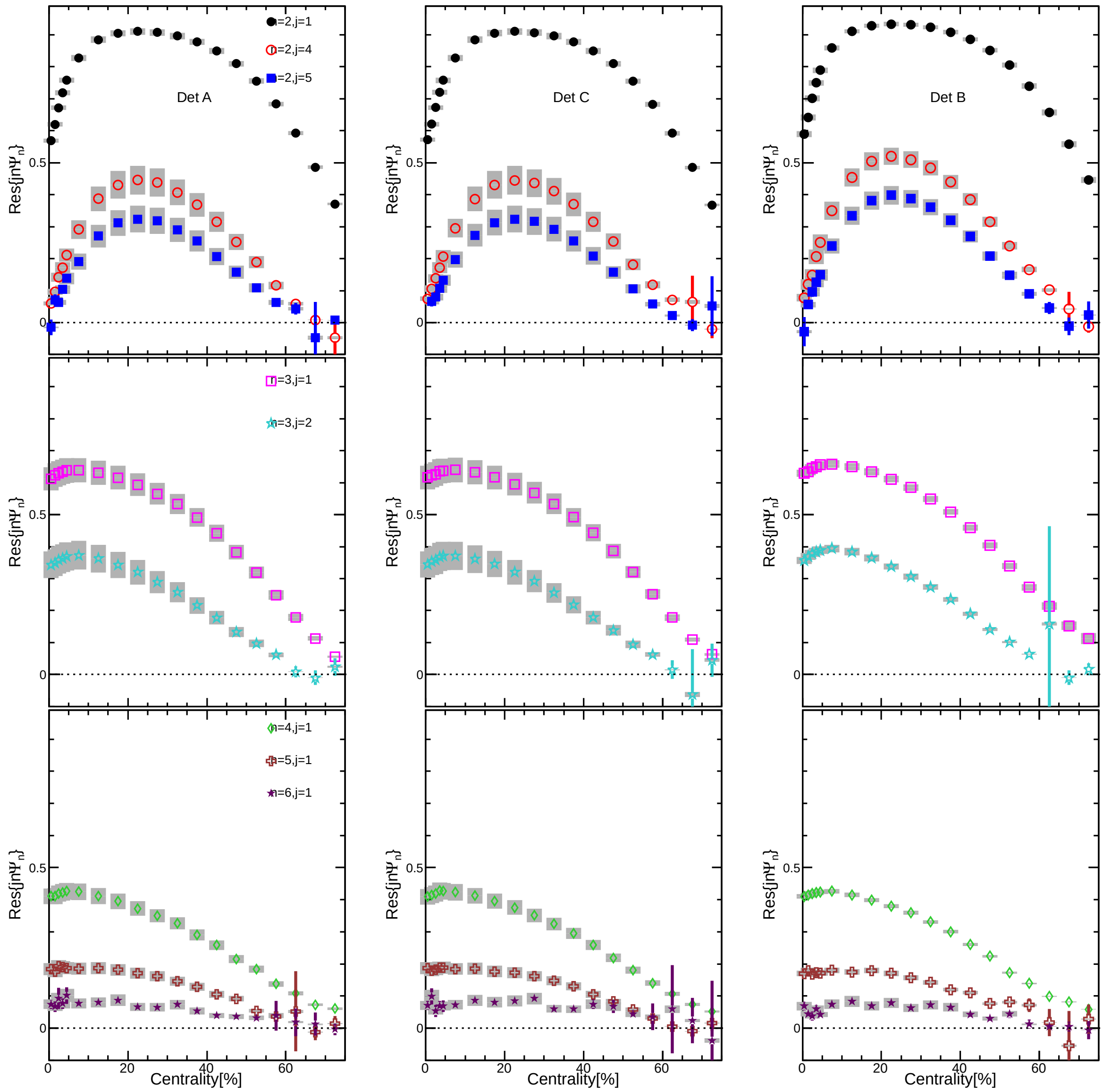


Figure 51: Centrality dependence of the resolution for individual event-planes associated with the three detectors used in the three-plane correlations.

Not reviewed, for internal circulation only

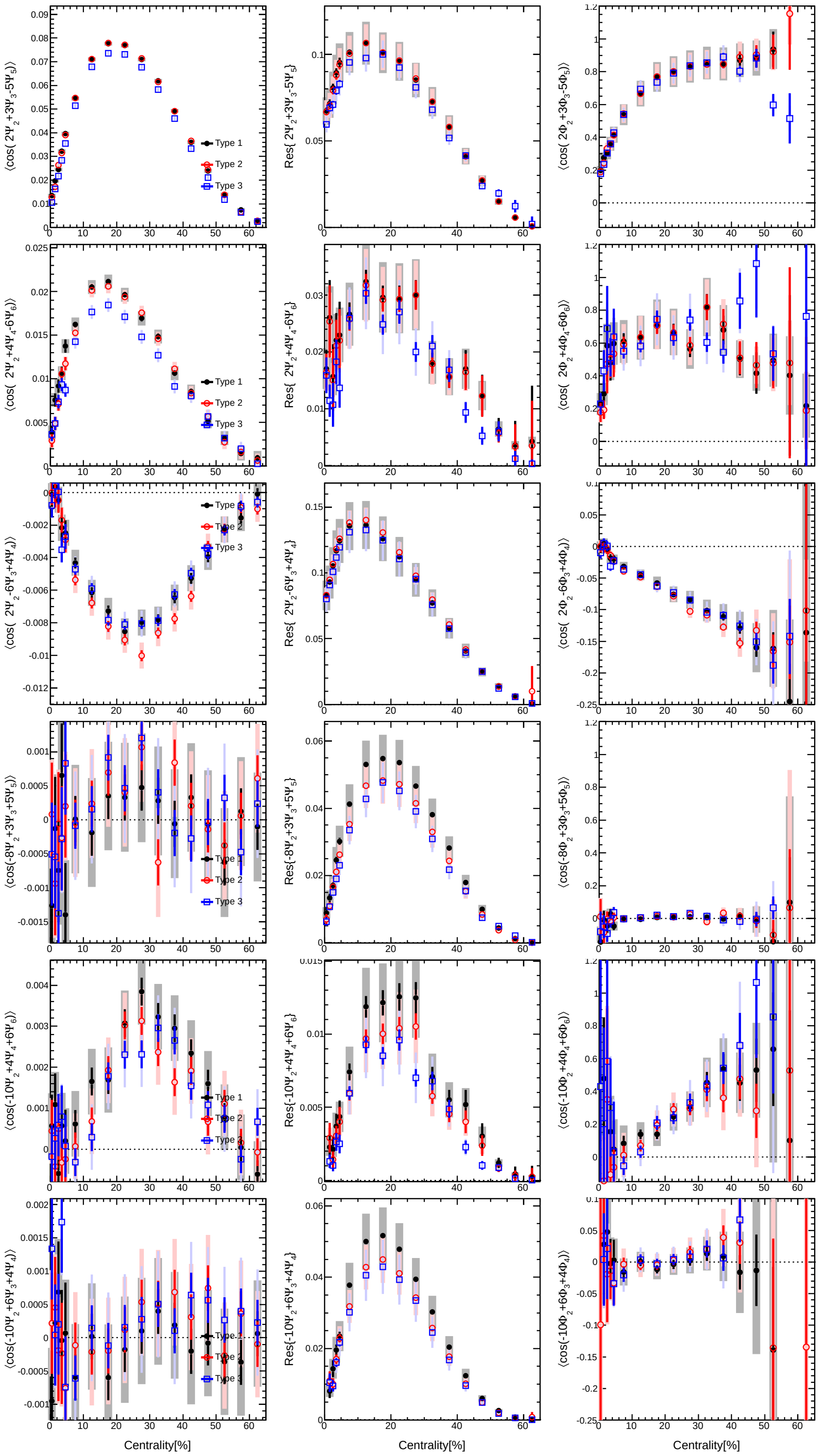

Figure 52: Centrality dependence of the raw signal (left column), combined resolution (middle column) and correlated correlation (right column) for $\langle\cos(2\Phi_2 + 3\Phi_3 - 5\Phi_5)\rangle$, $\langle\cos(2\Phi_2 + 4\Phi_4 - 6\Phi_6)\rangle$, $\langle\cos(2\Phi_2 - 6\Phi_3 + 4\Phi_4)\rangle$, $\langle\cos(-8\Phi_2 + 3\Phi_3 + 5\Phi_5)\rangle$, $\langle\cos(-10\Phi_2 + 4\Phi_4 + 6\Phi_6)\rangle$ and $\langle\cos(-10\Phi_2 + 6\Phi_3 + 4\Phi_4)\rangle$ from top to bottom row. The three set of data points correspond to the three types of correlations in Eq. 24-26.

| Error for Res$\{jn\Psi_n\}$ | | | | | |
|---|---|---|---|---|---|
| n | 2 | 3 | 4 | 5 | 6 |
| Detector A&C | 1.1, 10.0, 13.0% (j=1,4,5) | 6.0, 12.0% (j=1,2) | 6.0% (j=1) | 10.0% (j=1) | 13.0 (j=1) |
| Detector B | 0.7, 5.0, 7.0% (j=1,4,5) | 1.75, 3% (j=1,2) | 1.75% (j=1) | 5.0% (j=1) | 20% (j=1) |

| Error for three-plane correlators: $\langle\cos(\sum\Phi)\rangle$ | | | | | | | | | |
|---|---|---|---|---|---|---|---|---|---|
| $\sum\Phi$ | $2\Phi_2+3\Phi_3-5\Phi_5$ | | | $2\Phi_2+4\Phi_4-6\Phi_6$ | | | $2\Phi_2-6\Phi_3+4\Phi_4$ | | |
| | Type-1 | Type-2 | Type-3 | Type-1 | Type-2 | Type-3 | Type-1 | Type-2 | Type-3 |
| Combined resolution | 11.7% | 10.2% | 7.9% | 20.9% | 20.1% | 20.9% | 13.4% | 7.8% | 12.2% |
| raw distribution ($\times10^{-4}$) | 2-10 | | | | | | | | |
| | $-8\Phi_2+3\Phi_3+5\Phi_5$ | | | $-10\Phi_2+4\Phi_4+6\Phi_6$ | | | $-10\Phi_2+6\Phi_3+4\Phi_4$ | | |
| | Type-1 | Type-2 | Type-3 | Type-1 | Type-2 | Type-3 | Type-1 | Type-2 | Type-3 |
| Combined resolution | 12.7% | 14.3% | 12.7% | 22.1% | 23.9% | 24.6% | 15.1% | 14.6% | 17.8% |
| raw distribution ($\times10^{-4}$) | 2-10 | | | | | | | | |

Table 9: Summary of relative systematic uncertainties for individual Res$\{jn\Psi_n\}$ terms (top part) and the final three-plane correlators (bottom part). Note that the uncertainty of Res$\{jn\Psi_n\}$ are found to be proportional to values of $j$.

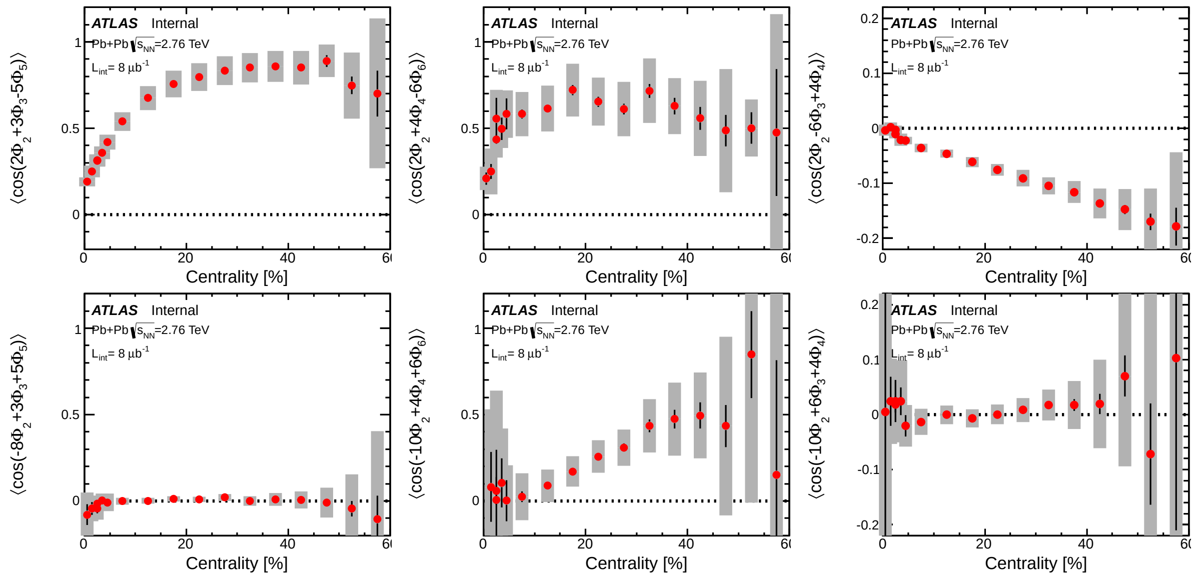


Figure 53: Centrality dependence of the corrected correlation signal for the six types of three-plane correlators.

## 5.2 Cross check with other detectors

Three additional three-plane correlation analysis with different choices of detectors have been carried out. The choice of the detectors are listed in Table 10. The first check also uses only Calorimeters, but have quite different rapidity coverage for the three subevents from the default detector. The second cross-check has very similar $\eta$ coverage of subevents as the first check, except that the subevent A and C are chosen as part of the inner detectors. These two cross-checks have comparable precision as the default measurement, hence can better reveal any potential systematic effects. The third cross-check involves only inner detectors, hence provide very different set of systematics. This cross-check have a 0.5 unit gap between the three subevents, however as we have demonstrated in Section 4.4.1, a gap of $> 0.4$ is more than enough to suppress the influence of autocorrelations on the correlation as well as the resolution determination.

| Combination | A | B | C | |
|---|---|---|---|---|
| 1 | (FCal+EMEC2)$_P$ $\eta \in$(2.7,4.8) | EMBR $\eta \in$(-1.5,1.5) | (FCal+EMEC2)$_N$ $\eta \in$(-4.8,-2.7) | |
| 2 | ID1234$_P$ $\eta \in$(0.5,2.5) | FCal $\lvert\eta\rvert \in$(3.3,4.8) | ID1234$_N$ $\eta \in$(-2.5,-0.5) | |
| 3 | ID34$_P$ $\eta \in$(1.5,2.5) | ID01 $\eta \in$(-1,1) | ID34$_N$ $\eta \in$(-2.5,-1.5) | |
| Default | BR12EC01$_P$ $\eta \in$(0.5,2.7) | FCal $\lvert\eta\rvert \in$(3.3,4.8) | BR12EC01$_N$ $\eta \in$(-2.7,-0.5) | |

Table 10: Detectors that provide cross-checks for the three-plane correlation results.

The entire analysis procedure is repeated for each cross-check (the detailed results of this study for the tracking detectors are included in Appendix II). Figure 54 compares the results from default detector to those obtained from the three cross-checks. Good agreements are seen within their own systematic uncertainties. In particular, good consistency are observed when comparing with the ID results, despite of its bigger fluctuations due to limited $\eta$ range of its subevents. Since the ID is an entirely different detector, this consistency give us confidence that the measured results are robust.

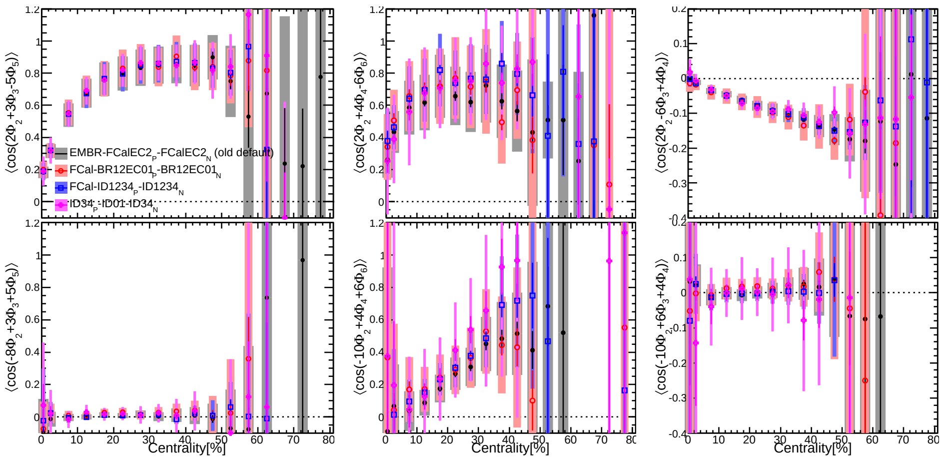


Figure 54: Comparison of the six three-plane correlators between the default detector and cross-check detectors.

# 6 Other systematics

## 6.1 Trigger and event selections

As mentioned in Section 2, the efficiency for selecting the minimum bias Pb-Pb events is 98±2% [14]. The variation of this efficiency leads to a slightly different definition of the centrality class: in the case of 96% (100%) efficiency, the events passing the selection criteria are effectively grouped into 96 (100) percentile bins. The change of the centrality definition mainly leads to a rescaling of the x-axis in Figure 41 and 42 by ±2%. This scaling mostly affects the most peripheral events, but has very little influence in the central events (as the left end of the x-axis is essentially fixed). The changes in centrality range can be approximated as $\delta_x = \pm 0.02 x_i$ for $i^{th}$ data point. The influence for each data point is estimated based on a interpolation procedure between the neighboring bins: $\delta_i = (y_{i+1} - yi) \times \frac{\pm 0.02 x_i}{x_{i+1} - x_i}$. The results of this estimation, in terms of the fractional variation, is shown in Fig. 55 for various two-plane correlators. The estimated changes, when converted into percentage values, are typically less than 1-3% most cases (and centrality dependent); In other case, the changes are slightly bigger, but they are typically associated with the large point-to-point statistical fluctuations and/or because the values themselves are very small.

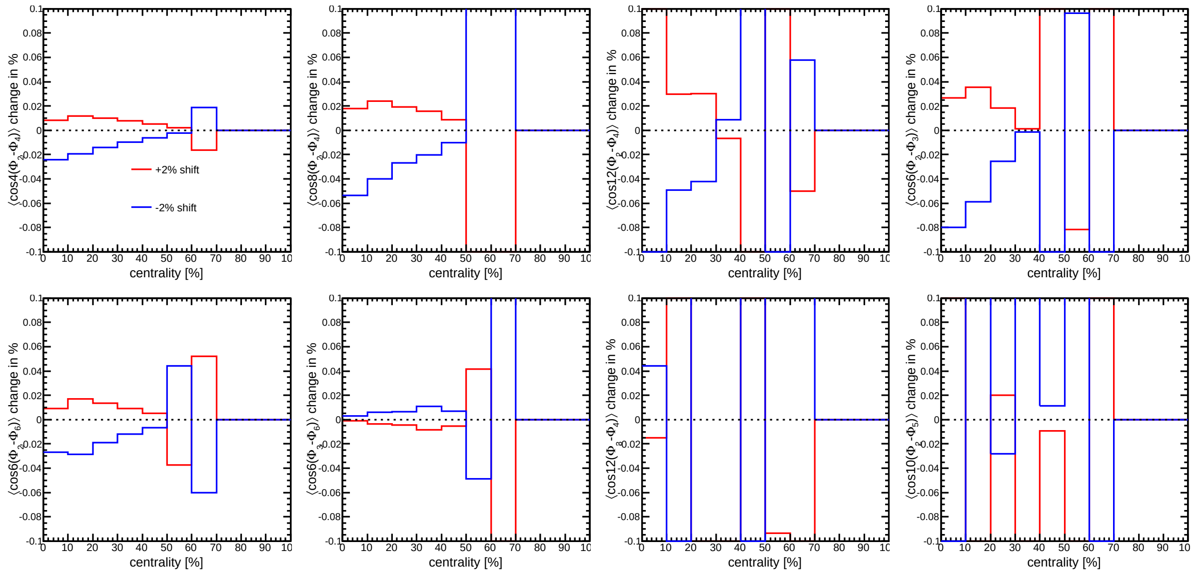


Figure 55: The fractional change in the values of the two-plane correlation signal associated with the uncertainty in trigger and event selections.

The uncertainty associated with centrality definition is repeated for three-plane correlators, and the results are shown in Fig. 56. The relative variation is on the order of 1-4% depending on centrality and the types of correlators.

## 6.2 Run-by-run dependence

The ATLAS detector performance could also vary from run to run. Such variation in principle should largely be smoothed out when we present the results for the full datasets. Nevertheless, it is important to see whether the detector is stable over the time of the whole heavy ion running, and the extent of any change in the correlation signal. To carry out this check, we organize all the runs into 3 different running periods or groups with approximately the same statistics. The run ranges and corresponding luminosity

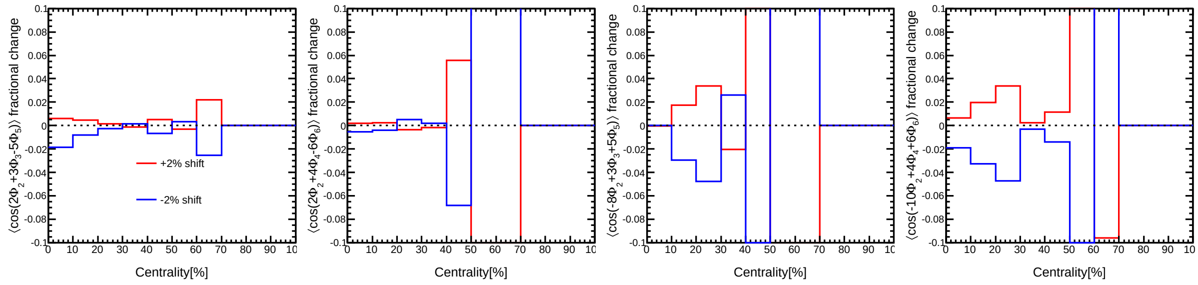


Figure 56: The fractional change in the values of the three-plane correlation signal associated with the uncertainty in trigger and event selections.

are listed in Table 11. The way we used to check the variation is by taking the ratio of the signals obtained in each run group with those for the full statistics.

| Run range | 169045-169627 | 169648-169966 | 170002-170482 |
|---|---|---|---|
| luminosity($\mu b^{-1}$) | 2550.5 | 2398.6 | 2544.0 |

Table 11: The four run groups and corresponding integrated luminosity.

Figure 57-58 shows the variation of the two-plane correlation with various run groups. The check is carried out by taking the ratio of results from each run range to the results from the full statistics. Overall we do not see a clear systematic variation with centrality, although the ratios shows larger spread due to increasing statistical error. The level of centrality dependent deviations beyond statistical fluctuation are conservatively estimated in terms of either percentage (when the signals are large) or as absolute values (when signals are small). They are $<$ 0.5%, 1%, 5%, 0.004, 3%, 3%, 0.02, and 0.02 for the eight cases, respectively.

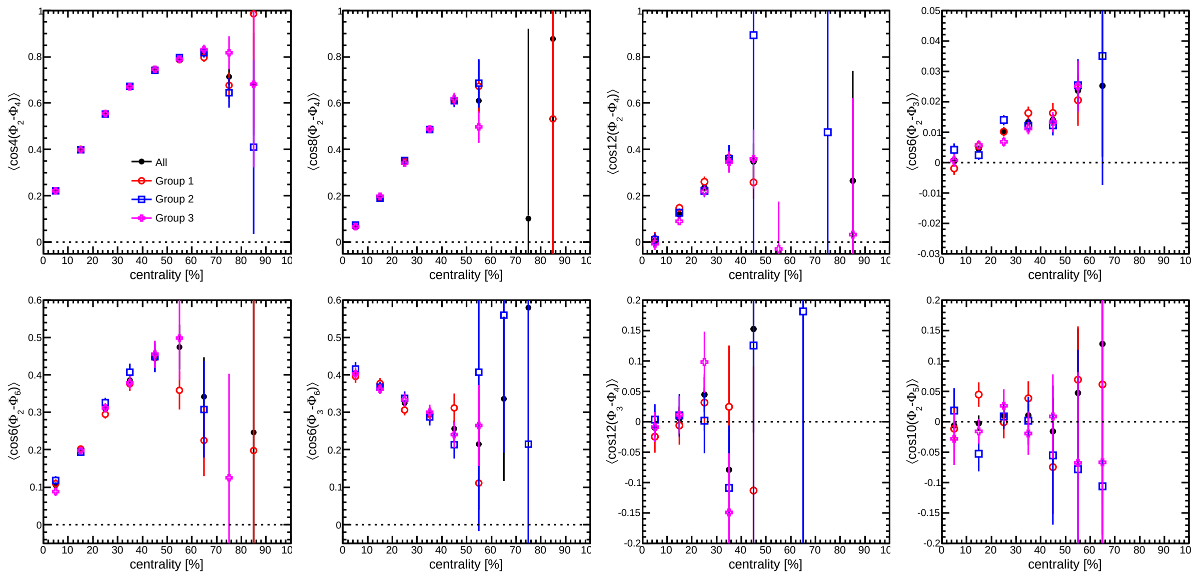


Figure 57: Stability of the results for three running periods for eight cases of $\langle \cos k\,(\Phi_n - \Phi_m)\rangle$. They are compared with the results for the full dataset (black).

Figure 59-60 shows the variation of the three-plane correlation with various run groups. The level of

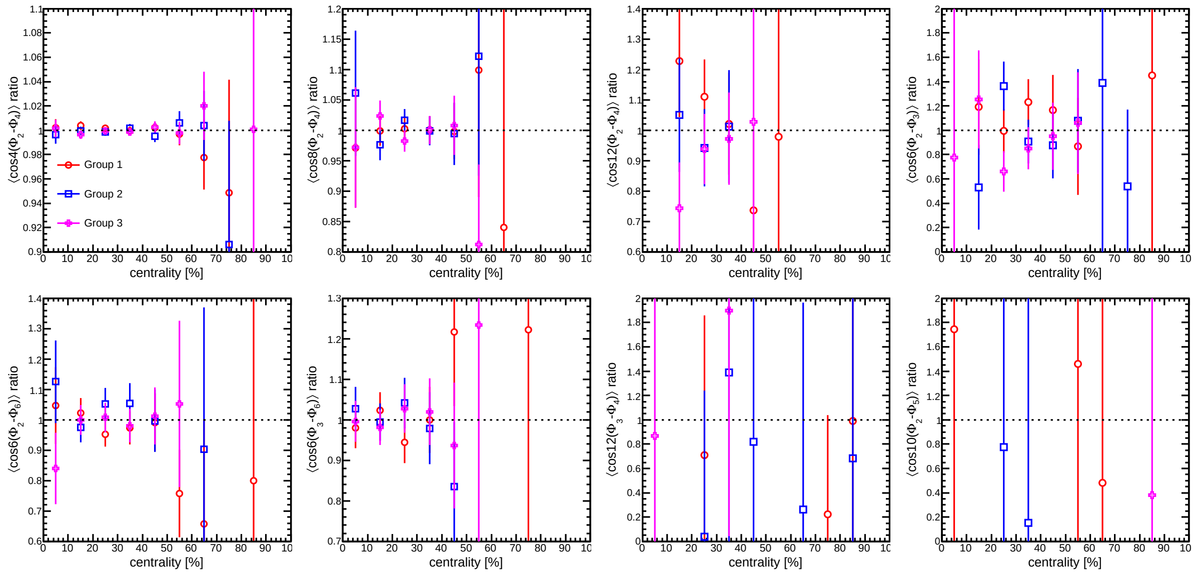


Figure 58: Ratios of results for each of the three running periods to the results for the full dataset for eight cases of $\langle \cos k\,(\Phi_n - \Phi_m)\rangle$.

deviations are estimated to be 1.5%, 5%, 5%, 0.01, 0.07, 0.03 for the four cases (from left to right and top to bottom), respectively.

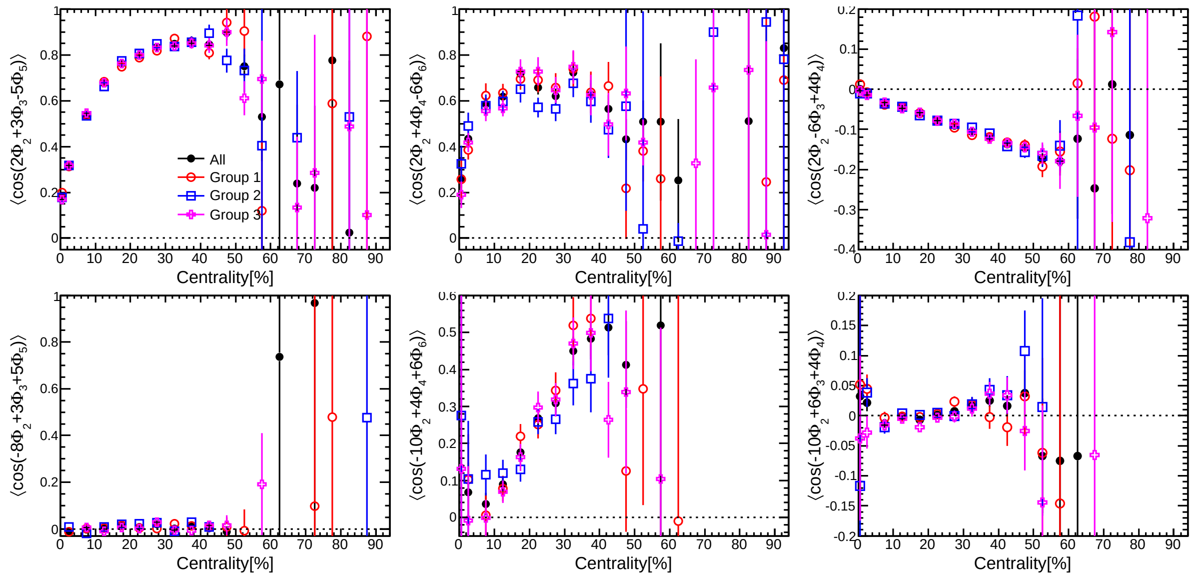


Figure 59: Stability of the results for three running periods for the six types of three-plane correlators. They are compared with the results for the full dataset (black).

The errors from these two sources (Trigger efficiency, Run-by-Run checks) are listed in Tables 12 and 13 for the two and three-plane correlators respectively.

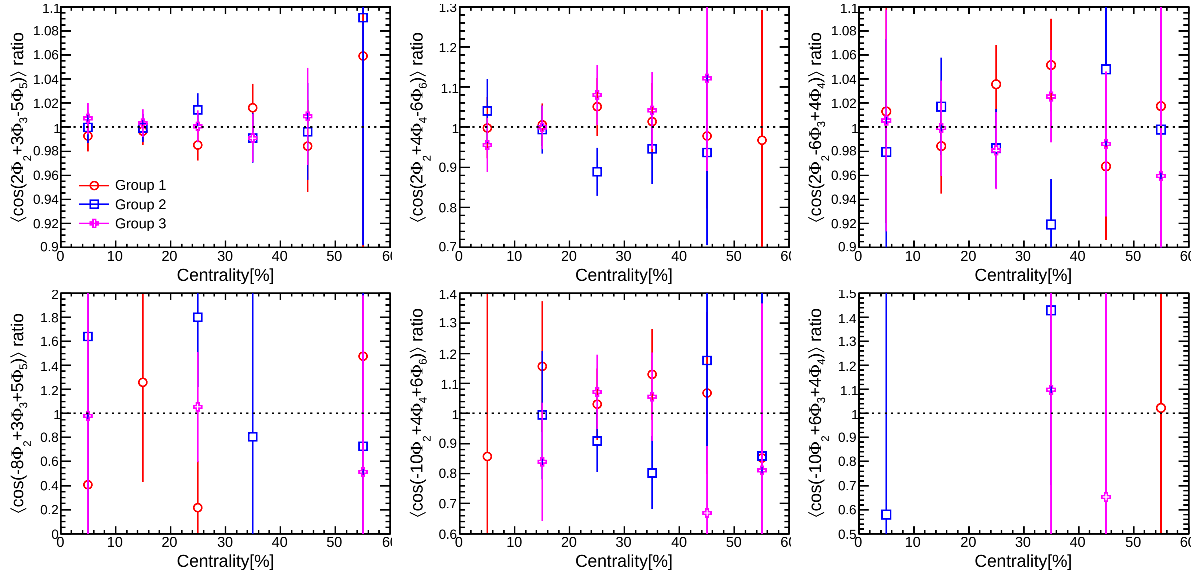


Figure 60: Stability of the results for three running periods for the six types of three-plane correlators. They are compared with the results for the full dataset (black).

| Error for $\langle \cos jk(\Phi_n - \Phi_m)\rangle$ correlators | | | | | | | | |
|---|---|---|---|---|---|---|---|---|
| (j,n,m) | (1,2,4) | (2,2,4) | (3,2,4) | (1,2,3) | (1,2,6) | (1,3,6) | (1,3,4) | (1,2,5) |
| Trigger&event selection | 0.5-2% | 1-4% | 3% | 3% | 1-2% | 0.5-2% | $< 1\%$ | $< 1\%$ |
| Run periods | $< 0.5\%$ | 1% | 5% | 0.004 | 3% | 3% | 0.02 | 0.02 |

Table 12: Summary of systematic uncertainties for various two-plane correlators from Trigger efficiency and run by run dependence. Note the uncertainties are given either as percentage or absolute.

| Error for various three-plane correlators $\langle \cos(\sum \Phi)\rangle$ | | | |
|---|---|---|---|
| $\sum \Phi$ | $2\Phi_2 + 3\Phi_3 - 5\Phi_5$ | $2\Phi_2 + 4\Phi_4 - 6\Phi_6$ | $2\Phi_2 - 6\Phi_3 + 4\Phi_4$ |
| Trigger&event sel. | 1-2% | 1% | 3-4% |
| Run periods | 1.5% | 5% | 5% |
| $\sum \Phi$ | $-8\Phi_2 + 3\Phi_3 + 5\Phi_5$ | $-10\Phi_2 + 4\Phi_4 + 6\Phi_6$ | $-10\Phi_2 + 6\Phi_3 + 4\Phi_4$ |
| Trigger&event sel. | 1-3% | 1-3% | 1-3% |
| Run periods | 0.01 | 0.07 | 0.03 |

Table 13: Summary of systematic uncertainties for various three-plane correlators from Trigger efficiency and run by run dependence. Note the uncertainties are given either as percentage or absolute

# 7 Summary of results

Table 6 and 9 summarize various sources of systematic uncertainties for event-plane correlations. Additional uncertainties from Trigger efficiency and run by run checks are given in Tables 12 and 13. The uncertainties of the final results are calculated as the quadrature sum of all these sources. They are shown as shaded bands in the results plots Fig. 61-64. Our final results are presented as a function of number of participating nucleons $N_{\mathrm{part}}$ calculated from the Glauber model that has been adapted to ATLAS as documented in Ref. [14]. They are also used in previous ATLAS publications [24, 25]. This way of presenting the centrality dependence of the measurement is quite standard in the heavy ion community. We refer to Ref. [14] for details of the setup of the Glauber model, and here we simply summarize the relationship between the average $N_{\mathrm{part}}$ and centrality percentile from Ref. [14] in Table 14.

TLhe centrality dependence of various two- and three-plane correlations can be compared with the predictions from the Glauber model given in Fig. 6. We want to emphasize that these predictions represents the correlations between the major axes of the planes in configuration space, and they do not have any final state effects from hydrodynamic evolution. Nevertheless, the features for several correlators are similar. In particular, the large signal in mid-central collisions predicted for "2-4", "2-6", "3-6", "2-3-5" and "2-4-6" are observed. We see very weak correlations for "2-3", "3-4" and "2-5" similar to the model. Further work is needed to establish a complete theoretical understanding of the correlations presented here, which may lead to new insights on the nature of the fluctuation of the created matter at the initial state as well as the subsequent hydrodynamic evolution. In the future, one should explore other two- and three-plane or even four-plane correlators that are not covered in this study.

Finally, Figure 65 compares our results with the ALICE measurement for $\langle\cos 6(\Phi_2 - \Phi_3)\rangle$ [11, 12]. It is important to point out that the ALICE result was obtained using a different method. However the general agreement is very good.

| | | | | | |
|---|---|---|---|---|---|
| Centrality | 0-1% | 1-2% | 2-3% | 3-4% | 4-5% |
| $\langle N_{\mathrm{part}}\rangle$ | 400.6 ± 1.3 | 392.6 ± 1.8 | 383.2 ± 2.1 | 372.6 ± 2.3 | 361.8 ± 2.5 |
| Centrality | 0-5% | 5-10% | 10-15% | 15-20% | |
| $\langle N_{\mathrm{part}}\rangle$ | 382.2 ± 2.0 | 330.3 ± 3.0 | 281.9 ± 3.5 | 239.5 ± 3.8 | |
| Centrality | 20-25% | 25-30% | 30-35% | 35-40% | 40-45% |
| $\langle N_{\mathrm{part}}\rangle$ | 202.6 ± 3.9 | 170.2 ± 4.0 | 141.7 ± 3.9 | 116.8 ± 3.8 | 95.0 ± 3.7 |
| Centrality | 45-50% | 50-55% | 55-60% | 60-65% | 65-70% |
| $\langle N_{\mathrm{part}}\rangle$ | 76.1 ± 3.5 | 59.9 ± 3.3 | 46.1 ± 3.0 | 34.7 ± 2.7 | 25.4 ± 2.3 |
| Centrality | 0-10% | 10-20% | 20-30% | 30-40% | 40-50% |
| $\langle N_{\mathrm{part}}\rangle$ | 356.2 ± 2.5 | 265.7 ± 3.7 | 186.4 ± 4.0 | 129.2 ± 3.9 | 85.5 ± 3.6 |
| Centrality | 50-60% | 60-70% | | | |
| $\langle N_{\mathrm{part}}\rangle$ | 53.0 ± 3.2 | 30.5 ± 2.5 | | | |

Table 14: Relationship between the centrality percentile and the $N_{\mathrm{part}}$ estimated from a Glauber model.

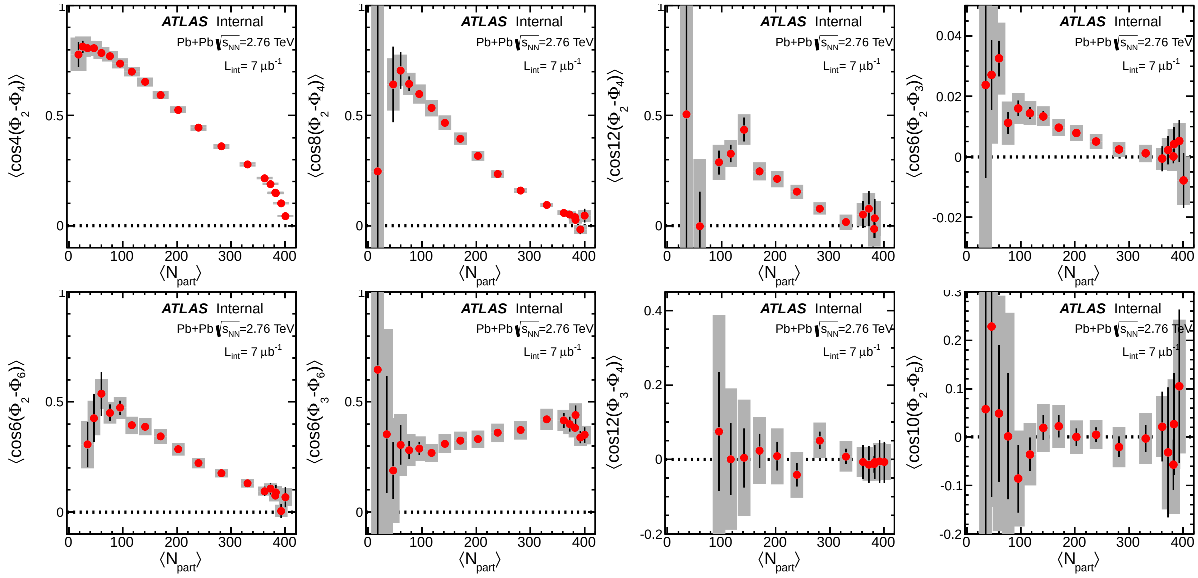


Figure 61: The centrality dependence of two-plane correlators in 5% bins. with 1% bins for 0-5%.

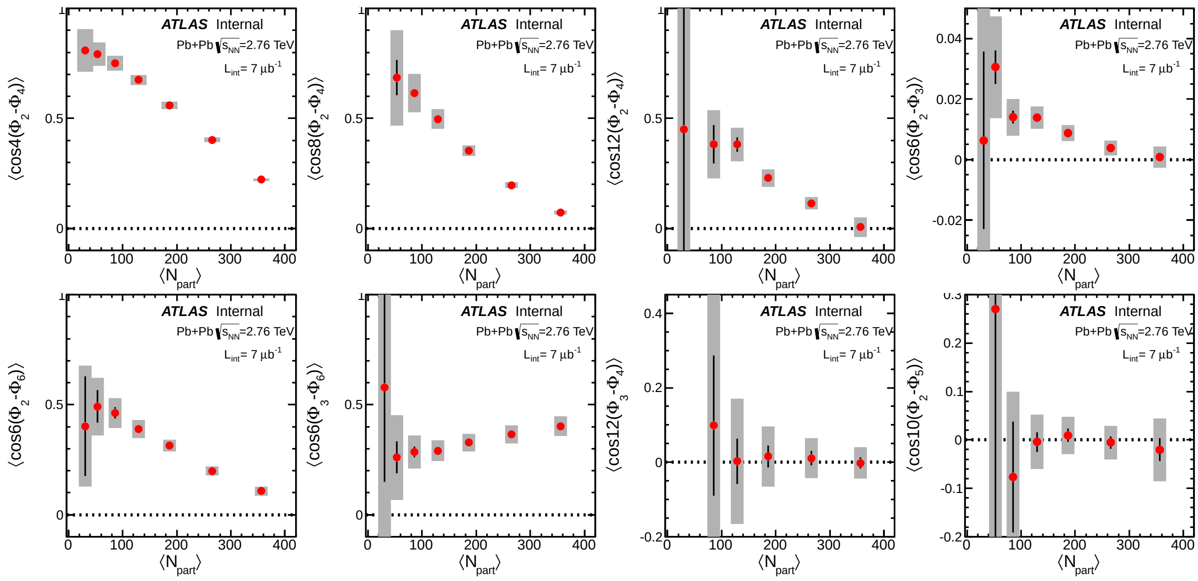


Figure 62: The centrality dependence of two-plane correlators in 10% bins.

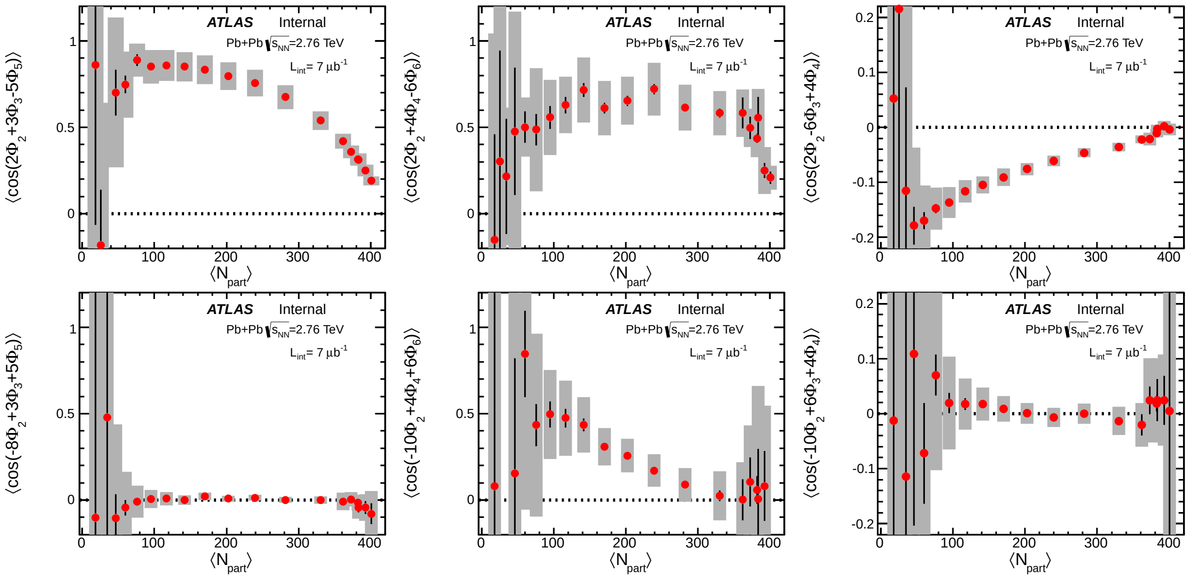


Figure 63: The centrality dependence of three-plane correlators in 5% bins, with 1% bins for 0-5%.

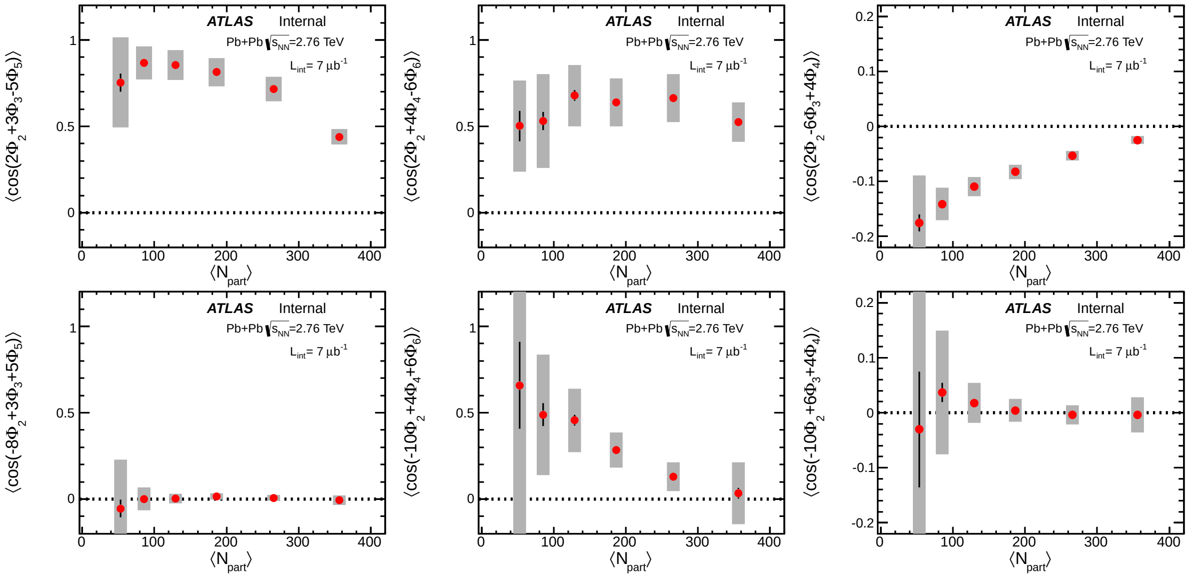


Figure 64: The centrality dependence of three-plane correlators in 10% bins.

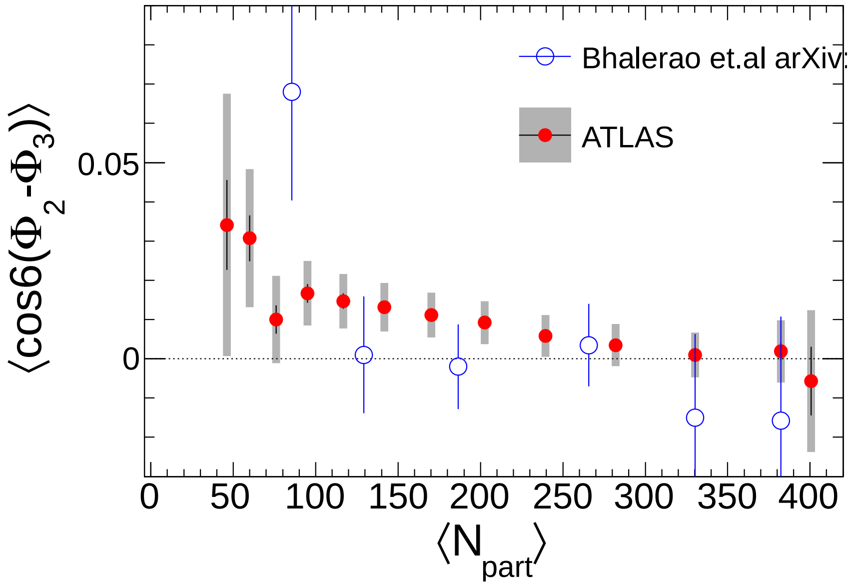


Figure 65: Comparison with ALICE result for $\langle \cos 6(\Phi_2 - \Phi_3) \rangle$.

# 8 Weighted correlations

After the EP-Correlations results in the previous sectionswere presented at HardProbes2012 Conference, there was considerable feed back from the theory community. In general one consideration that they had was that the EP method assumes that the EP resolution ($\mathrm{Res}\{\mathrm{k}\Psi_\mathrm{n}\}$) is identical for all events in the same centrality class. However in reality the resolution depends on the $v_n$ signal: Events with larger $n^{\mathrm{th}}$ order flow have better resolution of the $n^{\mathrm{th}}$ order harmonic plane. This coupled with the fact that there are large event-by-event (EbyE) fluctuations in the $v_n$ themselves as outlined in a recent ATLAS publication [26], implies that all events a centrality class do not have the same EP resolution. Thus the procedure of applying the same "resolution correction" factor to all events, does not properly correct for the resolution.

As a reminder, the formula for measuring the correlations in the previous sections is given by:

$$\langle\cos(nc_n\Phi_n + lc_l\Phi_l + ...mc_m\Phi_m\rangle = \frac{\langle\cos(nc_n\Psi_n + lc_l\Psi_l + ...mc_m\Psi_m\rangle}{\mathrm{Res}\{nc_n\Psi_n\}\mathrm{Res}\{lc_l\Psi_l\}...\mathrm{Res}\{mc_m\Psi_m\}} \tag{40}$$

Where the $\Phi's$ refer to the true event-planes and the $\Psi's$ refer to the measured event-planes. The numerator is the measured raw correlation. And the denominator is the combined resolution for the correlator, which is simply the product of the individual single-plane resolutions. The resolution is typically measured by the two sub-event method by correlating symmetric detectors at the positive (P) and negative (N) $\eta$ sides as:

$$\mathrm{Res}\{\mathrm{k}\Psi_\mathrm{n}^{\mathrm{P/N}}\} = \sqrt{\langle\cos(k\Psi_n^P - \Psi_n^N)\rangle} \tag{41}$$

It was pointed out in [27, 28] that a modification of the above equation can remove all the effects that are introduced by the $v_n$ fluctuations, their proposal for the observable for measuring the EP correlations is to measure the following quantity:

$$\frac{\langle q_n^{c_n} q_l^{c_l} ... q_m^{c_m} \cos(nc_n\Phi_n + lc_l\Phi_l + ...mc_m\Phi_m\rangle}{\sqrt{\langle q_n^{2c_n}\rangle}\sqrt{\langle q_l^{2c_l}\rangle}...\sqrt{\langle q_m^{2c_m}\rangle}} \tag{42}$$

Where $q_n = Q_n/Q_0$ and $Q_n$ are the $n^{\mathrm{th}}$ order flow vectors. In terms of observed quantities ($q_n^{obs}$ and $\Psi_n$) the above correlator is given by:

$$\frac{\langle(q_n^{obs})^{c_n}(q_l^{obs})^{c_l}...(q_m^{obs})^{c_m}\cos(nc_n\Psi_n + lc_l\Psi_l + ...mc_m\Psi_m\rangle}{\sqrt{\langle(q_n^{obs,P}q_n^{obs,N})^{c_n}\cos(c_n(\Psi_n^P - \Psi_n^N))\rangle}\sqrt{\langle(q_l^{obs,P}q_l^{obs,N})^{c_l}\cos(c_l(\Psi_n^P - \Psi_n^N))\rangle}...\sqrt{\langle(q_m^{obs,P}q_m^{obs,N})^{c_m}\cos(c_m(\Psi_n^P - \Psi_n^N))\rangle}} \tag{43}$$

where the claim made in [27, 28] is that the above measured correlator (Eq. 43) is unambiguously equivalent to the true correlator (Eq.42) , unlike in Eq.40, where the LHS and RHS were equivalent only in the case of small $v_n$ fluctuations.

It is quite straightforward to extend the EP analysis to this "weighted" correlation case. The raw correlators as well as the resolutions are simply weighted by the appropriate $q_n^{obs}$ as:

$$Raw\ signal = \langle(q_n^{obs})^{c_n}(q_l^{obs})^{c_l}...(q_m^{obs})^{c_m}\cos(nc_n\Psi_n + lc_l\Psi_l + ...mc_m\Psi_m\rangle \tag{44}$$

and

$$\begin{aligned} Resolution \quad = \quad & \sqrt{\langle(q_n^{obs,P}q_n^{obs,N})^{c_n}\cos(c_n(\Psi_n^P - \Psi_n^N))\rangle}\sqrt{\langle(q_l^{obs,P}q_l^{obs,N})^{c_l}\cos(c_l(\Psi_n^P - \Psi_n^N))\rangle} \\ & ...\sqrt{\langle(q_m^{obs,P}q_m^{obs,N})^{c_m}\cos(c_m(\Psi_n^P - \Psi_n^N))\rangle} \end{aligned} \tag{45}$$

The remaining analysis steps as well as cross-checks remain identical to the unweighted case.

# 9 Two-Plane Correlations Weighted

The analysis for the two-plane correlations case is done only for the Default detector ECalFCal (Detector 16 in Table 4) which consists of calorimeter towers spanning $\eta \in (0.5, 4.8)$. The correlations are cross-checked are done with measurements using the tracking detectors.

## 9.1 Raw Correlations

As was done with the unweighted correlation analysis, the raw correlations are obtained by an event mixing procedure. This is best explained by taking as an example the $4(\Psi_2 - \Psi_4)$ correlator. First a foreground distribution of the form $4(\Psi_2 - \Psi_4)$ is made by correlating event-planes $\Psi_2$ and $\Psi_4$ measured in the same event. However, instead of each event having a weight of 1.0 as was in the unweighted case, in this weighted distribution, the contribution for each event is weighted by the factor $(q_2^{obs})^2 q_4^{obs}$ in the event. Similarly a mixed event background is made by correlating the $\Psi_2$ and $\Psi_4$ from individual events of the form : $4(\Psi_2^{evten1} - \Psi_4^{event2})$ with the weight for each entry as $(q_2^{obs,event1})^2 q_4^{obs,event2}$. Finally the correlation is obtained by dividing the foreground distribution by the mixed event distribution.

Some such foreground, background and correlation distributions are shown in Figs. 66-71 (Similar plots for the unweighted cases were shown in Figs. 10-15). Note that separate distributions are made for each of the $j4(\Psi_2 - \Psi_4)$ distributions (for $j$=1,2,3) as the weighting factors are different for the three correlators. For $j$=1 the weight is $(q_2^{obs})^2 q_4^{obs}$ while for $j$=2 and 3 the weights are $(q_2^{obs})^4 (q_4^{obs})^2$ and $(q_2^{obs})^6 (q_4^{obs})^3$ respectively. So unlike the unweighted case where the $4(\Psi_2 - \Psi_4)$ distribution contained the full information of the $8(\Psi_2 - \Psi_4)$ and $12(\Psi_2 - \Psi_4)$ distributions (via a simple rescaling of the x-axis followed by a refolding into $(-\pi, \pi)$), in the weighted case they have to be evaluated separately. The $y$-axis in these figures is rescaled to have a mean value of 1.0. for the foreground, background and correlation so that they can be easily compared to the Unweighted case (Figs. 10-15). However while calculating the $\langle \cos jk(\Psi_n - \Psi_m) \rangle$ the overall scaling is kept.

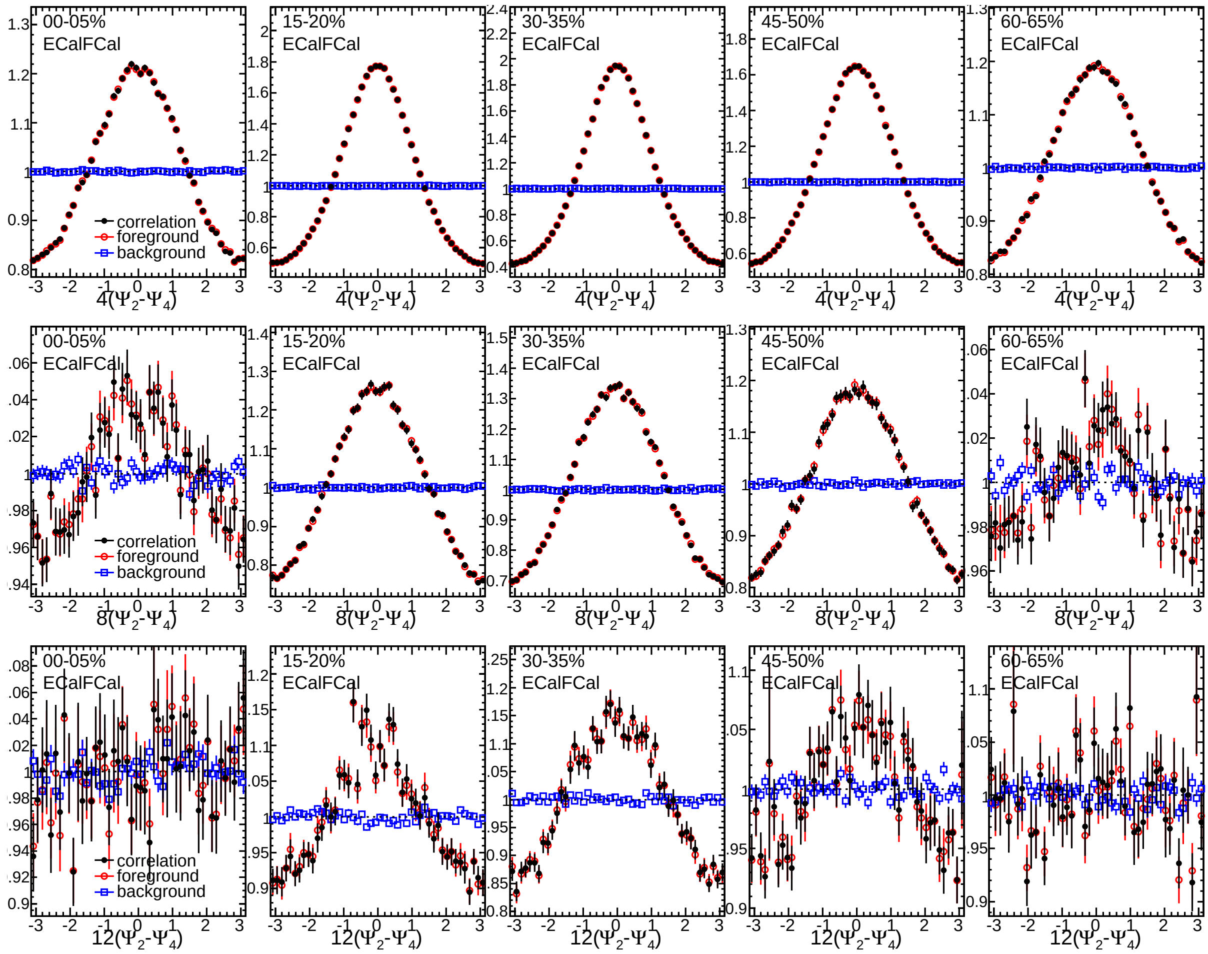


Figure 66: The distributions for the two plane angle differences $j4(\Psi_2 - \Psi_4)$ for several centrality intervals.

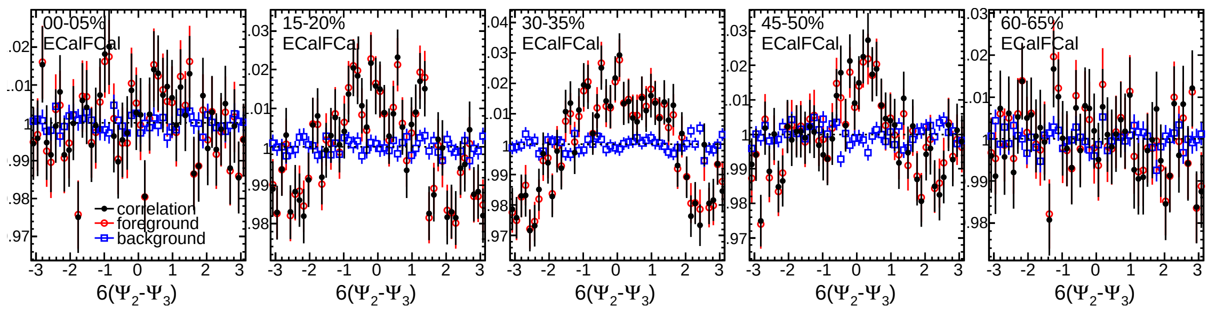


Figure 67: The distributions for the two plane angle differences $6(\Psi_2 - \Psi_3)$ for several centrality intervals.

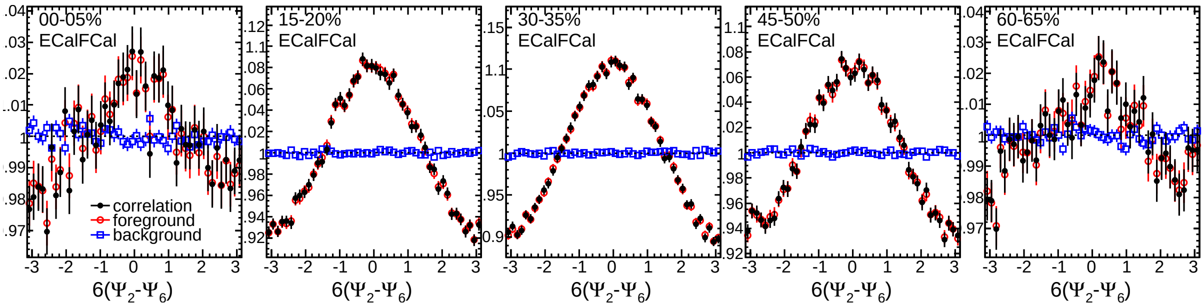


Figure 68: The distributions for the two plane angle differences $6(\Psi_2 - \Psi_6)$ for several centrality intervals.

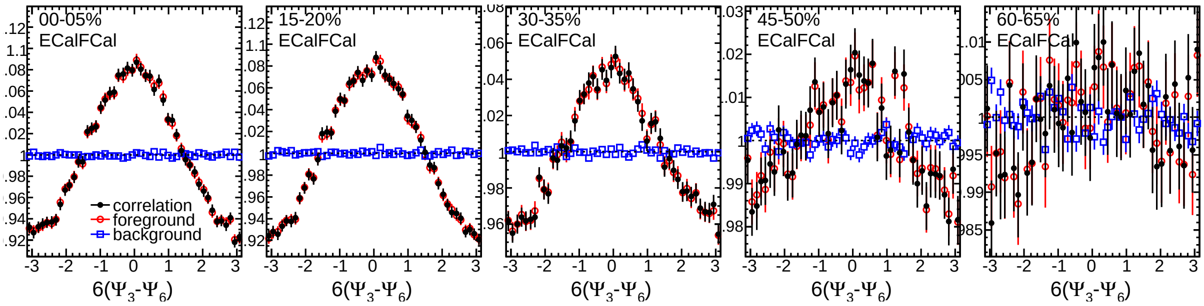


Figure 69: The distributions for the two plane angle differences $6(\Psi_3 - \Psi_6)$ for several centrality intervals.

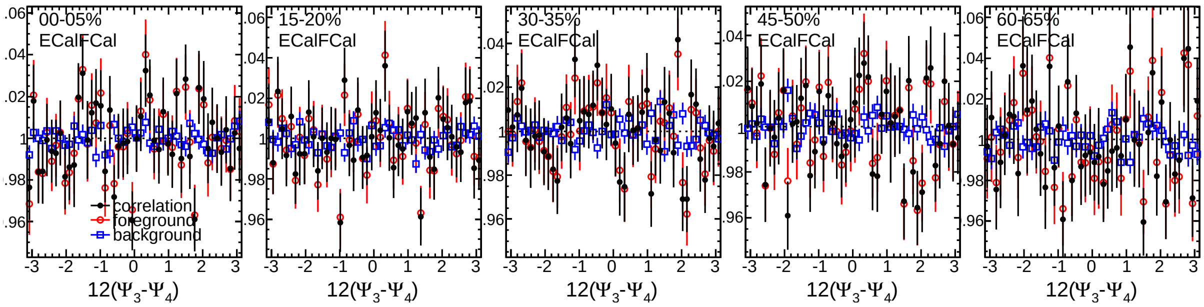


Figure 70: The distributions for the two plane angle differences $12(\Psi_3 - \Psi_5)$ for several centrality intervals.

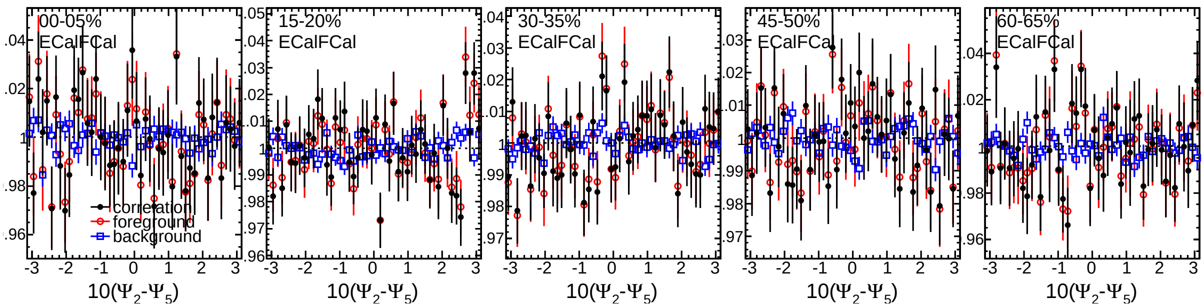


Figure 71: The distributions for the two plane angle differences $10(\Psi_2 - \Psi_5)$ for several centrality intervals.

Fig. 72 shows the centrality dependence of the raw correlations $\langle\cos jk(\Psi_n - \Psi_m)\rangle$ for the weighted case. Also shown are the $\langle\sin\rangle$ terms in the correlation as well as the $\langle\cos\rangle$ and $\langle\sin\rangle$ terms for the mixed background which are used to estimate the systematic uncertainties. In these plots, the first 5 points are 1% centrality bins (from 0-5% centrality) and the next points are 5% bins (from 5-70% centrality), the last bin which spans the range 75-80% is actually the (0-5)% centrality bin. In the final results when the 1% bins have large fluctuations, they are replaced by the combined (0-5)% bin.

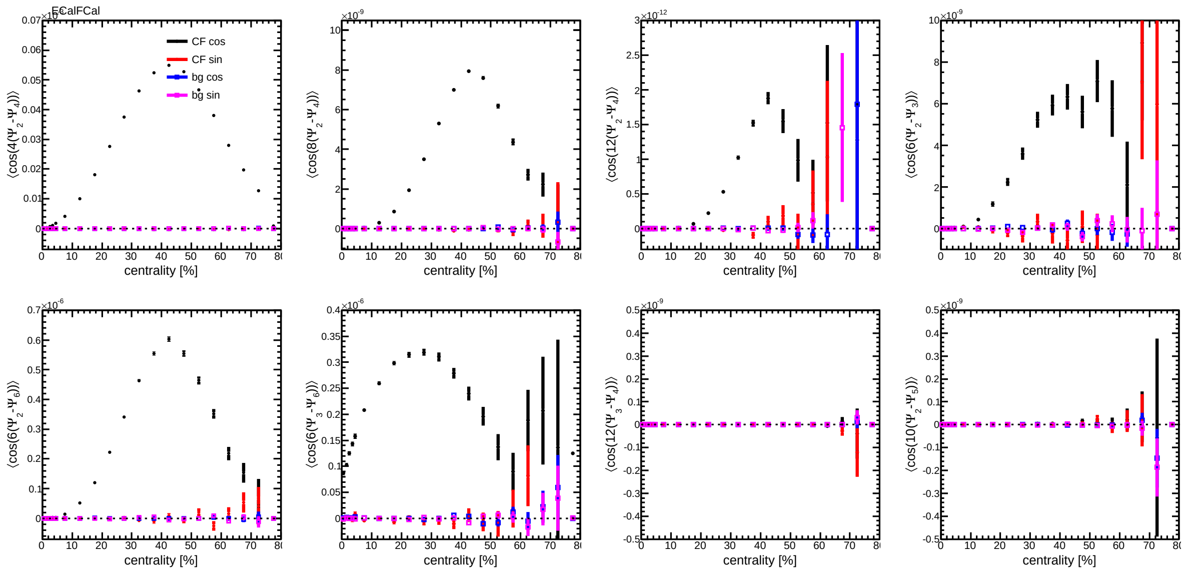


Figure 72: The weighted $\langle\cos jk(\Psi_n - \Psi_m)\rangle$ obtained from the correlations (Figs. 66-71) as a function of centrality. Also shown are the $\langle\sin\rangle$ terms in the correlation as well as the $\langle\cos\rangle$ and $\langle\sin\rangle$ terms for the mixed background which are used to estimate the systematic uncertainties. The first 5 points are 1% centrality bins (from 0-5% centrality) and the next points are 5% bins (from 5-70% centrality), the last bin which spans the range 75-80% is actually the (0-5)% centrality bin.

## 9.2 Resolution

## 9.3 Single-plane resolutions

For the resolution also an identical procedure is followed as with the unweighted analysis. From Eq.43 it can be seen that the denominator (i.e.) the resolution is a product of several single-plane resolutions. In the unweighted case the single-plane resolutions were of the form $\sqrt{\langle\cos kn(\Psi_n^P - \Psi_n^N)\rangle}$ while in the weighted case the resolutions are $\sqrt{\langle (q_n^{obs,P} q_n^{obs,N})^k \cos kn(\Psi_n^P - \Psi_n^N)\rangle}$. The single-plane resolutions are calculated by making distributions of $kn(\Psi_n^P - \Psi_n^N)$ weighted by $(q_n^{obs,P} q_n^{obs,N})^k$ with $\Psi_n^P$ and $\Psi_n^N$ measured in the same event. A mixed -event distribution of $kn(\Psi_n^{P,event1} - \Psi_n^{N,event2})$ is made using $\Psi_n^P$ and $\Psi_n^N$ measured in different events weighted by $(q_n^{obs,P,event1} q_n^{obs,N,event2})^k$. And finally the correlation of the two sub-events is obtained by dividing the foreground distribution by the mixed event distribution. Examples of such distributions are shown in Figs. 73-77. The $y$-axis in these figures is rescaled to have a mean value of 1.0. for the foreground, background and correlation so that they can be casually compared to the Unweighted case (Fig. 20). However while calculating the $\langle\cos kn(\Psi_n^P - \Psi_m^N)\rangle$ the overall scaling is kept. The resolutions are obtained by calculating the $\sqrt{\langle\cos kn(\Psi_n^P - \Psi_n^N)\rangle}$ from these correlation distributions.

Again, it is worth explicitly pointing out that in the unweighted case all the $\sqrt{\langle\cos kn(\Psi_n^P - \Psi_n^N)\rangle}$ (for different $k$) could be obtained from the $n(\Psi_n^P - \Psi_n^N)$ distributions. While for the weighted case a separate

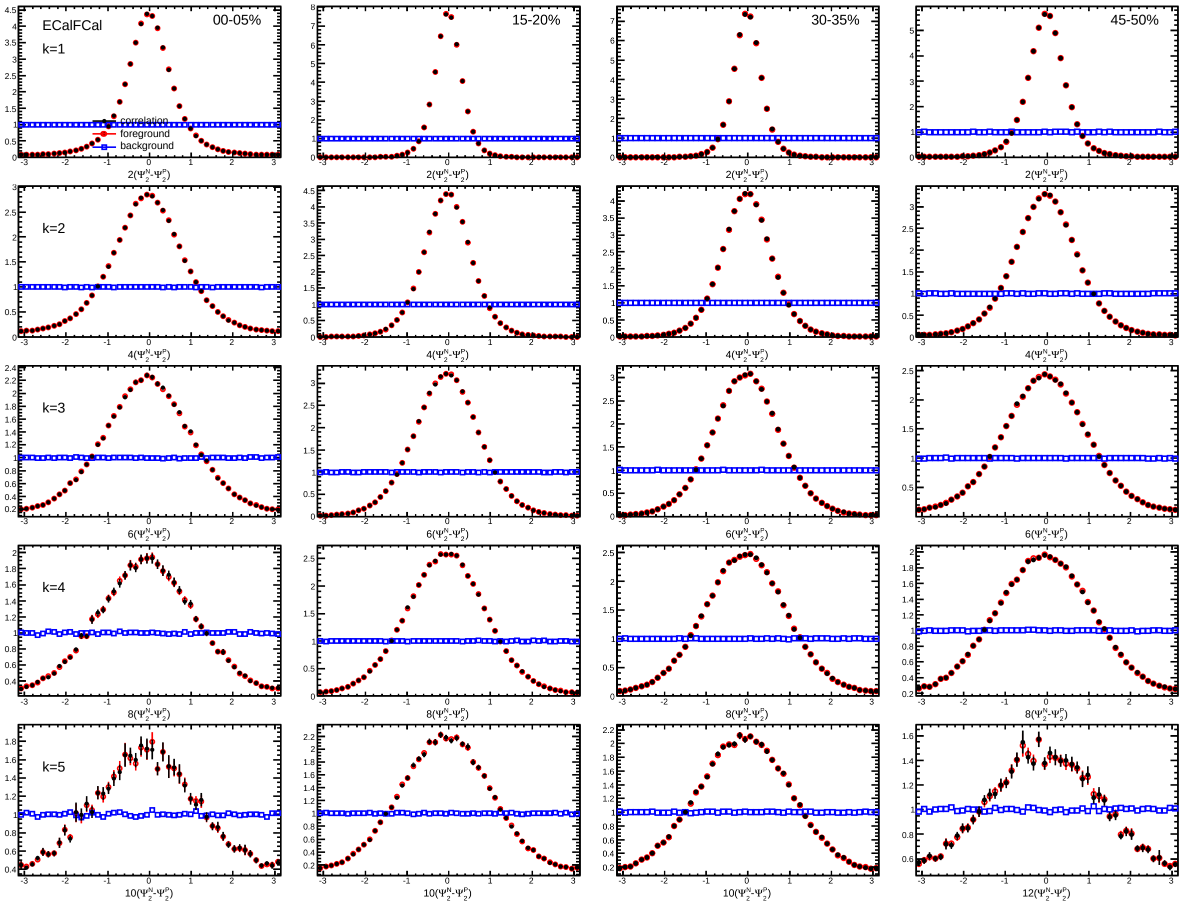


Figure 73: The distributions for the two plane angle differences $2k(\Psi_2^P - \Psi_2^N)$ for different centrality classes (left-right) and different k (top-bottom). Only those values of $k$ that are used in the analysis are shown.

distribution needs to be make for each of the different $k$ values, as the weighting factor is different for them.

## 9.4 Systematic Errors for resolution

The systematic errors for the resolution are obtained by the following two sources:

1. Calculating the $\langle \sin jn(\Psi_n^P - \Psi_n^N)) \rangle$ terms in the correlations in between the two sub-events. This is used as an estimate of the systematic error on the $\langle \cos jn(\Psi_n^P - \Psi_n^N) \rangle$ term as:

$$\frac{\Delta\langle\cos\rangle}{\langle\cos\rangle} = \frac{\sqrt{\langle\cos\rangle^2 + \langle\sin\rangle^2} - \langle\cos\rangle}{\langle\cos\rangle} \approx \frac{1}{2}\frac{\langle\sin\rangle^2}{\langle\cos\rangle^2} \tag{46}$$

   This error is then propagated to the error of the resolution (which is obtained as $\sqrt{\langle\cos\rangle}$). This is identical to waht was done for the "Unweighted" correlations.

2. Several three-subevent (3SE) cross-checks are done to independently determine the single-plane resolutions. The deviation from the default resolutions are considered as systematic errors on the single-plane resolutions and are propagated into the combined resolution (which is the product of

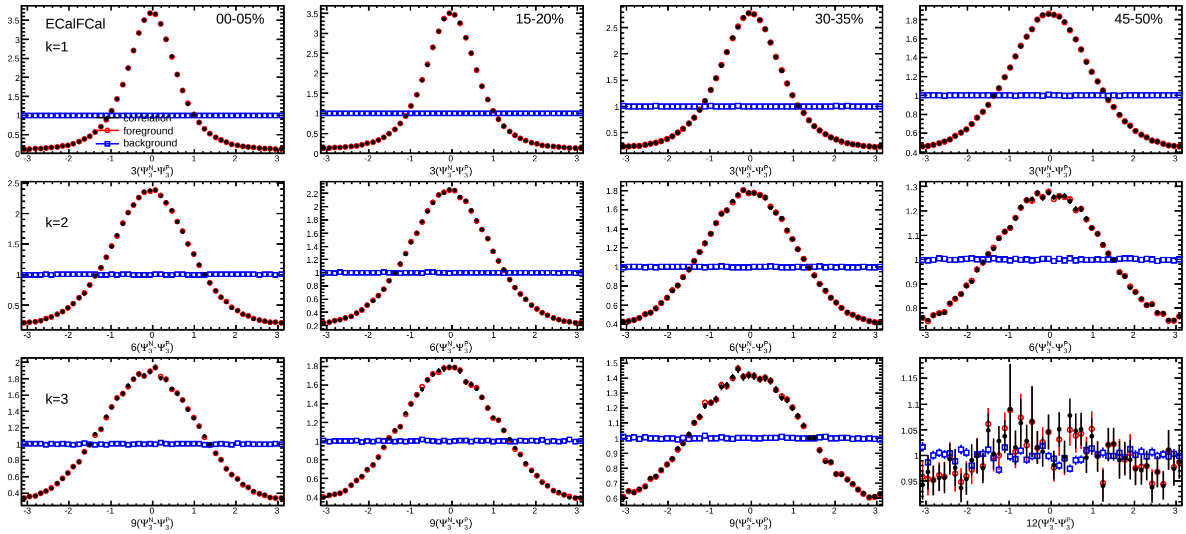


Figure 74: The distributions for the two plane angle differences $3k(\Psi_3^P - \Psi_3^N)$ for different centrality classes (left-right) and different k (top-bottom). Only those values of $k$ that are used in the analysis are shown.

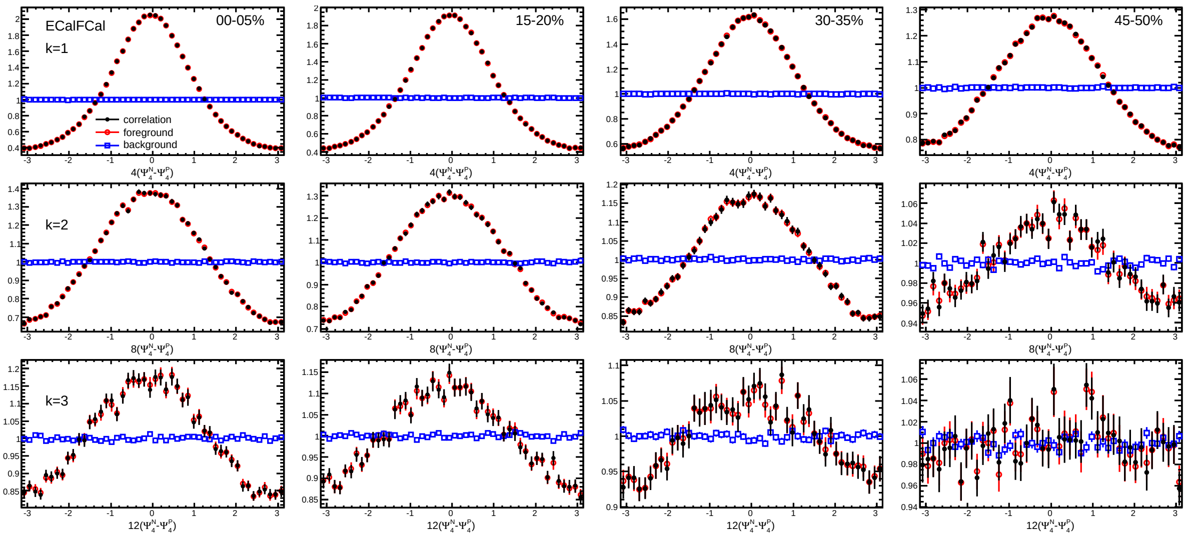


Figure 75: The distributions for the two plane angle differences $4k(\Psi_4^P - \Psi_4^N)$ for different centrality classes (left-right) and different k (top-bottom). Only those values of $k$ that are used in the analysis are shown.

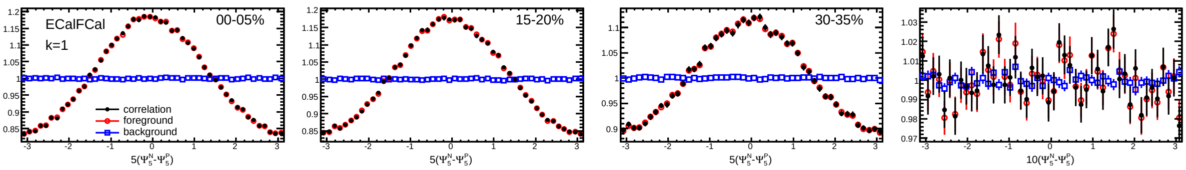


Figure 76: The distributions for the two plane angle differences $5k(\Psi_5^P - \Psi_5^N)$ for different centrality classes (left-right) and different k (top-bottom). Only those values of $k$ that are used in the analysis are shown.

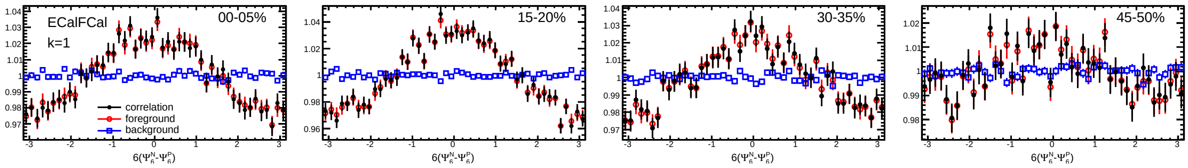


Figure 77: The distributions for the two plane angle differences $6k(\Psi_6^P - \Psi_6^N)$ for different centrality classes (left-right) and different k (top-bottom). Only those values of $k$ that are used in the analysis are shown.

the individual single-plane resolutions). The choice of reference detectors for the 3SE checks is identical to the unweighted case.

### 9.4.1 Sine terms in two-subevent resolution

Figure 78 shows the ratio of the $\langle \sin jn(\Psi_n^P - \Psi_n^N)) \rangle$ to the $\langle \cos jn(\Psi_n^P - \Psi_n^N) \rangle$ terms for the ECalFCal. Only those values of $j$ that are used in the analysis are shown. It is seen that the weighted and unweighted resolutions have identical nearly identical ratios for this terms wherever statistics allow. This is especially clear in the $\langle \sin j2(\Psi_2^P - \Psi_2^N)) \rangle$ case (first plot). Thus this error is completely correlated between the weighted and unweighted cases. The fine-dashed (long-dashed) lines show the mean value of the ratio for the Weighted (Unweighted) case in the (0-50)% centrality interval. The means are calculated by statistical weighting (i.e. the points are weighted by $1/(stat\ err)^2$ while calculating the mean). These mean deviations are quoted as the value of the $\langle \sin \rangle / \langle \cos \rangle$ over the whole centrality range.

It is also worth pointing out that as per Eq.46, these errors becomes much smaller when propagated into the error of the $\langle \cos \rangle$ term. For example a 20% value of the $\langle \sin \rangle$ term relative to the $\langle \cos \rangle$ term translates to :

$$\langle \sin \rangle / \langle \cos \rangle = 0.2 \tag{47}$$

$$\Longrightarrow \frac{\Delta \langle \cos \rangle}{\langle \cos \rangle} = \frac{1}{2} 0.2^2 = 0.02 \tag{48}$$

only a 2% relative error on the $\langle \cos \rangle$ term.

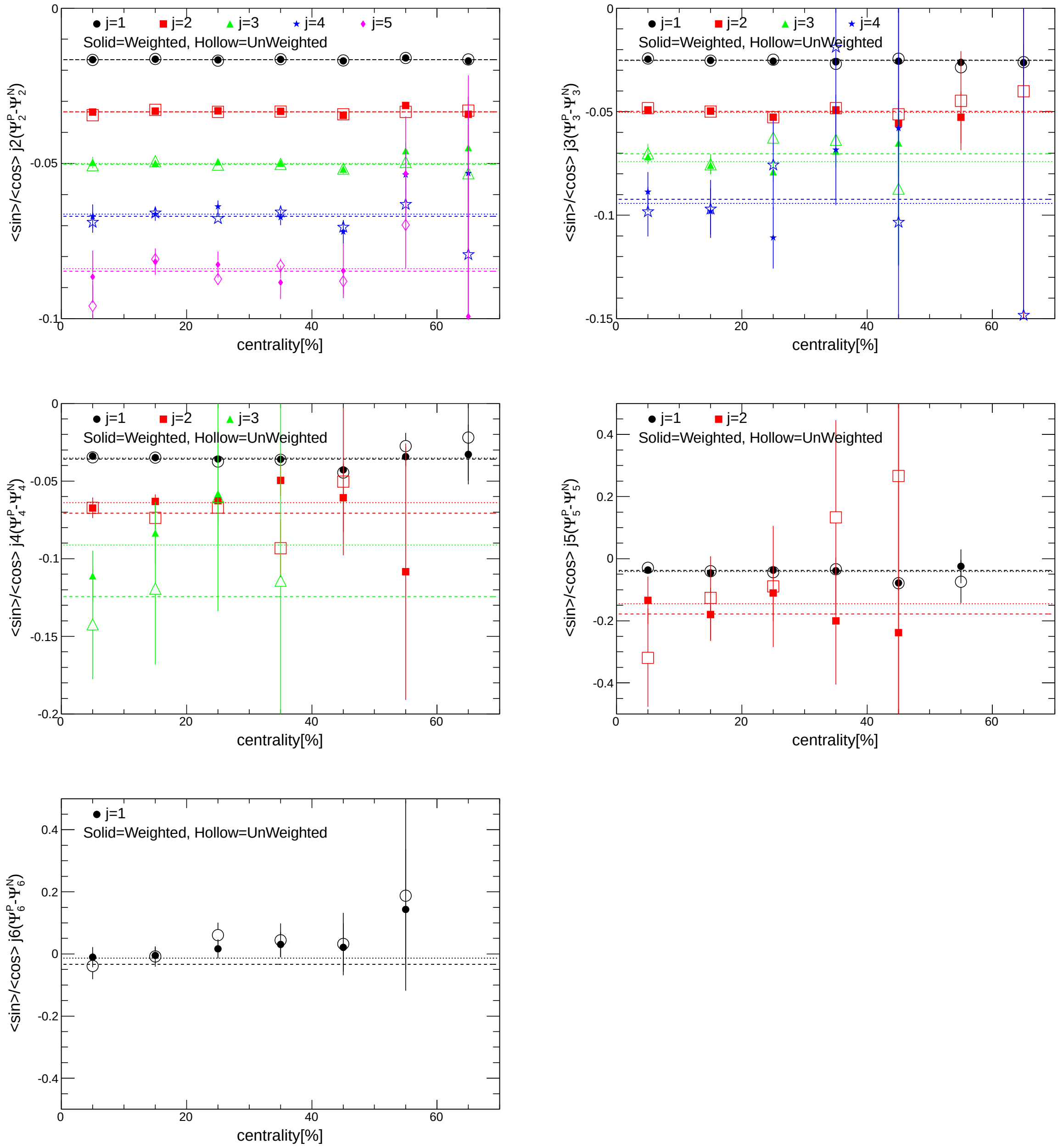


Figure 78: The $\langle\sin\rangle$ terms obtained in the two-subevent angle differences $jn(\Psi^P_n - \Psi^N_n)$ relative to the $\langle\cos\rangle$ terms, as a function of centrality for different $j$. Both weighted and unweighted cases are shown. Only those values of $j$ that are used in the analysis are shown. The fine-dashed (long-dashed) lines show the mean value of the ratio for the weighted (Unweighted) case in the (0-50)% centrality interval .

### 9.4.2 Three-subevent resolution cross-checks

Several three sub-event checks are done to determine the systematic errors for the unweighted and weighted single-plane resolutions. The reference detectors used for the 3SE cross-checks are the same ones as described in Table 5 where the checks for the Unweighted case were done (Section 4.2.2). The unweighted cases are shown here again for comparison. The ratio of the resolution from the 3SE measurements to the 2SE values are shown in Figs. 79-83 for both the unweighted (left) and unweighted (right) cases. The colored-continuous lines show the mean deviation of the 3SE value from the default 2SE value in the (10-50)% centrality range, while the dashed-colored lines show the error of the mean deviation. The mean deviations are obtained by statistically combining the points in the 10-50% centrality range. The thick-dashed black lines show the error quoted from this check (the errors are taken symmetric about 1.0). The assigned errors are generally centrality independent except for the Res$\{4\Psi_2\}$ and Res$\{6\Psi_2\}$ cases where the peripheral bins are assigned larger errors. The Unweighted and Weighted cases show nearly similar deviations, but in most cases the Unweighted case has slightly larger deviations. However for simplicity, both are assigned identical errors, by choosing the larger of the deviations as the common systematic error. The final errors were already quoted for the "Unweighted" correlations in Table 6. The error for the weighted case are identical.

The problem with the 3SE resolution estimates as mentioned before is that when the reference detectors have poor resolution, it automatically results in larger deviations for the ECalFCal. Thus in most cases the errors are being overestimated.

Except for the Res$\{12\Psi_4\}$ (Fig. 81) and Res$\{10\Psi_5\}$ (Fig. 82) the assigned error easily cover the deviations seen in the (10-50)% interval where the statistical errors are manageable.

For the Res$\{12\Psi_4\}$ and Res$\{10\Psi_5\}$ the statistical errors in the deviations are too large to allow for a meaningful estimation of the deviation. Instead the linearity of the increase with $j$ of $\Delta$Res$\{jn\Psi_n\}$ is used. This gives for Res$\{12\Psi_4\}$ a 7.5% error, and for Res$\{10\Psi_5\}$ a 7.0% error (see Table 6).

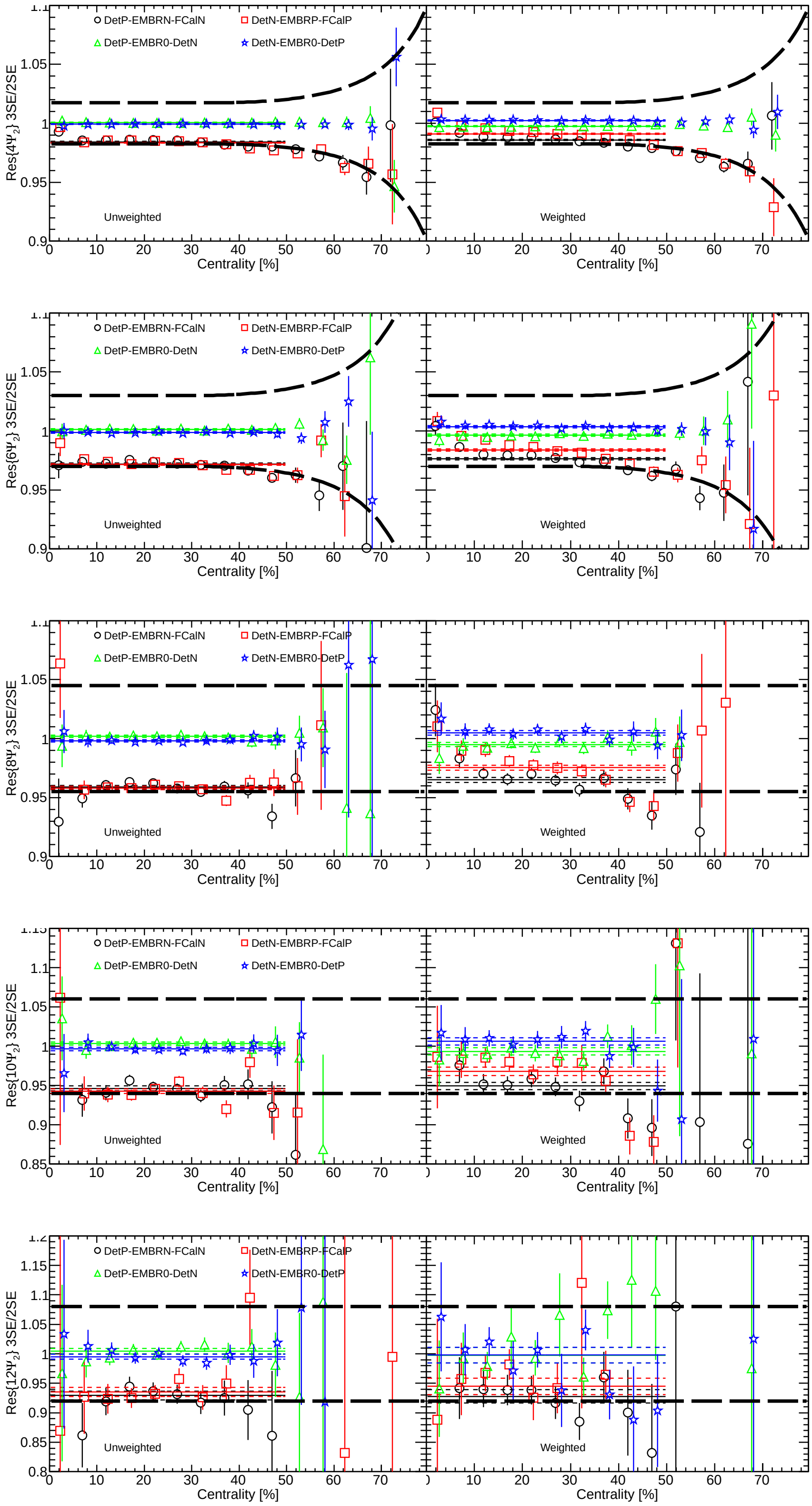


Figure 79: The ratio of the resolution for the ECalFCal$^{\mathrm{P/N}}$ obtained from several three-subevent checks to the default two-subevent resolution for Res$\{j2\Psi_2\}$ as a function of centrality. From top to bottom the plots correspond to different values of $j$. The left (right) plots correspond to the Unweighted (Weighted) case. The colored-continuous lines show the mean deviation of the 3SE value from the default 2SE value in the (10-50)% centrality range, while the dashed-colored lines show the error of the mean deviation. The thick-dashed black lines show the error quoted from this check. Only those values of $j$ that are used in the analysis are shown.

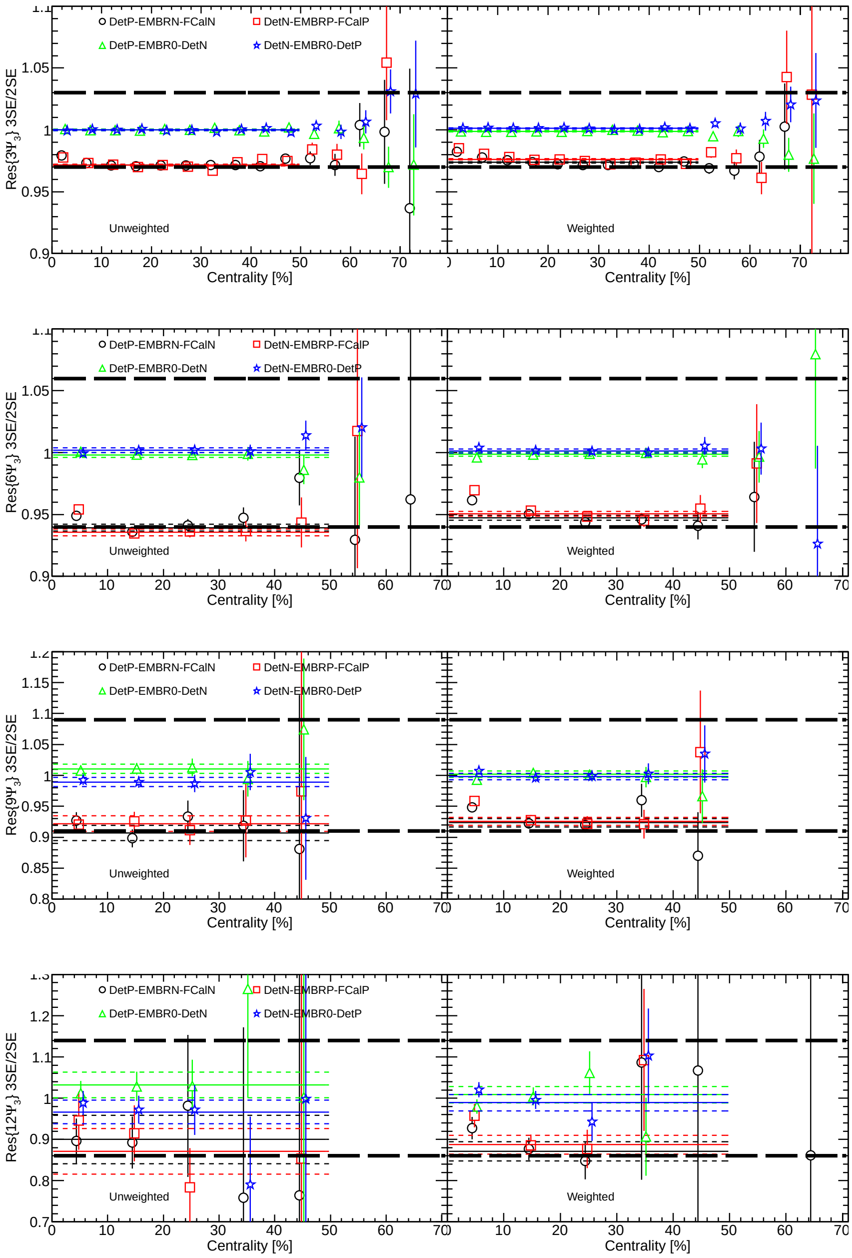


Figure 80: Same as previous plot but for Res$\{j3\Psi_3\}$ for \$j\$=1-4.

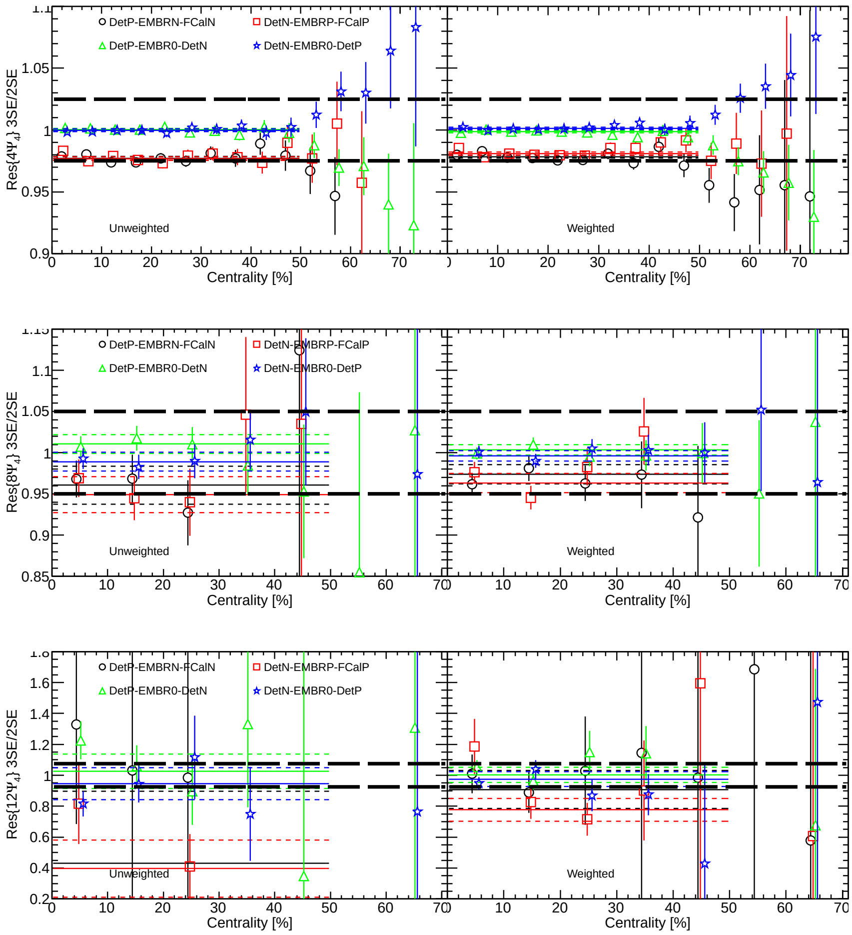


Figure 81: Same as previous plot but for Res$\{j4\Psi_4\}$. Only those values of $j$ that are used in the analysis are shown.

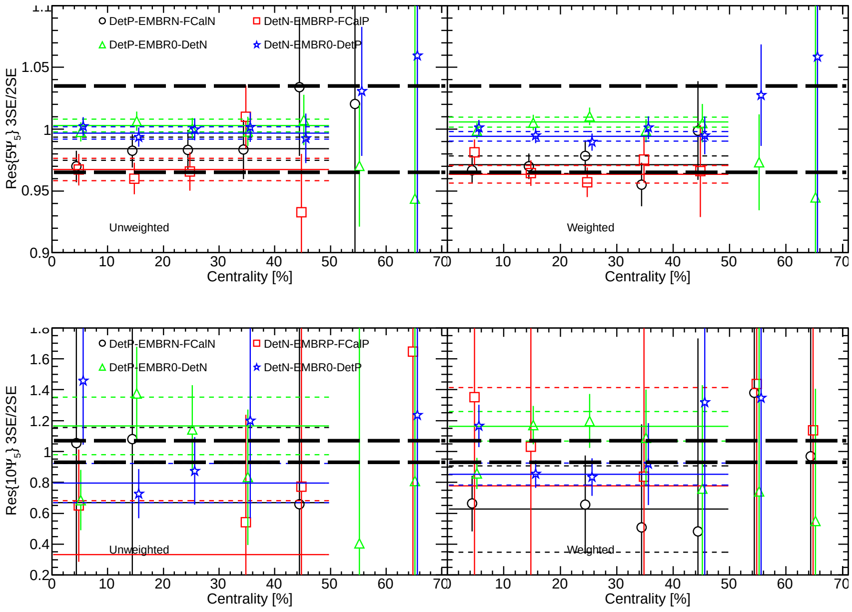


Figure 82: Same as previous plot but for Res{$j5\Psi_5$} for \$j\$=1, 2. Only those values of $j$ that are used in the analysis are shown.

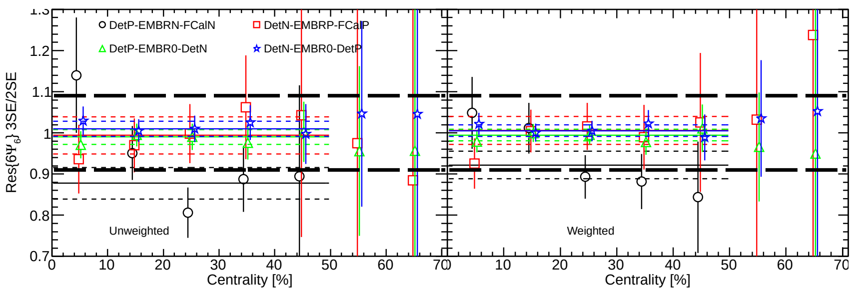


Figure 83: Same as previous plot but for Res{$j6\Psi_6$}. Only those values of $j$ that are used in the analysis are shown.

### 9.5 Uncorrelated resolution errors

Later on comparison plots will be made between the weighted and unweighted cases. In these comparisons the correlated systematic errors must be removed. It was already seen that the sine terms in the 2SE calculations of the single-plane resolutions are completely correlated. Similarly a strong correlation was seen in the 3SE resolution estimates (which is the main source of systematic error for the resolutions). Here the uncorrelated errors in the resolutions (from 3SE checks) are calculated.

The 3SE ratios shown in Section.9.4.2 indicate the variation in the unweighted and weighted resolutions when calculated using different reference detectors. In order to get the fractional change of the Weighted resolution w.r.t. to Unweighted resolution, a double ratio of the form:

$$Uncorrelated\ err = \frac{(3SE/2SE)\ Weighted}{(3SE/2SE)\ Unweighted} \tag{49}$$

is made. In this double ratio, the correlated deviations cancel out and the extra deviation that the Weighted resolutions have w.r.t. the Unweighted ones are obtained. Such Plots are shown in Figs. 84-88.

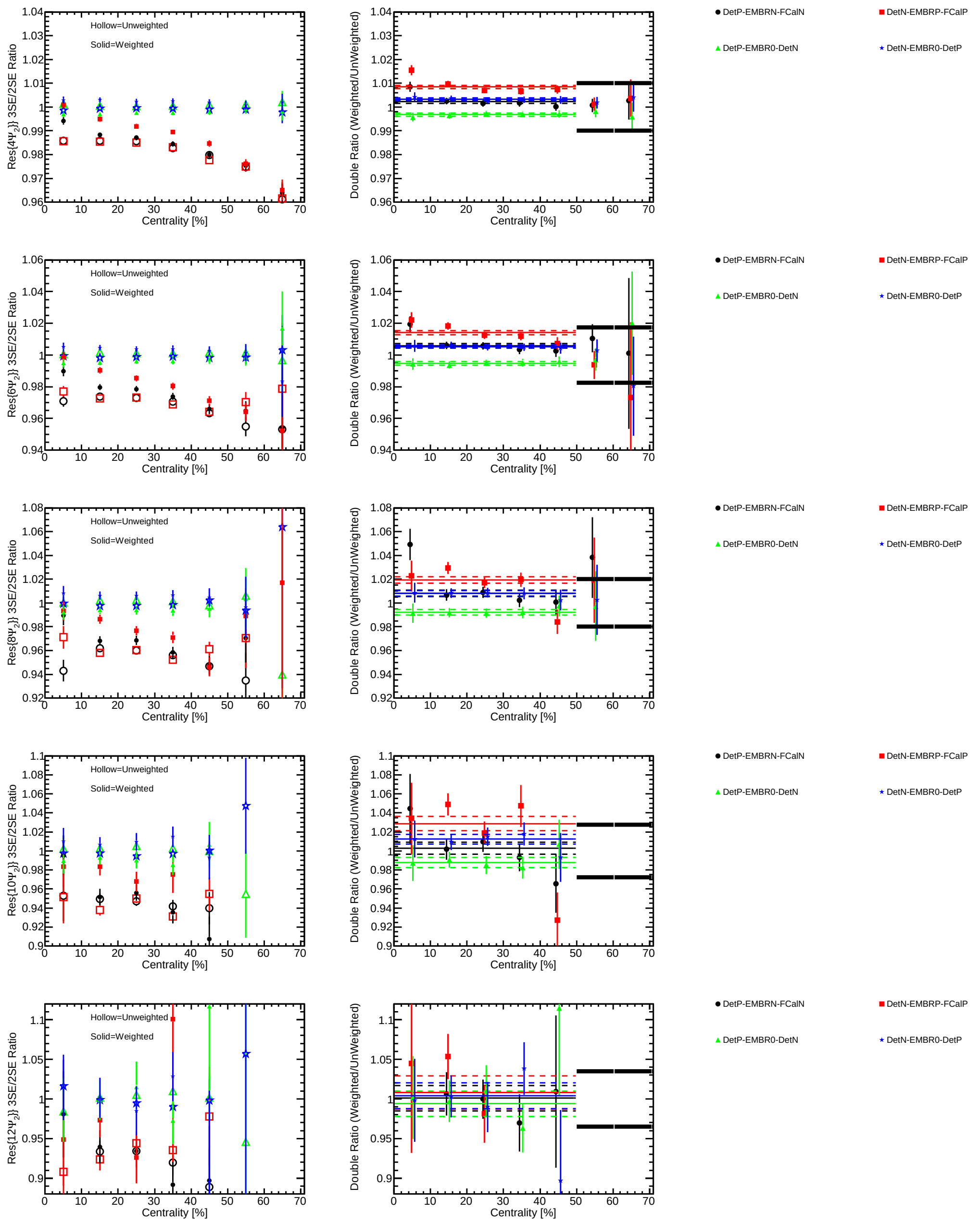


Figure 84: Left plot: The ratio between the 3SE and 2SE(default) resolutions for the unweighted (hollow) and weighted (solid) resolutions for Res$\{j2\Psi_2\}$. The right plot shows the double ratio for the weighted/unweighted. This double ratio is used to estimate the uncorrelated systematic errors between the weighted and unweighted case. The horizontal continuous coloured lines in the right plots show the mean value of the double ratio for different 3SE double-ratios, while the corresponding dashed lines show the $1\sigma$ error bands for the mean values. The thick-dashed black lines indicate the assigned uncorrelated error.

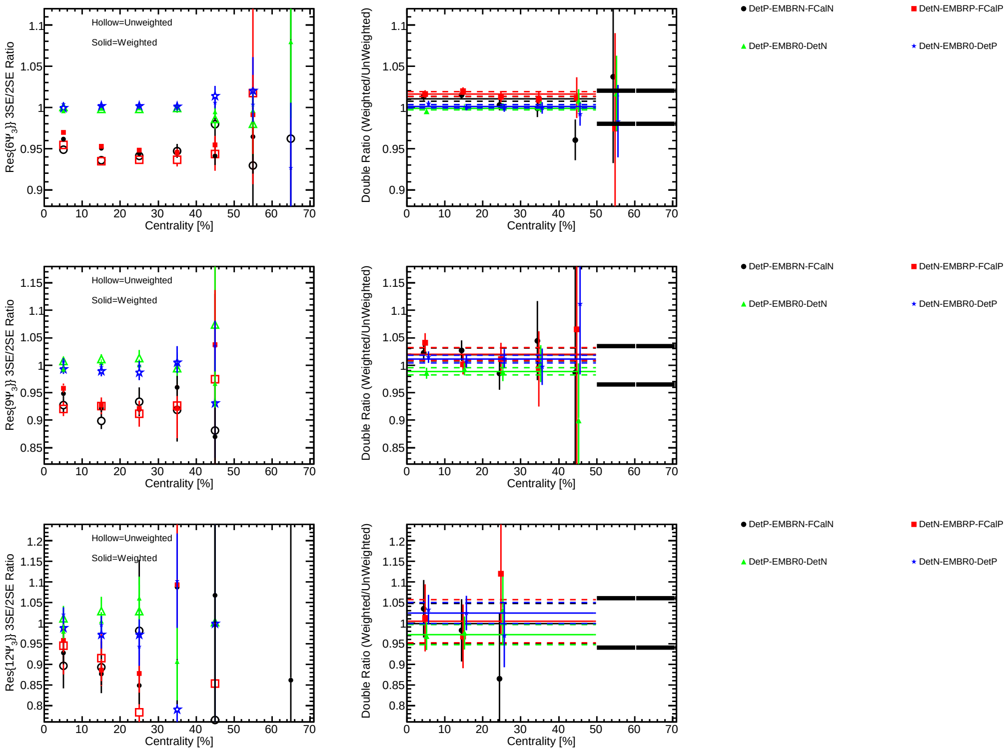


Figure 85: Same as previous plot but for Res$\{j3\Psi_3\}$.

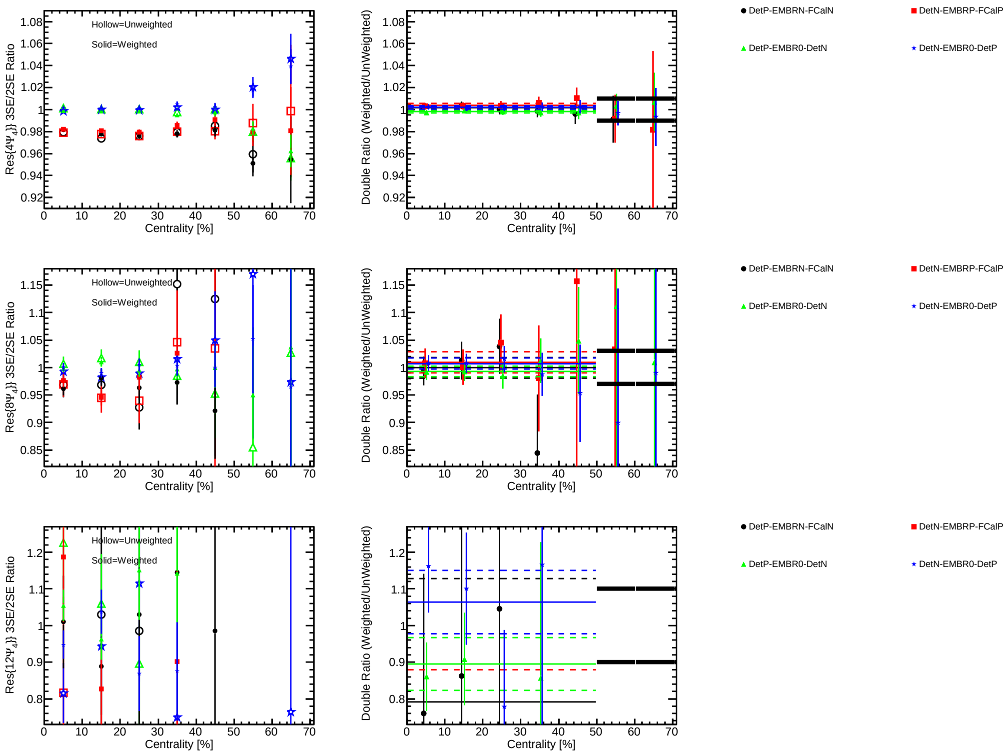


Figure 86: Same as previous plot but for Res$\{j4\Psi_4\}$.

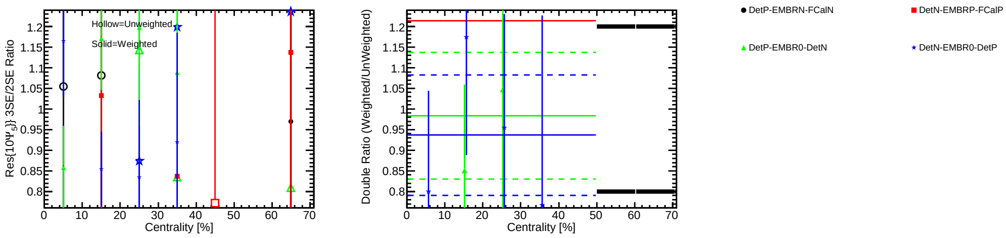


Figure 87: Same as previous plot but for Res$\{2 \times 5\Psi_5\}$.

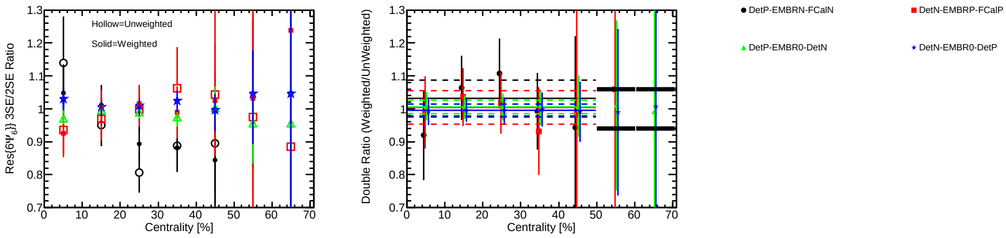


Figure 88: Same as previous plot but for Res$\{6\Psi_6\}$.

## 9.6 Final Plots

The systematic errors for the weighted correlations are listed in Table 15. They are identical to the errors for the unweighted correlations (Table 6) as shown in the last section. Table 16 lists the relative errors for the Weighted to Unweighted case for single-plane resolutions as well as the corresponding errors propagated the the correlators. Note that the relative errors are only listed for the four strong non-zero correlators for which the ratios (Weighted-correlator/Unweighted-correlator) will be shown later.

| Error for Res$\{jn\Psi_n\}$ | | | | | |
|---|---|---|---|---|---|
| $n$ | 2 | 3 | 4 | 5 | 6 |
| 3SE comparison | $0.85j\%(j \le 2)$<br>$3\%(j{=}3)$<br>4.5%,6%,8% ($j$=4,5,6) | $3.0j\%$ | $2.5j\%$ | $3.5j\%$ | $9j\%$ |
| sin component | $0.5 \times (0.085jn)^2\%$ | | | | |

| Error for $\langle\cos jk(\Phi_n - \Phi_m)\rangle$ correlators | | | | | | | | |
|---|---|---|---|---|---|---|---|---|
| $(j,n,m)$ | (1,2,4) | (2,2,4) | (3,2,4) | (1,2,3) | (1,2,6) | (1,3,6) | (1,3,4) | (1,2,5) |
| Res$\{jk(\Psi_n - \Psi_m)\}$ | 3.06% | 6.73% | 11.0% | 6.71% | 9.49% | 10.8% | 15.9% | 9.24% |
| Raw distribution from sine and mixed-events (absolute error on raw $\times 10^{-4}$) | 5-15 | | | | | | | |

Table 15: Top table: summary of sources of systematic uncertainties for individual Res$\{jn\Psi_n\}$ terms coming from 2SE/3SE comparision and sine component of the 2SE correlations. Bottom table: summary of sources of systematic uncertainties for the final correlators $\langle\cos jk(\Phi_n - \Phi_m)\rangle$, including those for the combined resolution caculated from Res$\{jn\Psi_n\}$ terms, and the raw correlations.

| Relative error for Res$\{jn\Psi_n\}$ (Weighted vs Unweighted) | | | | | |
|---|---|---|---|---|---|
| $n$ | 2 | 3 | 4 | 5 | 6 |
| Error [%] | 1.0,1.75,2.0 ($j$=2,3,4)<br>2.75,3.5 ($j$=5,6) | 2.0,3.5,6.0 ($j$=2,3,4) | 1.0,3.0,10.0 ($j$=1,2,3) | 20 ($j$=2) | 6 ($j$=1) |

| Relative Error for $\langle\cos jk(\Phi_n - \Phi_m)\rangle$ correlators (Weighted vs Unweighted) | | | | |
|---|---|---|---|---|
| $(j,n,m)$ | (1,2,4) | (2,2,4) | (1,2,6) | (1,3,6) |
| Error [%] | 1.41% | 3.61% | 6.25% | 6.32% |

Table 16: Top table: Relative systematic uncertainties for individual Res$\{jn\Psi_n\}$ terms coming from 2SE/3SE double-ratios. Bottom table: Relative ystematic uncertainties between the weighted and unweighted cases for the final correlators. For the lower table only the four strong-correlators are listed.

### 9.6.1 Raw Correlations

Figs. 89 and 90 show the raw correlation for the Unweighted and Weighted cases respectively. The systematic error is calculated as the quadrature sum of the $|\langle\sin k(\Psi_n - \Psi_m)\rangle|$ and mixed background $|\langle\cos k(\Psi_n - \Psi_m)\rangle|$ term. The shapes of the correlations seem to be different for the Unweighted and Weighted cases. For example for the $\langle\cos 4(\Psi_2 - \Psi_4)\rangle$ correlation, the Unweighted case peaks at $N_{\rm part} \sim 150$ while for the Weighted case it peaks at $N_{\rm part} \sim 100$. This is a trivial consequence of applying the $q_n$ as the weights. Since the $q_n$ are larger for mid-central/peripheral events. Thus the more peripheral events are multiplied by larger factors in the Weighted case and hence reach their maximum at more peripheral values. The corresponding resolutions also show this trend between the Weighted and Unweighted case, however this effect largely cancels out for the corrected correlations (i.e. when the raw signals are divided by the resolutions).

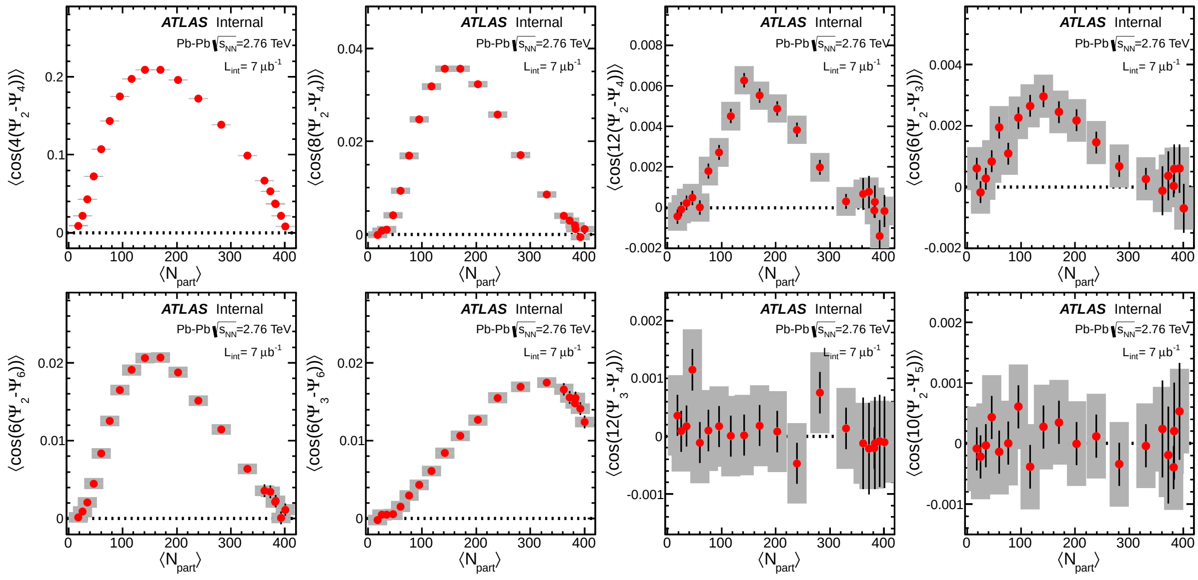


Figure 89: The raw correlations as a function of $\langle N_{\mathrm{part}} \rangle$ for the Unweighted case.

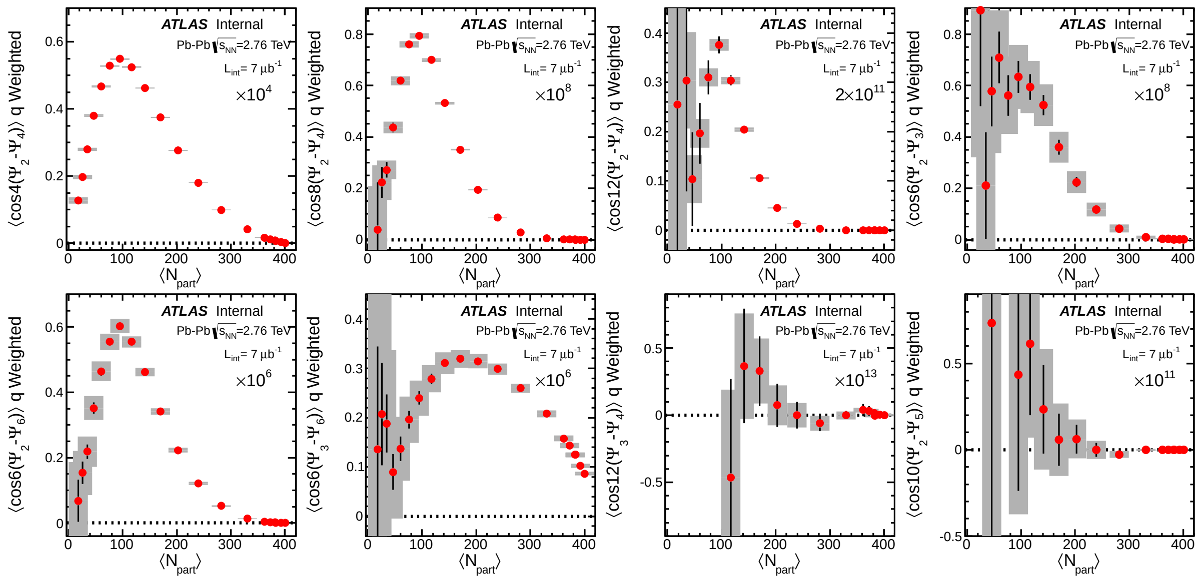


Figure 90: The raw correlations as a function of $\langle N_{\mathrm{part}} \rangle$ for the Weighted case. The different plots are scaled by various multiplicative factors (mentioned on the plots) to keep the y-axis range reasonable.

### 9.6.2 Combined resolutions

Figs. 89 and 90 show the resolution for the Unweighted and Weighted cases respectively (which are the products of the single-plane resolutions). The systematic error is calculated as the quadrature sum from the 3SE deviations and the ⟨sin⟩ terms in the single-plane resolutions. As explained before, for the weighted case, the resolutions have identical systematic errors as the unweighted ones.

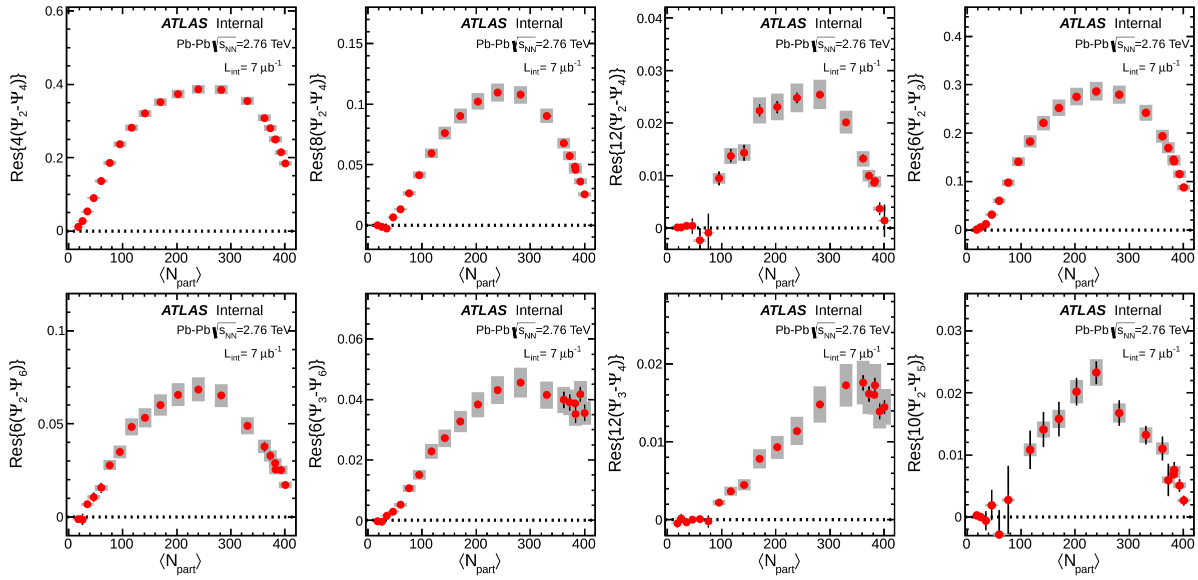


Figure 91: The combined resolutions as a function of $\langle N_{\text{part}} \rangle$ for the Unweighted case.

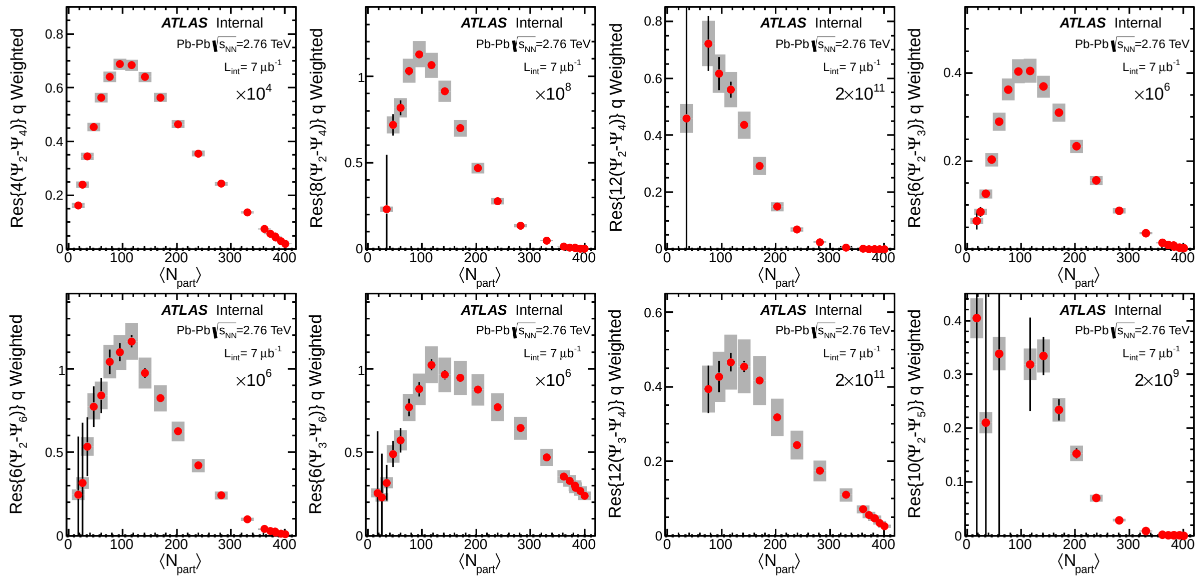


Figure 92: The combined resolutions as a function of $\langle N_{\text{part}} \rangle$ for the Weighted case. The different plots are scaled by various multiplicative factors (mentioned on the plots) to keep the y-axis range reasonable.

### 9.6.3 Corrected Correlations

Fig.93 shows the final correlated two-plane correlations for the Unweighted and Weighted cases. Fig.94 shows the ratio of the Weighted and Unweighted correlations for the four strong correlations. The correlated systematic errors are cancelled out in the ratio. The Unweighted and Weighted correlations have very similar centrality dependence and behavior. Typically the weighted correlations are larger than the unweighted ones, this is especially clear from the ratio plot 94. In general when lower powers of the $q$ vectors are used in the weighting, the smaller is the difference between the weighted and unweighted case. For example, for the $\langle\cos 4(\Psi_2 - \Psi_4)\rangle$ correlation the weighting factor is $(q_2)^2 q_4 \sim q^3$ and the maximum deviation between the Weighted and Unweighted cases is $\sim$ 12%, while for the $\langle\cos 8(\Psi_2 - \Psi_4)\rangle$ where the weighting factor is $(q_2)^4 (q_4)^2 \sim q^6$, the maximum deviation increases to $\sim$ 30%.

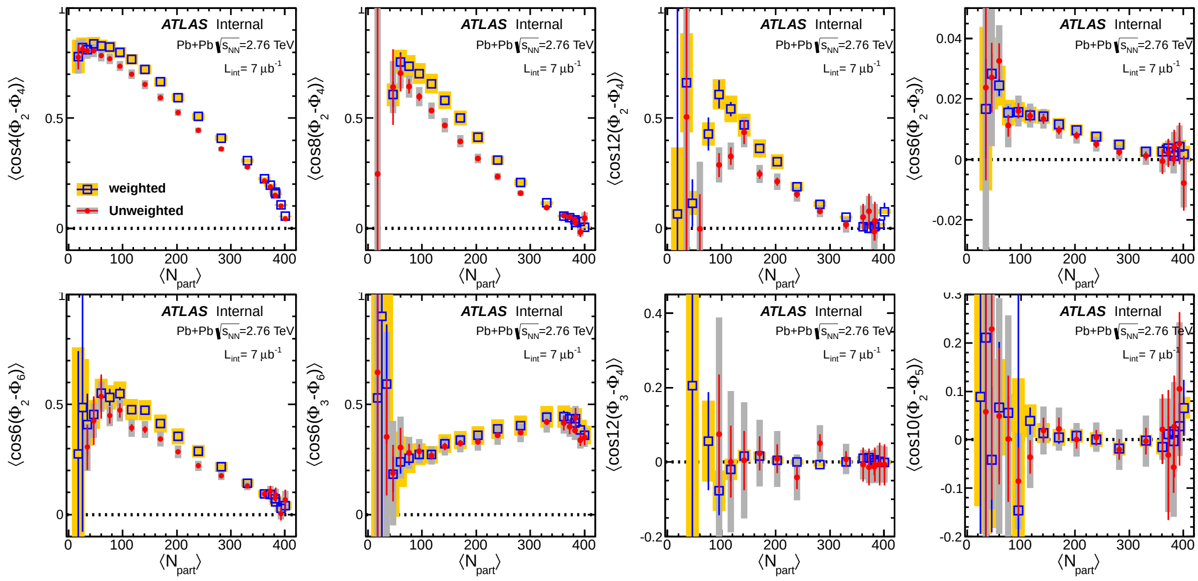


Figure 93: Comparison of the corrected correlations for the Weighted and Unweighted case as a function of $\langle N_{\text{part}}\rangle$.

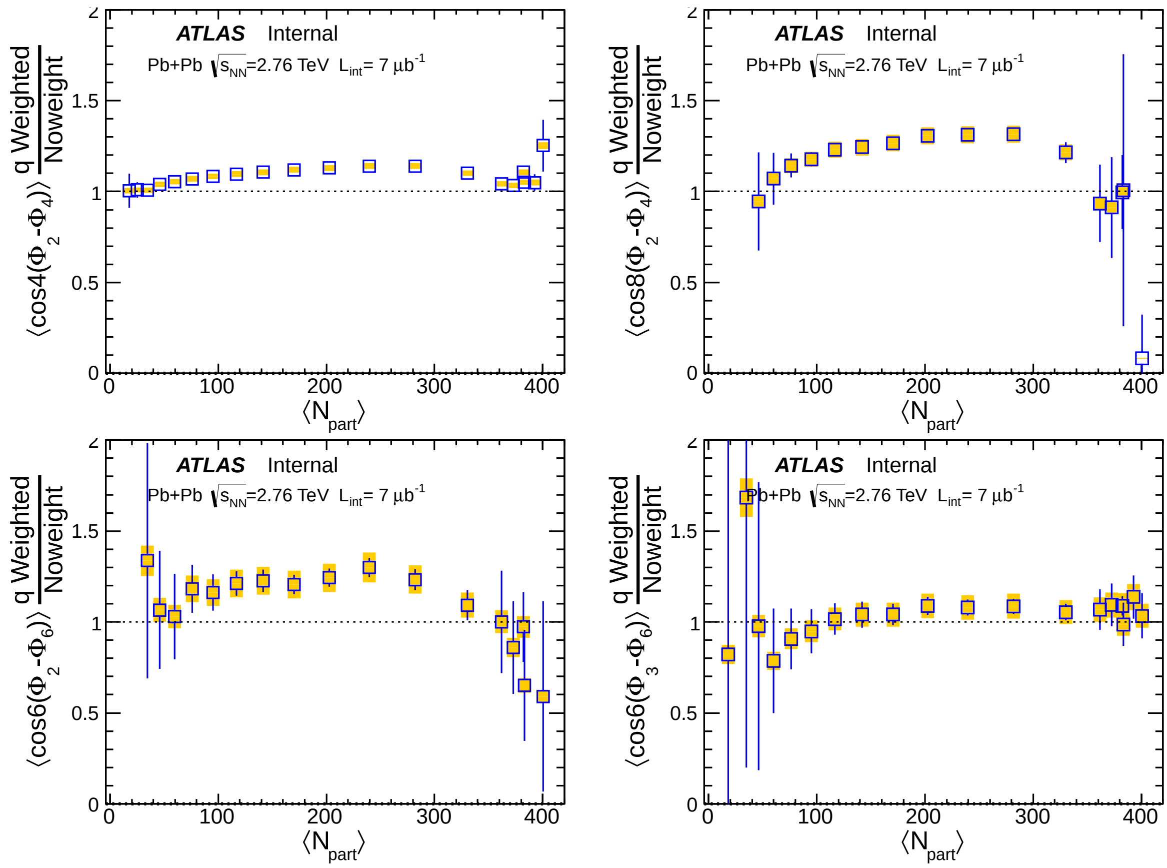


Figure 94: Ratio of the corrected correlations for the Weighted to the Unweighted case as a function of $\langle N_{\text{part}}\rangle$. The ratios are shown only the four strong correlations.

### 9.6.4 Cross-checks with tracking detectors

The whole analysis is repeated with the Tracking detectors and the results are compared to the ECalFCal results for both the weighted and Unweighted cases. The details for the tracking detector based analysis are given in Appendix-I. For the Tracking detectors, the two sub-events have $\eta$ coverage of $\eta \in (-2.5, -0.5)$ and $\eta \in (0.5, 2.5)$ and are made with charged tracks with $p_{\mathrm{T}} \in (0.5, 10)$GeV. The Tracks are $p_T$ weighted while calculating the $Q$ vectors. In general very good agreement is seen between the tracking detector based results and the Calorimeter based results for both the Unweighted (Figs.95 and 96) and Weighted (97 and 98) case.

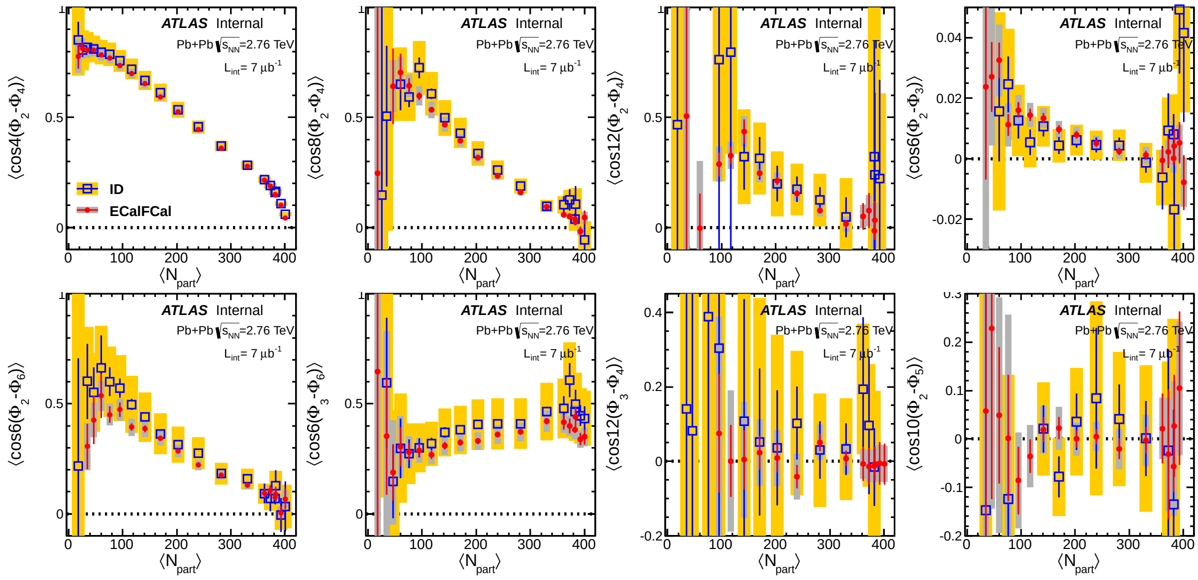


Figure 95: Comparison of the corrected correlations for the Unweighted case as a function of $\langle N_{\mathrm{part}} \rangle$ as measured by the ECalFCal (Default) and Tracking detectors.

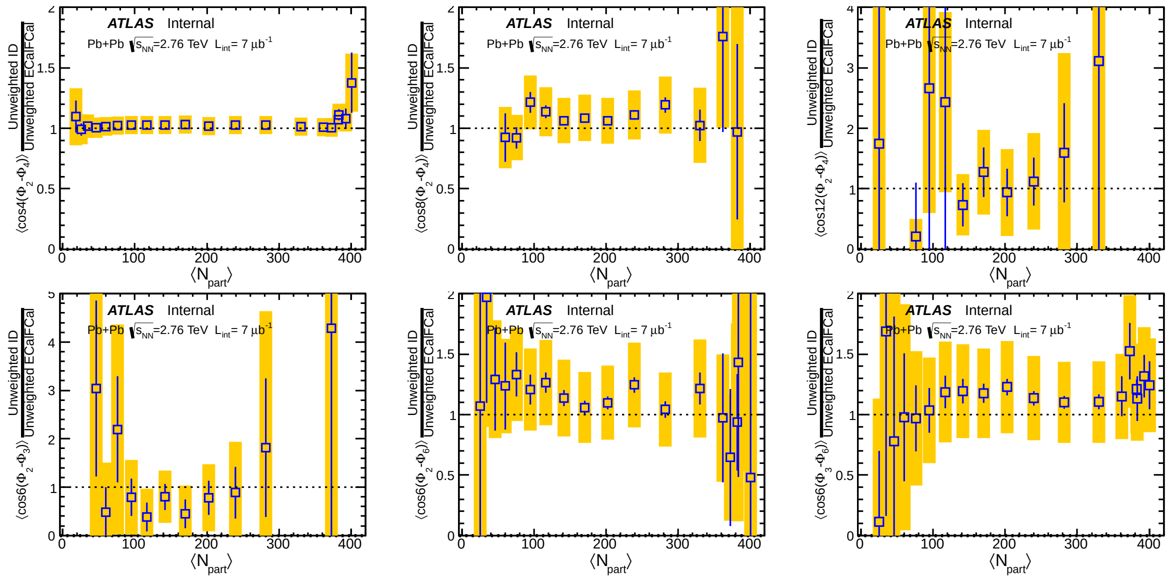


Figure 96: Ratio of the corrected correlations for the Unweighted case as measured by the Tracking detectors and by ECalFCal (Default), as a function of $\langle N_{\text{part}} \rangle$. The ratios are made only for the six non-zero correlations.

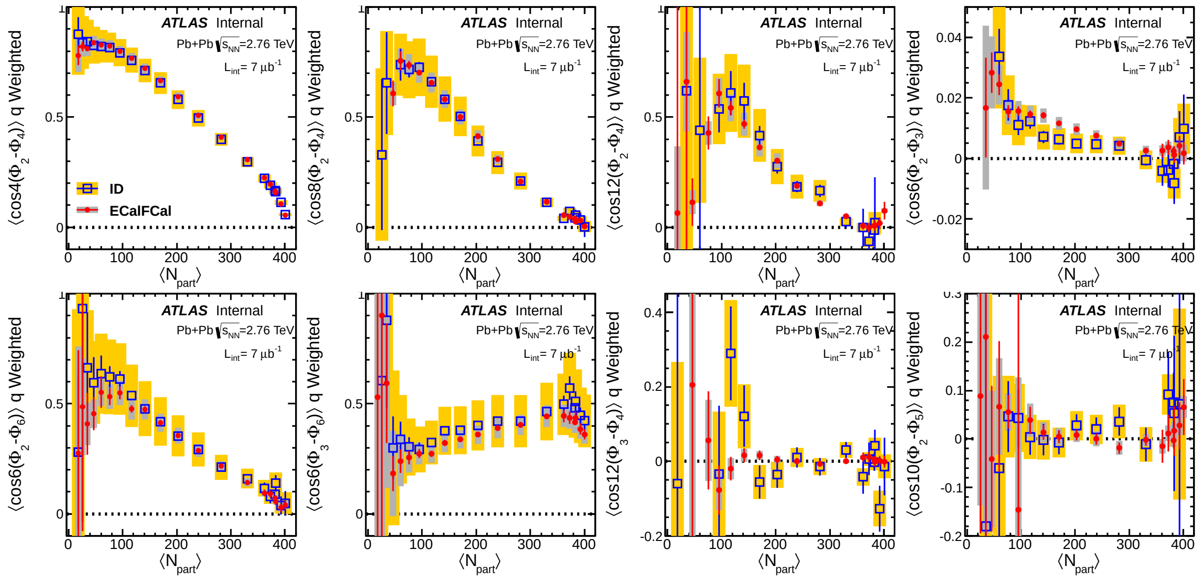


Figure 97: Comparison of the corrected correlations for the Weighted case as a function of $\langle N_{\text{part}} \rangle$ as measured by the ECalFCal (Default) and Tracking detectors.

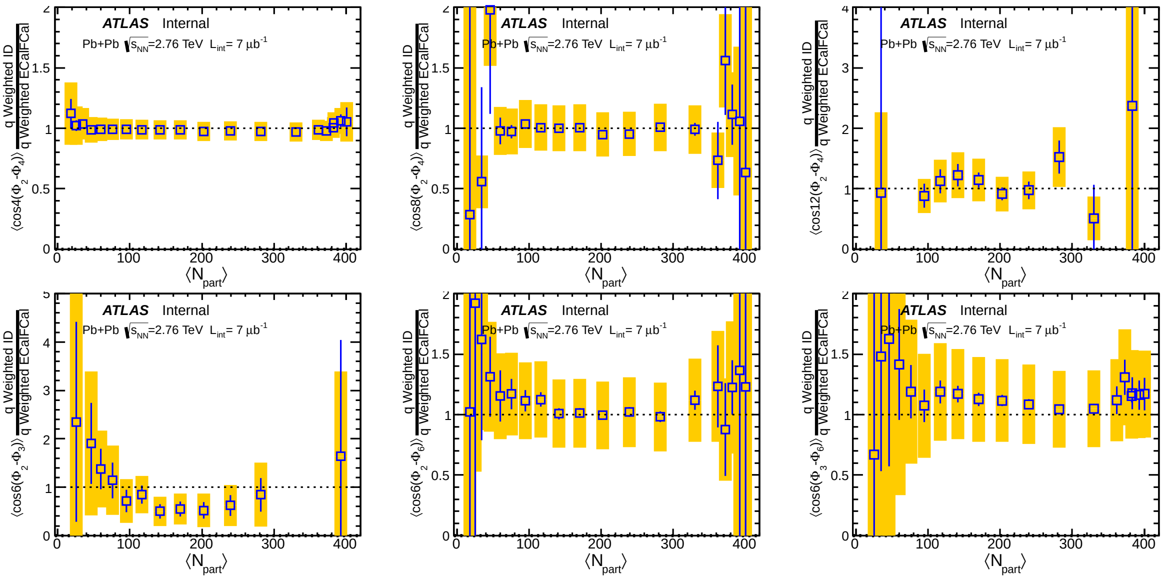


Figure 98: Ratio of the corrected correlations for the Weighted case as measured by the Tracking detectors and by ECalFCal (Default), as a function of $\langle N_{\text{part}} \rangle$. The ratios are made only for the six non-zero correlations.

# 10 Three-plane correlations: Weighted

The steps of the three-plane correlations analysis are identical to the two-plane correlations: The raw signals and resolutions are determined weighted by the $q_n$ and finally the raw correlators are divided by the resolutions to obtain the corrected correlators. The analysis is done with the default detector combination that was used in Section 5.1 (also see Fig. 43). Cross-checks are done using the tracking detectors.

## 10.1 Raw Correlations

Figures 99-104 show the relative angle distributions for the six three-plane correlators for three different centralities for the weighted case, these are analogous to Figs. 44-49. Note that there are three “Types” for each correlation as described in Section 5.1. As with the weighted two-plane correlations, these are rescaled to mean value of 1.0. The raw correlators are calculated from these distributions with $\langle \sin \rangle$ terms taken as the systematic errors at the raw level. Figure. 105 shows the raw signal for the six different correlators Also shown are the $\langle \sin \rangle$ terms as well as the $\langle \sin \rangle$ and $\langle \cos \rangle$ values for the mixed background. This plot is the analogue of Fig. 50.

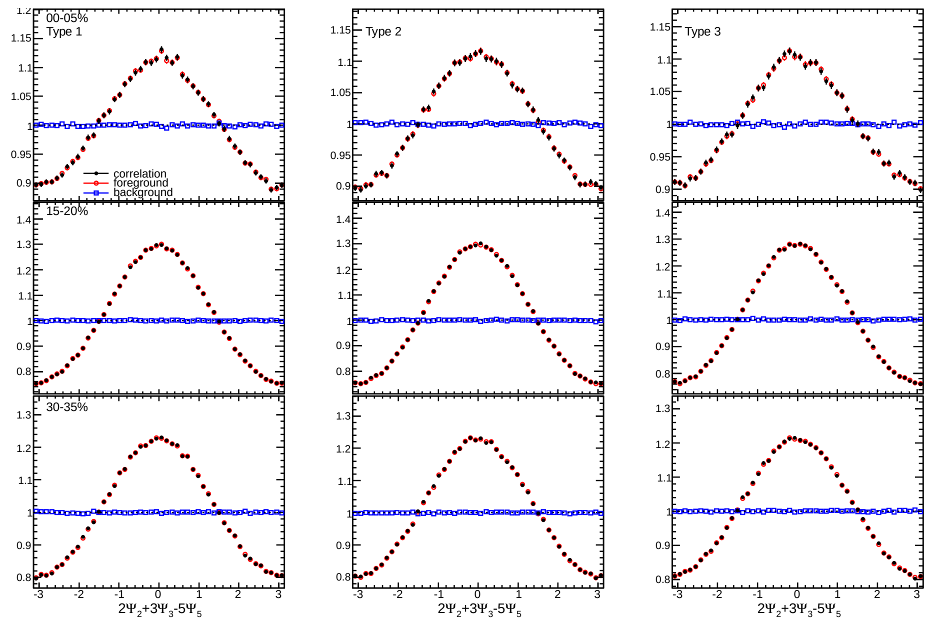


Figure 99: The distributions for the Weighted three plane angle differences $(2\Psi_2 + 3\Psi_3 - 5\Psi_5)$ for several centrality intervals, and the three types.

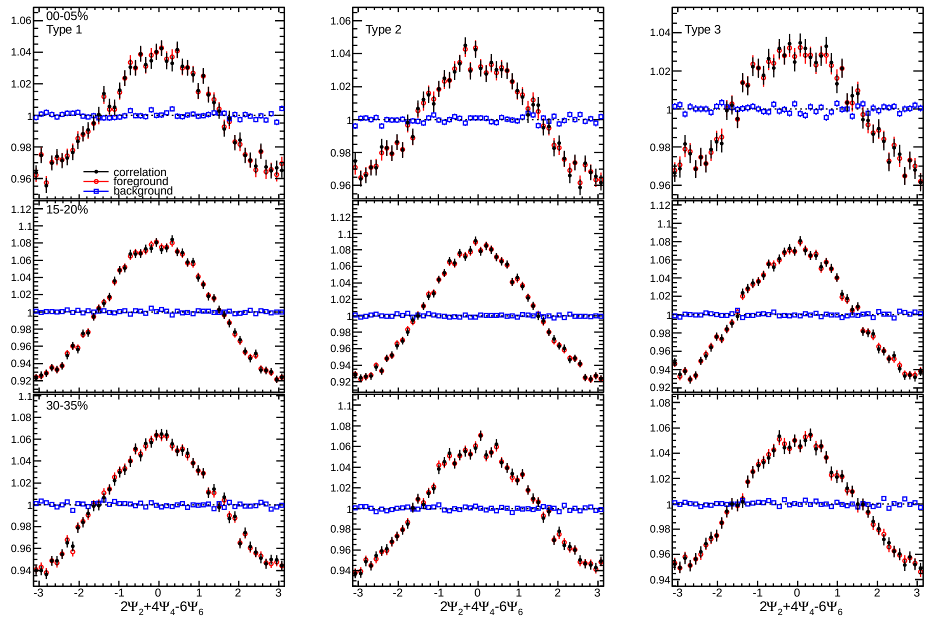


Figure 100: The distributions for the Weighted three plane angle differences ($2\Psi_2 + 4\Psi_4 - 6\Psi_6$) for several centrality intervals, and the three types.

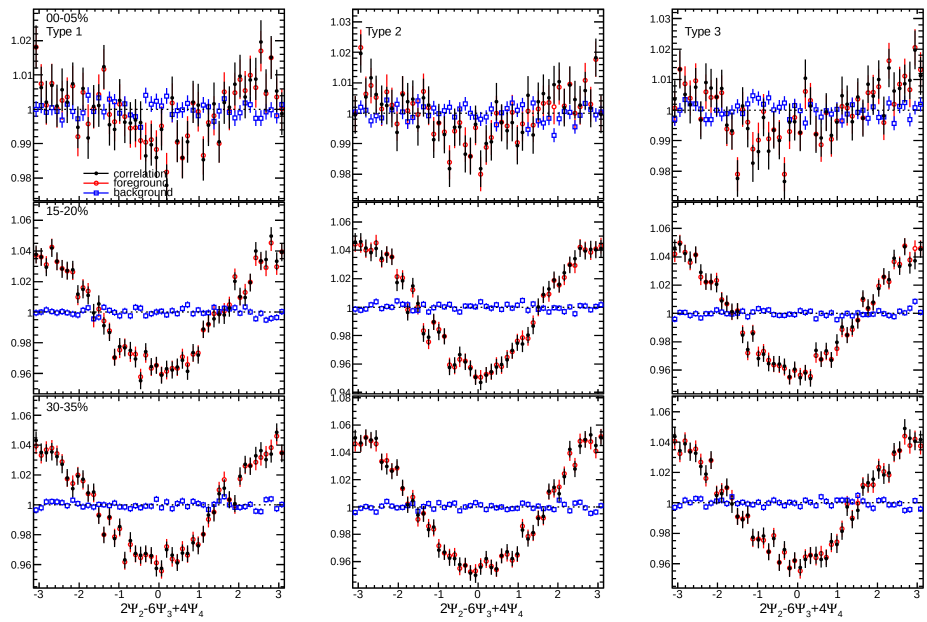


Figure 101: The distributions for the Weighted three plane angle differences ($2\Psi_2 - 6\Psi_3 + 4\Psi_4$) for several centrality intervals, and the three types.

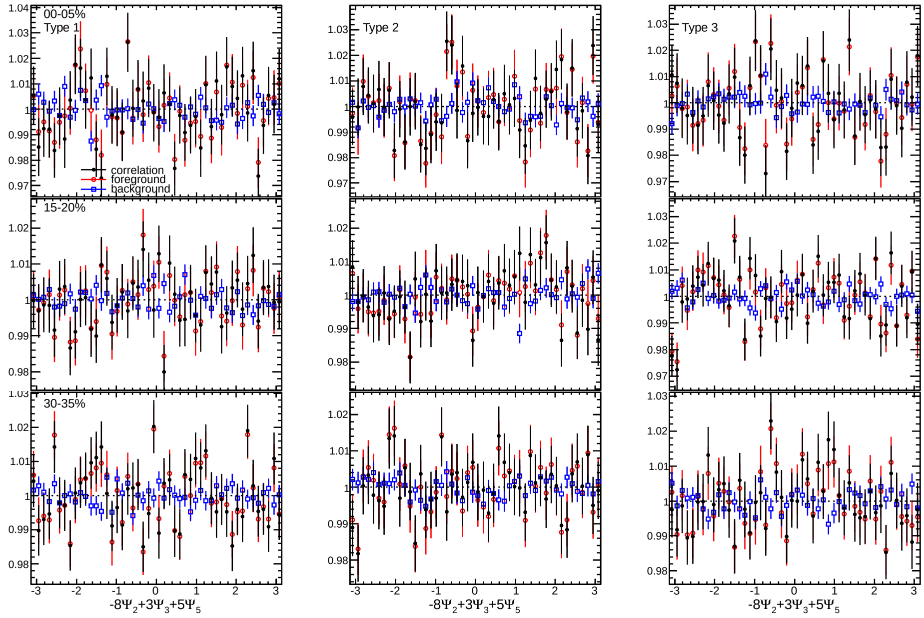


Figure 102: The distributions for the Weighted three plane angle differences $(-8\Psi_2 + 3\Psi_3 + 5\Psi_5)$ for several centrality intervals, and the three types.

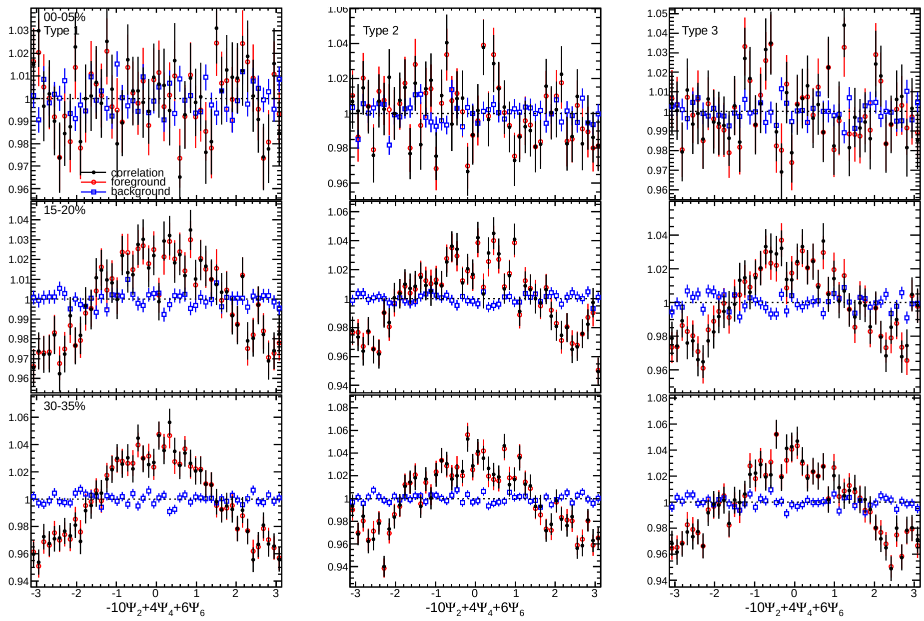


Figure 103: The distributions for the Weighted three plane angle differences $(-10\Psi_2 + 4\Psi_4 + 6\Psi_6)$ for several centrality intervals, and the three types.

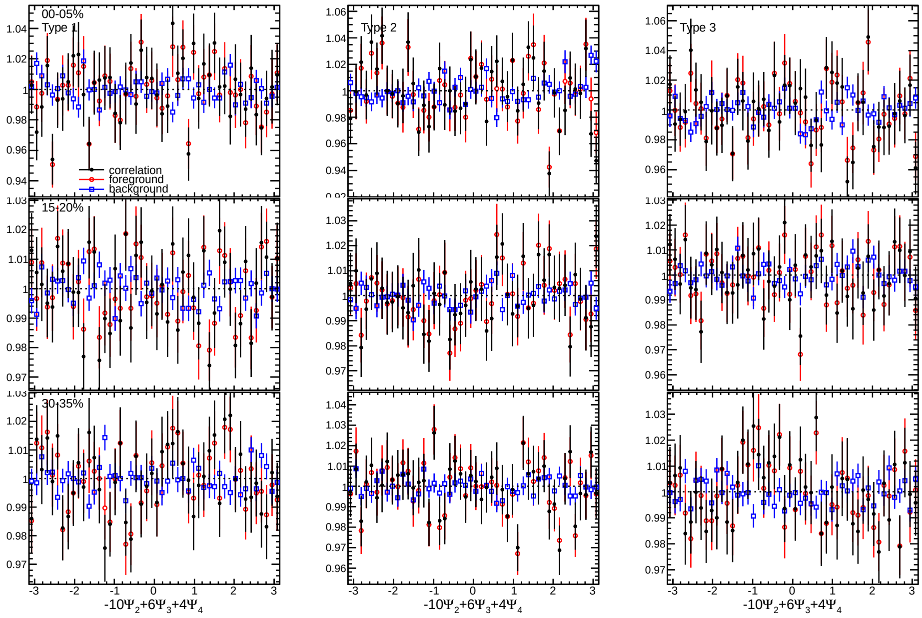


Figure 104: The distributions for the Weighted three plane angle differences ($-10\Psi_2 + 6\Psi_3 + 4\Psi_4$) for several centrality intervals, and the three types.

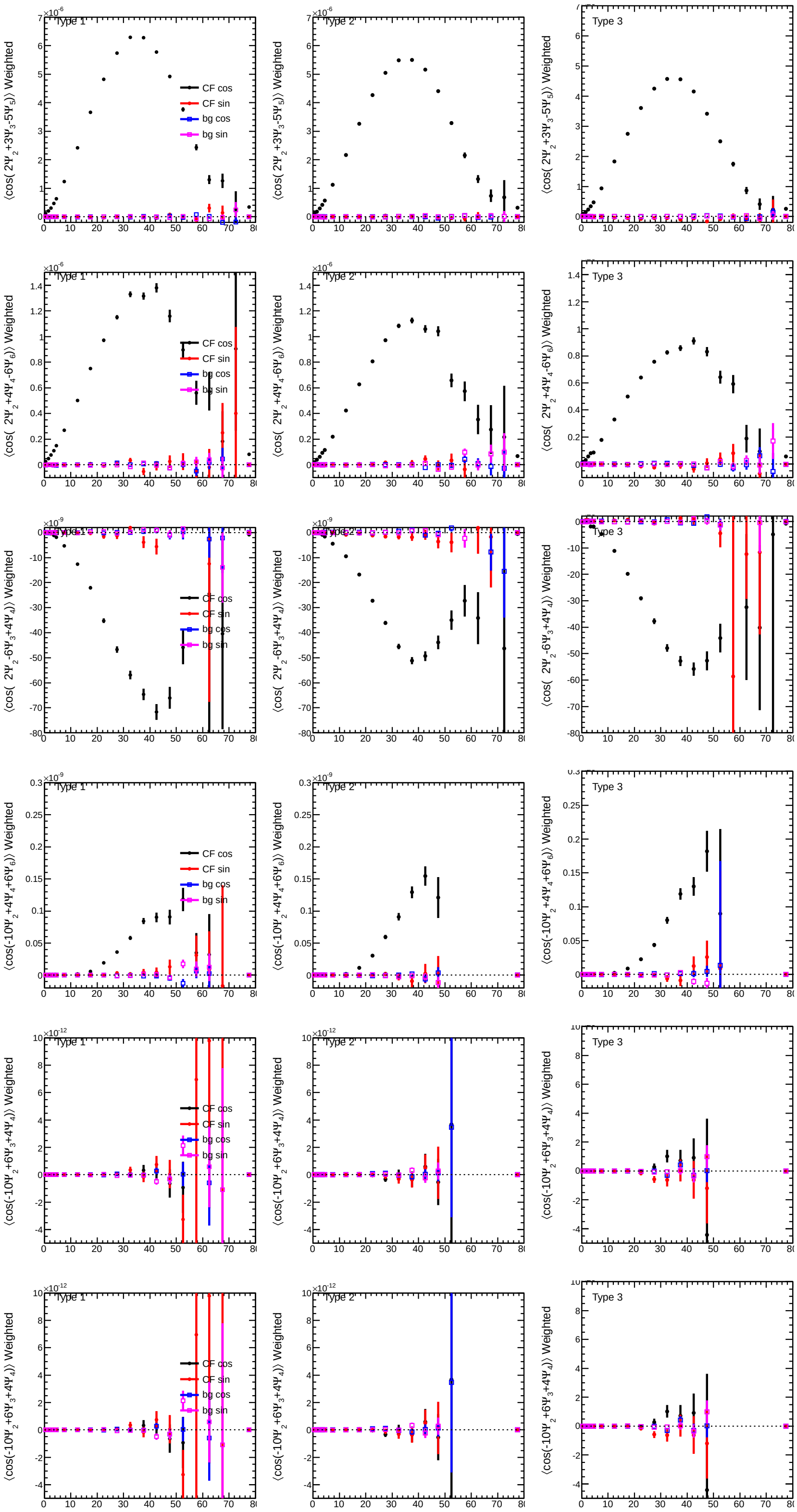


Figure 105: Centrality dependence of the raw cosine signal for the Weighted three-plane correlators. They are compared with the sine values as well as the sine and cosine obtained from mixed-events. The last bin (75-80) is actually the (0-5)% bin.

## 10.2 Resolutions

The single-plane for the three detectors are obtained by 3SE or 2SE methods. For the $ECal_{P/N}$ the default resolution is obtained by the 2SE method by correlating $ECal_P$ with $ECal_N$ as:

$$\mathrm{Res}\{jn\Psi_n, ECal_{P/N}\} = \sqrt{\cos(jn(\Psi_n^{ECal_P} - \Psi_n^{ECal_N}))} \tag{50}$$

While for the $FCal$ the default resolution is obtained by the 3SE method by correlating it with the $ECal_{P/N}$ as:

$$\mathrm{Res}\{jn\Psi_n, FCal\} = \sqrt{\frac{\cos(jn(\Psi_n^{FCal} - \Psi_n^{ECal_N}))\cos(jn(\Psi_n^{FCal} - \Psi_n^{ECal_P}))}{\cos(jn(\Psi_n^{ECal_P} - \Psi_n^{ECal_N}))}} \tag{51}$$

This was also the default method for obtaining the resolutions used in the Unweighted analysis. Several 3SE checks are done to determine the systematic errors in the resolutions. The deviation of the 3SE checks from the default value for the $ECal$ are shown in Figs. 106-108 for both the Unweighted (left panels) and Weighted (right panels) cases. The thick dashed lines show the errors quoted for the single-plane resolutions for the ECal (The errors are taken to be the same for $ECal_P$ and $ECal_N$). The Weighted and Unweighted cases are assigned identical systematic error bands. It can be seen from these plots that the largest deviations for the resolution occur when one of the three detectors used in the 3SE estimate is the $FCal_P$ (or $FCal_N$) . This occurs because of the very poor resolution of the $FCal_{P/N}$ which causes large deviations when used to determine the systematic error of the $ECal_{P/N}$.

Figs. 109-111 show similar 3SE calculations for the FCal single-plane resolutions. The uncertainties of the single-plane resolutions are then propagated into the combined resolution for the correlator.

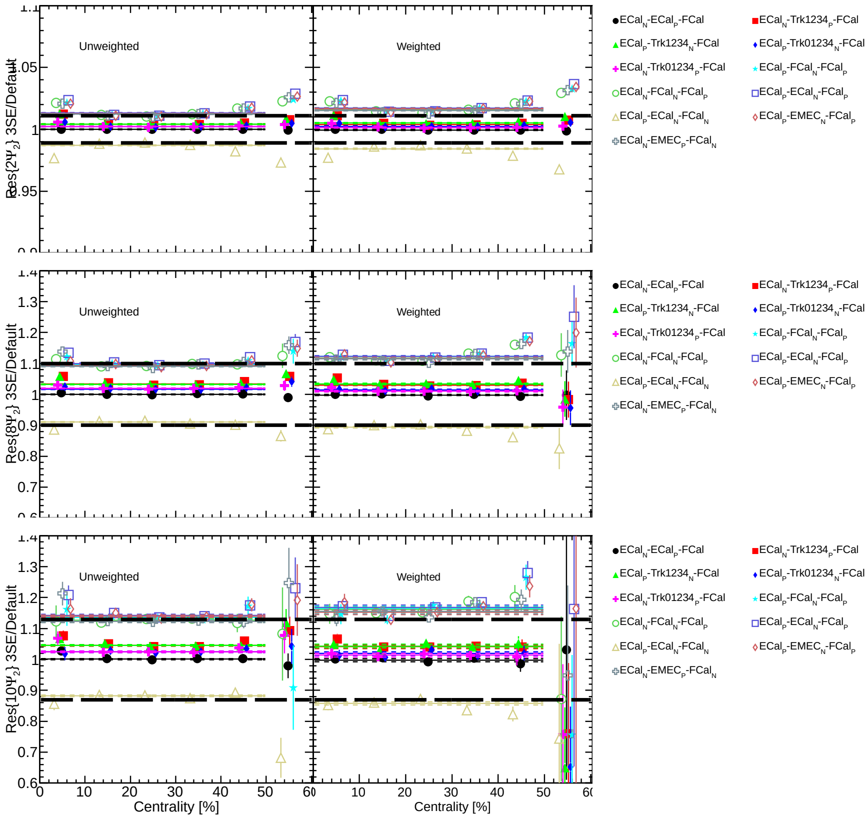

Figure 106: The ratio of the resolution for the $\mathrm{ECal}^{\mathrm{P/N}}$ obtained from several three-subevent checks to the default two-subevent resolution for Res$\{j2\Psi_2\}$ as a function of centrality. From top to bottom the plots correspond to different values of $j$. The left (right) plots correspond to the Unweighted (Weighted) case. The thick-dashed black lines show the error quoted from this check. Only those values of $j$ that are used in the analysis are shown.

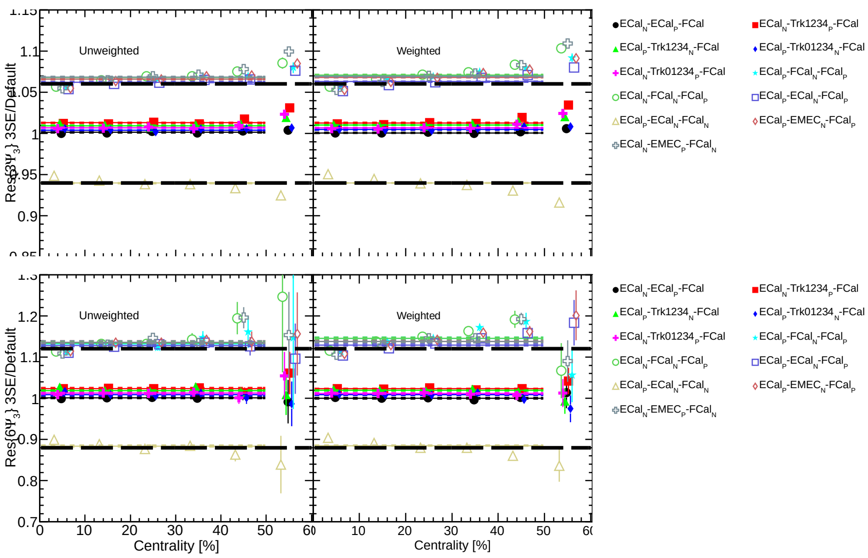

Figure 107: Same as previous plot but for Res$\{j3\Psi_3\}$(for ECal)

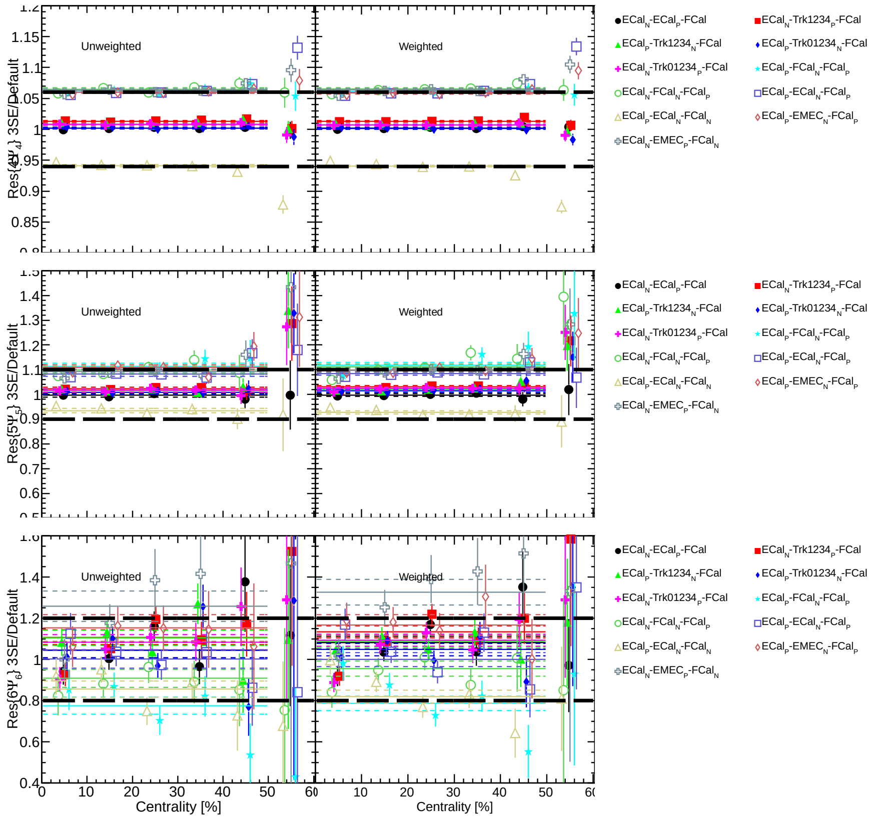

Figure 108: Same as previous plot but for Res{4Ψ$_4$} (Top) Res{5Ψ$_5$} (Middle) and Res{6Ψ$_6$} (Bottom) (for ECal)

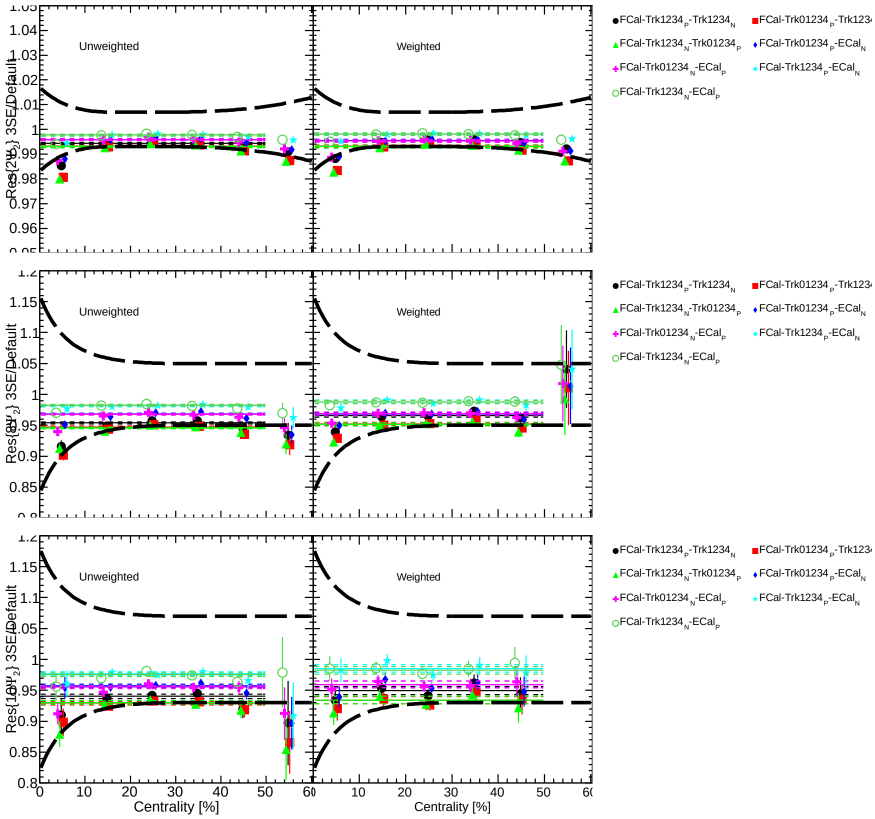


Figure 109: The ratio of the resolution for the FCal obtained from several three-subevent checks to the default two-subevent resolution for Res$\{j2\Psi_2\}$ as a function of centrality. From top to bottom the plots correspond to different values of $j$. The left (right) plots correspond to the Unweighted (Weighted) case. The thick-dashed black lines show the error quoted from this check. Only those values of $j$ that are used in the analysis are shown.

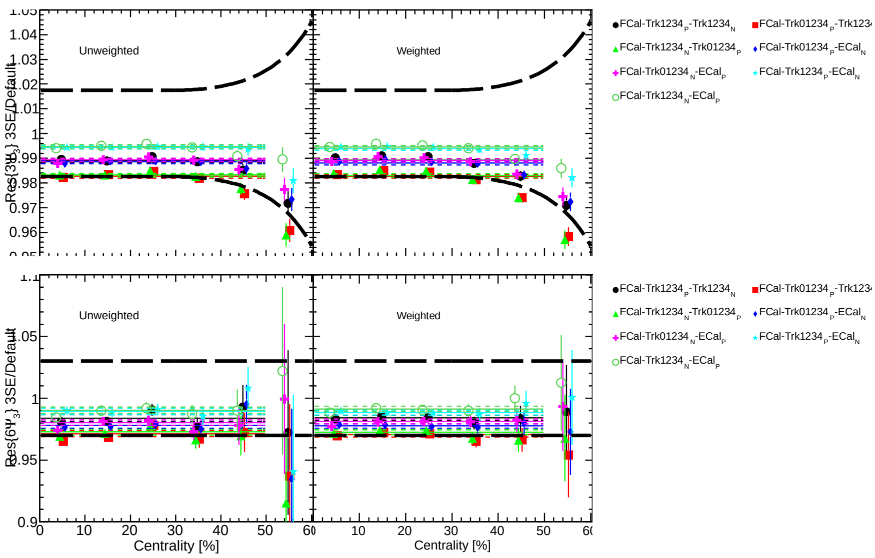


Figure 110: Same as previous plot but for Res$\{j3\Psi_3\}$(for FCal)

Not reviewed, for internal circulation only

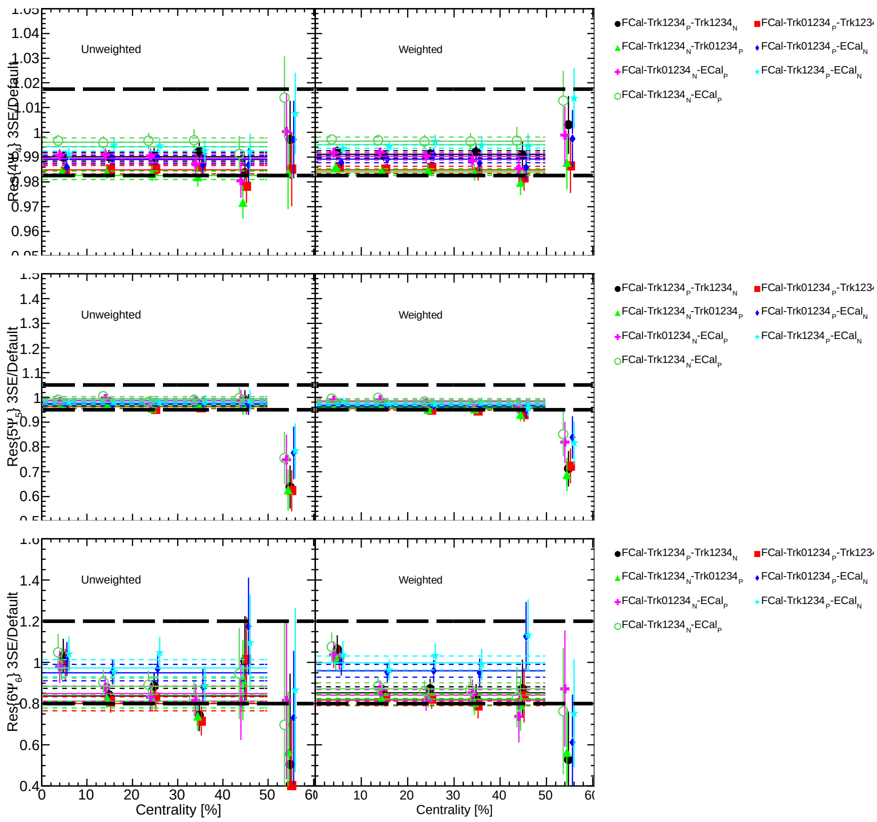

Figure 111: Same as previous plot but for Res{4$\Psi_4$} (Top) Res{5$\Psi_5$} (Middle) and Res{6$\Psi_6$} (Bottom) (for FCal)

## 10.3 Uncorrelated errors

It is clear from the plots in the previous section, that the errors for the Unweighted and Weighted single-plane resolutions are strongly correlated. To estimated the uncorrelated errors, a double ratio is made as in the two-plane case. The double-ratios and corresponding uncorrelated systematic errors are shown in the right panels of Figs. 112-114 for the ECal$_{\mathrm{P/N}}$ and in Figs. 115-117 for the FCal. The left panels in these plots show the Unweighted and Weighted 3SE/Default ratios that were plotted in Figs.106-111.

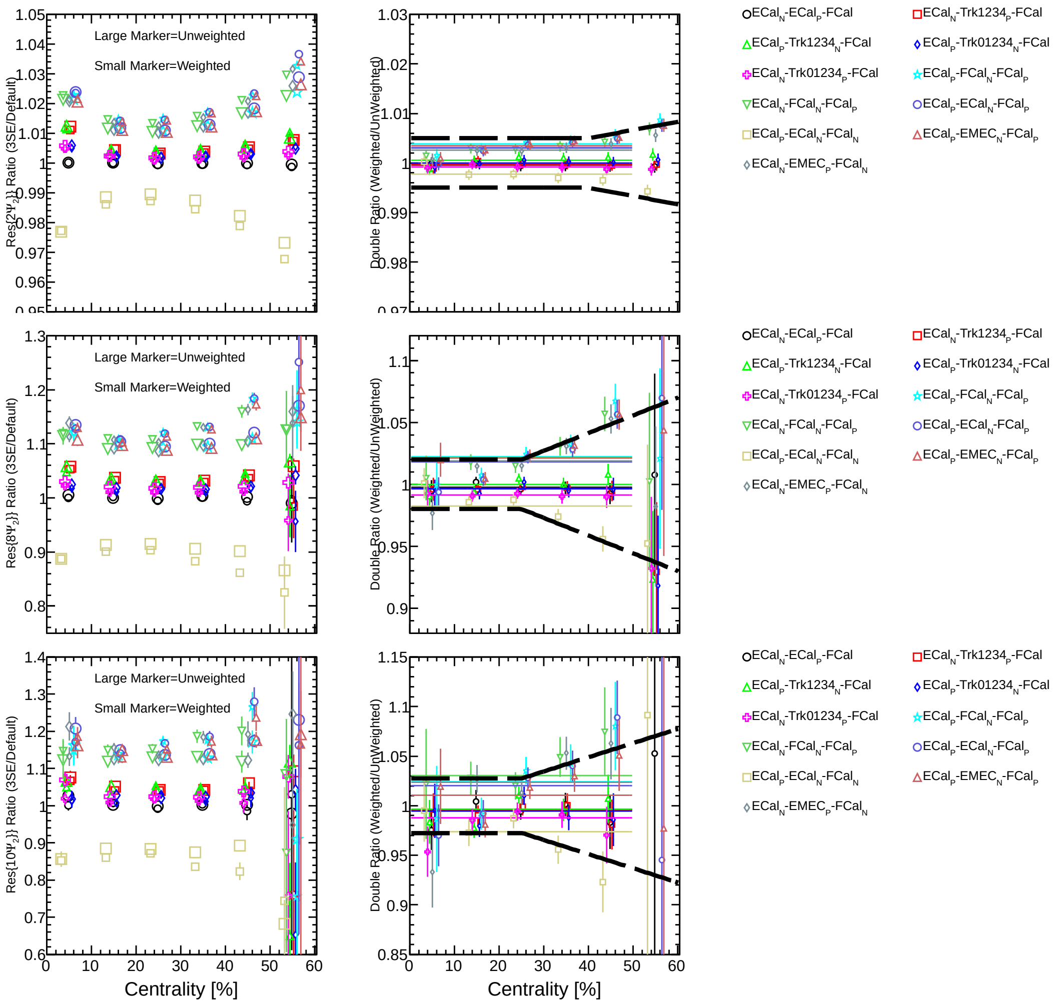


Figure 112: Left plot: The ratio between the 3SE and Default resolutions for the unweighted (hollow) and weighted (solid) resolutions for Res$\{j2\Psi_2\}$ for $ECal_{P/N}$, the larger (smaller) markers correspond to the Unweighted (Weighted) case. The right plot shows the double ratio for the weighted/unweighted. This double ratio is used to estimate the uncorrelated systematic errors between the weighted and unweighted case indicated by the thick dashed line. The colored horizontal lines show the mean deviations in the (10-50)% centrality interval for the individual double-ratios.

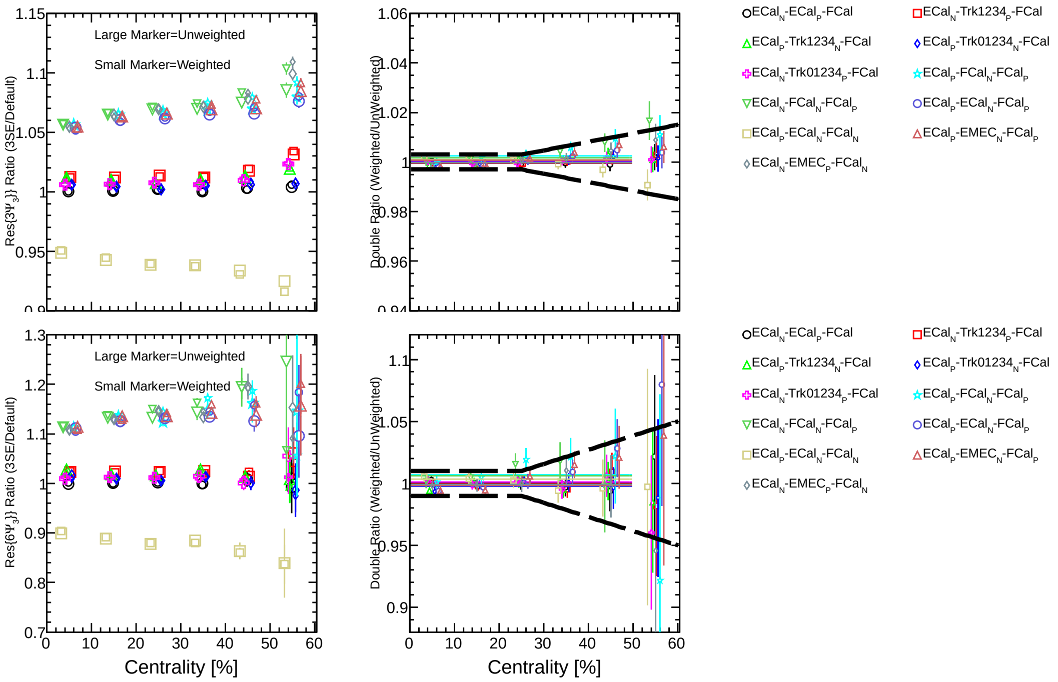

Figure 113: Same as previous plot but for Res$\{j3\Psi_3\}$ for $ECal_{P/N}$.

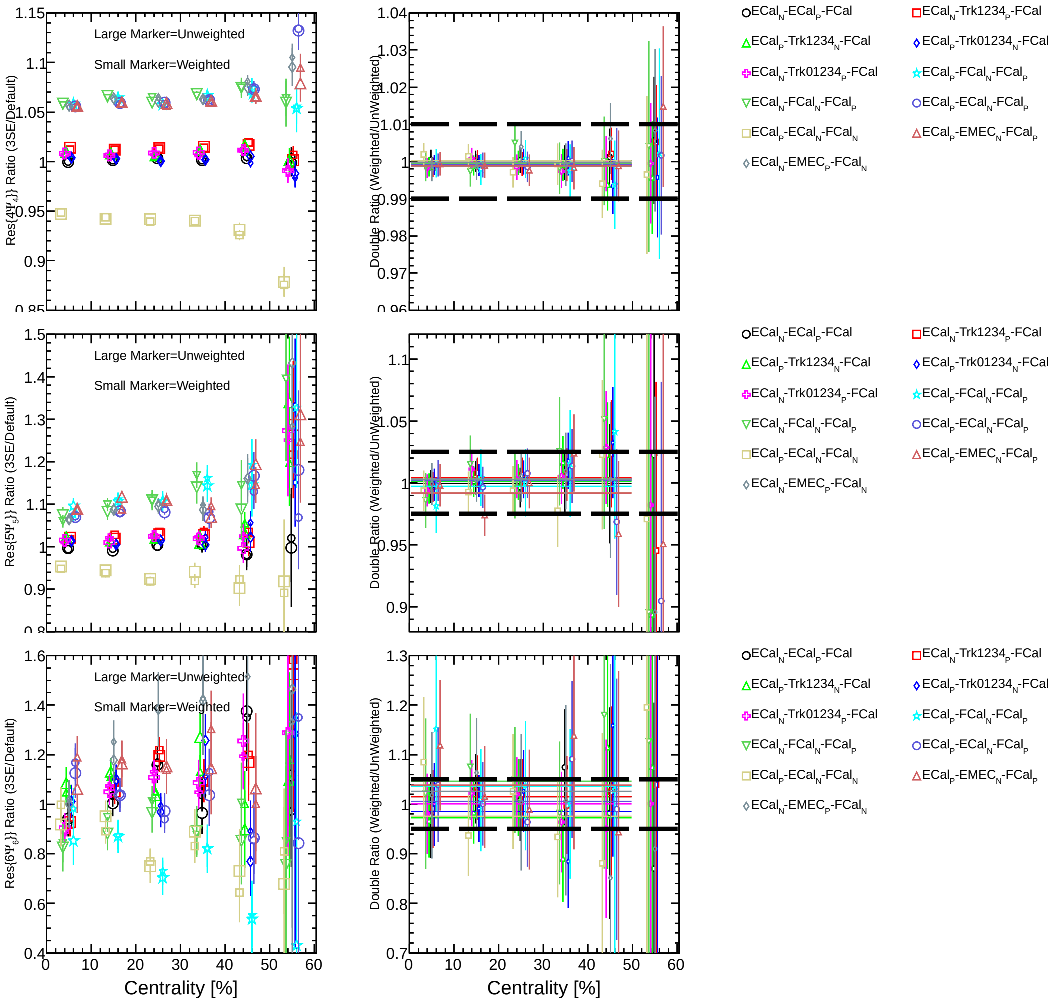


Figure 114: Same as previous plot but for Res{$4\Psi_4$} (Top), Res{$5\Psi_5$}(Middle) and Res{$6\Psi_6$} (Bottom) for $ECal_{P/N}$.

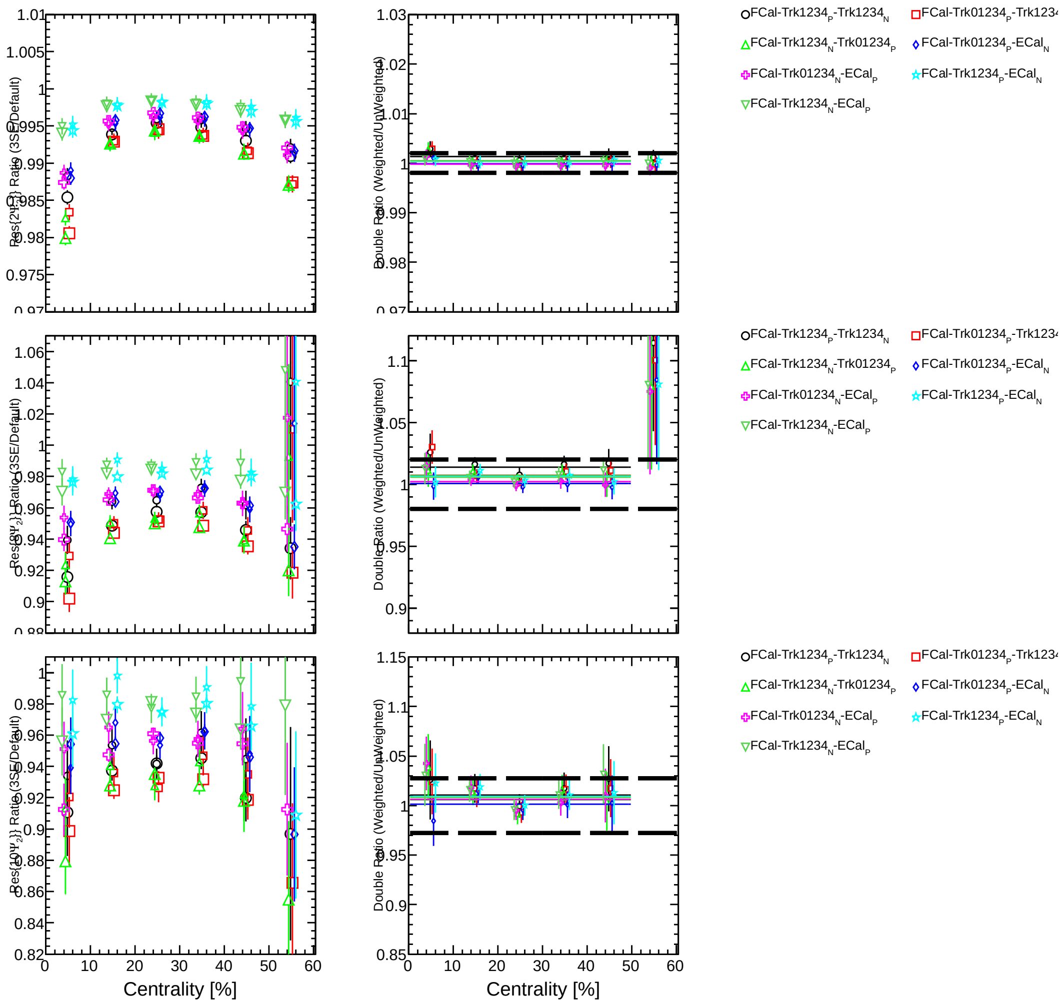


Figure 115: Left plot: The ratio between the 3SE and Default resolutions for the unweighted (hollow) and weighted (solid) resolutions for $\mathrm{Res}\{j2\Psi_2\}$ for $FCal$, the larger (smaller) markers correspond to the Unweighted (Weighted) case. The right plot shows the double ratio for the weighted/unweighted. This double ratio is used to estimate the uncorrelated systematic errors between the weighted and unweighted case indicated by the thick dashed line. The colored horizontal lines show the mean deviations in the (10-50)% centrality interval for the individual double-ratios.

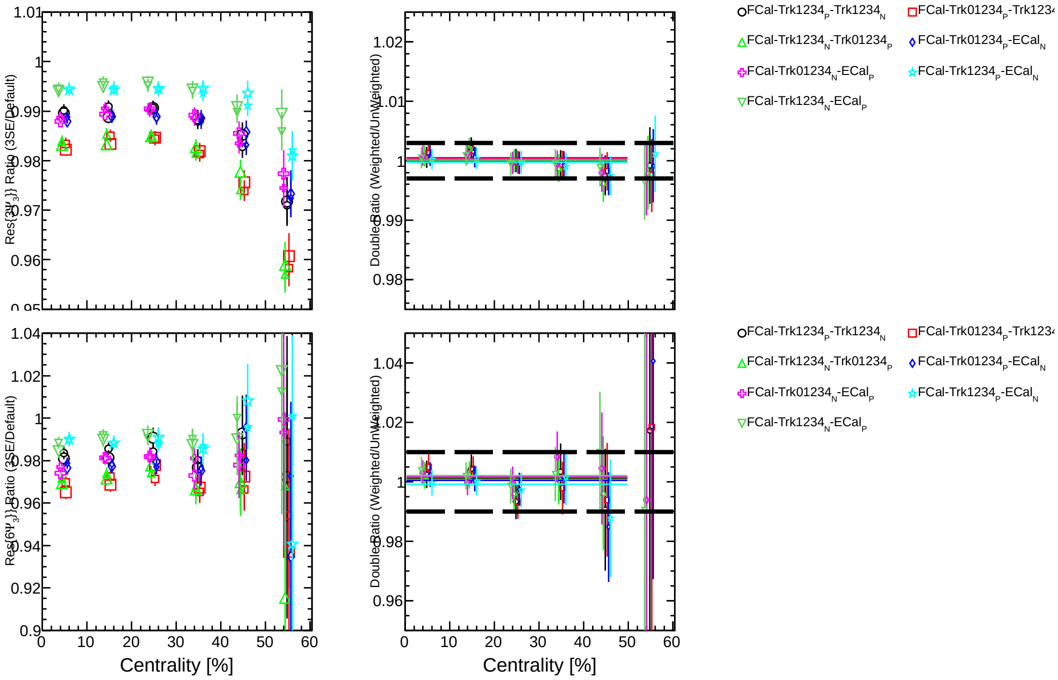


Figure 116: Same as previous plot but for Res$\{j3\Psi_3\}$ for *FCal*.

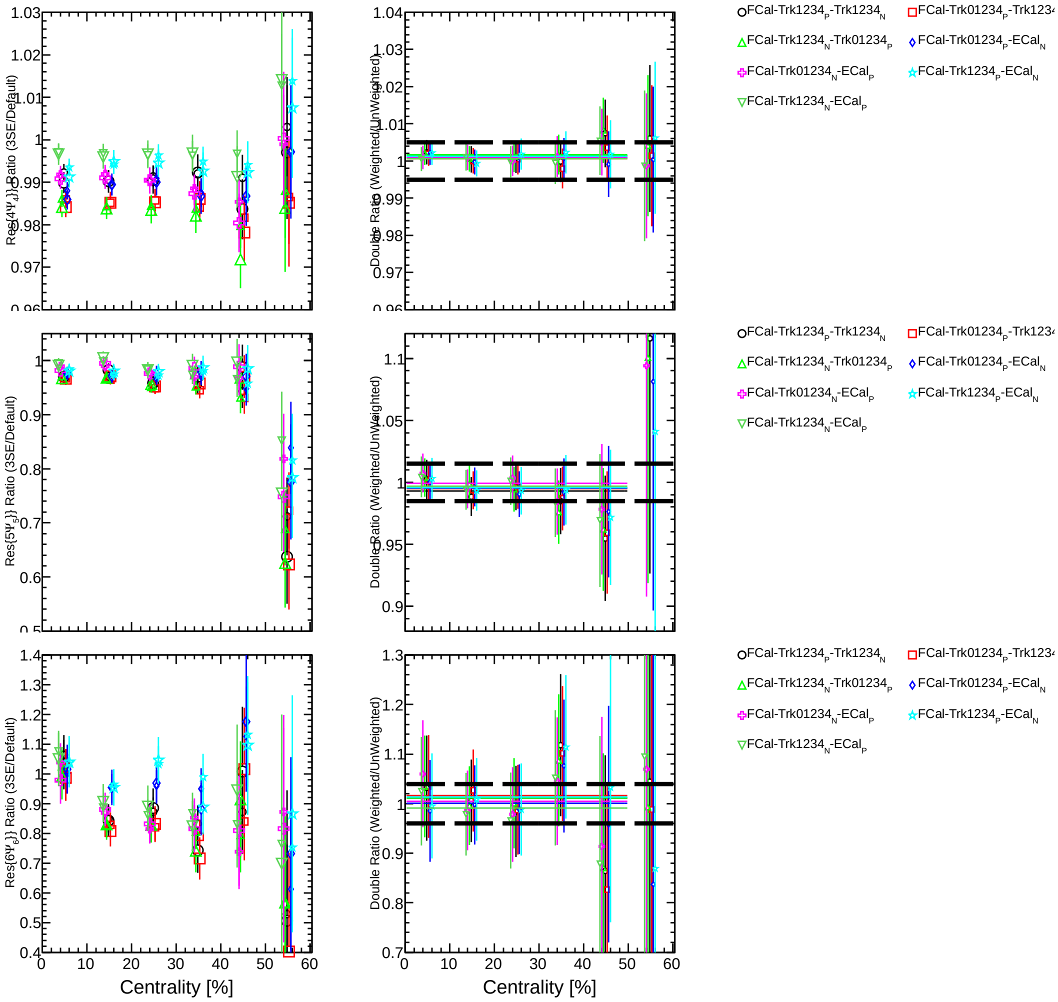


Figure 117: Same as previous plot but for Res{$4\Psi_4$} (Top), Res{$5\Psi_5$}(Middle) and Res{$6\Psi_6$} (Bottom) for *FCal*.

## 10.4 Corrected correlations

Fig. 118 shows the raw correlators, combined resolution and corrected correlator as a function of centrality. These three independent estimates are then combined to get the final results. While combining the three measurements, they are weighted by $1/(stat\ err)^2$. The final systematic errors are also weighted averages of the individual systematic errors (again weighted by $1/(stat\ err)^2$). Further the spread between the three estimates is taken as another source of systematic error, and added in quadrature (to the already calculated systematic error). The final plots are shown in the next section as a function of $\langle N_{\mathrm{part}}\rangle$.

Table 17 lists the errors for the weighted correlations. The errors are identical to the unweighted correlations as discussed in in the last section. Table 18 lists the relative errors for the weighted to unweighted single-plane resolutions. Some of the relative errors have centrality dependence (eg. Fig. 112) and this is listed in Table 18. The relative errors for the combined resolutions are obtained by adding these single-plane uncertainties in quadrature.

| Error for Res$\{jn\Psi_n\}$ | | | | | |
|---|---|---|---|---|---|
| n | 2 | 3 | 4 | 5 | 6 |
| Detector A&C | 1.1, 10.0, 13.0% (j=1,4,5) | 6.0, 12.0% (j=1,2) | 6.0% (j=1) | 10.0% (j=1) | 13.0 (j=1) |
| Detector B | 0.7, 5.0, 7.0% (j=1,4,5) | 1.75, 3% (j=1,2) | 1.75% (j=1) | 5.0% (j=1) | 20% (j=1) |

| Error for three-plane correlators: $\langle\cos(\sum\Phi)\rangle$ | | | | | | | | | |
|---|---|---|---|---|---|---|---|---|---|
| $\sum\Phi$ | $2\Phi_2+3\Phi_3-5\Phi_5$ | | | $2\Phi_2+4\Phi_4-6\Phi_6$ | | | $2\Phi_2-6\Phi_3+4\Phi_4$ | | |
| | Type-1 | Type-2 | Type-3 | Type-1 | Type-2 | Type-3 | Type-1 | Type-2 | Type-3 |
| Combined resolution | 11.7% | 10.2% | 7.9% | 20.9% | 20.1% | 20.9% | 13.4% | 7.8% | 12.2% |
| raw distribution ($\times10^{-4}$) | 2-10 | | | | | | | | |
| | $-8\Phi_2+3\Phi_3+5\Phi_5$ | | | $-10\Phi_2+4\Phi_4+6\Phi_6$ | | | $-10\Phi_2+6\Phi_3+4\Phi_4$ | | |
| | Type-1 | Type-2 | Type-3 | Type-1 | Type-2 | Type-3 | Type-1 | Type-2 | Type-3 |
| Combined resolution | 12.7% | 14.3% | 12.7% | 22.1% | 23.9% | 24.6% | 15.1% | 14.6% | 17.8% |
| raw distribution ($\times10^{-4}$) | 2-10 | | | | | | | | |

Table 17: Summary of systematic uncertainties for individual Res$\{jn\Psi_n\}$ terms (top part) and the final three-plane correlators (bottom part).

| Relative errors for Res$\{jn\Psi_n\}$ (Weighted vs Unweighted) | | | | | |
|---|---|---|---|---|---|
| n | 2 | 3 | 4 | 5 | 6 |
| Det A&C | $0.5+\Theta(cent-40)\times0.5/30$ (j=1)<br>$2.0+\Theta(cent-25)\times5.0/35$ (j=4)<br>$2.75+\Theta(cent-25)\times5.0/35$ (j=5) | $0.3+\Theta(x-25)\times1.2/35$ (j=1)<br>$1.0+\Theta(x-25)\times4.0/35$ (j=2) | 1.5 (j=1) | 2.5 (j=1) | 5.0 (j=1) |
| Det B | 0.2, 2.0, 2.75 (j=1,4,5) | 0.3, 1.0 (j=1,2) | 0.5 (j=1) | 1.5 (j=1) | 4.0 (j=1) |

Table 18: Summary of relative systematic uncertainties in percent for individual Res$\{jn\Psi_n\}$ terms for the weighted vs unweighted single-plane resolutions. Some of the uncertainities have centrality dependence (eg. Fig. 112) described by the function $\Theta(cent-cent_0)$, where *cent* is the centrality (in percentile) and $\Theta(x)=x\times H(x)$, where $H(x)$ is the step function.

Not reviewed, for internal circulation only

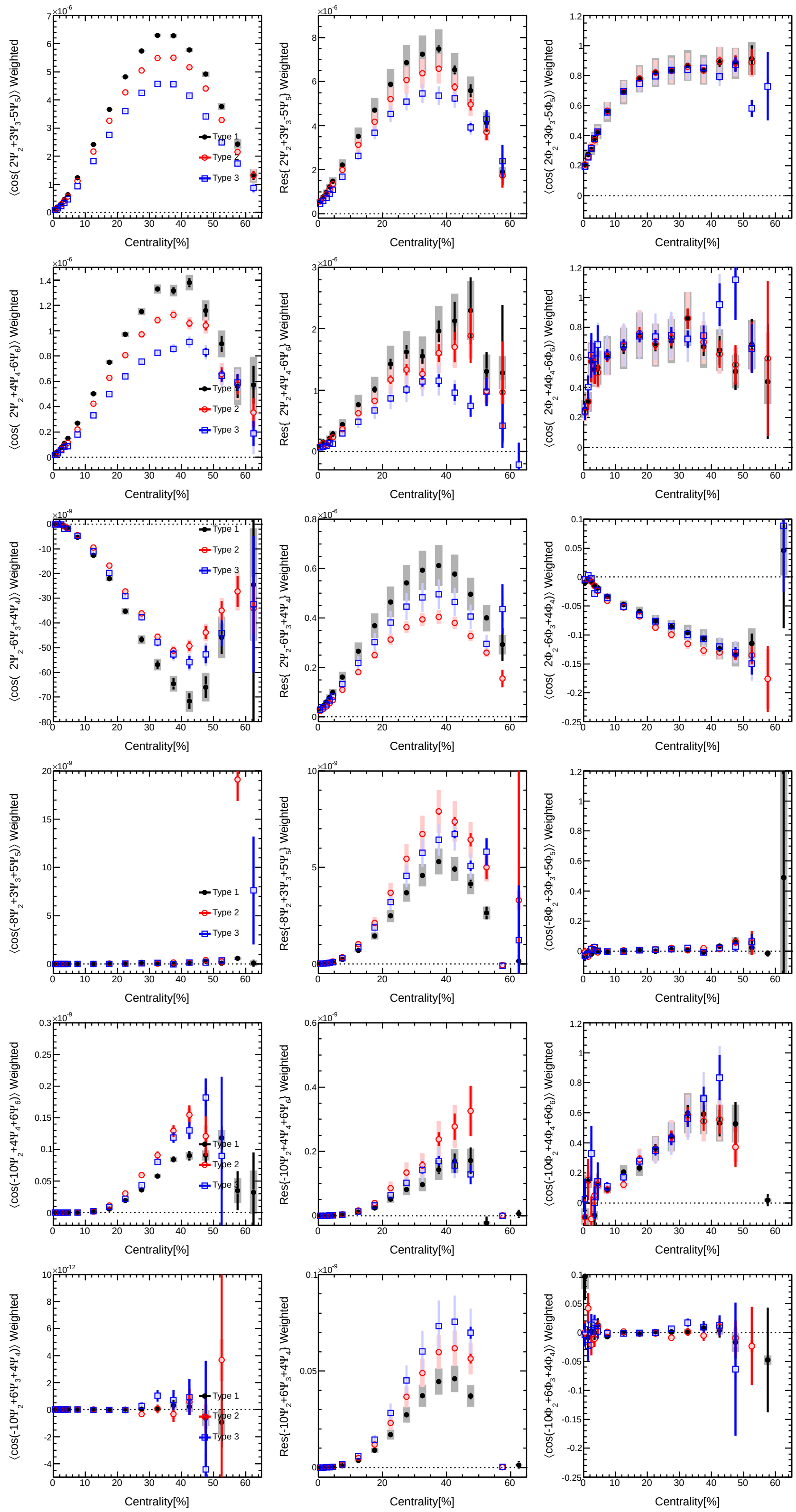

Figure 118: The raw signals (left plots), combined resolution corrections (middle plots) and corrected correlations (right plots) for the 3P correlators. The three sets of data points correspond to the three Types.

## 10.5 Final Plots

Figure 119 shows the final 3P correlations for the weighted and unweighted case obtained by combining the three independent estimates of the correlators. The Weighted correlators have quite similar centrality dependence as the Unweighted correlators. Fig. 120 shows the ratio of the weighted to the unweighted correlators for the four non-zero correlators. It can be seen that the $\langle\cos(2\Phi_2 + 3\Phi_3 + 5\Phi_5)\rangle$, $\langle\cos(2\Phi_2 + 4\Phi_4 - 6\Phi_6)\rangle$ and $\langle\cos(2\Phi_2 - 6\Phi_3 + 4\Phi_4)\rangle$ correlators the weighted and unweighted correlators are nearly identical. This can be understood from the fact that for these three correlators the $Q$ vectors are not raised to very high powers in the weighting.

Figures. 121 and 122 show the comparison of the Unweighted and weighted correlators measured by the default detectors to the measurements based on the tracking detectors. For the tracking detectors, the analysis is done in Appendix-II. The two measurements are very consistent in all cases except for the 2-4-6 correlators where the tracking detector results are larger than the Calorimeter based results. But even here, the results agree within systematic errors.

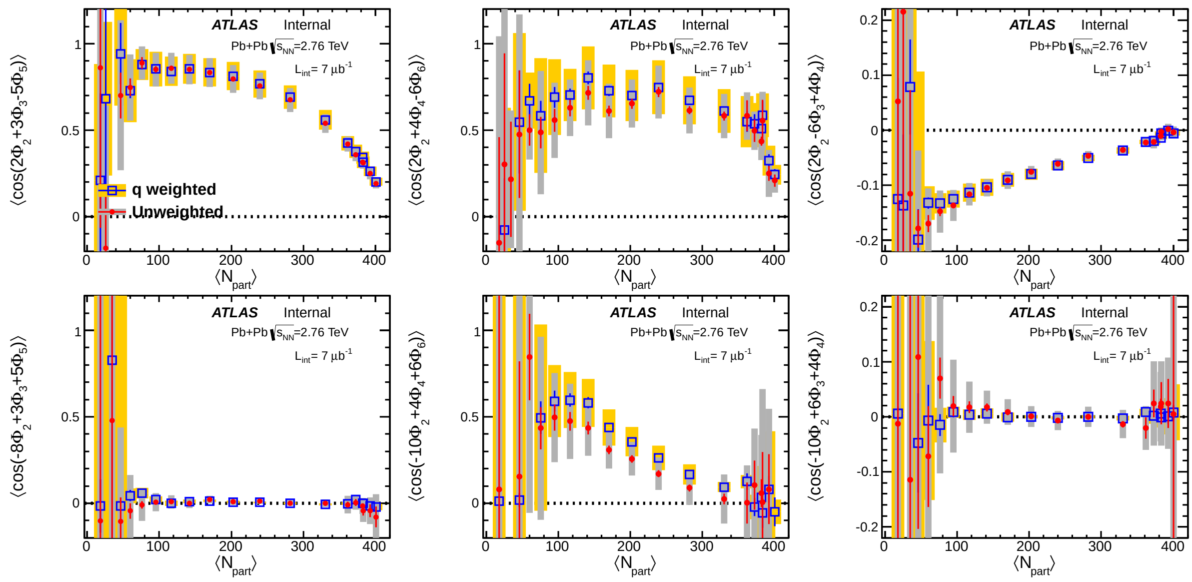


Figure 119: The corrected Unweighted and Weighted three-plane correlators.

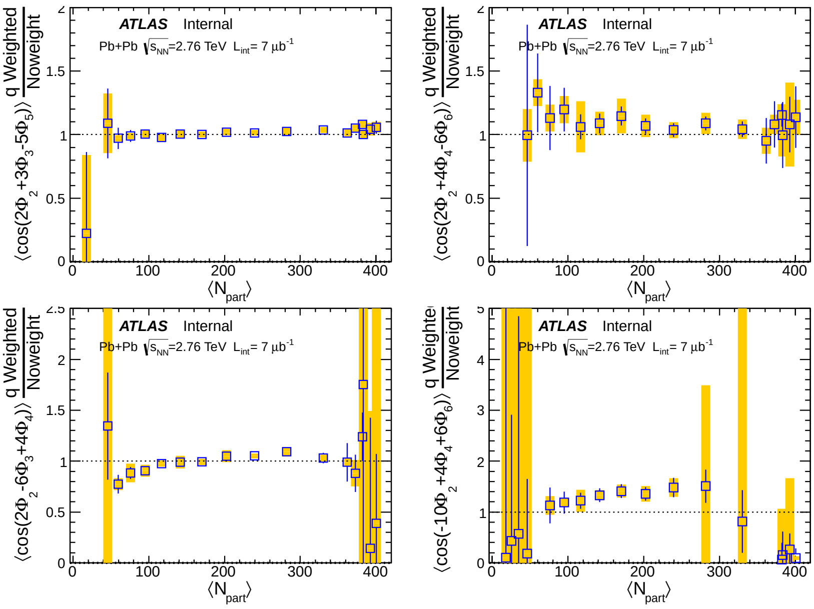

Figure 120: The Ratio of the corrected Weighted to the corrected Unweighted three-plane correlators.

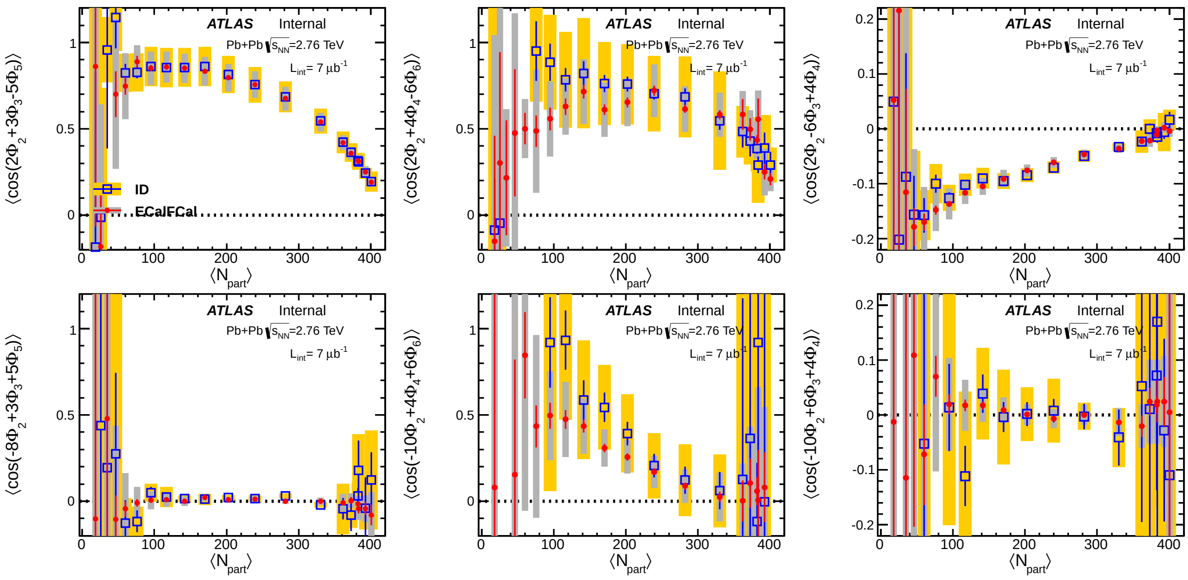

Figure 121: The corrected Unweighted three-plane correlators compared between the Calorimeter (Default) based results and the Tracking detector based results.

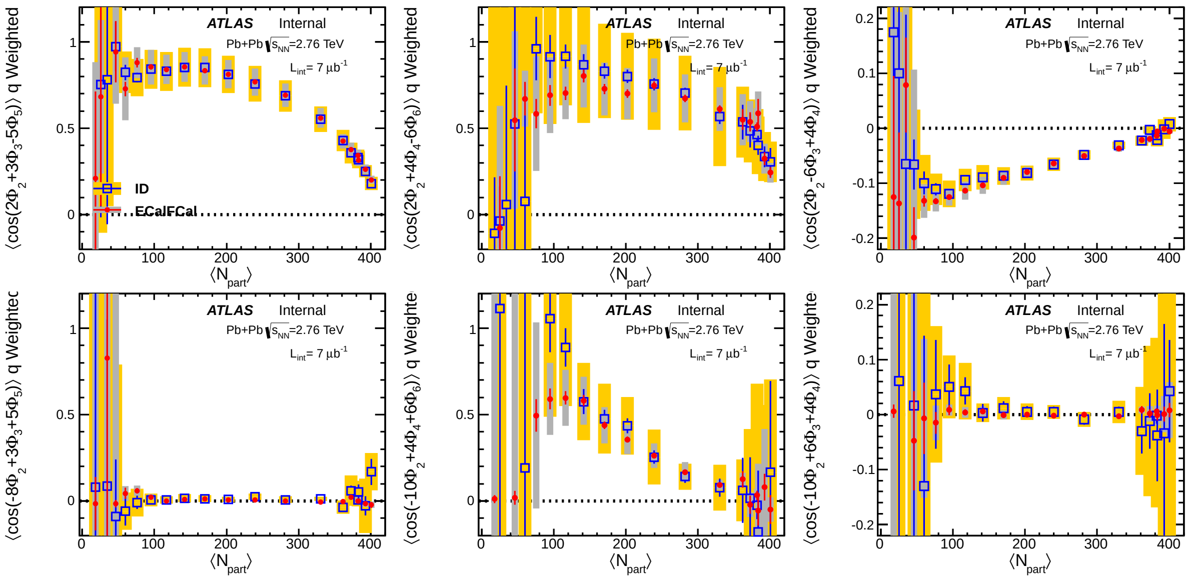


Figure 122: The corrected Weighted three-plane correlators compared between the Calorimeter (Default) based results and the Tracking detector based results.

# 11 Appendix-I : Two-plane corrselations from tracking detectors

The two-plane correlation analysis using the tracking dectors is done with symmetric detectors covering $\eta \in \pm(0.5, 2.5)$. Tracks with $p_T \in$(0.5,10.0) GeV are used (See Table 4).

## 11.1 Raw Correlations

Fig. 123 shows the centrality dependence of the raw correlations (unweighted case) as obtained from the ID. The systematic errors are obtained from $\langle \sin \rangle$ and $\langle \cos_{bg} \rangle$ terms (as with the ECal case).

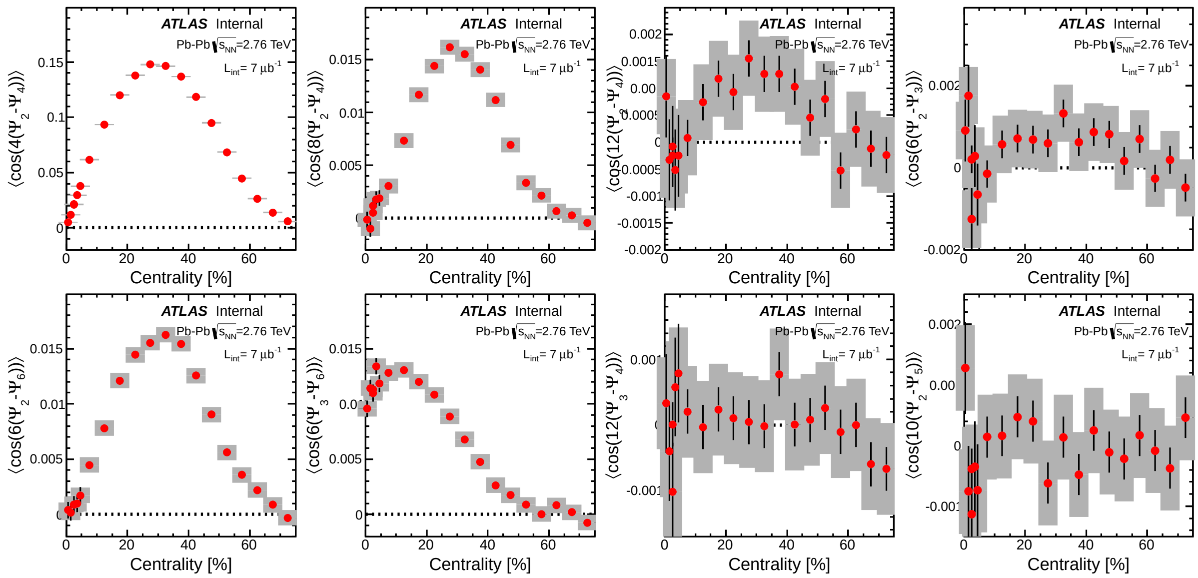


Figure 123: The Unweighted $\langle \cos jk(\Psi_n - \Psi_m) \rangle$ as measured using the ID as a function of centrality.

## 11.2 Resolutions

Figure 124 shows the single plane-resolutions for the tracking detectors (unweighted case). The systematic resolutions are determined using as usual the sine terms in the 2SE correlations as well as several 3SE checks. Fig. 125 shows the combined resolution for the two-plane corrs as measured by the ID for the unweighted case, obtained by multiplying the single-plane resolutions in Fig. 124. The contributions from the sine-terms relative to the cosine terms are shown in Fig. 126. No systematic sine terms are seen. and the error from this term are ignored in the final results (given that the 3SE errors are large, the sine terms in any case woule be negligible). The 3SE checks are shown in Figs 127-131 (See Table 4 for description of the detectors used in the 3SE checks). For $n$=2, the weighted and unweighted cases have somewhat larger differences for the 3SE checks and unlike the ECal case, different errors are assigned to the weighted and unweighted resolutions. The final errors for the raw signals and the resolutions are listed in Table 19.

| Error for Res$\{jn\Psi_n\}$ | | | | | |
|---|---|---|---|---|---|
| n | 2(unweighted,weighted) | 3 | 4 | 5 | 6 |
| 3SE comparison | 2.8%, 4.0% ($j$=2)<br>5.0%, 7.0% ($j$=3)<br>7.0%, 11.0% ($j$=4)<br>10.0%, 14.0% ($j$=5)<br>15.0%, 19.0%($j$=6) | 6.0 $j$% | 6.0 $j$% ($j$=1)<br>7.0 $j$% ($j$ >1) | 8.0 $j$% | 25.0 $j$% |

| Error for $\langle\cos jk(\Phi_n - \Phi_m)\rangle$ correlators | | | | | | | | |
|---|---|---|---|---|---|---|---|---|
| (j,n,m) | (1,2,4) | (2,2,4) | (3,2,4) | (1,2,3) | (1,2,6) | (1,3,6) | (1,3,4) | (1,2,5) |
| Res$\{jk(\Psi_n - \Psi_m)\}$(Unweighted) | 6.6% | 15.6% | 25.8% | 13.0% | 25.5% | 27.7% | 31.9% | 18.9% |
| Res$\{jk(\Psi_n - \Psi_m)\}$(Weighted) | 7.5% | 17.8% | 28.3% | 13.9% | 25.9% | 27.7% | 31.9% | 21.2% |
| Raw distribution<br>from sine and mixed-events<br>(absolute error on raw $\times 10^{-4}$)<br>(Unweighted, Weighted) | 7,15 | 7,15 | 7,15 | 7,15 | 7,15 | 7,15 | 7,15 | 7,15 |

Table 19: (top table) summary of sources of systematic uncertainties for individual Res$\{jn\Psi_n\}$ terms coming from 2SE/3SE comparision (Figs. 127-131). For $n$=2 the weighted and unweighted resolutions are assigned different systematic errors from the 3SE checks. (bottom table) summary of sources of systematic uncertainties for the final correlators $\langle\cos jk(\Phi_n - \Phi_m)\rangle$, including those for the combined resolution caculated from Res$\{jn\Psi_n\}$ terms, and the raw correlations.

Not reviewed, for internal circulation only

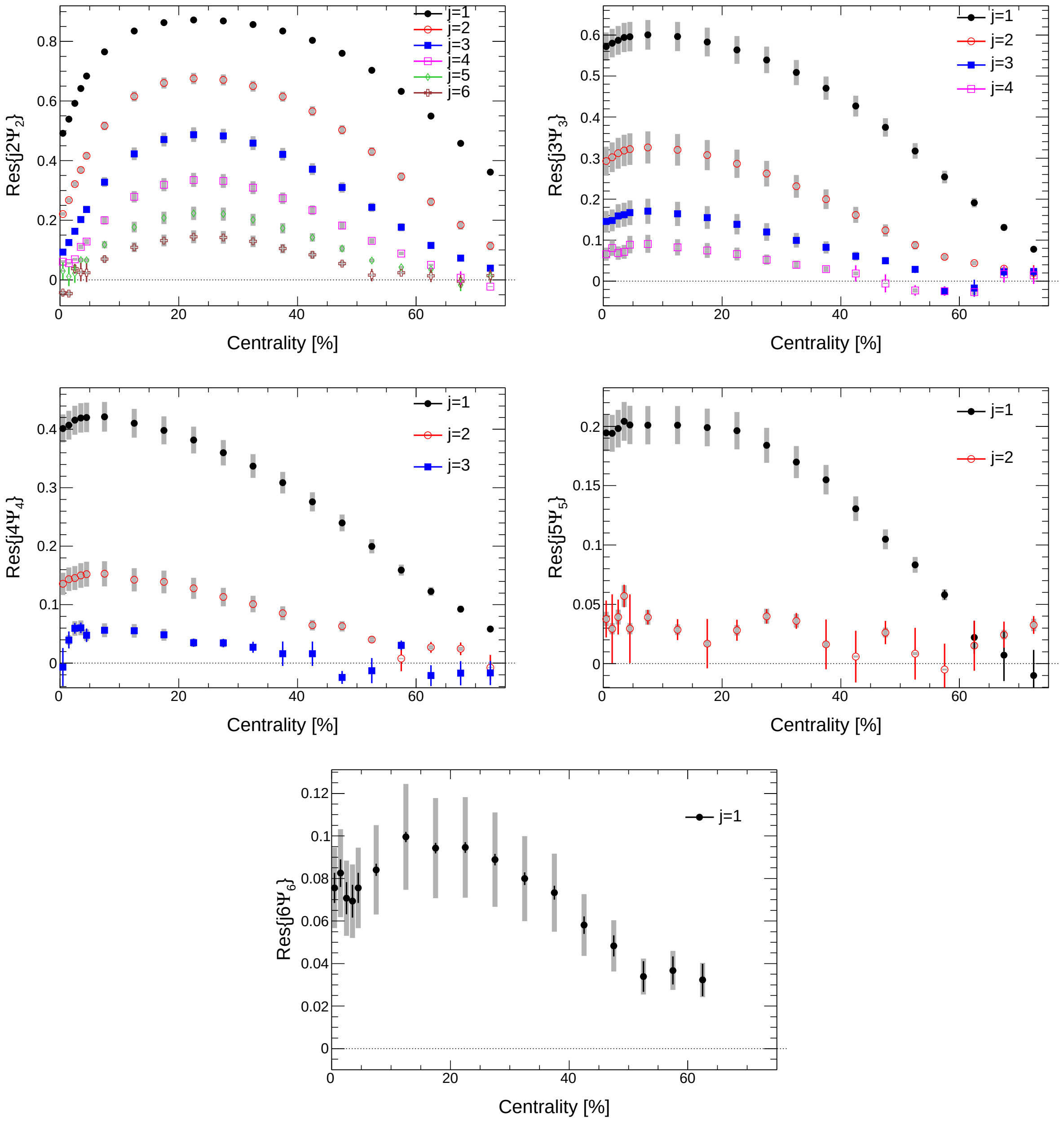


Figure 124: Summary of the event-plane resolution Res$\{jn\Psi_n\}$ and associated systematic uncertainties for n=2-6 and different values of $j$.

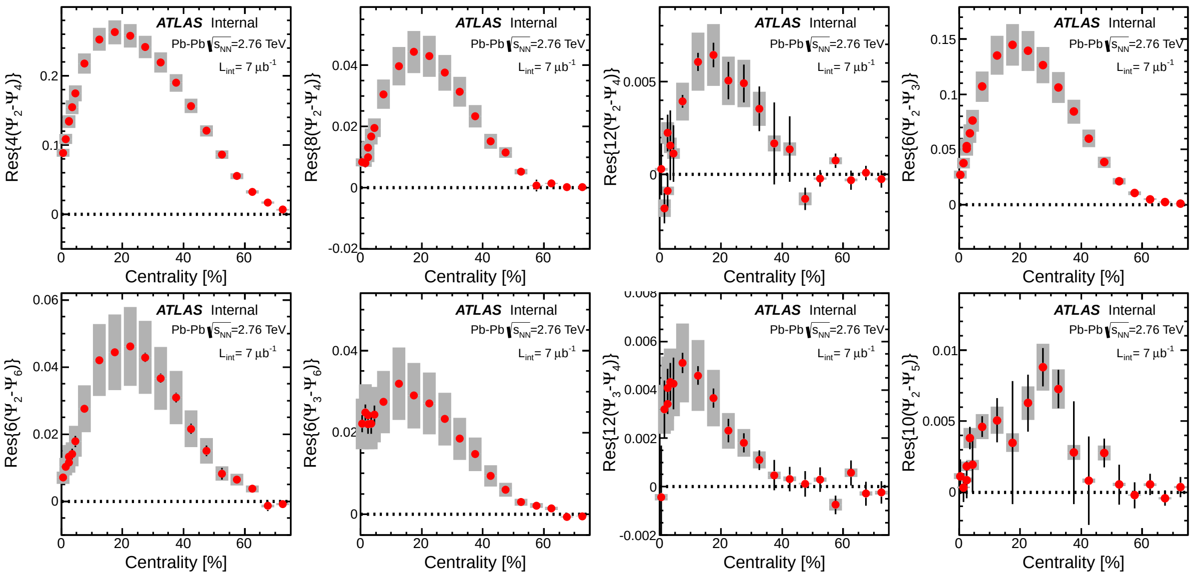


Figure 125: The Unweighted Res($jk(\Psi_n - \Psi_m)$) as measured using the ID as a function of centrality.

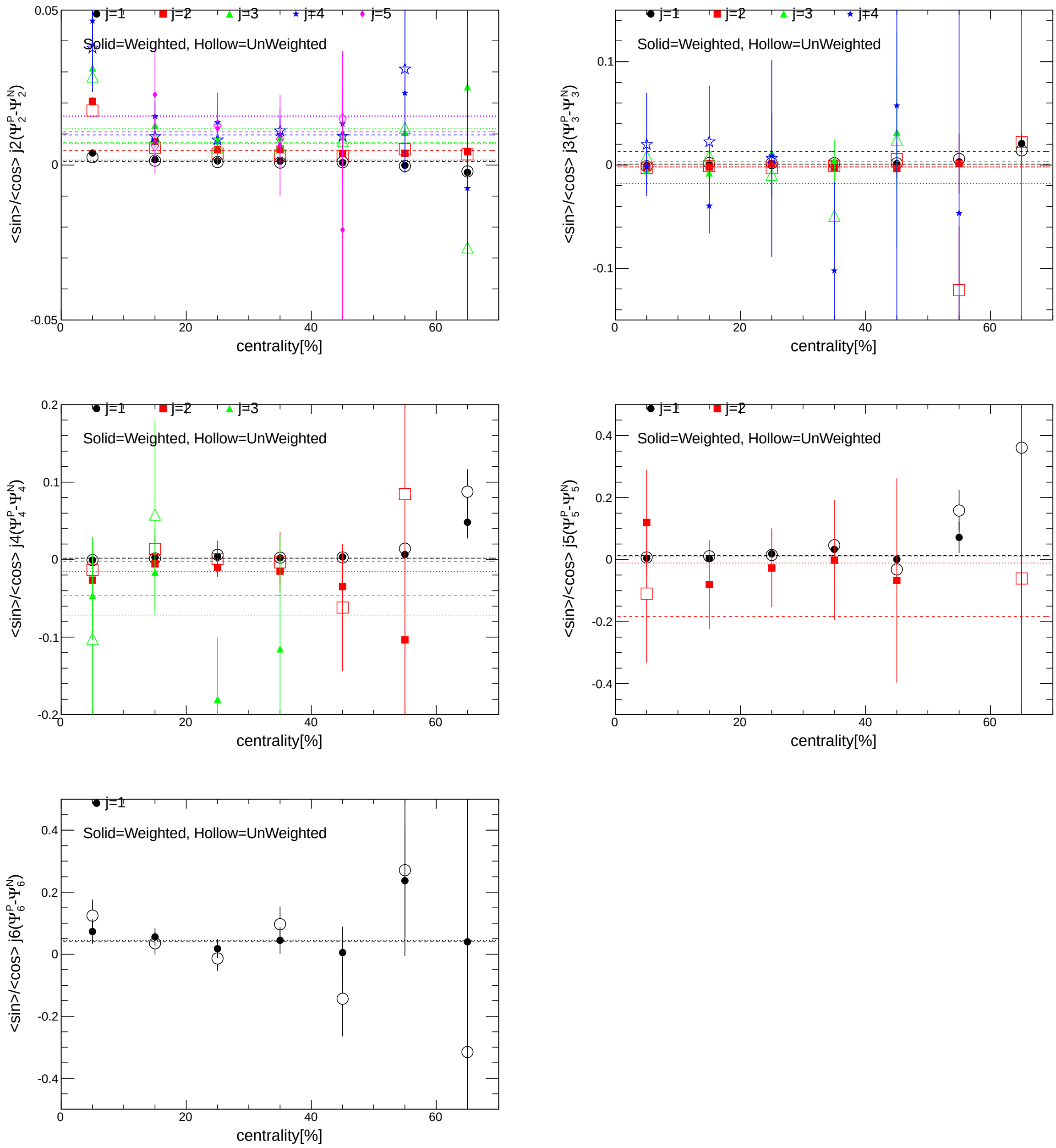


Figure 126: The $\langle \sin \rangle$ terms obtained in the two-subevent angle differences $jn(\Psi_n^P - \Psi_n^N)$ relative to the $\langle \cos \rangle$ terms, as a function of centrality for different $j$. Both weighted and unweighted cases are shown. Only those values of $j$ that are used in the analysis are shown. The fine-dashed (long-dashed) lines show the mean value of the ratio for the weighted (Unweighted) case in the (0-50)% centrality interval .

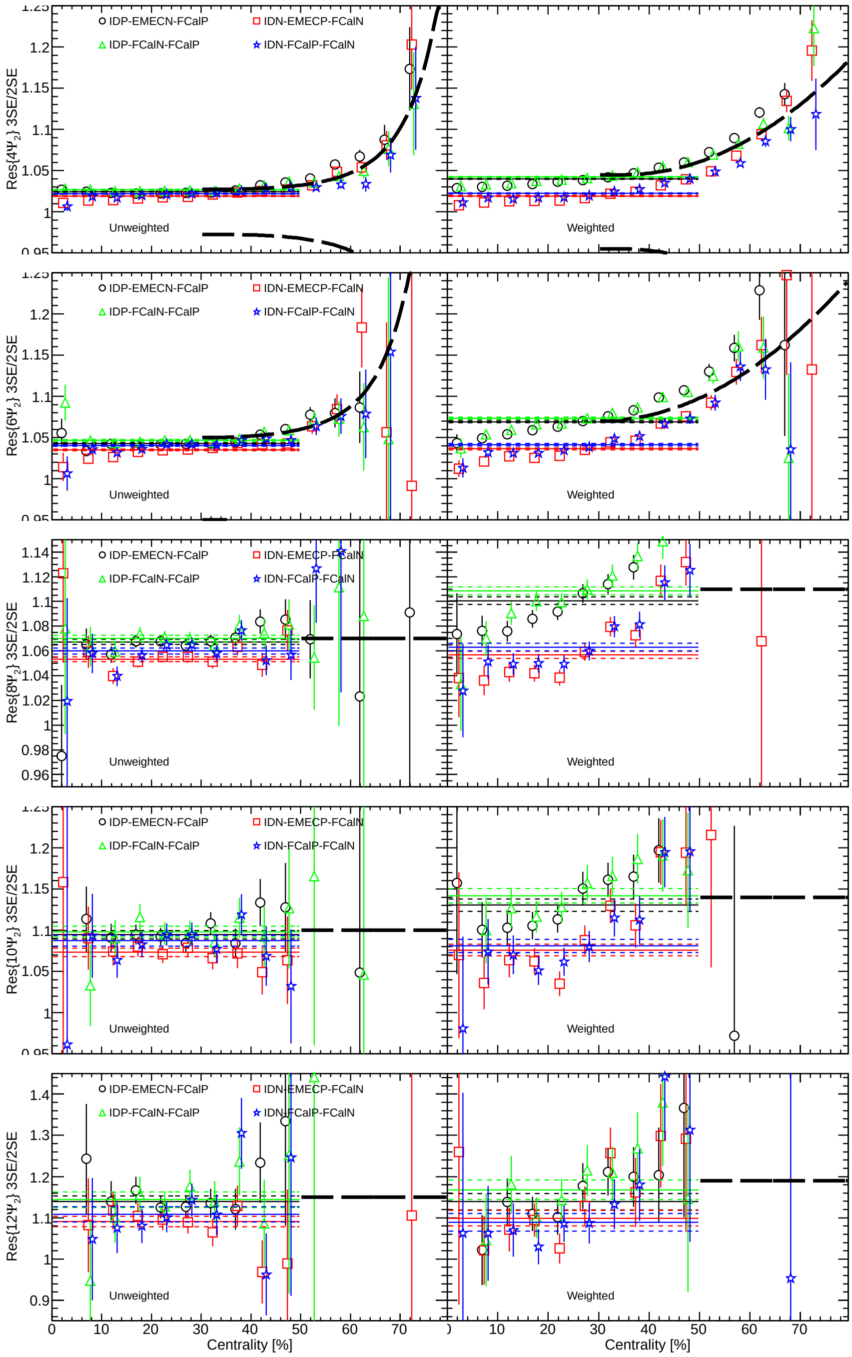


Figure 127: The ratio of the resolution for the ECalFCal$^{P/N}$ obtained from several three-subevent checks to the default two-subevent resolution for Res$\{j2\Psi_2\}$ as a function of centrality. From top to bottom the plots correspond to different values of $j$. The left (right) plots correspond to the Unweighted (Weighted) case. The colored-continuous lines show the mean deviation of the 3SE value from the default 2SE value in the (10-50)% centrality range, while the dashed-colored lines show the error of the mean deviation. The thick-dashed black lines show the error quoted from this check. Only those values of $j$ that are used in the analysis are shown.

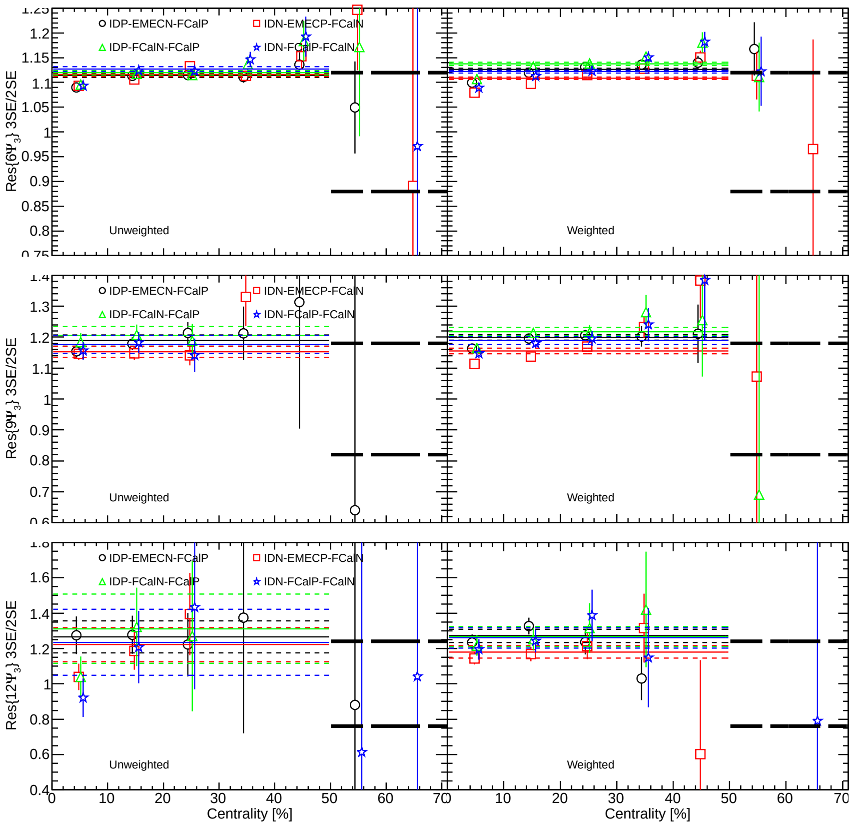


Figure 128: Same as previous plot but for Res$\{j3\Psi_3\}$ for $j$=1-4.

Not reviewed, for internal circulation only

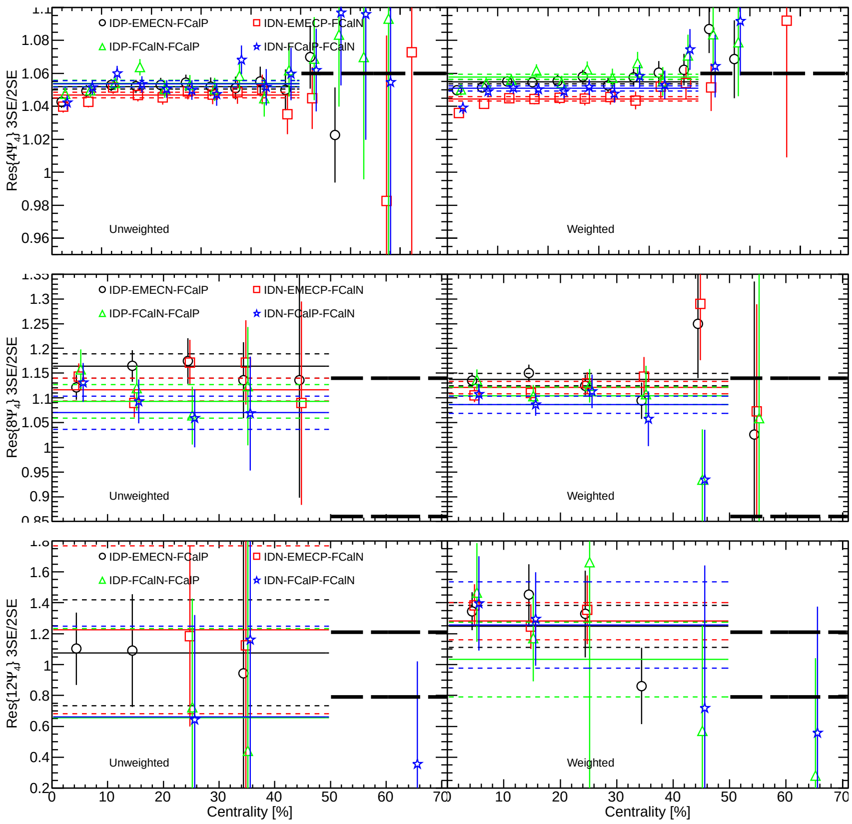


Figure 129: Same as previous plot but for Res$\{j4\Psi_4\}$.

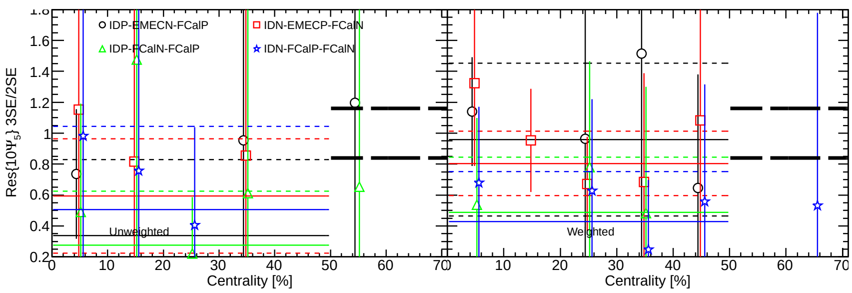


Figure 130: Same as previous plot but for Res$\{j5\Psi_5\}$.

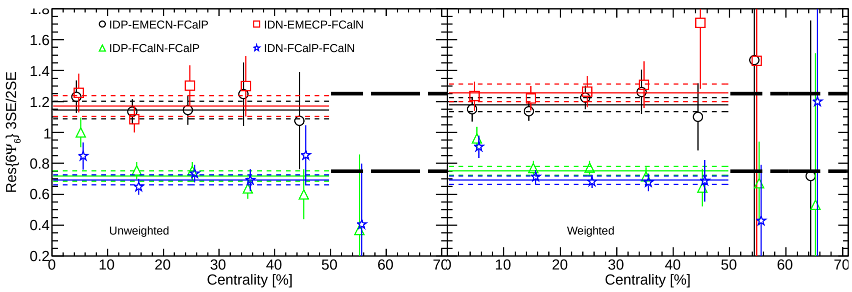


Figure 131: Same as previous plot but for Res$\{6\Psi_6\}$.

### 11.2.1 Final Plots

Fig. 132 and 133 show the final corrected two-plane correlators measured by the ID for the weighted and unweighted cases respectively. The systematic errors were listed in Table 19

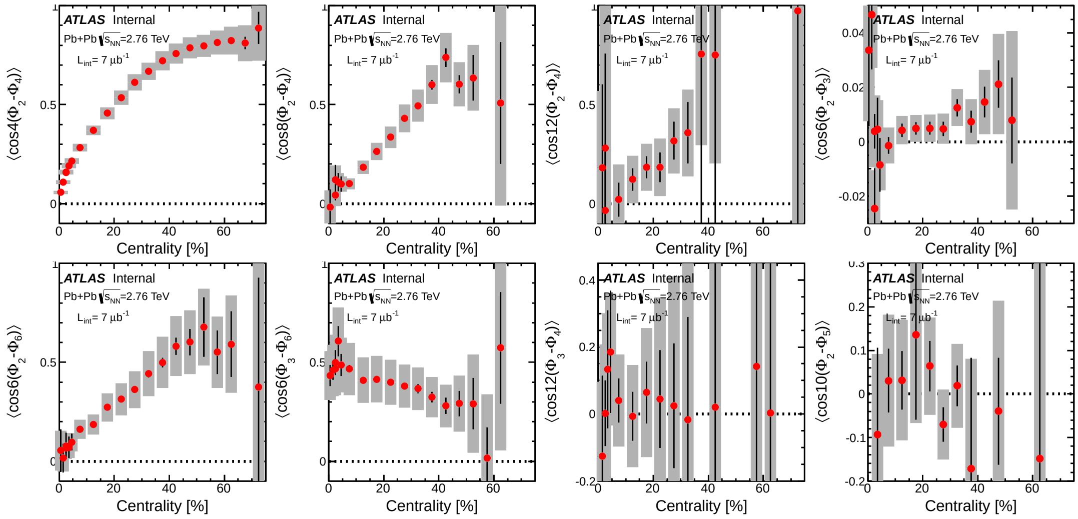


Figure 132: The centrality dependence of the Unweighted two-plane correlation results in fine centrality intervals for eight cases of $\langle \cos k\,(\Phi_n - \Phi_m)\rangle$ measured by the ID

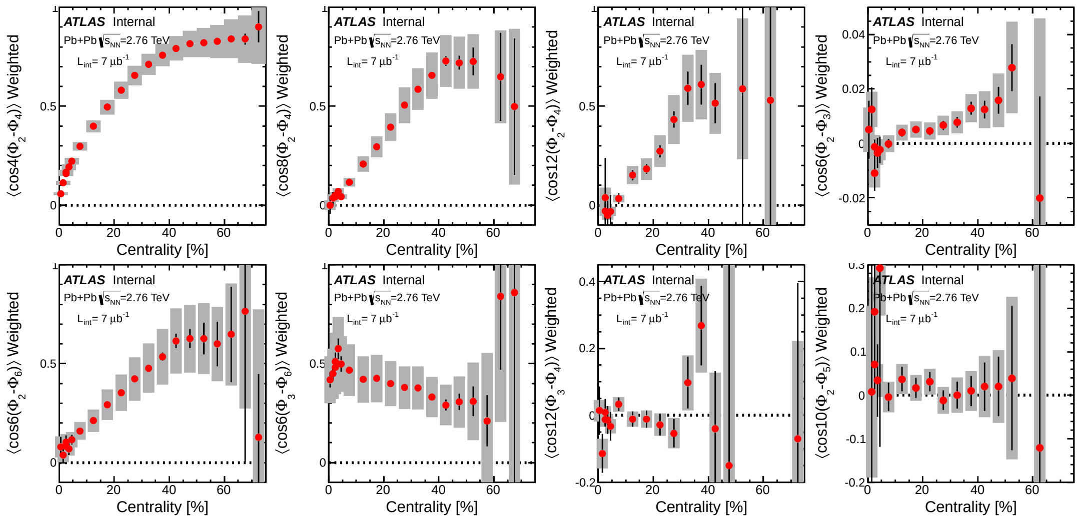


Figure 133: The centrality dependence of the Weighted two-plane correlation results in fine centrality intervals for eight cases of $\langle \cos k\,(\Phi_n - \Phi_m)\rangle$ measured by the ID

# 12 Appendix-II : Three-plane correlations from tracking detectors

The three-plane correlation analysis using the tracking dectors is done with two symmetric detectors covering $\eta \in \pm(1.5, 2.5)$ (Dets $A$ and $C$) and the third detector covering $\eta \in (-0.5, 0.5)$ (Det $B$). Tracks with $p_{\mathrm{T}}$ ∈(0.5,10.0) GeV are used. As with the Calorimeter based results, There are three independent estimated of the correlations which are then combined into one result. The three independent measurements are shown in Figs 134 and 135 for the unweighted and weighted corrs respectively. Table 20 lists the systematic errors for the three independent estimates of the correlations (for both the weighted and unweighted cases).

The errors on the resolutions are obtained by 3SE checks and sine terms. The single-plane resolutions for the unweighted case are shown in Fig 136. Figs 137-139 show the 3SE estimates of the single-plane resolution errors for Trk34 (both weighted and unweighted cases), while Figs 140-142 show similar plots for the Trk01 detector. (See Table 4 for description of the detectors used in the 3SE checks).

| Error for Res$\{jn\Psi_n\}$ | | | | | |
|---|---|---|---|---|---|
| n | 2 | 3 | 4 | 5 | 6 |
| Detector A&C | 2.0, 14.0, 20.0% (j=1,4,5) | 6.0, 10.0% (j=1,2) | 7.0% (j=1) | 8.0% (j=1) | 27.0 (j=1) |
| Detector B | 2.0, 14.0, 20.0% (j=1,4,5) | 8.0, 14.0% (j=1,2) | 8.0% (j=1) | 12.0% (j=1) | 30% (j=1) |

| Error for three-plane correlators: $\langle\cos(\sum\Phi)\rangle$ | | | | | | | | | |
|---|---|---|---|---|---|---|---|---|---|
| $\sum\Phi$ | $2\Phi_2 + 3\Phi_3 - 5\Phi_5$ | | | $2\Phi_2 + 4\Phi_4 - 6\Phi_6$ | | | $2\Phi_2 - 6\Phi_3 + 4\Phi_4$ | | |
| | Type-1 | Type-2 | Type-3 | Type-1 | Type-2 | Type-3 | Type-1 | Type-2 | Type-3 |
| Combined resolution | 14.5% | 13.5% | 11.5% | 31.1% | 30.9% | 28.2% | 16.2% | 13.0% | 15.8% |
| Raw distribution ($\times10^{-4}$) (Unweighted, Weighted) | 2-10 | | | 2-10 | | | 2-10 | | |
| | $-8\Phi_2 + 3\Phi_3 + 5\Phi_5$ | | | $-10\Phi_2 + 4\Phi_4 + 6\Phi_6$ | | | $-10\Phi_2 + 6\Phi_3 + 4\Phi_4$ | | |
| | Type-1 | Type-2 | Type-3 | Type-1 | Type-2 | Type-3 | Type-1 | Type-2 | Type-3 |
| Combined resolution | 20.1% | 19.4% | 18.0% | 36.9% | 36.7% | 34.5% | 25.7% | 23.7% | 25.4% |
| raw distribution ($\times10^{-4}$) (Unweighted, Weighted) | 2-10 | | | 2-10 | | | 2-10 | | |

Table 20: Summary of systematic uncertainties for individual Res$\{jn\Psi_n\}$ terms (top part) and the final three-plane correlators (bottom part), for both weighted and unweighted cases.

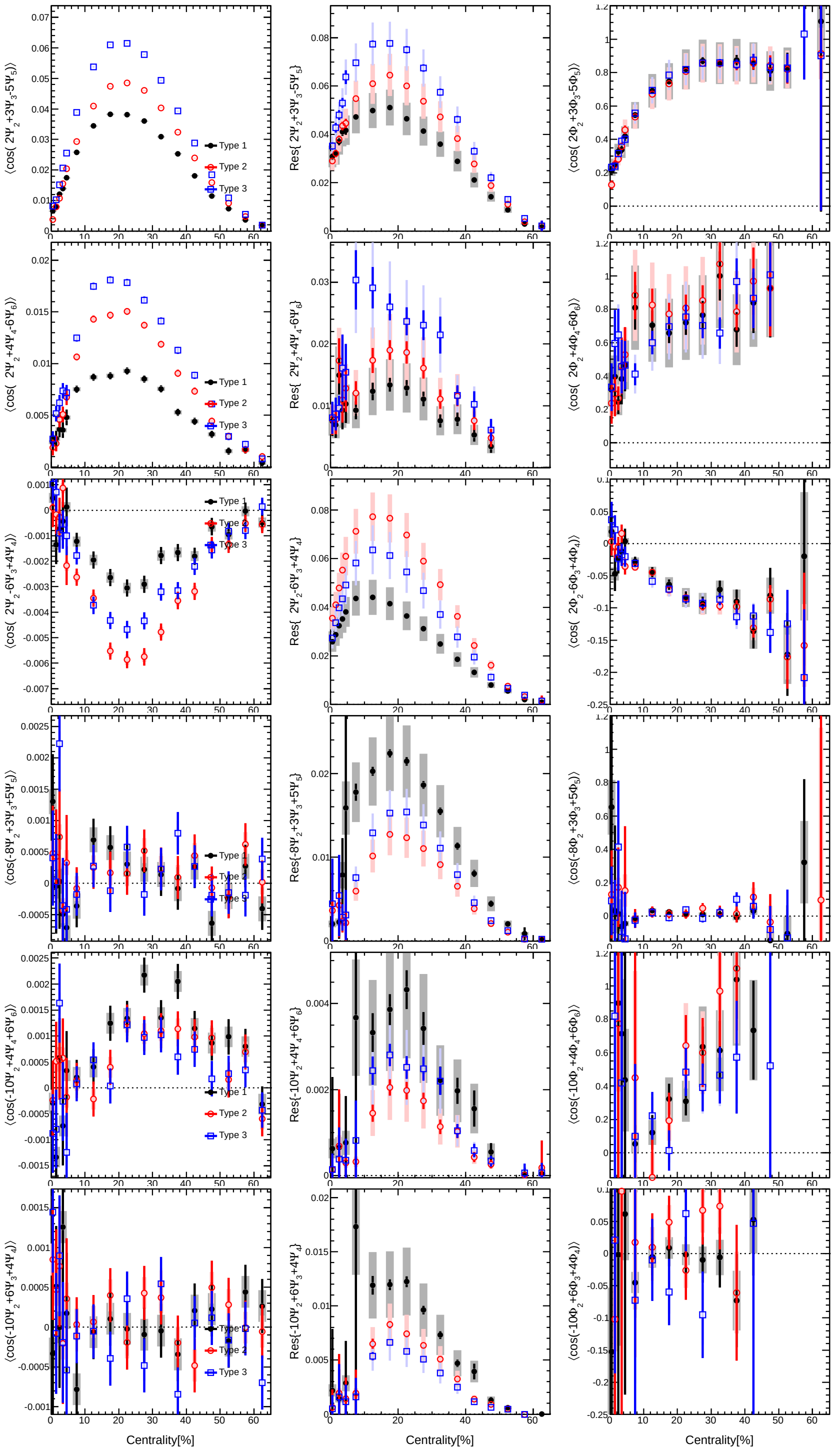

Figure 134: The raw signals (left plots), combined resolution corrections (middle plots) and corrected correlations (right plots) for the 3P correlators from tracking detectors for the Unweighted case. The three sets of data points correspond to the three Types.

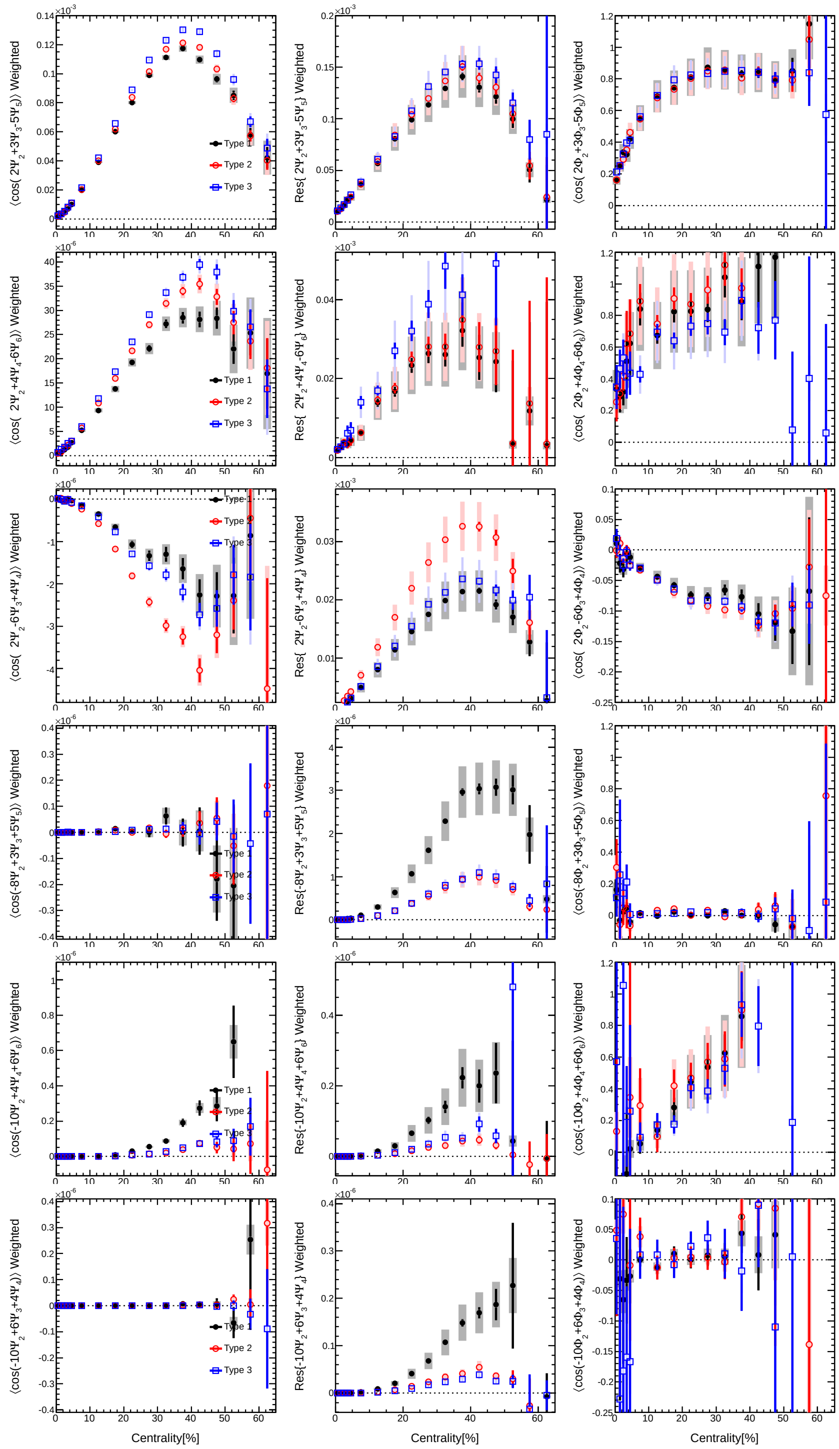


Figure 135: The raw signals (left plots), combined resolution corrections (middle plots) and corrected correlations (right plots) for the 3P correlators from tracking detectors for the weighted case. The three sets of data points correspond to the three Types.

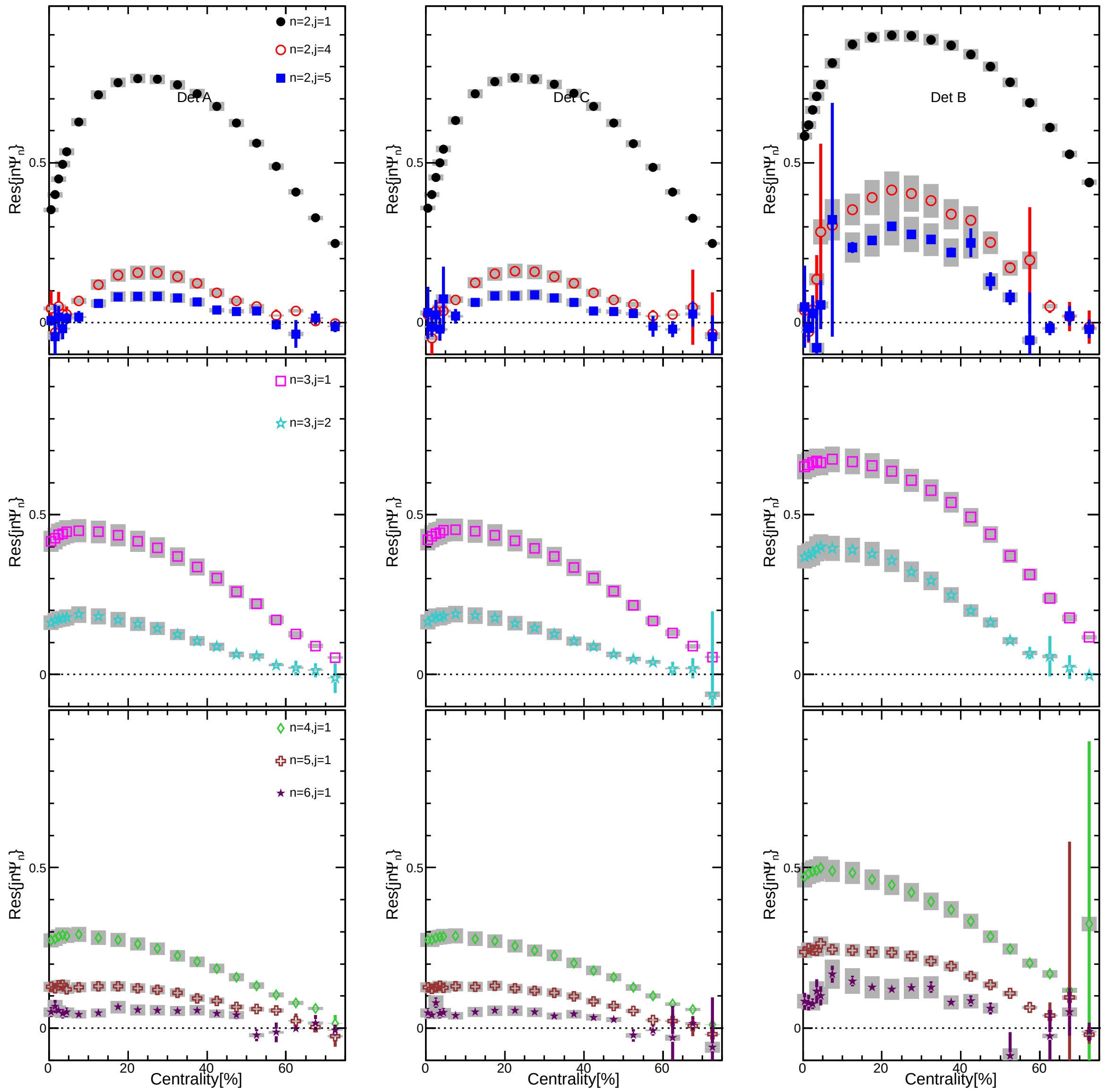


Figure 136: Centrality dependence of the resolution for unweighted individual event-planes associated with the three ID detectors used in the three-plane correlations.

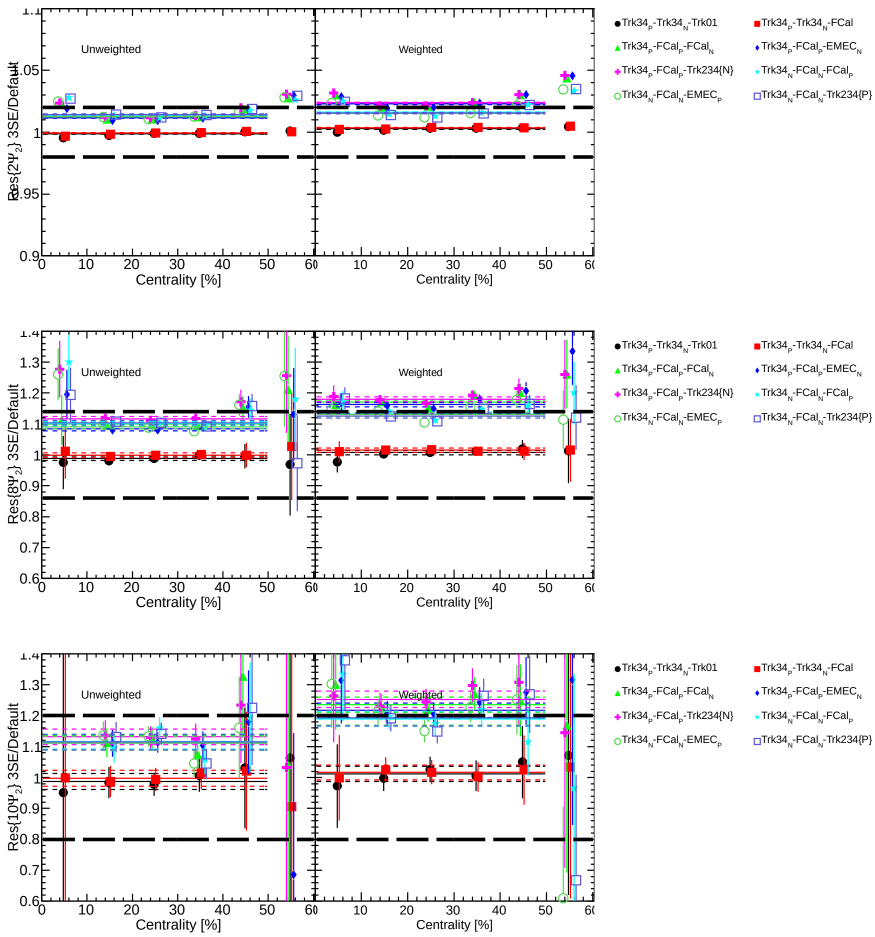


Figure 137: The ratio of the resolution for the Trk34$^{P/N}$ obtained from several three-subevent checks to the default two-subevent resolution for Res$\{j2\Psi_2\}$ as a function of centrality. From top to bottom the plots correspond to different values of $j$. The left (right) plots correspond to the Unweighted (Weighted) case. The colored-continuous lines show the mean deviation of the 3SE value from the default 2SE value in the (10-50)% centrality range, while the dashed-colored lines show the error of the mean deviation. The thick-dashed black lines show the error quoted from this check. Only those values of $j$ that are used in the analysis are shown.

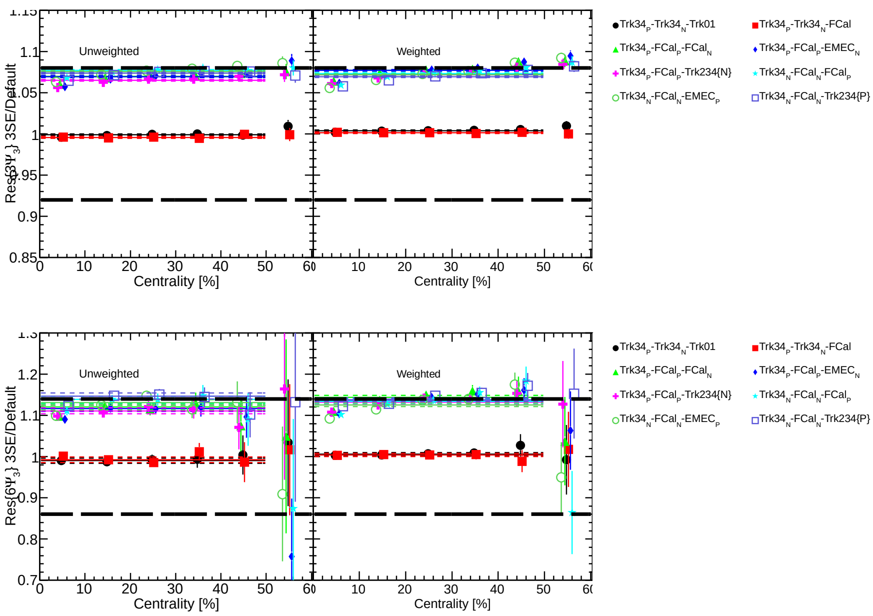

Figure 138: Same as previous plot but for Res{$j3\Psi_3$}(for Trk34)

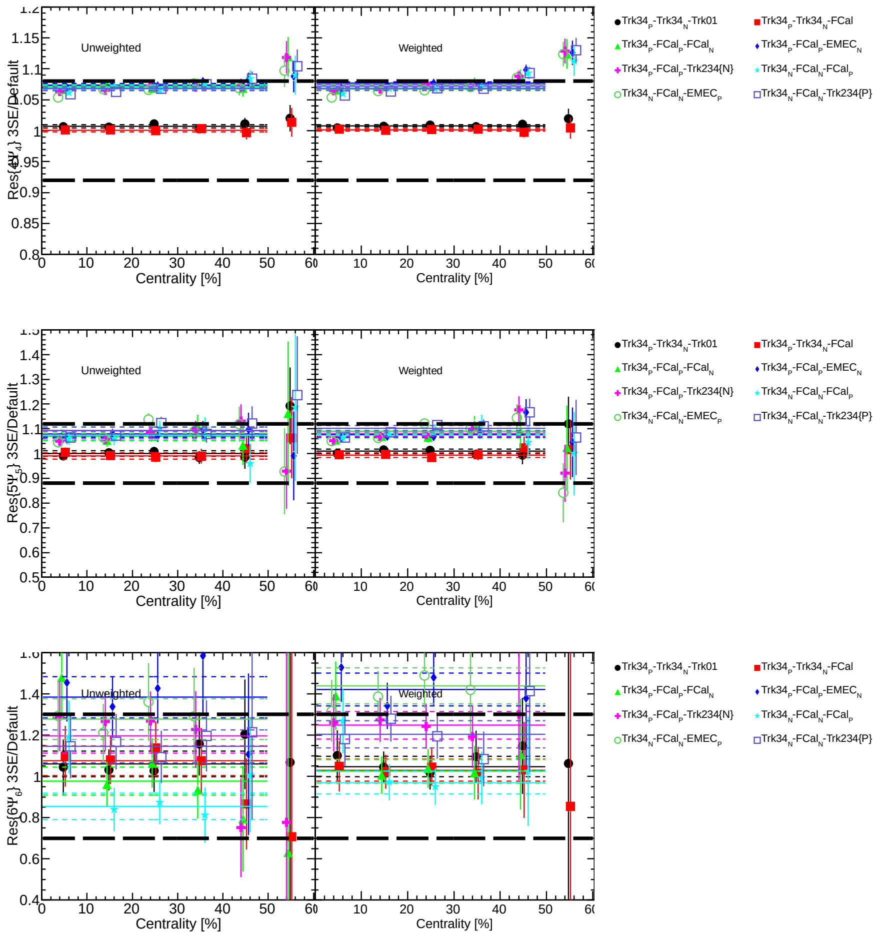


Figure 139: Same as previous plot but for Res{$4\Psi_4$} (Top), Res{$5\Psi_5$}(Middle) and Res{$6\Psi_6$}(Bottom) (for Trk34).

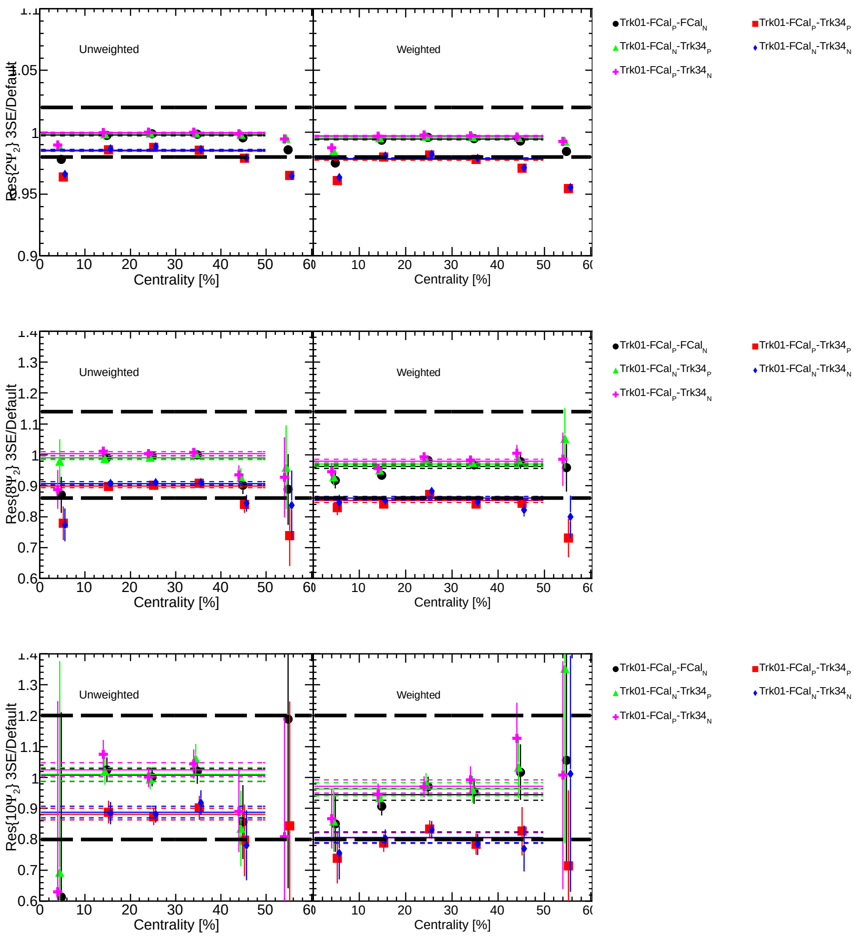


Figure 140: The ratio of the resolution for the $\mathrm{Trk01}^{\mathrm{P/N}}$ obtained from several three-subevent checks to the default two-subevent resolution for $\mathrm{Res}\{j2\Psi_2\}$ as a function of centrality. From top to bottom the plots correspond to different values of $j$. The left (right) plots correspond to the Unweighted (Weighted) case. The colored-continuous lines show the mean deviation of the 3SE value from the default 2SE value in the (10-50)% centrality range, while the dashed-colored lines show the error of the mean deviation. The thick-dashed black lines show the error quoted from this check. Only those values of $j$ that are used in the analysis are shown.

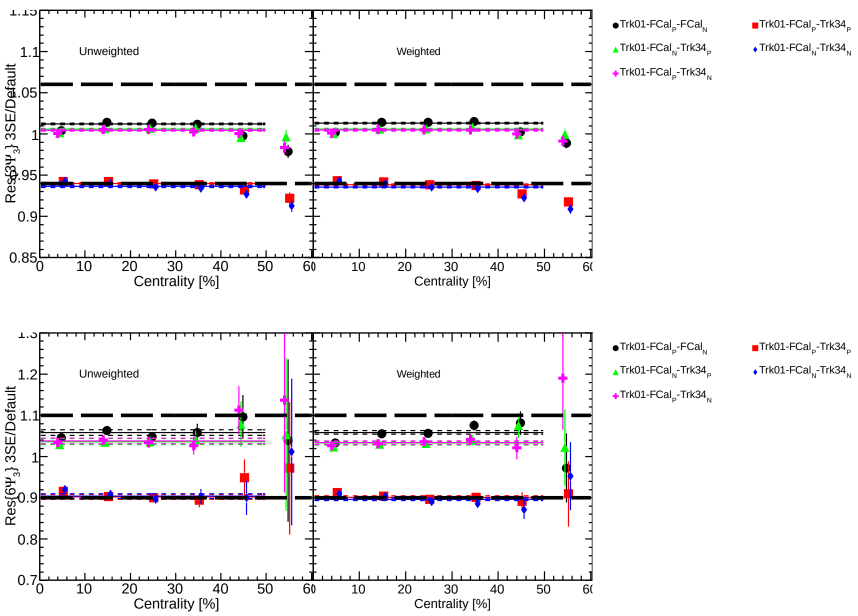


Figure 141: Same as previous plot but for Res$\{j3\Psi_3\}$(for Trk01)

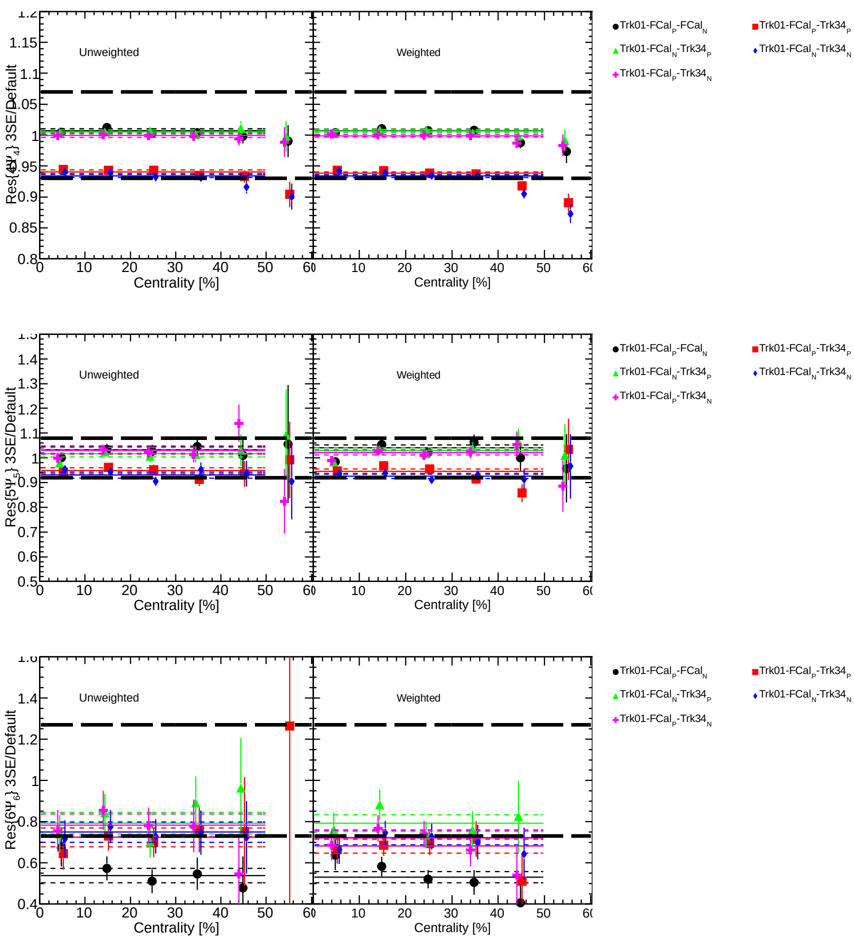


Figure 142: Same as previous plot but for Res{$4\Psi_4$} (Top), Res{$5\Psi_5$}(Middle) and Res{$6\Psi_6$}(Bottom) (for Trk01).

# 13 Appendix III: $|Q_n|$ for symmetric detectors (Weighted correlations)

For the weighted correlations it is ncesssary to ensure that the energy scale between the two-sides of the ECalFCal are identical. Otherwise using the 2SE method to obtain the resolutions can introduce some additional biases. This is also required in order to combine the symmetric measurements for the raw correlations.

The values for the $\langle Q_n \rangle$ and $\langle Q_n/Q_0 \rangle$ are shown in Figs. 143-144 for the ECalFCal and in Figs. 145-146 for the ID ($|\eta| \in (0.5, 2.5)$). These are the primary and cross-check detectors used for the 2P analysis. The difference between the two halves is at most 0.5% for the ECalFCal and 1.0% for the ID, and thus not large. Note that this difference is already accounted for while calculating the resolutions via 3SE checks and thus is not included as an additional error.

Similar plots for the symmetric detectors for the three-plane correlations analysis (the ECal) are shown in Figs. 147-148. The cross-check detector in this case was the ID with symmetric detectors made from $|\eta| \in (1.5, 2.5)$. Figs. 149-150 show similar plots for for the ID ($|\eta| \in (0.5, 2.5)$). In all cases the variation is less than 1%, and is already accounted for while calculating the resolution systematics vis 3SE methods.

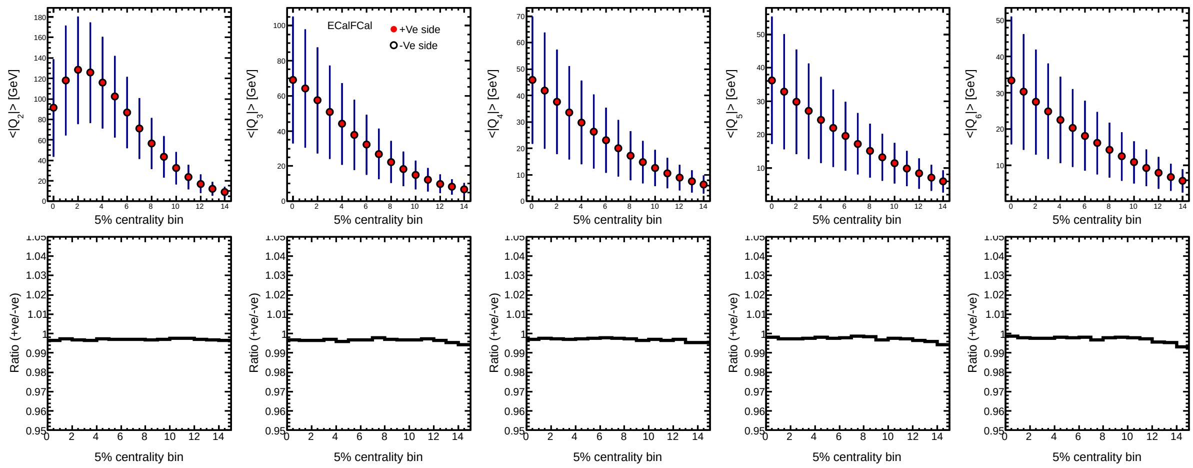


Figure 143: Top Panels: The $\langle Q_n \rangle$ for the +ve and -ve sides of the ECalFCal. The "Error-bars" are the rms-widths of the $Q_n$ distributions (and not the error of the $\langle Q_n \rangle$). Bottom panels show the ratio of the +ve to the -ve side. The ECalFCal is the main detector for the 2-plane correlation analysis.

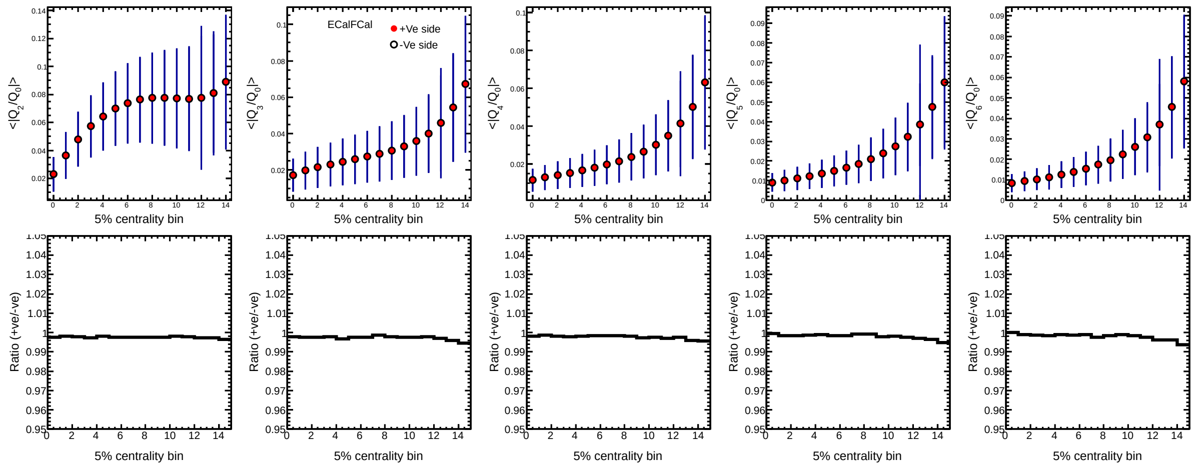


Figure 144: Top Panels: The $\langle Q_n/Q_0 \rangle$ for the +ve and -ve sides of the ECalFCal. Bottom panels show the ratio. The "Error-bars" are the rms-widths of the $Q_n/Q_0$ distributions (and not the error of the $\langle Q_n/Q_0 \rangle$). Bottom panels show the ratio of the +ve to the -ve side. The ECalFCal is the main detector for the 2-plane correlation analysis.

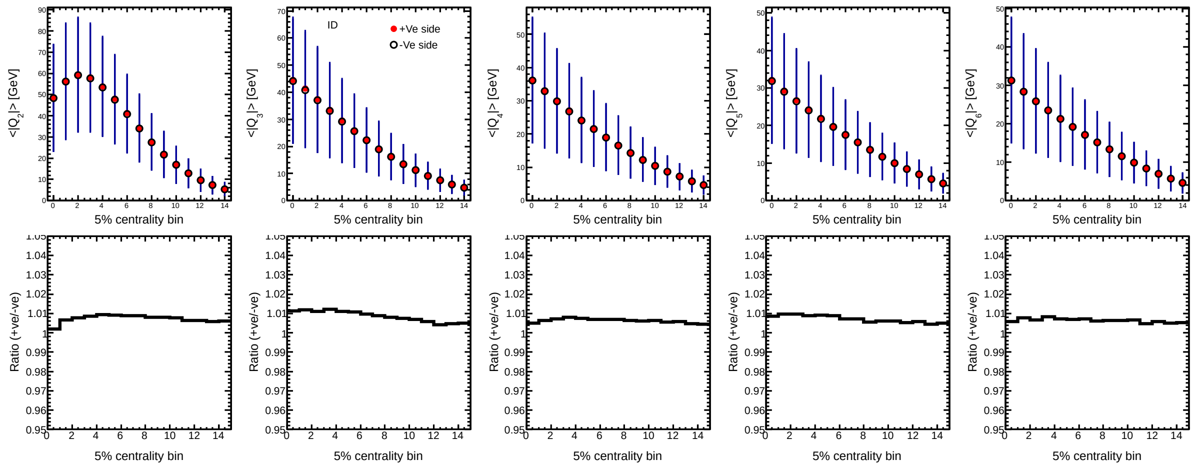


Figure 145: Top Panels: The $\langle Q_n \rangle$ for the +ve and -ve sides of the ID ($|\eta| \in (0.5, 2.5)$). Bottom panels show the ratio. The "Error-bars" are the rms-widths of the $Q_n$ distributions (and not the error of the $\langle Q_n \rangle$). Bottom panels show the ratio of the +ve to the -ve side. The ID ($|\eta| \in (0.5, 2.5)$) is the main cross-check detector for the 2-plane correlation analysis.

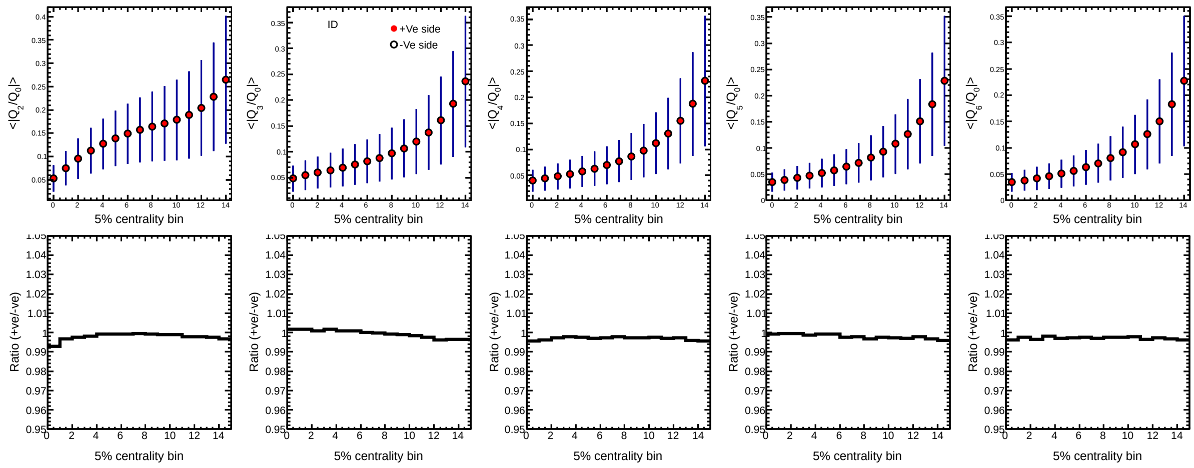


Figure 146: Top Panels: The $\langle Q_n/Q_0\rangle$ for the +ve and -ve sides of the ID ($|\eta| \in (0.5, 2.5)$). Bottom panels show the ratio. The “Error-bars” are the rms-widths of the $Q_n/Q_0$ distributions (and not the error of the $\langle Q_n/Q_0\rangle$). Bottom panels show the ratio of the +ve to the -ve side. The ID ($|\eta| \in (0.5, 2.5)$) is the main cross-check detector for the 2-plane correlation analysis.

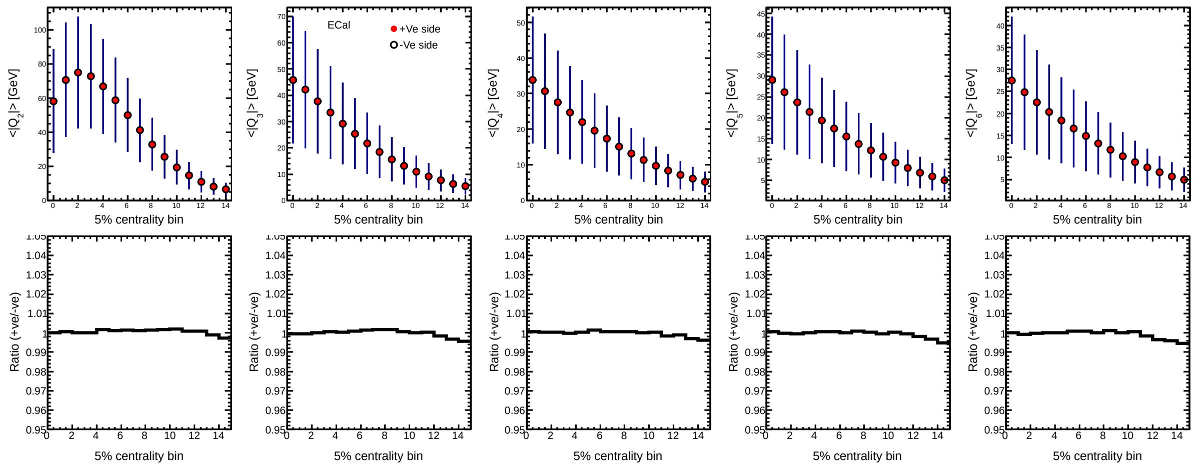


Figure 147: Top Panels: The $\langle Q_n\rangle$ for the +ve and -ve sides of the ECal. The “Error-bars” are the rms-widths of the $Q_n$ distributions (and not the error of the $\langle Q_n\rangle$). Bottom panels show the ratio of the +ve to the -ve side. The ECal is the main detector for the 3-plane correlation analysis.

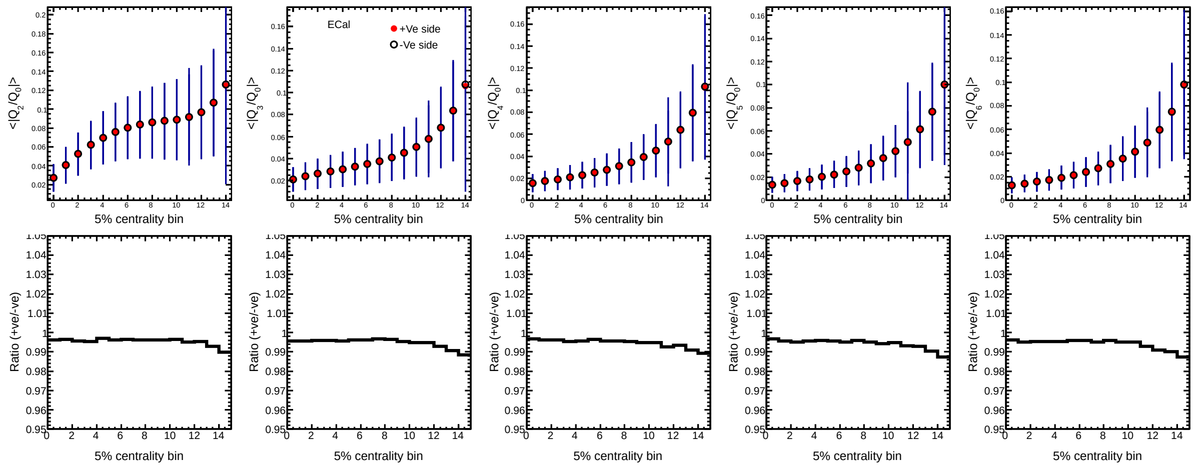


Figure 148: Top Panels: The $\langle Q_n/Q_0\rangle$ for the +ve and -ve sides of the ECal. Bottom panels show the ratio. The “Error-bars” are the rms-widths of the $Q_n/Q_0$ distributions (and not the error of the $\langle Q_n/Q_0\rangle$). Bottom panels show the ratio of the +ve to the -ve side. The ECal is the main detector for the 3-plane correlation analysis.

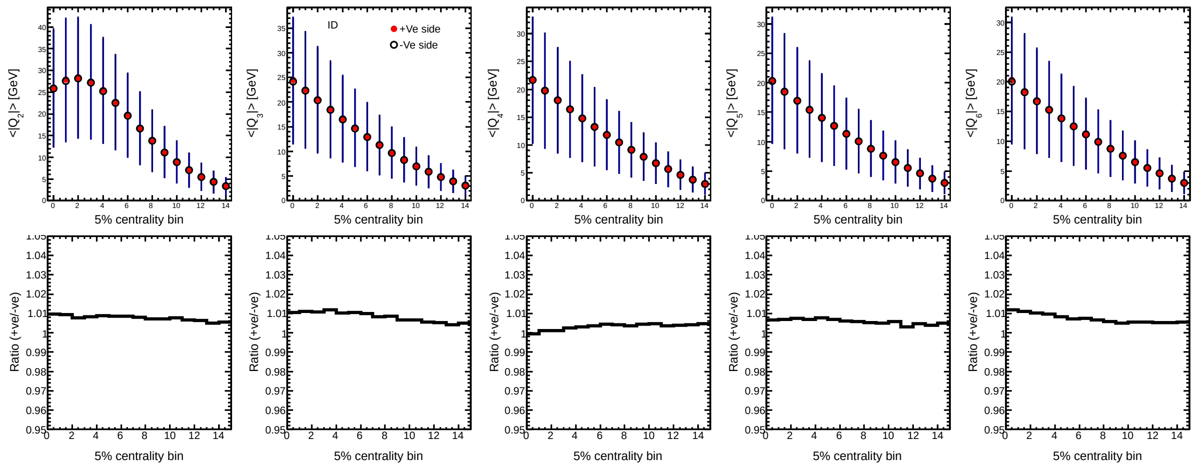


Figure 149: Top Panels: The $\langle Q_n\rangle$ for the +ve and -ve sides of the ID ($|\eta| \in (1.5, 2.5)$). Bottom panels show the ratio. The “Error-bars” are the rms-widths of the $Q_n$ distributions (and not the error of the $\langle Q_n\rangle$). Bottom panels show the ratio of the +ve to the -ve side. The ID is the main cross-check detector for the 3-plane correlation analysis.

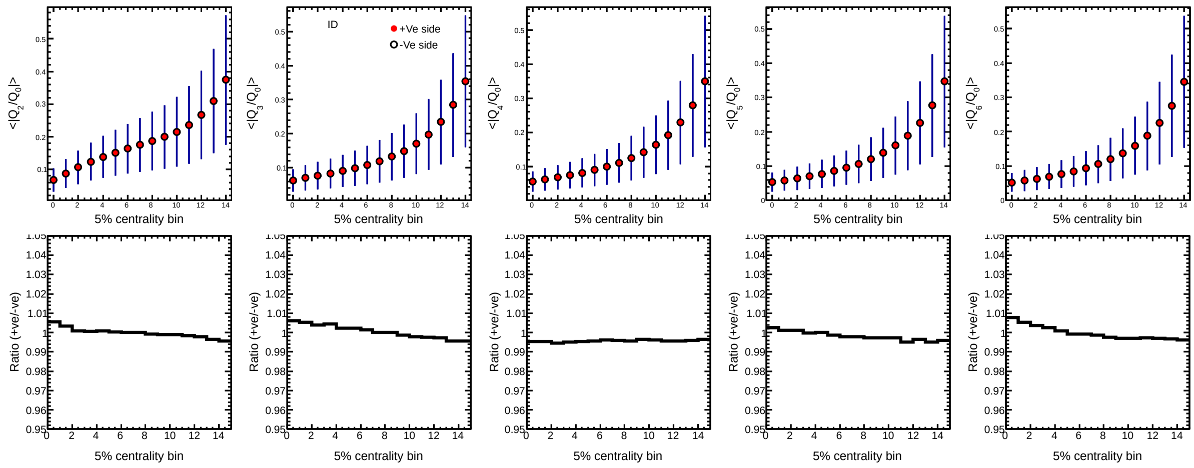


Figure 150: Top Panels: The $\langle Q_n/Q_0 \rangle$ for the +ve and -ve sides of the ID ($|\eta| \in (1.5, 2.5)$). Bottom panels show the ratio. The "Error-bars" are the rms-widths of the $Q_n/Q_0$ distributions (and not the error of the $\langle Q_n/Q_0 \rangle$). Bottom panels show the ratio of the +ve to the -ve side. The ID is the main cross-check detector for the 3-plane correlation analysis.

# 14 Appendix IV: $|Q_n|$ weighted correlations

The weighted correlations have been caluclated with the $q_n = Q_n/Q_0$ used as weights. In this section a comparison is done with the $Q_n$ used as the weighting factors. In such a scenario, the multiplicity fluctuations are also included in the correlations. Figs. 151 and 152 show the comparisons for the Two and Three-plane correlations (for default detectors). Thesystematic errors are not re-evaluated for the $Q_n$ weighting, instead identical values as the $q_n$ weighted case are used. The two-cases match almost exactly. This is not surprizing as The multiplicity in heavy-ion collisions is very large for EbyE fluctuations to have an appreciable effect.

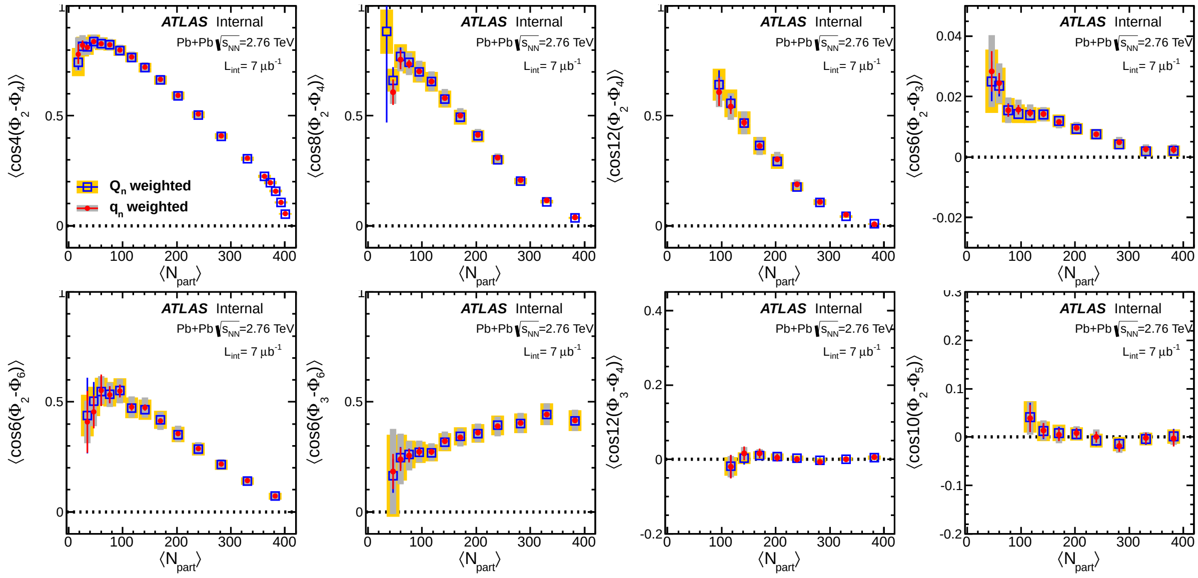


Figure 151: Comparison of the $q_n$ weighted Two-plane correlations to the $Q_n$ weighted correlations from the ECalFCal.

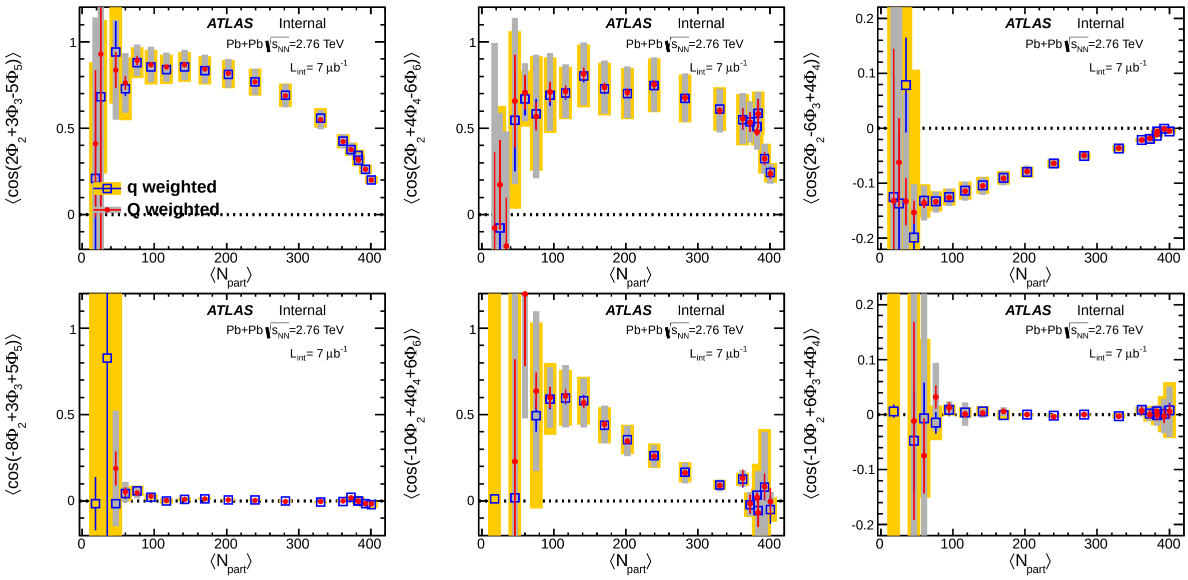


Figure 152: Comparison of the $q_n$ weighted Three-plane correlations to the $Q_n$ weighted correlations from the default detectors (ECal$_{P/N}$ & FCal).

# 15 Appendix V: Cross-check to evaluate effects of statistical fluctuations on weighted correlations

This section addresses a question raised by the Ed-board. The question was: since the weighted correlations have large powers of $q_n$ in the weighting, they can promote events that have fluctuated high which can affect the measured correlations. This section address that question.

It must be pointed out that the error calculations in the raw signals and resolutions properly accounts for statistical fluctuations. The errors are caluulated as "sum of weights squared". Thus if some events have large $q_n$ and contribute strongly to the correlations, their contribution to the statistical error will also be correspondingly large and will reflect in the final statistical error of the measurement

A data driven corss-check is also performed using the tracking detectors to further increase the confidence in the results. The two-plane correlators are measured by rejecting on average 50% of tracks in each event. This rejection enhances the effect of statistical fluctuations in the measurements and exposes the sensivivity of the measurements to such fluctuations. The results of this check are shown in Fig. 153. It is seen that the 50% rejected results are quite consistent with the default ID result. Note that the systematic errors have not been re-evaluated for the 50% rejected case instead the same systematic errors as the default ID are used. As the 50% rejected tracks are expected to have larger errors so the agreement would only improve.

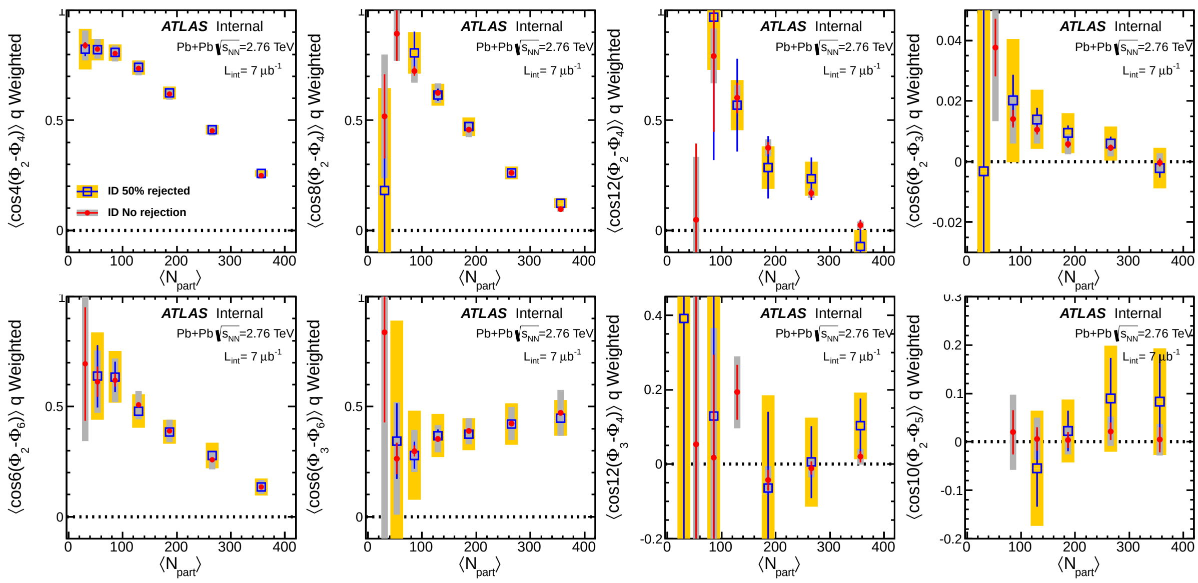


Figure 153: Comparison of the two-plane correlations as measured by the ID using all reconstructed tracks and ID with 50% tracks rejected at random.

# 16 Appendix VI: Some proofs

We shall demonstrate the correctness of Eq. 13. by using the two-plane correlator case as follows:

$$
\begin{aligned}
\langle \cos k(\Psi_n - \Psi_m) \rangle &= \langle \cos[k(\Psi_n - \Phi_n) - k(\Psi_m - \Phi_m) + k(\Phi_n - \Phi_m)] \rangle \\
&= \langle \cos k(\Psi_n - \Phi_n) \cos k(\Psi_m - \Phi_m) \cos k(\Phi_n - \Phi_m) \rangle \\
&\qquad + \text{terms with } \sin k(\Psi_n - \Phi_n), \sin k(\Psi_m - \Phi_m), \sin k(\Phi_n - \Phi_m) \text{ vanish} \qquad (52) \\
&= \langle \cos k(\Psi_n - \Phi_n) \cos k(\Psi_m - \Phi_m) \cos k(\Phi_n - \Phi_m) \rangle \qquad (53) \\
&= \langle \cos k(\Psi_n - \Phi_n) \rangle \langle \cos k(\Psi_m - \Phi_m) \rangle \langle \cos k(\Phi_n - \Phi_m) \rangle \qquad (54) \\
&= \mathrm{Res}\{k\Psi_n\} \mathrm{Res}\{k\Psi_m\} \langle \cos k(\Phi_n - \Phi_m) \rangle
\end{aligned}
$$

A few comments:

1. The average is always over several events.
2. The sine terms in Eq. 52 drop out because spread of $\Phi$ relative to $\Psi$ is independent between $n$ and $m$ (as they are measured in seperate detectors), and $\langle \sin k(\Phi_n - \Phi_m) \rangle = 0$ by construction since $dN/dk(\Phi_n - \Phi_m)$ distribution is an even function.
3. The average of the product of the cosine terms can be replaced by the product of the averages (from Eq. 53 to Eq. 54), because the spreads of $\Psi_n$ relative to $\Phi_n$, $\Psi_m$ relative to $\Phi_m$, and $\Phi_n$ relative to $\Phi_m$ are independent.

# References


[1] S. A. Voloshin, A. M. Poskanzer and R. Snellings, "Collective phenomena in non-central nuclear collisions," arXiv:0809.2949 [nucl-ex].

[2] D. A. Teaney, "Viscous Hydrodynamics and the Quark Gluon Plasma," arXiv:0905.2433 [nucl-th].

[3] H. Song, S. A. Bass, U. Heinz, T. Hirano and C. Shen, "Hadron spectra and elliptic flow for 200 A GeV Au+Au collisions from viscous hydrodynamics coupled to a Boltzmann cascade," Phys. Rev. C **83**, 054910 (2011) [arXiv:1101.4638 [nucl-th]].

[4] Z. Qiu and U. W. Heinz, "Event-by-event shape and flow fluctuations of relativistic heavy-ion collision fireballs," Phys. Rev. C **84**, 024911 (2011) [arXiv:1104.0650 [nucl-th]].

[5] ALICE Collaboration, Phys. Lett. B **708**, 249 (2012). arXiv:1109.2501 [nucl-ex].

[6] ATLAS Collaboration, arXiv:1203.3087 [hep-ex].

[7] CMS Collaboration, arXiv:1201.3158 [nucl-ex].

[8] J. L. Nagle and M. P. McCumber, Phys. Rev. C **83**, 044908 (2011), [arXiv:1011.1853 [nucl-ex]].

[9] D. Teaney and L. Yan, Phys. Rev. C **83**, 064904 (2011).

[10] PHENIX Collaboration, Phys. Rev. Lett. **105**, 062301 (2010) [arXiv:1003.5586 [nucl-ex]].

[11] ALICE Collaboration, Phys. Rev. Lett. **107**, 032301 (2011), [arXiv:1105.3865 [nucl-ex]].

[12] R. S. Bhalerao, M. Luzum and J. Y. Ollitrault, J. Phys. G **38** (2011) 124055, [arXiv:1106.4940 [nucl-ex]].

[13] R. S. Bhalerao, M. Luzum and J. Y. Ollitrault, Phys. Rev. C **84** (2011) 034910, [arXiv:1104.4740 [nucl-th]].

[14] A. Angerami, B. Cole, A. Milov and P. Steinberg "Cerntrality determination in 2010 Pb+Pb physics data collisions," ATLAS-COM-PHYS-2011-447, https://cdsweb.cern.ch/record/1347255

[15] J. Jia and S. Mohapatra, arXiv:1203.5095 [nucl-th].

[16] G. Aad *et al.* [ATLAS Collaboration], arXiv:1203.3087 [hep-ex];

[17] S. Milov, R. Debbe, M. Leyton, P. Steinberg "Support note on the measurement of the centrality dependence of charged particle spectra and RCP in lead-lead collisions at sNN = 2.76 TeV with the ATLAS detector at the LHC," https://cdsweb.cern.ch/record/1349513; ATL-COM-PHYS-2011-521, https://cdsweb.cern.ch/record/1351505; ATL-COM-PHYS-2011-790, https://cdsweb.cern.ch/record/1362023.

[18] "Measuring azimuthal anisotropy of particle productions in Pb+Pb collisions at 2.76 TeV using event plane method" ATL-COM-PHYS-2011-464, https://cdsweb.cern.ch/record/1349043

[19] "Fourier decomposition of two particle azimuthal correlations in Pb+Pb collisions at 2.76 TeV" ATL-COM-PHYS-2011-462; https://cdsweb.cern.ch/record/1349038

[20] A. M. Poskanzer and S. A. Voloshin, Phys. Rev. C **58**, 1671 (1998).

[21] PHENIX Collaboration, Phys. Rev. C **80**, 024909 (2009).

[22] E877 Collaboration, Phys. Rev. C **56**, 3254-3264 (1997).

[23] PHOBOS Collaboration, Phys. Rev. C **72**, 051901 (2005).

[24] ATLAS Collaboration, Phys. Lett. B **697**, 294 (2011), [arXiv:1012.5419 [hep-ex]].

[25] ATLAS Collaboration, Phys. Lett. B **710**, 363 (2012), [arXiv:1108.6027 [hep-ex]].

[26] ATLAS Collaboration, "Measurement of the distributions of event-by-event flow harmonics in lead–lead collisionsat $\sqrt{s_{NN}}$=2.76 TeV with the ATLAS detector at the LHC", arXiv:1305.2942 [hep-ex].

[27] M. Luzum and J.-Y. Ollitrault, "The event-plane method is obsolete", Phys. Rev. C 87, 044907 (2013) [arXiv:1209.2323 [nucl-ex]].

[28] R.S. Bhalerao, J. Y. Ollitrault and S. Pal, "Event-plane correlators", Phys. Rev. C 88, 024909 (2013)[arXiv:1307.0980 [nucl-th]].